CHEMICAL GENOMICS CENTRE
OF THE MAX PLANCK SOCIETY

technische universität
dortmund

MAX PLANCK INSTITUTE
OF MOLECULAR PHYSIOLOGY

Targeting the RNA-binding Proteins LIN28, METTL16 and YTHDF2 Using Small Molecules and Bifunctional Molecules

Dissertation

For the achievement of the academic degree of the

Doctor in Natural Sciences

(Dr. rer. Nat.)

Submitted to

The Faculty of Chemistry and Chemical Biology

Technical University Dortmund

by

Georg Lennart Goebel, M. Sc.

Born 24.08.1996 in Essen

Dortmund, 2024

1st Examiner:	Prof. Dr. Dr. h.c. Herbert Waldmann
2nd Examiner:	Prof. Dr. Hannes Mutschler
Supervisor:	V-Prof. Dr. Peng Wu

The work presented in this dissertation was performed under the supervision of V-Prof. Dr. Peng Wu at the Chemical Genomics Center of the Max Planck Institute of Molecular Physiology and the Faculty of Chemistry and Chemical Biology at the Technical University of Dortmund in the period from June 2021 to November 2024.

Results displayed in this dissertation contributed to the following publication:
(#: *These authors contributed equally to this work*.)

Goebel, Georg L.#; Giannino, Nicole#; Lampe, Philipp#; Qiu, Xiaqiu; Schloßhauer, Jeffrey; Sievers, Sonja; Imig, Jochen; Wu, Peng*. Profiling Cellular Morphological Changes Induced by Dual-targeting PROTACs of Aurora Kinase and RNA-binding Protein YTHDF2. *ChemBioChem*, **2024**, e202400183, doi:10.1002/cbic.202400183.

Liu, Yang#; **Goebel, Georg L.#**; Kanis, Laurin; Hastürk, Oguz; Kemker, Claus; Wu, Peng*. Aminothiazolone Inhibitors Disrupt the Protein−RNA Interaction of METTL16 and Modulate the m^6A RNA Modification. *JACS Au*, **2024**, *4*(4), 1436−1449.

Borgelt, Lydia#, Hohnen, Lisa#; Pallesen, Jakob S.#; Hommen Pascal#; **Goebel, Georg L.#**; Bosica Francesco; Liu, Yang; O'Mahony, Gavin*; Wu, Peng*. *N*-Biphenyl Pyrrolinones and Dibenzofurans as RNA-Binding Protein LIN28 Inhibitors Disrupting the LIN28–*Let-7* Interaction. *ACS Med. Chem. Lett.*, **2023**, *14*(12), 1707–1715.

Borgelt, Lydia#; Huang, Fubao#; Hohnen, Lisa; Qiu, Xiaqiu; **Goebel, Georg L.**; Hommen, Pascal, Wu, Peng*. Spirocyclic Chromenopyrazole Inhibitors Disrupting the Interaction between the RNA-Binding Protein LIN28 and *Let-7*. *ChemBioChem* **2023**, *24*(17), e202300168.

Goebel, Georg L.#; Hohnen, Lisa#; Borgelt, Lydia; Hommen, Pascal; Qiu, Xiaqiu; Lightfoot, Helen; Wu, Peng*. Small molecules with tetrahydroquinoline-containing Povarov scaffolds as inhibitors disrupting the Protein–RNA interaction of LIN28–*let-7*. *Eur. J. Med. Chem.*, **2022**, *228*, 114014.

Borgelt, Lydia#; Fu Li#, Hommen, Pascal#; Lampe, Philipp#; Hwang, Jimin; **Goebel, Georg L.**; Sievers, Sonja; Wu, Peng*. Trisubstituted Pyrrolinones as Small-Molecule Inhibitors Disrupting the Protein–RNA Interaction of LIN28 and *Let-7*. *ACS Med. Chem. Lett.*, **2021**, *12*(6), 893–898.

Jiang, Mao#; Giannino, Nicole; **Goebel, Georg L.**; Wu, Peng*. LIN28-Targeting Chromenopyrazoles and Tetrahydroquinolines Induced Cellular Morphological Changes and Showed High Biosimilarity with BRD PROTACs *ChemMedChem* **2024**, e202400547, doi.org/10.1002/cmdc.202400547.

Qiu, Xiaqiu#, Kemker, Claus#; **Goebel, Georg L.**; Lampe, Philipp; Gasper, Raphael; Wallis, Nadav; Schiller, Damian; Sievers, Sonja; Yeo, Gene W.; Wu, Peng*. Phenylpyrazoles as m^6A RNA-binding protein YTHDF2 inhibitors regulate the cellular RNA methylation level. [*Manuscript submitted*].

The work of the author also contributed to the following publications during the PhD studies:

Goebel, Georg L.#; Qiu, Xiaqiu; Wu, Peng. Kinase-targeting small-molecule inhibitors and emerging bifunctional molecules. *Trends Pharmacol. Sci.*, **2022**, *43*(10), 866-881.

Results displayed in this dissertation contributed to the following Master theses:

Hohnen, Lisa. "Assay development and biological evaluation of small-molecule inhibitors targeting the protein-RNA interaction of LIN28 and *let-7*", Master Thesis, **2021**.

Kanis, Laurin. "Design and Synthesis of Bifunctional Molecules as Degraders of the RNA-Binding Protein METTL16", Master Thesis, **2023**.

Kemker, Claus. "Identification and Evaluation of Small Molecules Targeting the m^6A RNA-modifying Proteins YTHDF2 and METTL16", Master Thesis, **2023**.

“Little by little, one travels far.”

- J.R.R. Tolkien

Acknowledgments

I am sincerely grateful for the opportunity to pursue my PhD at the Chemical Genomics Center in Dortmund. During my time as a PhD student, I gained invaluable experiences that significantly expanded my knowledge and skills. Although the journey was sometimes challenging, I cherish the many memories created through the supportive environment and especially the people at both the CGC and MPI. I very much appreciate everyone who contributed to this important phase of my life.

First and foremost, I would like to thank V-Prof. Dr. Peng Wu for his unwavering support and his motivating presence over the past four years. He has been a witness to my development from a master student to a PhD candidate, guiding me with indispensable insight and encouragement. Working on such challenging and impactful research topics was exciting and enabled me to become part of the chemical biology research community.

Second, I would like to express my appreciation to Prof. Dr. Dr. h.c. Herbert Waldmann for taking over the role of the first examiner. Also, I want to thank him for founding the Chemical Genomics Center and for fostering the vital alliance between academic and industrial research. Without these efforts, my pursuit of graduating as Dr. rer. nat. would not have been possible.

Third, I would like to thank Prof. Dr. Hannes Mutschler for taking responsibility as the second examiner of this thesis.

I am also grateful to Prof. Dr. Daniel Summerer and Prof. Dr. Markus Kaiser for being members of my Thesis Advisory Committee. They both initiated fruitful discussions, provided constructive feedback, and offered immense encouragement throughout my PhD.

Next, I would especially like to thank the talented biologists involved in the manifold evaluation of my compounds. Scientists to be mentioned are Dr. Lydia Borgelt, Lisa Hohnen, Yang Liu, Xiaqiu Qiu, and Leon Wagner. I appreciate their extensive testing of my compounds in numerous assays, which was crucial to the success of my research.

Special thanks go to my exceptional master students, Laurin Kanis and Claus Kemker. Both significantly contributed to my work, playing a key role in shaping our research projects. Besides our truly enjoyable time working together in A3.11, I deeply value every moment we shared, which helped us become the close friends we are today.

Furthermore, I would also like to extend my gratitude to all the co-authors of the publications resulting from this work for their valuable contributions.

I would like to acknowledge the Compound Management and Screening Center (COMAS) for conducting most of the small-molecule screenings from this work and for the discussions and suggestions on the screening assays. Names to be mentioned include Dr. Sonja Sievers, Dr. Philipp Lampe, and Carina Seitz.

Next, I want to thank both the NMR and Chromatography teams located in MPI and the TU Dortmund. Their efficient and reliable sample processing greatly enhanced the smooth workflow of my projects and was crucial to all the publications. A special thanks to Jens Warmers, who kept every instrument running at Department 4 and now continues to be of great value for the HRMS facility at TU Dortmund.

I would also like to thank Dr. Gavin O'Mahony and his team from AstraZeneca for their fruitful cooperation on the trisubstituted pyrrolinone project.

Furthermore, I am deeply grateful for the opportunity to be a member of the International Max Planck Research School for Living Matter. The many workshops, the symposium, the retreats as well as the many social gatherings not only contributed to my development as a researcher but also fostered new friendships. I especially want to acknowledge the opportunities to attend international conferences which were extremely valuable for scientific reasons and for cultural insights. All of this would not have been possible without Dr. Lucia Sironi and Christa Hornemann, who organized the excellent graduate program with expertise and passion.

I want to thank the current and former members of the Wu group, the CGC, and Department 4 at MPI of Molecular Physiology for providing a great working atmosphere and scientifically valuable discussions. Dr. Debora Bruzzese and Birgit Apprecht are greatly acknowledged for coordinating and supporting the CGC in many ways.

To conclude with the work-related part of this appreciation, I would like to express my gratitude to the many proofreaders who helped shape this thesis and made it more accessible to readers. Therefore, I thank V-Prof. Dr. Peng Wu once more, Siska Führer, Eric Ogel, Laurin Kanis, and Claus Kemker for the efficient and very helpful comments and corrections.

Alongside the many professional connections I made at CGC, I want to especially highlight the close friendships formed during my PhD. I am particularly grateful to Dr. Christian Grethe, Dr. Mirko Schmidt, and Sarah Recknagel, with whom I shared many thrilling climbing adventures.

I would also like to dedicate a special thanks to the 'AG Goebel & Friends,' including Laurin Kanis, Claus Kemker, Eric Ogel, Anna Schöne, Cedrik Kühling, and Kai Gallant. They created many enjoyable memories both at work and beyond. In particular, the various retreats we organized were a true pleasure and played a significant role in helping us form an exceptional team.

Last but not least, I want to thank my parents, my brothers, and my friends who supported and motivated me during my studies in many ways and made it much more bearable.

Table of Contents

Abstract

The interaction of RNA-binding proteins (RBPs) and corresponding RNAs plays a critical role in various cellular pathways, which once dysregulated can lead to numerous human diseases. Therefore, the discovery of small molecules disrupting these protein–RNA interactions represents a novel and rapidly emerging strategy for developing chemical probes to elucidate the cellular functions of RBPs and therapeutic agents with innovative mechanisms of action. Although some small-molecule inhibitors targeting selected RBPs have already been reported, there is huge potential to develop new inhibitors with improved potency, selectivity, or reduced cytotoxicity. In this thesis, I synthesized small-molecule inhibitors to target three distinct RBPs, the oncogenic miRNA-binding protein LIN28 regulating the miRNA biogenesis, the tumor-promoting *N*6-methyladenosine (m^6A) methyltransferase-like protein 16 (METTL16) installing m^6A mRNA modifications, and the YTH-domain containing family protein 2 (YTHDF2) recognizing and destabilizing m^6A mRNA.

First, LIN28 was found to negatively regulate *let-7* miRNAs which suppress the translation of numerous oncogenic proteins. Thus, overexpression of the RBP in many human cancers makes LIN28 a key driver of tumor progression and metastasis and it depicts a promising target to develop new anti-cancer therapeutics. The reported LIN28 inhibitors exhibit poor inhibitory potencies, insufficient characterization of their inhibitory modes, and poor cellular activity. In this part of the thesis, both scaffold- and screening-based approaches were employed to identify new LIN28 inhibitors with improved potencies. In the scaffold-based approach, a reported tetrahydroquinoline LIN28 inhibitor **8** was extensively investigated for its structure-activity relationship (SAR), leading to an analog with improved inhibitory activity. In the latter, screening-based approach a fluorescence polarization (FP)-based assay was utilized to identify new LIN28 inhibitors via screening of an in-house small-molecule library. After identifying the most active pyrrolinone **64**, a successive SAR study revealed biphenyl- and dibenzofuran compounds that showed a 5-fold improved cellular effect in inducing *let-7* maturation. By providing these well-characterized and potent inhibitors, a valuable foundation was established for developing LIN28-targeting chemical probes and novel anticancer drug candidates.

Second, the epitranscriptomic methylation of at the *N*6-positions of adenines (m^6A) represents a highly dynamic and reversible modification that not only alters the molecular characteristics of RNA but also impacts the landscape of natural binding partners which in turn tightly regulates the fate of the RNA. The installation of m^6A on several coding- and non-coding RNAs was found to be orchestrated by the methyltransferase-like protein 16 (METTL16), which plays a tumor-promoting role in cancers by co-functioning with other RBPs. Due to the lack of small-molecule modulators of METTL16, this work focused on the identification and evaluation of the first-in-class inhibitors using a discovery pipeline that started with an FP-based screening. Structural optimization of the initially identified aminothiazolone **105** yielded inhibitors, such as compound **154**, that showed potent single-digit micromolar inhibitory activity against METTL16–RNA interactions. The identification of the

aminothiazolone inhibitors provided useful probes for the elucidation of the biological function of METTL16 upon perturbation and set the foundation to evaluate the therapeutic potential of METTL16 inhibition via small molecules.

Third, besides the installation of m^6A modifications, accumulating evidence suggested that the m^6A-recognizing protein YT521B homology domain family 2 protein (YTHDF2) is associated with various biological processes impacting apoptosis, cell cycle change, metastasis, and proliferation in human diseases. The m^6A reader recently emerged as a promising drug target and only a few limited examples of inhibitors with non-favorable potency and selectivity are currently available. In this part of the thesis, efforts were made to target YTHDF2 with small molecules and associated bifunctional molecules: Initially, YTHDF2-degradation was induced by treating the RBP with pyrimidine-based PROTACs, setting the foundation for ongoing efforts in developing YTHDF2-selective degraders. Alternatively, the discovery of small-molecule inhibitors by means of a rational design- and a screening-based approach led to the identification of phenyl pyrazoles as one of the first structurally modified and characterized YTHDF2 inhibitor series. Structural optimization of the original hit compound revealed a 1-naphtoyl-containing analog **284** that showed potent anti-YTHDF2 activity *in vitro* and *in cellulo*, providing a feasible lead structure for the subsequent development of potent and selective small molecules targeting YTHDF2.

Collectively, the results of this thesis demonstrated the effectiveness of targeting therapeutically relevant RBPs using a variety of small-molecule-based strategies including both scaffold-based approaches and screening-based efforts that led to the identification of new chemical modalities. The characterized compounds, together with the established assays described in this thesis, will be of great value for the future development of small molecules targeting RBPs.

Zusammenfassung

Die Interaktion von RNA-bindenden Proteinen (RBP) und entsprechender RNA spielt eine entscheidende Rolle in verschiedenen zellulären Prozessen, die bei Fehlregulation zu zahlreichen Krankheiten führen können. Daher stellt die Entdeckung von *small molecules*, die diese Protein-RNA-Interaktionen inhibieren, eine neuartige Strategie zur Entwicklung chemischer Werkzeuge zur Aufklärung der zellulären RBP-Funktionen und therapeutischen Wirkstoffen mit innovativen Wirkmechanismen dar. Obwohl einige Berichte über *small-molecule* Inhibitoren bereits erwähnt wurden, gibt es einen erheblichen Spielraum für Verbesserungen hinsichtlich Potenz, Selektivität oder Zytotoxizität. In dieser Arbeit habe ich einzelne *small-molecule* Inhibitoren synthetisiert, um drei verschiedene RBP zu modulieren: Das onkogene miRNA-bindende Protein LIN28, die tumorfördernde *N*6-Methyladenosin (m^6A) Methyltransferase METTL16 und das m^6A RNA-destabilisierende Protein YTHDF2.

LIN28 reguliert die Reifung von *let-7* miRNAs, welche die Translation zahlreicher onkogener Proteine unterdrücken. Die Überexpression des RBP in vielen menschlichen Krebserkrankungen macht LIN28 daher zu einem Haupttreiber der Tumorprogression und Metastasierung, wodurch es ein vielversprechendes Ziel für die Entwicklung neuer Krebstherapeutika darstellt. Die wenig berichteten LIN28-Inhibitoren zeigen jedoch geringe inhibitorische Potenz, unzureichende Charakterisierung ihrer inhibitorischen Mechanismen und geringe zelluläre Aktivität. Für diese Arbeit wurden daher Scaffold- und Screening-basierte Ansätze verwendet, um neue LIN28-Inhibitoren mit verbesserter Potenz zu identifizieren. Im erstgenannten Ansatz wurde ein veröffentlichter Tetrahydroquinolin LIN28-Inhibitor **8** umfassend hinsichtlich seiner Struktur-Wirkungs-Beziehung (SAR) untersucht, was zu einem Analogon mit verbesserter inhibitorischer Aktivität führte. Im Gegensatz dazu beinhaltete der Screening-basierte Ansatz einen Fluoreszenz-Polarisations-basierten Assay zur Identifizierung neuer LIN28-Inhibitoren. Nach der Identifizierung des aktivsten Pyrrolinon **64** wurde eine nachfolgende SAR-Studie durchgeführt, die wiederum Biphenyl- und Dibenzofuran-Verbindungen mit fünffach verbesserten zellulären Effekten hinsichtlich der Induktion von *let-7*-Reifung hervorbrachte. Durch die Bereitstellung dieser gut charakterisierten und potenten Inhibitoren wurde eine wertvolle Grundlage für die Entwicklung von LIN28-addressierenden chemischen Werkzeugen und neuartigen Krebstherapeutika geschaffen.

Die epitranskriptomische Methylierung der *N*6-Positionen von Adeninen (m^6A) beschreibt eine dynamische und reversible Modifikation, die nicht nur die molekularen Eigenschaften von RNA verändert, sondern auch die Variation natürlicher Bindungspartner beeinflusst, die wiederum das Schicksal der RNA regulieren. Die Installation von m^6A auf verschiedenen kodierenden und nicht kodierenden RNA wird von dem methyltransferase-ähnlichen Protein 16 (METTL16) koordiniert, welches in Krebserkrankungen eine tumorfördernde Rolle spielt, indem es mit anderen RBP interagiert. Aufgrund fehlender experimenteller Berichte über *small-molecule* Modulatoren des RNA-

modifizierenden Proteins (RMP) konzentrierte sich diese Arbeit auf die Identifizierung und Evaluierung der ersten METTL16-Inhibitoren ihrer Art unter Verwendung einer Identifikationspipeline, die mit einem FP-basierten Screening begann. Die strukturelle Optimierung des anfänglich identifizierten Aminothiazolons **105** ergab Inhibitoren, wie bespielsweise Verbindung **154**, die eine potente einstellige mikromolare inhibitorische Aktivität gegen METTL16-RNA-Interaktionen zeigten. Die Identifizierung der Aminothiazolon-Inhibitoren liefert nützliche chemische Stoffe zur Aufklärung der biologischen Funktion von METTL16 und legt die Grundlage zur Bewertung des therapeutischen Potenzials der METTL16-Hemmung durch *small molecules*.

Neben der Installation von m^6A-Modifikationen deuten vermehrt Forschungsergebnisse darauf hin, dass das m^6A-erkennende Protein YT521B-Homologiedomäne-Familie 2 (YTHDF2) mit verschiedenen biologischen Prozessen in menschlichen Krankheiten in Verbindung steht, die Apoptose, den Zellzyklus, die Metastasierung oder die Proliferation beeinflussen. Das m^6A-lesende Protein hat erst kürzlich als vielversprechendes Ziel für Medikamente Aufmerksamkeit erlangt, weshalb Berichte über potente und selektive Modulatoren fehlen. In dieser Arbeit wurden zwei unterschiedliche Ansätze verfolgt, um YTHDF2 zu inhibieren. Zunächst wurde die YTHDF2-Degradation durch Behandlung des RBP mit pyrimidin-basierten PROTACs induziert, was die Grundlage für laufende Bemühungen zur Entwicklung von YTHDF2-selektiven PROTACs schaffen sollte. Alternativ führte die Entdeckung von *small-molecule* Inhibitoren mittels eines rationalen Design- und eines Screening-basierten Ansatzes zur Identifizierung von Phenylpyrazolen als eine der ersten gut charakterisierten YTHDF2-Inhibitoren. Die strukturelle Optimierung des ursprünglichen Treffers ergab ein 1-Naphthoyl enthaltendes Analogon **284**, das eine potente anti-YTHDF2-Aktivität *in vitro* und *in cellulo* zeigte und eine potenziell fundamentale Struktur für die weitere Entwicklung von *small molecules* zur Inhibierung von YTHDF2 für biologische und therapeutische Anwendungen darstellt.

Insgesamt konnten die Ergebnisse dieser Arbeit die Wirksamkeit der Inhibition therapeutisch relevanter RBP mittels verschiedener Strategien basierend auf *small molecules* demonstrieren. Während Scaffold-basierte Ansätze sich auf die Optimierung gegebener RBP-Inhibitoren konzentrierten, führten Screening-basierte Bemühungen zur Identifizierung neuer chemischer Modalitäten. Die identifizierten Verbindungen sowie die in dieser Arbeit etablierten Assays werden wertvoll für die zukünftige Entwicklung von *small molecules* zur Aufklärung und Modulation von RBP sein.

1 Introduction

1.1 Roles of RNA in biology

The central dogma of molecular biology postulated that ribonucleic acid acts as an intermediate between DNA and protein synthesis almost seven decades ago.[1] Although the fundamental concept of genetic information flow within a biological system remains one of the most important functions of RNA, recent efforts indicated that RNA could play diverse biological roles. While three-quarters of the human genome is transcribed into RNA, only about 1.5% of those RNA molecules were shown to encode for proteins.[2] Considering this remarkable discrepancy, many methods were developed to study the rather unexplored field of RNA biology. Major achievements in this regard were sequencing techniques to detect RNA species,[3] polymorphisms and expression levels of all types of RNAs,[2,4] helping society to better understand their cellular function and regulation.

Generally, coding RNA and non-coding RNA (ncRNA) are the two main classes of RNAs. Coding-RNAs consist of messenger RNAs (mRNAs) which are complementary nucleic acid sequences of a corresponding DNA section coding for proteins. The class of ncRNAs, on the other hand, is characterized by numerous different subclasses that are either directly involved in gene regulation or indirectly alter the process. Ribosomal RNA (rRNA) or transfer RNA (tRNA) for example are key players in the translation of mRNAs, while small nuclear RNAs (snRNAs) or small nucleolar RNAs (snoRNAs) were shown to be involved in RNA processing.[5] Another subclass of small ncRNAs consists of micro RNAs (miRNAs) which were shown to be mainly involved in post-transcriptional regulation of gene expression by silencing RNA translation into proteins.[6] Complementary to the small ncRNAs, long non-coding RNAs (lnRNAs) are defined as transcripts consisting of more than 200 nucleotides.[7] While several functions of lnRNAs involving regulation of gene transcription, epigenetics, or DNA replication were investigated over the last few decades, many roles of lnRNAs remain unknown.[8–10]

Despite the number and sequence of nucleotides characterizing RNA, functions of the individual transcripts were shown to be majorly dependent on their secondary- and tertiary structure.[11] Similar to proteins, many structural elements define the three-dimensional appearance of an RNA molecule and consequently its function. Next to helices, there are motifs such as a variety of loops (e.g. hairpin loops or internal loops), bulges, pseudoknots, or alternative base pairs (e.g. wobble base pairs or Hoogsteen base pairs).[12] With this plethora of structural elements, RNAs can interact with numerous binding partners such as other RNA molecules or proteins.[13,14] . In addition to the three-dimensional structures ensuring the interaction between different binding partners, the field of epitranscriptomics focuses on the impact of chemical RNA modifications and how small structural changes of transcripts can affect all steps of gene expression.

1.1.1 RNA modifications

Chemical modifications of RNA were first identified in the 1960s, introducing a new field of RNA biology. Today, more than 150 distinct RNA modifications have been identified which can alter molecular characteristics such as electrostatic charge, hydrophobic surface, or base pairing of RNA.[15] By varying structural properties of RNA molecules, expression levels of therapeutically relevant proteins were shown to be modulated which later was exploited for the clinical use of artificial RNAs. The groundbreaking findings of the Nobel laureates Katalin Karikó and Drew Weissman fundamentally changed the understanding of mRNA interactions in cells and ever since shaped the development of modern mRNA vaccines.[16–18]

Both coding and non-coding RNA structures were shown to carry chemical modifications on all four nucleosides. The most common modifications are methylation patterns of the purine or pyrimidine bases followed by pseudouridylation and adenosine-to-inosine (A-to-I) editing (Figure 1). While modifications of the RNA bases can be rather chemically diverse, the ribose moiety was found to be only methylated frequently in rRNA, tRNA, and snRNA.[15] The occurrence of such RNA modifications throughout the transcriptome was shown to broadly affect RNA metabolism, leading to alterations of gene expression on the (post-)transcriptional- and translational level. One prominent RNA modification is depicted by a 5' cap. This cap is built up by a rather unusual 5' to 5' triphosphate linkage connecting a methylated guanosine (m^7G) to an mRNA strand. This in turn can alter the stability of newly synthesized mRNA by protecting the transcript from degradation mediated through 5' exonucleases.[19] With the incorporation of the 5' cap, it shares chemical similarity to the 3' end of RNA and thus is not recognized by exonucleases but rather by the cap-binding complex (CBC) initiating the nuclear export or the interaction with eukaryotic translation initiation factors E and G (eIF4E and eIF4G).[20,21] Similar to the 5' cap, another protection layer is formed by the 3' polyadenylated tail (poly(A) tail) which additionally was shown to synergistically enhance translation through circularization of the respective mRNA and eIF4E/G.[22] Alternative modifications found in eukaryotic RNA include pseudouridine (ψ), inosine (I), and less frequently *N*1-methyladenosine (m^1A), 5-methylcytosine (m^5C), *N*4-acetylcytidine (ac^4C) and 5-hydroxymethylcytosine (hm^5C) (Figure 1). Besides the well-known function of ψ protecting RNA molecules from degradation, the other modifications are less well understood and require further investigation.

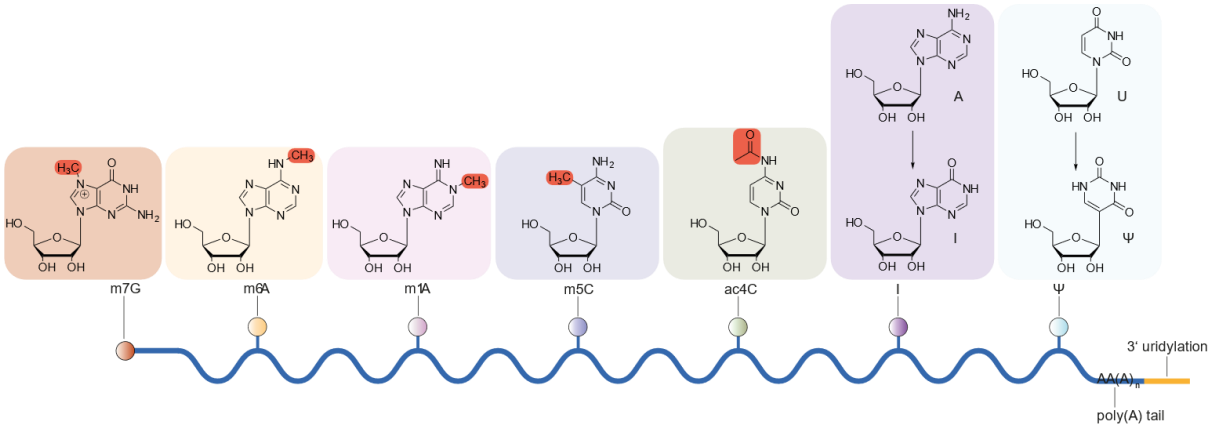

Figure 1: Chemical modifications of RNA molecules found in nature. From left to right: The 5' cap consists of a *N*7-methylguanosine (m^7G) cap. Internal adenosines within consensus DRACH sequences are converted into *N*6-methyladenosine (m^6A). Alternative modifications on adenosines and cytosines are *N*1-methyladenosine (m^1A), *N*5-methylcytosine (m^5C), or *N*4-acetylcytosine (ac^4C). Adenosines (A) can be converted into inosine (I) and uridines (U) were found to be edited into pseudouridine (ψ). While the polyadenylated tail (poly(A) tail) protects the RNA, 3' uridylation marks the nucleic acid for degrading enzymes.

The most abundant chemical modification found in RNA is *N*6-methyladenosine (m^6A) which can be found in almost all types of coding and ncRNAs throughout the majority of eukaryotic species including mammals, plants, insects, and certain viruses.[23–25] The deposition of m^6A was shown to commonly occur at a characteristic DRACH (D = G, A or U; R = G or A; H = A, C or U) sequence which is often enriched at the 3' untranslated region (3' UTR).[26] Once introduced, the methylation pattern can alter RNA metabolism including translation, export, splicing, processing, and RNA stability which underlines the significant impact of m^6A in actively regulating molecular signaling pathways.[27–29] Generally, m^6A is described as a highly dynamic and reversible modification due to regulation by two important RNA-modifying proteins (RMPs) which orchestrate the deposition as well as the removal of m^6A. The modification is first introduced by methyltransferases (writers) and can be removed by demethylases (erasers). The function implemented by m^6A is majorly dependent on specific RNA-binding protein (RBP) recognizing the methylation pattern (readers). Thereby, the m^6A modification shows the remarkable impact of minor chemical changes on RNA molecules. It not only alters molecular characteristics of the RNA itself but also impacts the landscape of natural binding partners which in turn tightly regulate the fate of the RNA. Altogether, this underlines the complex interplay between m^6A modifications, RBPs, and the function of RNA itself.

1.1.2 RNA-binding proteins

The research field of protein–RNA interactions (PRI) is rapidly emerging and already led to the discovery of diverse ribonucleoprotein (RNP) assemblies. Today, more than 2,000 proteins interacting with transcripts of all kinds have been identified and shown to regulate the life cycle of RNAs ubiquitously and potently.[30] These RBPs were shown to have a crucial impact on post-transcriptional gene regulation by altering the maturation, the transport, or the stability of cellular RNAs.[31] How RBPs

selectively interact with their natural binding partners is not always fully understood, but many studies try to unravel the notable interplay. Techniques varying from next-generation sequencing or deep-sequencing (e.g. crosslinking and immunoprecipitation followed by sequencing (CLIP-seq) or RNA immunoprecipitation and sequencing (RIP-seq)) to modern protein mass spectrometry revealed not only the binding range of RBPs but could also show that many proteins interact with thousands of cellular transcripts at defined binding sites.[31–33] Therefore, it is not surprising that not only single-protein-RNA element interactions exist but also large assemblies of multiple RBPs and RNAs were identified over the last decades.[34] One prominent example of such a large RNP assembly is depicted by the spliceosome which is responsible for the maturation of mRNA.[35]

The functional units responsible for recognizing and binding to RNA molecules are known as RNA binding domains (RBDs). Studying these domains can be crucial to decipher the mechanisms of RBPs in a cellular context, although it should be noted that RBDs are very heterogeneous and cannot be categorized easily.[31] Methods like X-ray crystallography, nuclear magnetic resonance (NMR), or cryogenic electron microscopy (cryo-EM) however helped to resolve numerous protein–RNA complexes and their corresponding types of intermolecular interactions.[36,37] Prominent molecular interactions in protein-RNA structures thereby vary from hydrogen bonds and Van der Waals interactions to hydrophobic and π-interactions or stacking.[34] These interactions were shown to occur dynamically and involve the binding of the RNA base, the RNA sugar, or the RNA backbone.[38] Considering the combination of multiple RNA-binding regions involved in diverse interactions cumulatively enables RBPs to specifically bind to RNA regions. By co-existing in one RBP, multiple RBDs can either increase specificity in a cooperative or an independent manner.[39] Moreover, studies revealed that RBDs can facilitate protein-protein interactions (PPIs) alongside RNA binding, adding another layer of diverse functionalities within the cellular environment. Classifying PRIs by their target RNA revealed that the most frequently targeted RNAs are represented by mRNAs (~45%) followed by ribosomal RNAs (~11%), tRNAs (~10%) and other ncRNAs (~34%).[31] This outlines the crucial participation of RBPs in orchestrating RNA maturation, transport, function, stability, metabolism, and RNA degradation.[40] However, once dysregulated, RBPs can promote the pathogenesis of diverse human diseases making them promising targets for the development of chemical probes and therapeutic agents.[41] Prominent examples of RBPs that have been targeted by using small molecules are the post-transcriptional gene editing Musashi proteins (MSI and MSII),[42] the eukaryotic translation initiation factors 4A and 4E (eIF4A and eIF4E)[43,44] and more recently also the RNA methyltransferase complex of METTL3/14.[45] Within this thesis, three different RBPs were targeted using small-molecule modulators: The miRNA-binding protein LIN28, the m^6A methyltransferase METTL16, and the m^6A recognizing protein YTHDF2.

1.1.3 RNA-modifying proteins

One major subgroup of RNA-binding proteins is summarized as RNA-modifying proteins (RMPs). This group consists of enzymes placing a covalent modification on RNA molecules, removing a covalent modification, and proteins that recognize and selectively interact with the modified RNA. The research field describing the installation, recognition, and removal of these post-transcriptional modifications has been referred to as epitranscriptomics. As summarized in section 1.1.1, a plethora of covalent RNA modifications has been identified over the last years. However, to understand the regulation and function of each RNA modification, it is crucial to not only investigate the transcripts individually but also the natural binding partners involved in each step.

For m^6A, there have been developed many techniques which try to unravel the complex regulatory network of RNA methylation, leading to the identification of several m^6A writers, readers, and erasers (see section 1.3).[46] Most of the methods rely on combinations of sequencing methods and other emerging tools (e.g. genome-editing tools).[47–51] For less abundant RNA modifications, however, it remains rather challenging to investigate the regulatory networks and to identify the involved RMPs.

Another extensively studied PRI describes the interplay between RNA containing pseudouridine (ψ) and pseudouridine synthase (PUS) enzymes. PUS enzymes were shown to catalyze the isomerization of uridine to ψ and thus stabilize the respective transcript. To identify ψ sites and the corresponding isomerase catalyzing the conversion, N_3-CMC (cyclohexyl-*N*-*b*-(4-methylmorpholinium) ethylcarbodiimide)–enriched pseudouridine sequencing (CeU-seq) depicts a selective chemical labeling and pulldown method.[52] In addition to uridine to ψ isomerization, A-to-I editing was also investigated thoroughly, leading to the discovery of adenosine deaminases acting on RNA (ADARs). The family of human ADARs consists of three members (ADAR1, 2, 3) which were shown to catalyze the hydrolytic deamination reaction converting adenosine into inosine. Interaction of inosine with the translation machinery results in base-pairing with cytosine instead of uracil and thus can cause the incorporation of amino acids that are not directly encoded in the genome.[53] A-to-I editing is found in both coding and noncoding RNAs. In tRNA, an A-to-I conversion at the wobble position enables this base to pair with uridine, adenosine, or cytidine nucleosides in the codon of an mRNA.[54] This, in turn, leads to a reduction in the number of tRNA molecules required to decode the full range of mRNA codons.[55] In miRNAs, A-to-I editing was shown to occur rather frequently (20% of pri-miRNAs) mostly causing an inhibition of the miRNA biogenesis.[56] The following paragraph describes the canonical pathway of miRNAs in more detail and how the prominent RBP LIN28 alters the maturation of *let-7* miRNAs.

1.2 The microRNA-binding protein LIN28

Since its discovery in 1984, the human abnormal cell lineage protein 28 (LIN28) has emerged as one of the best characterized RBPs.[57,58] Especially, precedents in *Caenorhabditis elegans* helped to understand the fundamental function of LIN28 in embryonic development. In mouse embryonic stem

cells (ESCs) mammalian LIN28 is highly abundant but the expression level decreases upon differentiation.[59] Along with Oct4, Sox2, and Nanog, LIN28 was later used to reprogram human fibroblasts into induced pluripotent stem cells (iPSCs) which further corroborated the function of LIN28 as a pluripotency factor.[60] Further studies revealed that the reprogramming process simultaneously increased the cell proliferation rate. Consequently, LIN28 was identified as a proliferation regulator that is activated during cell growth and inhibited at high cell densities.[61] The mechanism of LIN28 downregulation later was shown to be dependent on sequestration from the cytoplasm by unphosphorylated Merlin/NF2. At low cell density, Merlin/NF2 is phosphorylated, which prevents the interaction with LIN28. However, cell-cell contact triggers the dephosphorylation of Merlin/NF2, causing LIN28 recruitment in the cytoplasm and thus inhibiting proliferation.[62]

In mammals, two different *LIN28* genes are expressed, LIN28A and LIN28B. Both isoforms consist of an *N*-terminal cold shock domain (CSD) and a *C*-terminal zinc knuckle domain (ZKD).[63] The proteins both are evolutionary highly conserved and share functions such as the regulation of tissue development, cell growth, metabolism, and pluripotency.[59] While LIN28A (~ 23 kDa) consists of 209 amino acids, the sequence of LIN28B comprises 250 amino acids. This discrepancy can be explained by an extended *C*-terminal acidic stretch and the occurrence of nuclear (NLS) and nucleolar (NoLS) localization signals of LIN28B (Figure 2). With these localization signals and under conditions such as S-phase or G2-phase, LIN28B can localize to the nucleus or the nucleolus, respectively.[64] Predominantly, however, LIN28A and LIN28B are located in the cytoplasm. Structural investigations of both isoforms could show that the CSD is built up by a β-barrel consisting of five antiparallel β-sheets.[65] Connected to the CSD via a positively charged and flexible linker (~ 15 amino acids) is the ZKD featuring two prominent Cys-Cys-His-Cys (CCHC)-type zinc-finger motifs. In each motif, Zn^{2+} ions are coordinated by three cysteines and one histidine residue that enables the resembling of retroviral nucleocapsid proteins.[66,67]

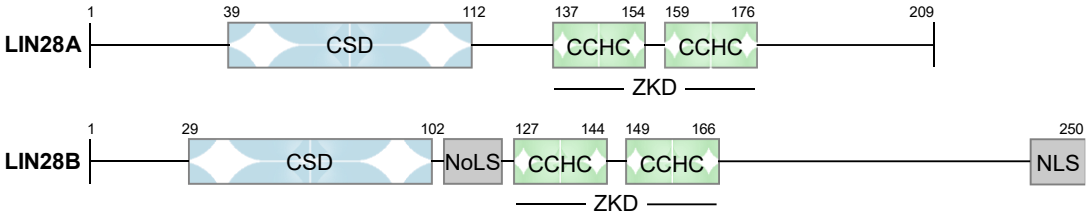

Figure 2: Schematic comparison of LIN28A and LIN28B sequences.

The predominant binding partner of LIN28 is the non-coding, tumor-suppressive miRNA *lethal-7* (*let-7*), which was shown to interact with both the CSD and the ZKD.[68] Generally, it was found that the PRI of LIN28 and *let-7* results in posttranscriptional inhibition of *let-7* biogenesis. Besides this crucial and thoroughly studied interaction with the miRNA *let-7* (see section 1.2.2), LIN28 was shown to interact with thousands of exonic and 3' untranslated region (UTR)-binding sites. Using CLIP-seq, Wilbert *et al.* were able to identify an enriched GGAGA motif in LIN28-binding sites.[69] Among several

mRNA targets, they found evidence for LIN28 autoregulation and effects on protein abundances of splicing regulators such as hnRNP F, TIA-1, or FUS/TLS.[69] Further studies could also show the binding of LIN28 to a subset of mRNAs encoding for cell cycle regulators (e.g. cyclin A and B) or the epigenetic regulator DNMT3a.[70,71] These findings all demonstrate that LIN28 can alter crucial regulatory functions by directly interacting with mRNA. The mechanisms of how LIN28 alters cell growth and maintains pluripotency by interacting with mRNAs however are not yet fully understood and require further investigations. The perturbation of *let-7* maturation on the other side depicts one of the most extensively studied PRIs today and still holds great potential considering the function of LIN28 in a cellular environment.

1.2.1 The *let-7* miRNA family

After the first discovery of human miRNAs over a decade ago, examples of miRNA-mediated regulation were found for almost every cellular process.[72–74] The small ncRNA molecules are described as regulators of gene expression and commonly show a length of about 22 nucleotides.[75] One of the first known human miRNAs was *lethal-7* (*let-7*) which was originally found in *C. elegans* and later identified as a regulator of several cell-fate decisions.[76] By binding to transcripts including oncogenic mRNAs such as *c-Myc*, *Ras*, or *HMGA2*, and cell-cycle factors (e.g. CyclinD1, D2), *let-7* is recognized as a crucial tumor-suppressive miRNA.[77–79]

There are twelve known members of the *let-7* miRNA family: *let-7a-1*, *let-7a-2*, *let-7a-3*, *let-7b*, *let-7c-1*, *let-7c-2*, *let-7d*, *let-7e*, *let-7f-1*, *let-7f-2*, *let-7g*, *let-7i* and *miR-98* (Figure 3C).[80] Although their sequences differ at the highlighted nucleotides, the mature sequence of *let-7* and its function in development are conserved among species.[81] To finally act as a mature miRNA that induces RNA interference (RNAi), *let-7* has to undergo a series of canonical processing steps after transcription (Figure 3A). First, RNA polymerase II transcribes primary *let-7* (pri-*let-7*) which is equipped with a protective 5' cap and a 3' poly(A) tail. The precursor miRNA contains at least one hairpin structure and an imperfectly base-paired stem showing a length of about 33 base pairs (bp). [82] Additionally, it contains a terminal loop, also known as pre-element (preE) loop, and a flanking single-stranded RNA segment at the opposite end (Figure 3B). This flanking region is essential for pri-*let-7* to undergo the first processing step in the nucleus. By interacting with the RNAse III enzyme Drosha in complex with the microprocessor complex subunit DGCR8 (*DiGeorge syndrome critical region 8*) the 5'cap and 3'poly(A) tail containing, unpaired overhang is cleaved off. This nucleolytic cleavage results in the 60-70 nucleotide long preliminary *let-7* (pre-*let-7*) miRNA which shows a two nucleotide long 3'-overhang.[83] Subsequently, pre-*let-7* interacts with Exportin-5 (XPO5) which in complex with the small GTPase RAN can actively export pre-*let-7* into the cytosol through nuclear pore complexes (NPCs).[84] Once out of the nucleus, another RNAse III enzyme called Dicer in complex with TRBP (transactivation response element RBP), selectively recognizes the terminal loop region of pre-*let-7* and cleaves off both strands of the base-paired stem.[85,86] The resulting cleavage product consists of a ~22 nucleotide-long

double-stranded (ds) RNA which contains the mature, single-stranded (ss) *let-7* miRNA.[87] Then, the dsRNA is loaded into the RNA-induced silencing complex (RISC), mediated by the Dicer-TRBP complex and Argonaut (AGO) family proteins resulting in the unwinding of the passenger strand. In the RISC, the ssRNA can finally bind to complementary 2-8 nucleotide long seed sequences of corresponding mRNAs to repress their translation (Figure 3A and 3C).[88] The seed binding sequences are usually located at the 3' UTR of mRNAs which previously needs to be decapped and deadenylated to be targeted by *let-7*.

Besides the prominent examples of oncogenic mRNAs targeted by *let-7*, several other genes are known to be repressed by the miRNA. Two examples are the cell cycle progression regulators like cyclin-dependent kinase 6 (CDK6), or M-phase inducer phosphatase 1 (CDC25A) which could explain the effect of *let-7* on cell proliferative processes.[89] Altogether, the targeted mRNA transcripts underline *let-7*'s important role as a master regulator of cell differentiation and proliferation. Thus, deregulation of the *let-7* maturation was shown to influence the tumorigenicity of many cancer cells. The major negative regulator of *let*-7 is the RBP LIN28 which is aberrantly expressed in several cancers and thus causes the arrest of *let-7* biogenesis.[83]

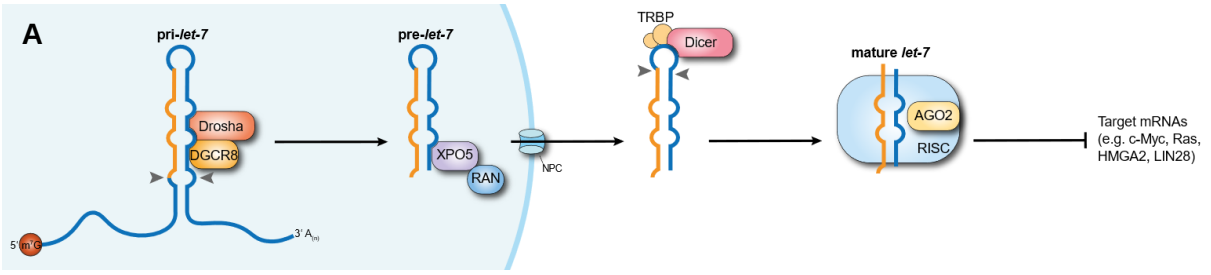

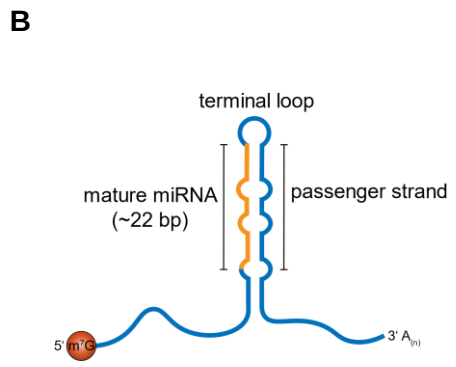

C

	1 2 3 4 5 6 7 8 9 10 11 12 13 14 15 16 17 18 19 20 21 22
Consensus	U G A G G U A G U A G G U U G U A U A G U U
let-7a-1	U G A G G U A G U A G G U U G U A U A G U U
let-7a-2	U G A G G U A G U A G G U U G U A U A G U U
let-7b	U G A G G U A G U A G G U U G U **G** U **G** G U U
let-7c-1	U G A G G U A G U A G G U U G U A U **G** G U U
let-7c-2	U G A G G U A G U A G G U U G U A U **G** G U U
let-7d	**A** G A G G U A G U A G G U U G **C** A U A G U U
let-7e	U G A G G U A G **G** A G G U U G U A U **G** G U U
let-7f-1	U G A G G U A G U A G **A** U U G U A U A G U U
let-7f-2	U G A G G U A G U A G **A** U U G U A U A G U U
let-7g	U G A G G U A G U A G **U** U U G U A **C** A G U U
let-7i	U G A G G U A G U A G **U** U U G U **G C U** G U U
mir-98	U G A G G U A G U A **A** G U U G U A U **U** G U U

Figure 3: (A) Canonical pathway of the *let-7* maturation process. After transcription by RNA polymerase II, pri-*let-7* is processed by Drosha in the nucleus and exported by Exportin 5. In the cytosol, pre-*let-7* is once more processed by Dicer and then loaded onto the RISC to interfere with mRNA translation. (B) Scheme of Pri-*let-7* with representative motifs. (C) Members of the *let-7* family and their corresponding sequences. The seed binding sequence is marked in red. Differences in individual *let-7* sequences compared to the consensus sequence are highlighted in bold font.

1.2.2 The natural role of the LIN28–*let-7* interaction

To understand the phenomenon of LIN28 being a proliferation regulator that is activated especially during cell growth, the interaction with *let-7* needs to be examined more carefully. LIN28 consists of two distinct domains which both were shown to be involved in *let-7* binding (Figure 4A). While the ZKD was consistently shown to bind single-stranded GGAG or GGUG sequences with high specificity, there is still no clear consensus about the interaction between *let-7* and the CSD of LIN28.[90] It could be demonstrated by Nam *et al.* that most contacts of *let-7* to the CSD are created through the preE loop. The RNA bases thereby form several π-stacking interactions with aromatic side chains, and additional hydrogen bonds or steric exclusions increase the specificity towards the CSD. However, a clear consensus sequence could not be identified, not even after the efforts of Maryr *et al.* who identified a binding motif of LIN28 with a preference for the CSD to bind pyrimidine-rich heptanucleotides showing the common sequence: GUNNUNN (N = any base).[91] Later studies focused on single-nucleotide-resolution mapping of LIN28, revealing a clearer (U)GAU motif which was shown to partition the *let-7* miRNA family into two subclasses. Members such as *let-7b*, *let-7d*, *let-7f*, or *let-7g* which possess the (U)GAU motif, bind both the CSD and ZKD and are referred to as CSD^+, while other members without a CSD binding motif are described with $CSD^–$. These findings could be validated by showing different affinities of CSD^+ miRNAs compared to $CSD^–$ miRNAs to LIN28 in biochemical assays.[92]

The binding of LIN28 to the preE loop of precursor *let-7* generally blocks the interaction with the RNAse III enzymes Drosha and Dicer. This blockage depicts one of the mechanisms of how LIN28 regulates the maturation of *let-7* miRNAs (Figure 4B).[93] Alternatively, LIN28 can recruit terminal uridylyl transferases (TUTases) such as TUT4 or TUT7 which oligouridylate pre-*let-7* at the 3' end.[94–96] Recruitment of these noncanonical poly(A) polymerases was shown to occur through the ZKD of LIN28A binding to the *N*-terminal LIN28-interacting module (LIM) of TUT4 and 7. The uridylation on the other side is executed at the *C*-terminal catalytic module (CM) and was shown to be dependent on UTP.[68] Generally, marking pre-*let-7* with an oligouridyl tail leads to the recruitment of the 3' to 5' exonuclease DIS3L2 which successively degrades the tail, followed by the miRNA itself. Therefore, binding of LIN28A to pre-*let-7* indirectly induces the decay of the miRNA and thus its ability to get loaded into the RISC (Figure 4B).[97]

Another way how LIN28 can alter the biogenesis of precursor *let-7* miRNAs was described with the competitive binding of LIN28 and AGO. Depending on the expression levels, *let-7* is recruited by LIN28 and thus cannot be loaded into the RISC. This, in turn, causes alternative, low-abundant miRNAs to bind to AGO and induces the respective RNA silencing.[98] In summary, LIN28 regulates the processing of *let-7* through three mechanisms: it binds directly to the miRNA, preventing its interaction with Drosha and Dicer; LIN28 recruits post-transcriptional modifiers that lead to the recruitment of RNA degraders; and it restricts the localization of *let-7* to specific cellular compartments.

Strikingly, *let-7* was also shown to bind the *LIN28a/b* genes resulting in inhibition of LIN28 translation and thus forming a prominent bistable switch.[99] Depending on the individual expression levels of LIN28 or *let-7*, this switch mechanism can decide the cell state. With high levels of LIN28, *let-7* maturation is suppressed causing a pluripotent state. Alternatively, high levels of *let-7* inhibit *LIN28* expression which in contrast causes cell differentiation (Figure 4C).[100] This highlights the substantial impact of the regulatory interplay between LIN28 and *let-7* on cell proliferation and differentiation. Therefore, it is unsurprising to observe that dysregulation of this interaction is implicated in numerous human diseases, particularly cancers.[101–103]

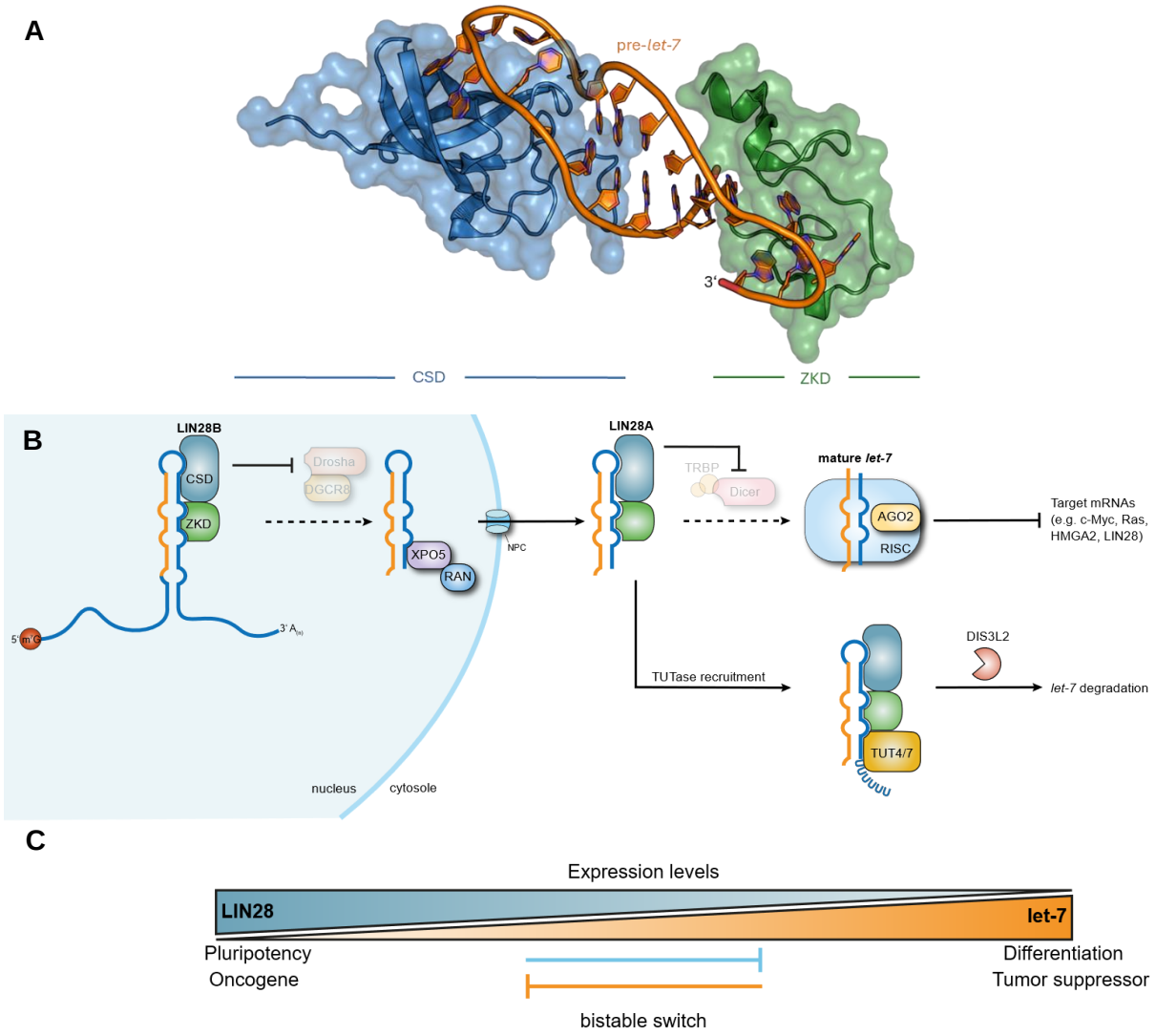

Figure 4: The LIN28-let-7 interaction. (A) Crystal structure of LIN28 in complex with truncated preE-*let-7f-1* (depicted as orange ribbon structure) (PDB: 5UDZ). The cold shock domain (CSD) is colored in blue, while the zinc knuckle domain (ZKD) is shown in green. (B) Schematic visualization of LIN28 interacting with precursor *let-7* miRNAs and the effects. In the nucleus, predominantly LIN28B binds to pri-*let-7* and thus inhibits processing by the Drosha-DGCR8 complex. In the cytosol, the PRI of LIN28 and *let-7* blocks the processing by Dicer and alternatively leads to the recruitment of TUTases (TUT4 or 7) marking the miRNA for degradation. (C) LIN28 and *let-7* form a bistable switch determining the differentiation state of cells. Once LIN28 levels are high a pluripotent cell state can be observed and *let-7* levels are suppressed leading to increased tumorigenicity in cancer cells.

1.2.3 LIN28 as a potential therapeutic target

LIN28 is found to be overactivated in ~15% of human cancers which causes the inhibition of *let-7* maturation and thus expression of *let-7* target genes.[104] Typically, high LIN28 levels are related to an advanced disease stage among multiple tumor types and are associated with poor clinical prognosis. The targets of the LIN28/*let-7* axis generally were shown to have a significant impact on each hallmark of cancer underlining the significant impact of the perturbed bistable switch on tumorigenesis.[105,106] Additionally, there is growing evidence that LIN28, as a stem cell pluripotency regulator, is important in forming cancer stem cells (CSCs) in certain cancers accelerating tumor progression.[107] CSCs are subpopulations of tumor cells that can drive tumor initiation, impair differentiation, and can cause relapses.[108] It was claimed that the LIN28/*let-7* axis causes a "reprogramming-like" mechanism allowing cancer cells to dedifferentiate into CSCs which in turn can evade defense mechanisms as well as numerous cancer therapies. Regardless of the mechanism, LIN28 is commonly recognized as a biomarker for CSCs.[109]

Besides the crucial interplay between LIN28 and *let-7,* there is growing evidence for additional feedback loops promoting pathogenesis significantly. One important regulatory network involves *c*-Myc, *let-7,* and LIN28: While LIN28 and *let-7* form a bistable switch regulating each other, *c*-Myc was shown to transcriptionally activate *LIN28* leading to a shift of the LIN28/*let-7* axis.[110,111] A similar positive feedback loop, described by Iliopoulos *et al.* involves NF-κB, LIN28B, *let-7,* and IL-6. Thereby, NF-κB was shown to increase the expression of LIN28B causing the repression of *let-7* which in turn increases the expression of IL-6. Finally, IL-6 itself was shown to activate NF-κB thus completing the feedback loop.[112] HMGA2, another target of *let-7,* promotes epithelial-to-mesenchymal transition (EMT) which is known to be a key event in cell development and metastasis.[111113] This underlines the fact that LIN28 is specifically activated in high-grade and advanced-stage tumors emphasizing its significant role, especially in later tumorigenesis.[114] Considering all of the aforementioned impacts of the LIN28/*let-7* axis, there is a high demand for understanding the precise role of LIN28, not only in physiological development but also in its function during tumorigenesis.

Ever since its discovery in the 80s, LIN28 has been extensively studied and today depicts a well-validated oncogene. Thus, inhibition of the RBP displays a promising strategy to balance the impaired LIN28/*let-7* axis. One attempt by Trang *et al.* was to recover the function of *let-7* by intratumorally delivering *let-7* and thus utilizing the miRNA itself as an inhibitor of LIN28.[115] Later, this approach was optimized by using hydrophobically modified *let-7b* to enhance the biodistribution and downregulate HMGA2.[116] While *in vitro* studies could show a significant decrease of LIN28 levels, i*n vivo* results indicated that most of the miRNAs were detected in the clearance organs of mice used as a model organism.[117] This underlines that the emerging field of therapeutic oligonucleotides, despite having several advantages over conventional drugs, still suffers from several limitations. Next to systematic clearance, drawbacks such as delivery-associated toxicity, poor transfection efficiency, non-

specific biodistribution, and degradation have been described.[118] In another proof-of-concept study, oligonucleotides were converted into proteolysis targeting chimeras (PROTACs) linking a section of the *let-7* sequence to a von Hippel-Lindau (VHL) E3 ligase recruiting small molecule.[119] The general concept of PROTACs describes a heterobifunctional molecule consisting of two active domains and a linking moiety. One domain binds the protein of interest (POI) while the other binds and recruits an E3 ubiquitin ligase to form a ternary complex which triggers the ubiquitin transfer of the POI. The ubiquitinylated POI is subsequently harnessed by the ubiquitin-proteasome system (UPS) finally causing the degradation of the POI mediated through the proteasome.[120] In their study, Ghidini *et al.* report the first RNA-PROTAC of LIN28 which was able to inhibit and degrade the RBP both *in vitro* and *in vivo* at micromolar concentrations. However, the RNA-PROTAC strategy also suffers from previously stated drawbacks and thus does not depict the optimal strategy to target the LIN28/*let-7* axis.[119]

Therefore, inhibiting LIN28 with small-molecular entities, exhibiting better activity, stability, and permeability becomes increasingly desirable. Such LIN28 inhibitors not only should help to understand alternative biological roles of the miRNA-binding protein but also hold great potential as anticancer therapeutics. Despite the relevance to target oncogenic LIN28, small-molecule inhibitors of the RBP only sporadically have been reported since 2016. Nevertheless, there are several studies which utilized fluorescence-based high-throughput screens to identify inhibitors disrupting the PRI of LIN28 and *let-7* at micromolar concentrations. One of the first LIN28 inhibitors was discovered in a Förster resonance energy transfer (FRET) assay-based screening involving 16,000 compounds.[121] By using a GFP-labelled LIN28 and a black-hole quencher (BHQ)-labeled *let-7a-2*, Roos *et al.* were able to identify a triazolopyridazine (1632) (**1**) and a phenethylacetamide (1036) (**2**) to block the LIN28/*let-7* interaction with half-maximal inhibitory concentrations (IC_{50}) of 14 µM and 8 µM, respectively. The LIN28-inhibitory activity of 1632 (**1**) also led to rescued *let-7* processing, induction of cell differentiation of mouse ESCs, suppression of programmed cell death ligand 1 (PD-L1) expression, and tumor growth in mice.[122] Furthermore, a biotinylated derivative of 1632 (**1**) was synthesized and used in a pulldown assay to capture LIN28 from cell lysates. Besides the proven binding of LIN28 however, the probe also showed micromolar binding affinities for different bromodomains (bromodomain of BRD4; K_D = 7 µM and cAMP-response element binding (CREB)-binding protein (CREBBP); K_D = 25 µM). Nevertheless, the compound (**1**) was later used as a chemical probe in several studies involving LIN28 inhibition. For example, 1632 (**1**) was shown to protect against lipid accumulation in cells and mouse models of hepatic steatosis, highlighting the possibility of treating hepatic disorders of abnormal lipid deposition.[123] In another study, 1632 (**1**) was used to restore *let-7* levels to reduce replication of the severe-acute-respiratory-syndrome coronavirus 2 (SARS-CoV-2) and to secret inflammatory cytokines.[124]

Another FRET-based screening of a diversity-oriented synthesis (DOS) library revealed a tricyclic chromeno[4,3-*c*]pyrazole SB1301 (**3**) inhibiting the LIN28/*let-7* interaction with low micromolar IC_{50} values (4 µM).[125] By using Cy3-labelled LIN28A and a BHQ-2-labelled preE-*let-7a-1*, the compound

was able to restore the Cy3 fluorescence signal and was consequently further evaluated in an orthogonal electrophoretic mobility shift assay (EMSA). In the orthogonal EMSA, SB1301 (**3**) disrupted the ribonucleoprotein (RNP) complex formation of recombinant LIN28A and Cy5-labelled *let-7*, giving evidence of PRI inhibition. Subsequent surface plasmon resonance (SPR) and differential scanning fluorimetry experiments indicated a binding of SB1301 (**3**) to the CSD of LIN28. While not clarifying a precise binding mode, a structure-activity relationship (SAR) study involving nine analogs of the parent compound (**3**), underlined the importance of the carboxylic acid moiety. All analogs missing the carboxylic acid either showed significantly reduced activity or a complete loss of activity against LIN28. In cells, SB1301 (**3**) increased levels of mature *let-7* at concentrations of 20-40 µM, as shown with reverse transcription PCR (rtPCR) analysis. Additionally, protein expressions of *c*-Myc, Ras, and HMGA2 (*let-7* targets) were shown to be downregulated upon compound treatment, indicated by western blot analysis.[125] Following the study of Lim *et al.* another screening of 8,400 compounds in a similar FRET assay led to the discovery of the quinoline KCB3566 (**4**), showing an IC_{50} value of 11 µM. Structural optimization of KCB3566 (**4**) revealed a slightly more active analog KCB3602 (**5**) (IC_{50} = 4.8 µM) in a dose-dependent EMSA study.[126] Additionally, the authors claimed that optimization at the 2-phenylamino group may lead to even higher potencies against LIN28. In biophysical and cellular assays, compound KCB3602 (**5**) could reduce the protein expression of *let-7* target genes, similar to SB1301 (**3**) but with a higher potency.[126]

An alternative assay that has been established to screen for LIN28 inhibitors involves a fluorescence polarization (FP)-based readout. Utilizing this assay to screen 2,769 pharmacologically active small molecules, led to the identification of several compounds that inhibited the interaction between pre-*let-7g* and LIN28 by >50%. To validate the activity of preliminary hits an EMSA and a Dicer cleavage assay were developed revealing that, out of four hit compounds, only the benzo[*a*]phenoxazine-5-one SBZW0065 (**6**) and 6-hydroxy-$_{DL}$-DOPA (**7**) was able to restore LIN28-mediated inhibition of Dicer-processing of pre-*let-7g*. While activity *in vitro* could be demonstrated for both compounds, in LIN28-expressing P19 embryonal carcinoma cells, the hit compounds did not show any effect.[127] One of the most extensive screenings to identify LIN28 inhibitors, involved the combination of 17 compound libraries, containing more than 100,000 small molecules. In this FP assay-based screening, using LIN28A and FAM-labelled preE-*let-7f-1*, 53 compounds were shown to dose-dependently inhibit the PRI with IC_{50} values ranging from 0.2 µM to 10 µM. To note, a truncated version of human LIN28 was used for the screening, only containing residues 16-187 and an F73A point mutation lowering the affinity between CSD and *let-7* and thus increasing the sensitivity of compounds binding to the ZKD.[72,94] Initial hit compounds were subsequently tested in a *let-7* oligouridylation inhibition assay, leading to the validation of six LIN28 inhibitors (Figure 5). A tricyclic cyclopenta[*c*]quinoline (LI71) (**8**), tetrakis(2-pyridylmethyl)ethylenediamine (TPEN) (**9**), and gossypol (**10**) were shown to completely abolish LIN28-mediated oligouridylation at 40 µM, leading to binding mode studies using heteronuclear, single-quantum, coherence (HSQC)-spectroscopy. Here, it was demonstrated that LI71

(**8**) modulated the *let-7* binding activity of the CSD, while TPEN (**9**) destabilized the ZKD, most likely due to Zn^{2+} chelation. Because of its chelating effect, the toxicity observed in LIN28-expressing mouse ESCs upon TPEN (**9**) treatment, needs to be scrutinized carefully. To further elaborate the binding of LI71 to the CSD of LIN28, a saturation transfer difference (STD) experiment was conducted, indicating that the carboxylic acid and the ethoxy residue of LI71 (**8**) both contribute to the interaction with LIN28. This could also be confirmed by a concise SAR analysis involving four LI71 derivatives and the corresponding enantiomer. In cellular assays, LI71 (**9**) could increase levels of mature *let-7*(*a-g* and *let-7i*) in LIN28-dependent cancer cells and embryonic stem cells. As the carboxylic acid moiety proofed to be beneficial for LIN28 inhibition, another focused screening was performed, revealing a 5-(methylamino)nicotinic acid fragment (**11**) to act as a weak LIN28 inhibitor *in vitro* ($IC_{50} \geq 76$ µM) and *in cellulo*.[128]

Next to the fluorescence polarization, also the fluorescence intensity (FI) of fluorophores coupled to pre-*let-7* was shown to be influenced by LIN28 binding, giving another read-out to screen for small-molecule inhibitors. Utilizing this technique led to the identification of four initial hits, the pyrazoyl thiazolidinedione KCB170522 (**12**), luteolin (**13**), an alkaloid rhynchophylline (**14**), and the saponine tenuifolin. Byun *et al.* then focused on KCB170522 (**12**) and investigated the structure-activity relationship by synthesizing four derivatives. After showing robust activity against LIN28 in the FI assay and in EMSA, JAR cells were treated with the most potent KCB170522 (**12**) resulting in the upregulation of mature *let-7* levels and downregulated expression of *let-7* target genes (*c*-Myc and Ras).

In 2016, Lorenz and Ganer established a catalytic enzyme-linked click chemistry assay (cat-ELCCA) to later screen a collection of 127,007 compounds from various sources.[129–131] In their assay, LIN28 with an *N*-terminal HaloTag fusion protein labeled with biotin and 5'-*trans*-cyclooctene labeled pre-*let-7d* were used to monitor a subsequent reaction with tetrazine-labeled horseradish peroxidase. Once a compound interferes with *let-7* binding, it demolishes the click reaction, and thus no luminescence signal can be amplified. Two compounds, CCG-233094 (**15**) and CCG-234459 (**16**) could show this inhibitory effect in a dose-dependent manner and were subsequently subjected to EMSA showing similar outcomes. However, no clear inhibition mechanism of the two aryl bis-sulfonamides was stated, leading to the assumption that the compounds might extract the Zn^{2+} ions from the ZKD to destabilize the PRI of LIN28 and *let-7*. Another recent effort of the Garner lab involved the establishment of a live-cell assay technology, RNA interaction with protein-mediated complementation assay (RiPCA), for high-throughput screening to identify small molecule inhibitors of the *let-7* and LIN28A interaction. The screening of a biased library resulted in the identification of the Wee1 kinase inhibitor SID-415260 (**17**) which was able to inhibit the pre-*let-7d*–LIN28A PRI with an IC_{50} value of 7.6 µM.[132]

To summarize, several research groups already identified small-molecule LIN28 inhibitors which show significant impact by restoring levels of mature *let-7* not only *in vitro* but also *in vivo*. However, no inhibitor reached the submicromolar potency leading to only minor effects in mouse models or cellular effects thus creating much space for improvement. Most of the inhibitors identified so far suffer

from limited characterization which handicaps structural optimization of the compounds to improve LIN28 binding. Additionally, no co-crystal structure showing LIN28 in complex with an inhibitor has been reported to date, which could be helpful in understanding and optimizing a binding mode more rationally. Another drawback created by most of the compounds obtained from the screening approaches is their lack of selectivity. As shown for 1632 (**1**), the compound interacts with different bromodomains in a similar affinity compared to LIN28 and thus does not allow for effective therapeutic usage. Also, ZKD binders such as TPEN (**9**), CCG-233094 (**15**), and CCG-234459 (**16**) harbor symmetrical nitrogen moieties with lone pairs which potentially complex different zinc ions throughout the cell and thus decrease the selectivity of the small molecules. Therefore, more extensive evaluation of the target specificity and structural optimization is needed to obtain better LIN28 inhibitors as useful probes in chemical biology or as potential lead structures for drug development.

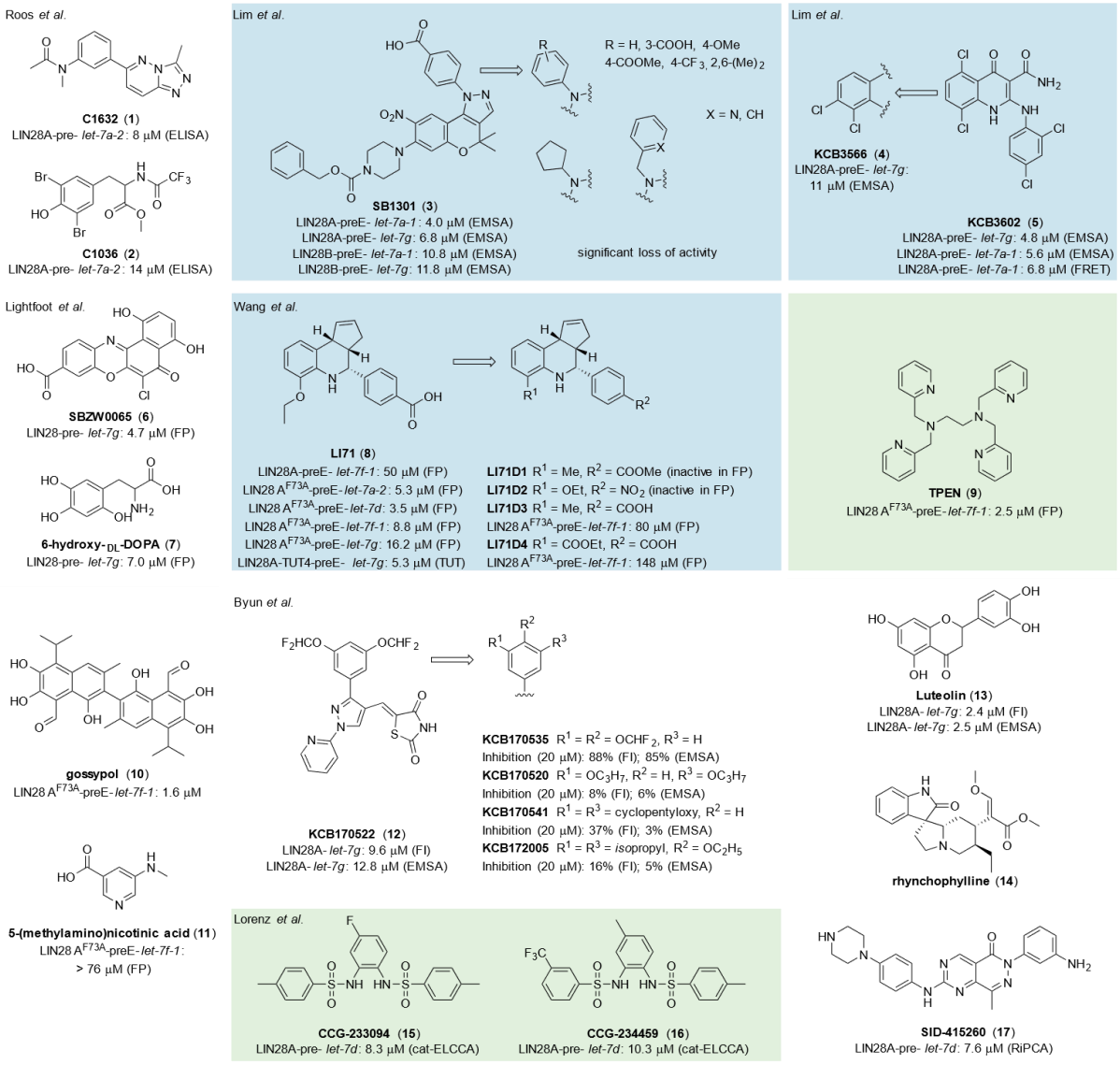

Figure 5: Small molecules inhibiting the protein-RNA interaction of LIN28 and let-7. Listed are the different structures and the corresponding IC_{50} values as well as the assay used to identify the inhibitory effect. Blue boxes indicate CSD binders and green boxes indicate ZKD binders. No box indicates unclear inhibition mechanisms.

1.3 m^{6}A RNA-modifying proteins

All major macromolecules (DNA, RNA, proteins, lipids, and carbohydrates) found in nature were shown to undergo covalent modifications that impact their structure, function, and stability.[133] Installation of these modifications mainly occurs through enzymatic catalysis. The field of epitranscriptomics describes the impact of diverse post-transcriptional modifications found on RNA throughout the transcriptome and how these modifications can alter the translation of proteins.[134] The enzymes catalyzing the installation of RNA modifications in many cases are yet to be identified and characterized in detail. Proteins involved in *N*6-methylation of adenosines however have been particularly well studied in recent years due to the severe effects of *N*6-methyladenosine (m^{6}A) in many cellular functions. M^{6}A has emerged as the most abundant and prevalent RNA modification in nature, underlining the need to comprehensively understand its functional significance and its interactome throughout the cell. Deposition of transcriptome-wide m^{6}A modifications is majorly mediated by the m^{6}A methyltransferase complex (MTC) consisting of several proteins such as methyltransferase-like 3 (METTL3), METTL14, Wilms' tumor 1-associating protein (WTAP), vir-like m^{6}A methyltransferase-associated (VIRMA), Cbl proto-oncogene-like 1 (HAKAI), zinc finger CCCH-type containing 13 (ZC3H13), and RNA-binding motif protein 15/15B (RBM15/15B).[135–139] Thereby, the enzyme mainly catalyzing the *S*-adenosylmethionine (SAM)-dependent methyl transfer was shown to be the tight heterodimer of METTL3 and METTL14, while the other proteins act as regulator factors (Figure 6).[137] Besides the transfer of m^{6}A onto a plethora of RNAs, ZC3H4, and METTL5 in complex with tRNA methyltransferase activator subunit 11-2 (TRMT112) were reported to methylate 28S and 18S rRNA, respectively leading to a promoted global translation rate.[140–143] Another more specifically methylating RMP is depicted by METTL16, which installs m^{6}A in U6 snRNAs and the mRNA *MAT2A* and thereby regulates RNA splicing and SAM homeostasis, respectively.[144–146]

Similar to the introduction of m^{6}A, there is another class of RMPs catalyzing the removal of the RNA modification, the class of m^{6}A erasers. To date, two erasers could be identified, both belonging to the alkylation B (AlkB) family of Fe(II)/ α-ketoglutarate-dependent dioxygenase superfamily.[147] Fat mass and obesity-associated protein (FTO) was shown to remove the methyl group in a two-step oxidation mechanism creating *N*6-hydroxymethyladenosine (hm^{6}A) first and then fragmenting the intermediate into adenosine and formaldehyde. However, it was also reported that FTO produces a mixture of adenosine, hm^{6}A, and *N*6-formyladenosine (f^{6}A) giving evidence that the eraser not efficiently removes all methylation marks.[148–151] On the other side human AlkB homologue 5 (AlkBH5) depicts another m^{6}A eraser which similarly oxidizes m^{6}A by converting 2-oxoketoglutarate into succinate under oxygen consumption to create carbon dioxide and hm^{6}A. In contrast to FTO, only demethylated adenosine has been observed in AlkBH5 catalysis, showing the ability to remove the methylation pattern more effectively (Figure 6).[152–154] The occurrence of writers and erasers generally makes m^{6}A a highly dynamic modification which can be actively regulated by diverse signaling pathways.

Proteins recognizing m^6A and thereby implementing cellular functions are called m^6A readers. Depending on the subcellular localization, readers can influence the fate of m^6A in numerous ways. Among the best-characterized readers today are the YT521-B homology (YTH) domain family members YTHDF1-3 and YTHDC1-2, all sharing a similar m^6A recognition motif but manifesting diverse effects on RNA fate.[155,156] While YTHDF1 and YTHDF3 are mainly actively accelerating protein synthesis by interacting with the translation machinery,[157,158] YTHDF2 was shown to alter the stability of RNA by recruiting RNA-degrading enzymes (Figure 6) (for a more detailed description see section 1.3.3).[159,160] Similarly, YTHDC1 is actively regulating the decay of m^6A-modified chromosome-associated regulatory RNAs (carRNAs) through nuclear exosome targeting–mediated degradation. In a different study however, YTHDC1 was shown to promote exon inclusion by recruiting splicing enhancer-binding SR protein 3 (SRSF3) and thus actively regulating mRNA splicing.[161–163] Reminiscent of YTHDC1, the role of YTHDC2 is also not fully understood as underlined by studies demonstrating either an alteration of m^6A RNA stability or an upregulation of the translation machinery.[164,165] Another group of m^6A readers recognizing the methylation mark through K-homology domains are insulin-like growth factor 2 mRNA-binding proteins (IGF2BPs). The three members IGF2BP1-3 were majorly shown to increase mRNA stability and enhance translation.[166] Eukaryotic initiation factor 3 (eIF3) similarly can promote the translation of m^6A mRNAs by recruiting 43S complexes to initiate the protein synthesis which mainly can be observed upon cellular stress induction.[167,168]

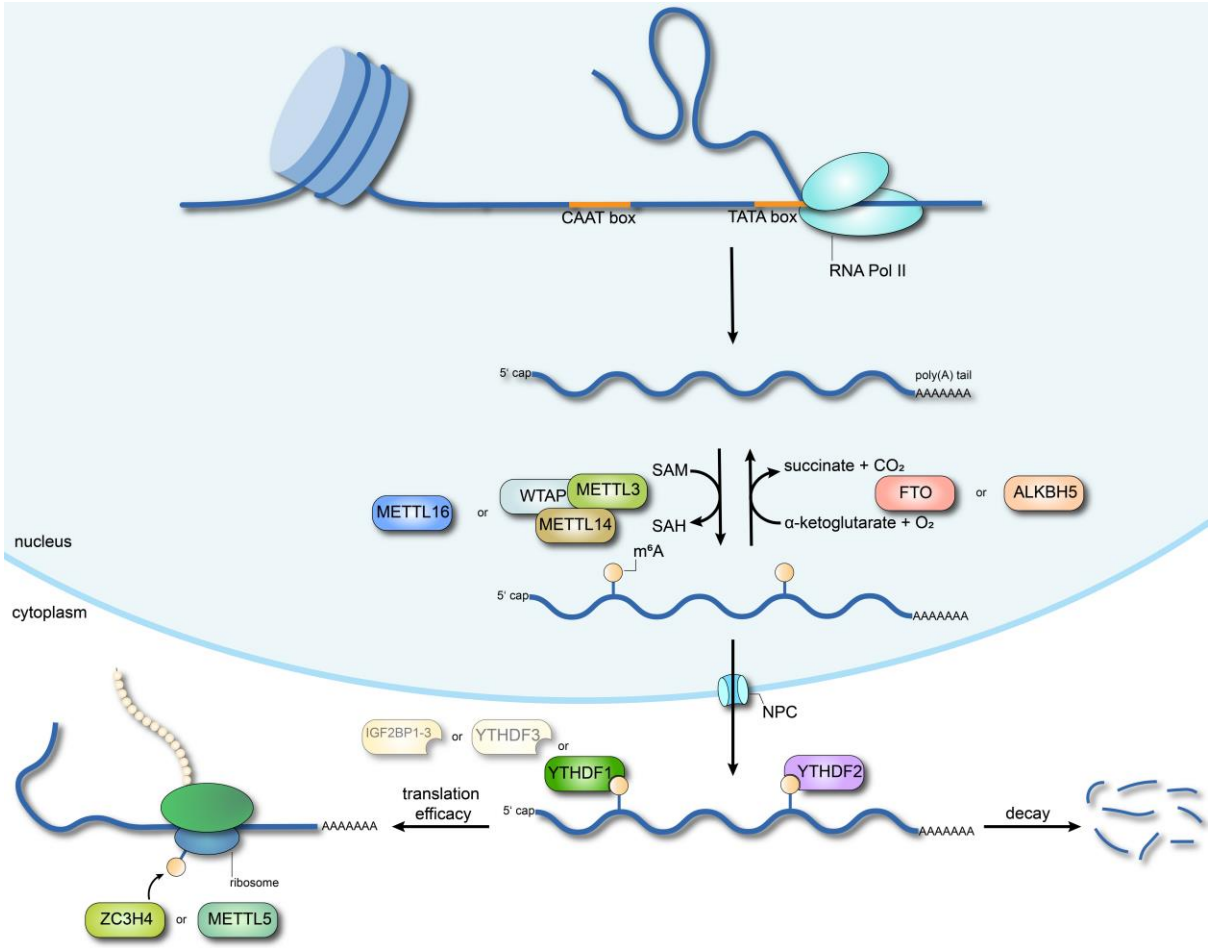

Figure 6: Schematic representation of the m^{6}A pathway. The RNA is first transcribed by RNA polymerase II and then further processed to give a 5' capped and polyadenylated RNA. Then, m^{6}A writers can install the methyl group on *N*6 positions of adenine bases which is subsequently recognized by m^{6}A readers to implement a specific function. Here depicted is the oppositional outcome of YTHDF1 or YTHDF2 interaction. m^{6}A erasers together with α-ketoglutarate are found to remove the methyl group by means of oxygen consumption.

Next to the m^{6}A recognition on coding RNAs, heterogeneous nuclear ribonucleoprotein (HNRNP) family members, including HNRNPC, -G, and -A2B1, can identify m^{6}A on precursor miRNAs (pre-/pri-miRNA). By recruitment of the miRNAs, either nucleocytoplasmic trafficking is regulated, or splicing of the ncRNA is mediated.[169–171]

Collectively, m^{6}A depicts a dynamic and tightly controlled RNA modification with crucial roles in processes such as RNA transcription, maturation, function, metabolism, and localization.[172,173] But not only the mark itself regulates the molecular signaling pathways, but also the RMPs involved in the network of m^{6}A RNA. Thus, it is unsurprising that all components of m^{6}A regulators (writers, readers, and erasers) have been connected with several types of human cancer.[174–176] Despite being rather poorly understood, their disease association makes RMPs of the m^{6}A network, an attractive new target class for the discovery of novel therapeutic candidates.[133,172,177] Therefore, the identification of modulators targeting m^{6}A RMPs not only should help to better understand the m^{6}A pathway, but it also forms a foundation for modern drug discovery.

1.3.1 The m^{6}A writer METTL16

Although the majority of RNA was shown to be methylated at the *N*6 position by the nuclear MTC, consisting of active methyltransferase-like proteins METTL3 and METTL14, there is growing interest in unraveling the function of another m^{6}A methyltransferase called METTL16. Human METTL16 consists of 562 amino acids which form a catalytic *N*-terminal methyltransferase domain (MTD) and a *C*-terminal domain composed of two vertebrate-conserved regions (VCRs).[178] In-depth structural investigations of the MTD could show that METTL16 is a class I SAM-MTase that uses a conserved Rossmann fold to bind SAM, as methyldonor, and a large positively charged groove to interact with RNA substrates. The conserved MTase core (residues 79-288) consists of mostly parallel, seven-stranded β-sheets (β1- β7) which are stabilized by a disulfide bridge between C183 and C247 to link β4 with β5. Interestingly, this disulfide bridge was found to be absent in the *S*-adenosyl-$_L$-homocysteine (SAH) bound state of METTL16.[179] Compared to the METTL3/METTL14 complex, METTL16 possesses several structural elements unique to its structure that most likely contribute to the RNA substrate specificity. Especially, the *N*-terminal residues 1-78 are thought to be majorly determining this selectivity. Nevertheless, uncertainty persists regarding how METTL16 recognizes its RNA substrates, mainly attributed to potential conformational changes upon RNA binding and the missing structural clarification of the *C*-terminal domain which may also contribute to substrate recognition.[179] Studies involving METTL16 and U6 snRNA or *MAT2A*, two confirmed substrates of the RMP, provided more details about the PRI showing that METTL16 accommodates single-stranded bulges in a ~37 × 18 Å groove which are flanked by double-stranded RNA.[179–181] Moreover, conserved residues, essential for methyl transfer catalysis, could be identified: N184, P185, P186, F187 (Figure 7A). This $_{184}$NPPF$_{187}$ motif is located between the SAM/SAH-binding site and the positively charged groove and was proposed to use the oxygen atom of N184 and the carbonyl oxygen of P185 to negatively polarize the *N*6 amino group via hydrogen bonding (Figure7A). Subsequently, the amino group accepts the methyl group from SAM in a nucleophilic substitution reaction (S_N2) to give SAH and an *N*6-methylammonium adenosine cation which may be stabilized further by the $_{184}$NPPF$_{187}$ amino acids. In addition to the $_{184}$NPPF$_{187}$ motif several aromatic residues (Y, F, or W) are located at the active site of METTL16 to hold the extrahelical, 180°-rotated adenine in place by π-π stacking.[179]

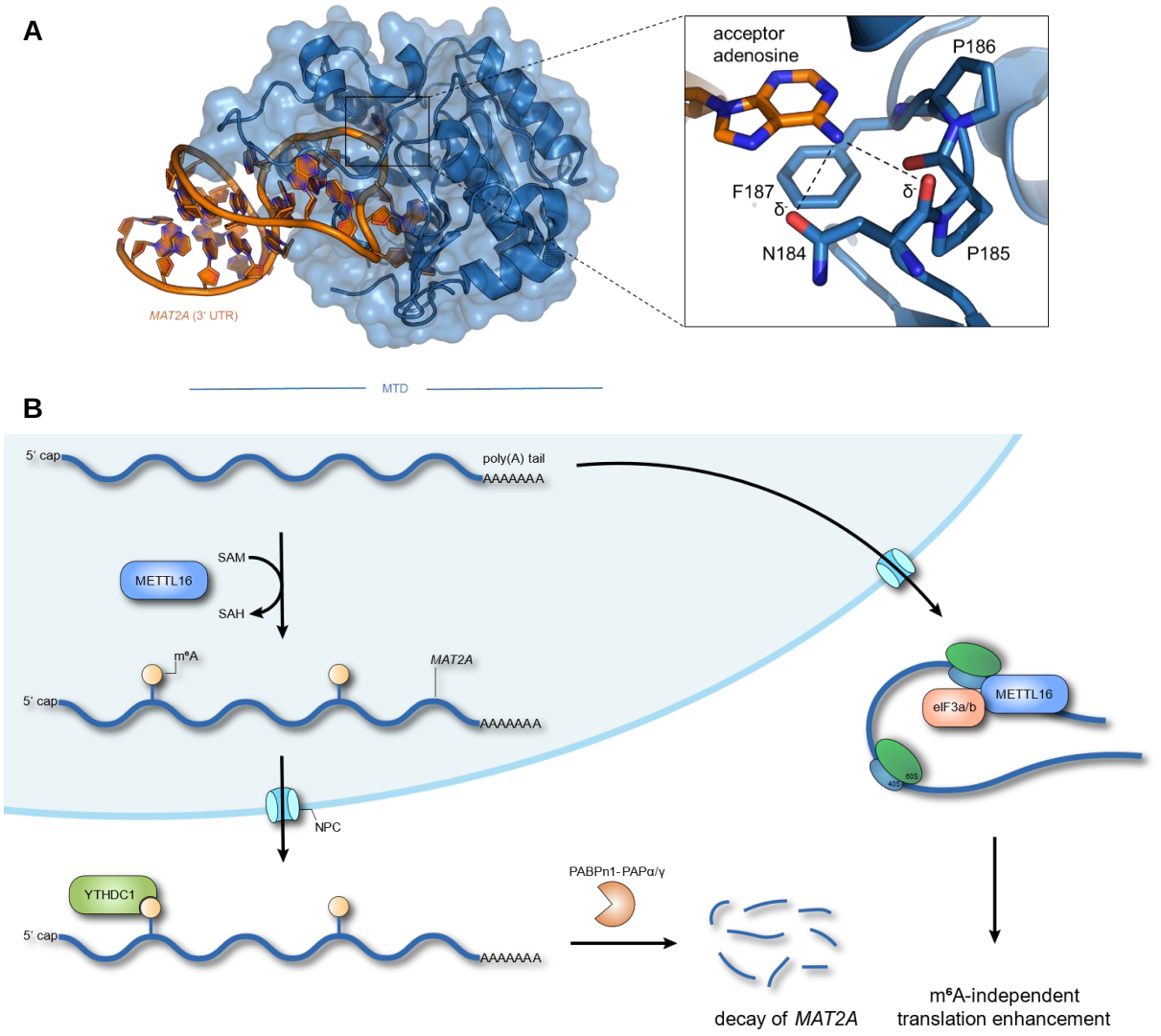

Figure 7: (A) Co-crystal structure of METTL16 (MTD) in complex with the 3' UTR of *MAT2A* (PDB: 6DU5). The $_{184}$NPPF$_{187}$ motif is shown in more detail, highlighting the potential activation of the *N*6 amino group. (B) The dual functionality of METT16 depends on the localization in the nucleus or the cytosol. Nuclear METTL16 binds *MAT2A* and thus regulates SAM homeostasis, while cytosolic METTL16 was shown to promote the translation of mRNAs independent from m^{6}A.

In a crosslinking experiment, the interaction of METTL16 with several cellular RNAs was demonstrated which were subsequently subjected to Illumina deep sequencing to reveal U6 snRNA as one of the most abundant binding partners of METTL16. Furthermore, the methyl mark of U6 snRNA was identified at A43 as being part of the commonly recognized UAC**A**GAGAA (the target adenosine is marked in bold and underlined) motif.[179,181] This nonameric sequence motif is known for its unique three-dimensional structure and was later found to be recognized commonly by METTL16.[180] *Methionine adenosyltransferase 2A* (*MAT2A*) is another transcript to be methylated by METTL16 at the UAC**A**GAGAA motif in 3' UTR hairpins. *MAT2A* encodes for a SAM synthetase and thus drives SAM production to regulate numerous methylation events in the cell.[182] The methylation of *MAT2A* by means of METTL16 was shown to either promote splicing of the mRNA or to retain an intron at the hairpin 1 (hp1) of *MAT2A* dependent on intracellular SAM levels. In limited SAM supply, METTL16

has a slower turnover and thus halts on hp1 which in turn induces splicing of *MAT2A*. Once there is high availability of SAM in the cell, hp1 is rapidly methylated, METTL16 dissociates from the RNP complex, and no splicing event occurs.[180,183] The retained intron on hp1 subsequently marks nuclear *MAT2A* for YTHDC1 recognition leading to RNA degradation, mediated by poly(A)-binding protein 1 (PABPn1) in complex with poly(A)-polymerases α/γ (PAPα/γ).[184,185] This SAM-dependent interplay is thought to allow cells to monitor and maintain intracellular SAM levels, highlighting the intricate role of METTL16 in SAM homeostasis (Figure 7B).

Independent from its methyltransferase activity, METTL16 more recently was found to contribute to gene regulation distinctly. While occurring in the nucleus, the RMP functions as m^6A writer, but once it localizes in the cytosol, METTL16 was shown to promote the translation of more than 4,000 mRNA transcripts.[186] This function as a translation-initiating facilitator is based on direct interaction between METTL16, eucaryotic initiation factor 3a/b (eIF3a/b), and the rRNA of ribosomes. As demonstrated by Crosslinking immunoprecipitation and quantitative PCR (CLIP-qPCR), the MTD of METTL16 interacts with the 18S rRNA and eIF3a/b, facilitating the binding of eIF3a/b to the 40S ribosomal subunit and causing the formation of an active 80S translation-initiation complex (TIC) (Figure 7B).[187,188]

Taken together, METTL16 is a m^6A methyltransferase responsible for the methylation of only a few hundred transcripts. Among those, *MAT2A* is most striking, as the mRNA decoding for a SAM synthetase directly influences SAM levels in cells. Depending on the m^6A mark, *MAT2A* splicing was found to be either promoted or retained and thus an intricate interplay between METTL16 and *MAT2A* is generated. Dependent on its localization, METTL16 was identified to facilitate in translation-initiation, promoting thousands of transcripts to be translated into proteins. With this crucial dual functionality METTL16 not only gains more recognition as RMP but also as a therapeutic target since overexpression was found to mediate tumorigenesis.[180,186,189]

Many RNA-modifying proteins have been associated with a variety of human diseases (e.g. cancer, infectious diseases, inflammatory and autoimmune diseases).[190–194] Especially METTL3, as being the major methyltransferase to form m^6A modifications, is upregulated in many cancers such as lung– and liver cancer or acute myeloid leukemia.[195–197] However, dependent on which mRNA is methylated by the METTL3-METTL14 complex, it was shown to have opposite effects with either an oncogenic or a tumor-suppressive outcome.[198] The underlying cause of this striking behavior warrants further investigation, yet accumulating evidence indicates that cancer-specific downstream targets may be pivotal drivers. In 2021, the first potent and selective METTL3 inhibitor UZH2 (**18**) was reported to reduce m^6A levels in MOLM-13 (AML) and PC-3 (prostate cancer) cells. With a single-digit nanomolar potency, the inhibitor since then served as an important chemical probe to study the METTL3 biology and may act as a lead for further optimization.[199] Another important milestone of METTL3 inhibition was the identification and structural optimization of the pyridopyrimidine compound STM2457 (**19**)

which shows an IC_{50} value of 16.9 nM on the PRI of METTL3 and m^6A RNA.[200] Notably, together with the derivative STC-15 (**20**), the METTL3 inhibitors entered clinical trials in 2022 (Figure 8).[201] Overall, these efforts in inhibitor discovery could highlight the effects of 'hijacking' the disease-related m^6A pathway.

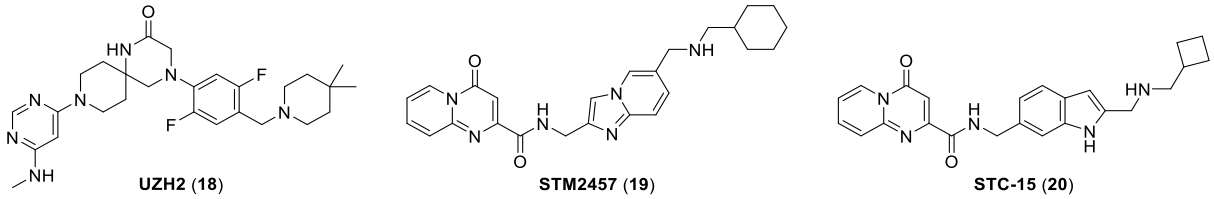

Figure 8: Reported METTL3 inhibitors with their respective IC_{50} values and the assay used to calculate the inhibitory effect. STM2457 and STC-15 are currently being investigated in phase I clinical trials.

Similar to the contradictory effects of METTL3 in different cancers, the exact role of METTL16 in pathology remains rather poorly understood. Besides the crucial effect on maintaining cellular SAM levels, METTL16 was shown to methylate the lncRNA metastasis-associated lung adenocarcinoma transcript 1 (*MALAT1*).[202] This lncRNA was found to act as both an oncogene as well as a tumor suppressor in different cancers.[203] Additionally, recent studies could visualize the cytosolic role of METTL16 which exerts an m^6A-independent function to facilitate translation of numerous mRNAs. In the same study, overexpression of METTL16 in liver cancer cells was identified to be the pathogenic driver by promoting the translation of oncogenic mRNAs. Genetic depletion of *METTL16* significantly inhibited growth, migration, and invasion of hepatocellular carcinoma (HCC) cells and suppressed tumor growth *in vivo*.[186] Given that the MTD of METTL16 is structurally characterized and was found to be critical for both m^6A-dependent and -independent activities, the development of effective inhibitors targeting the MTD of METTL16 would be promising and hold great therapeutic potential for cancer treatment.

Because the tumorigenic role of METTL16 only recently has been recognized, there are very limited studies focusing on small molecules to inhibit the methyltransferase. Today, there is only one published report utilizing a virtual screening to identify approved drugs such as VX-809 Lumacaftor[204] or kinase-inhibiting Nilotinib[205] as potential inhibitors of METTL16. However, these results are based on theoretical calculations and require further experimental validation.[206] Another report which is still being revised by the scientific community describes thiourea fragments as potent METTL16 inhibitors. Although the authors claim that the identified compounds are highly selective and inhibit METTL16 at nanomolar concentrations, the research work also requires further validation and insights into the inhibitory mechanisms of their METTL16-inhibiting fragments.[207] Therefore, the discovery of a first reported, potent, and validated METTL16 inhibitor represents a unique opportunity for researchers. The identification of such an inhibitor could serve as a valuable tool in chemical biology research or as a potential starting point for drug development.

1.3.2 The m^{6}A reader YTHDF2

After methyl transfer mediated by writers, m^{6}A is considered a unique recognition element for binding of specific RBPs which facilitates numerous biochemical processes. One of the most extensively studied m^{6}A readers are the members of the YT521-B homology (YTH) domain family, whose name-giving YTH domain recognizes m^{6}A specifically.[133,208–210] Despite this commonality, the different members exert diverse effects on RNA fate leading to alternative cellular outcomes.[157,160] One of the first discovered m^{6}A readers is YTHDF2, which binds m^{6}A mainly in the cytoplasm to efficiently orchestrate the degradation of RNAs.[211] Structural insights of YTHDF2 not only visualized the unique domains of the reader but also helped to understand the molecular mechanism for specific m^{6}A recognition. The reader protein consists of a conserved *C*-terminal YTH domain (residues 410-554) that specifically binds to m^{6}A-containing RNA and a P/Q/N-rich *N*-terminus.[212–214] A crystal structure of the YTH domain revealed a mixed α-helix-β-sheet fold composed of three α-helices (α1-3), eight β-sheets (β1-8), and two 3_{10} helices. While the β-sheets are arranged in a β-barrel fold, the α-helices were shown to cover the β-barrel and thereby form a hydrophobic core. Upon binding of an m^{6}A mononucleotide α1 and β2, β4 and β5 tightly lock the nucleotide in this hydrophobic pocket.[212] Particularly, m^{6}A interacts with an aromatic cage consisting of four aromatic amino acids (Y418, W486, W432, W491) (Figure 9A).[213] The aromatic rings of W432 and W491 were shown to undergo induced flipping coupled with m^{6}A binding and are nearly parallel to each other forming two aromatic walls. Studies involving W432A, W486A, or W491A mutations could show a significant loss of binding affinity to m^{6}A RNA and confirmed the importance of the aromatic cage. In addition to aromatic interactions, m^{6}A was also found to form several intermolecular hydrogen bonds. The *N*1 nitrogen for example interacts with the side chain carbonyl oxygen of D422, the *N*3 nitrogen atom with the NH of Y418, and the *N*6 nitrogen atom with the backbone of C433. Altogether, the specific interaction with m^{6}A is facilitated by several π-π and π-cation interactions as well as hydrogen bonds, all contributing to a well-organized pocket for m^{6}A reading.[212]

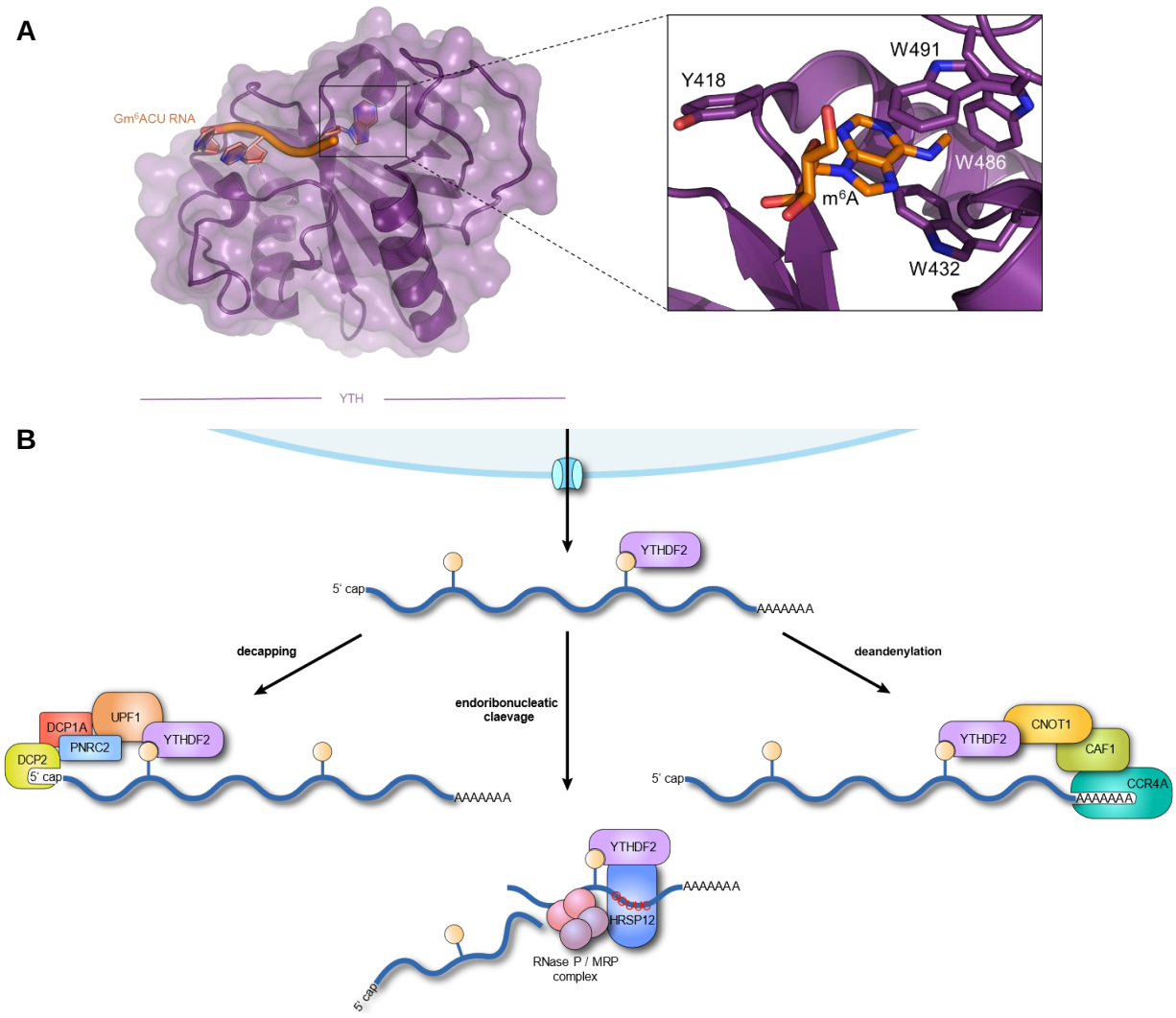

Figure 9: Structure of the m^{6}A reader YTHDF2 and the resulting effect on m^{6}A RNA in cells. (A) The co-crystal structure of the YTH domain in complex with a short m^{6}A oligomer (PDB: 7Z26) with the close-up showing the aromatic cage (Y418, W432, W486, and W491) and the corresponding interaction with an m^{6}A mononucleoside (PDB: 4RDN). (B) Schematic representation of YTHDF2 interacting with m^{6}A RNA through the *C*-terminal YTH domain. The *N*-terminus of YTHDF2 recruits different protein complexes to create a multi-layered regulation of m^{6}A RNA stability. Recruitment of UPF1 leads to a decapping mediated degradation, interaction with the RNase P/MRP complex induces endoribonucleolytic cleavage, and recruitment of the CCR4-NOT complex leads to deadenylation followed by degradation.

While the *C*-terminal YTH domain selectively binds m^{6}A RNA, the *N*-terminal P/Q/N-rich domain was shown to recruit different protein complexes which facilitate RNA degradation diversely. The first report of a YTHDF2-mediated decay of m^{6}A RNA-proofed CCR4-NOT complex recruitment which initiates deadenylation of the RNA (Figure 9B). This complex comprises nine subunits among which are the two deadenylases chromatin assembly factor 1 (CAF1) and carbon catabolite repressor protein 4A homolog (CCR4A). In a co-immunoprecipitation study the SH-domain of CCR4-NOT transcription complex subunit 1 (CNOT1) was revealed to directly interact with the *N*-terminus of YTHDF2, thus bringing the two deadenylases in close proximity to the m^{6}A RNA mediating the decay.[211] Another complex to be recruited by YTHDF2 is the RNase P/MRP complex consisting of the two ribonucleases

P and RNase for mitochondrial RNA processing (MRP) (Figure 9B). In their study, Park *et al.* immunoprecipitated YTHDF2 with heat-responsive protein 12 (HRSP12) which functions as an adapter between the *N*-terminal P/Q/N-rich domain of YTHDF2 and the RNase P/MRP complex. By linking the proteins, the RNases are brought in closer proximity to the m^{6}A RNA which results in endoribonucleolytic cleavage.[215] Lastly, a recent report identified the recruitment of upstream frameshift 1 (UPF1) to add another layer of m^{6}A RNA degradation mediated through a decapping mechanism (Figure 9B). UPF1, as ATP-dependent RNA helicase, previously was shown to act as a key player in nonsense-mediated mRNA decay (NMD) by interacting with endoribonucleases (e.g. SMG6) either directly or by recruiting adaptor proteins connected to such. To further elucidate the mechanism of YTHDF2-mediated decay of m^{6}A RNA, Boo *et al*. confirmed the recruitment of UPF1 together with the adaptor protein PNCR2 mediated by *N*-terminal YTHDF2 residues 101-168.[216] PNCR2 subsequently was shown to promote decapping of the RNA to finally initiate the degradation (Figure 9B). Furthermore, transcriptome-wide analyses revealed a correlation between m^{6}A RNAs that are not substrates for the RNase P/MRP mediated cleavage to be more dependent on decay by UPF1.[216] Collectively, these studies indicate a multilayered and dynamic regulation of m^{6}A RNA stability and highlight the importance of the m^{6}A reader YTHDF2.

YTHDF2 presents a dual functionality in many human cancers by altering the proliferation and migration of tumor cells.[217,218] While YTHDF2 was found to act oncogenic in cancers such as AML, lung cancer, and gastric cancer, it served as a tumor suppressor in osteosarcoma and melanoma.[219–221] In most cases, an upregulation of YTHDF2 expression was found to correlate with its oncogenic role. As a result, YTHDF2 was shown to alter a variety of essential cellular pathways such as the pentose phosphate pathway, TNF pathway, PI3K/AKT pathway, or the Wnt/β-catenin pathway.[222–225] In contrast, mRNA degradation of transcripts involved in the MAPK/ERK pathway, Hippo/YAP pathway, or the inflammatory pathway, involving an interplay between YTHDF2 and interleukin-11 and Serpin E2, could show the tumor suppressive effect of the m^{6}A reader in cancers.[226–228] This intricate effect of YTHDF2 generally demonstrates the clinical prognostic and therapeutic value of the m^{6}A reader in various cancers and highlights the need for developing effective modulators of YTHDF2 to provide novel strategies for anticancer treatment.

However, given the fact that the exact function of YTHDF2 still needs to be further explored in terms of cancer treatment, there is a scarcity of reports on small-molecule YTHDF2 inhibitors. In 2021, Einstein *et al.* demonstrated that downregulation of YTHDF2 could trigger proteotoxic cell death in triple-negative, MYC-driven, breast cancer cells and tumors.[229] Their study not only emphasized the crucial pathological role of YTHDF2 but also underlined that targeting the RBP should hold great potential for minimally toxic and highly specific treatment modalities in specific cancers. To date, only a few YTHDF2-binding fragments (**21**-**24**) and two small-molecule inhibitors have been reported showing both poor selectivity and potency as represented by similar inhibitory effects against

YTHDF1.[230–232] Although Micaelli *et al.* could characterize the binding mode of ebselen (**25**) to YTHDF2, it is noteworthy to mention that this selenazolone compound is known to act in a covalent and non-selective manner.[233] Therefore, the binding of ebselen to a variety of off-target proteins besides YTHDF1 cannot be excluded. Another inhibitor to disrupt the m^{6}A–YTHDF2 interaction is DC-Y13-27 (**26**) showing a reversible-covalent α-cyanoacrylamide warhead. An AlphaScreen-based assay could demonstrate the inhibitory effect of the compound on the PRI of the YTH domain and m^{6}A RNA (IC_{50} = 21.8 μM) whereas YTHDF2-binding could be confirmed via microscale thermophoresis (K_D = 37.9 μM) and surface plasmon resonance (SPR) studies. Furthermore, a selectivity evaluation was conducted involving potential inhibition of YTHDF1. Here, a significantly reduced inhibitory potency (IC_{50} = 165.2 μM) could demonstrate a preferred binding of DC-Y13-27 (**25**) to YTHDF2. Together with ionizing radiation treatment, the inhibitor also was able to inhibit NF-κB activation, a known target of YTHDF2. However, treatment of tumor-bearing mice with the compound did not show any inhibitory effect on tumor growth, underlining that the moderate micromolar inhibitory potency of the small molecule still holds great potential for further optimization.[231]

Taken together, YTHDF2 plays opposite roles in different cancers for which the reasons are yet to be elucidated in more detail. Thus, the RBP depicts a bona fide example to be further investigated using chemical biology approaches and to establish the foundation for m^{6}A-related drug discovery.

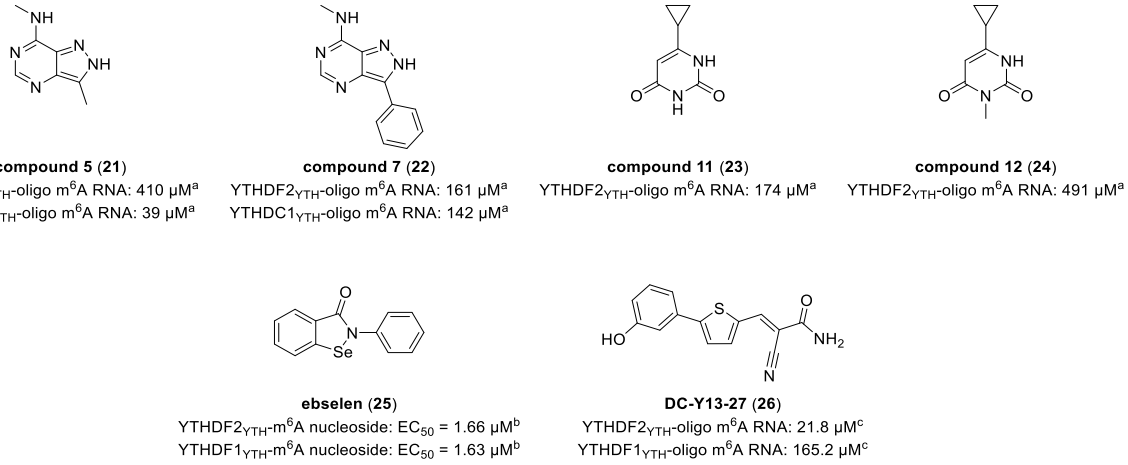

Figure 10: Reported fragments and small-molecule inhibitors of YTHDF2. [a]IC_{50} values were determined based on a homogeneous time-resolved fluorescence (HTRF) assay. [b]EC_{50} values were measured based on a tryptophan quenching assay. [c]IC_{50} values were determined based on an AlphaScreen assay.

2 Aim of this thesis

RBPs crucially participate in the orchestration of RNA biology and thus modulate numerous transcriptional and translational processes. Alteration of RBP-associated pathways can affect RNA life cycles, produce abnormal protein phenotypes, and thus lead to the occurrence and development of many human diseases. As a consequence, targeting RBPs that were found to promote pathogenesis has gained increasing attention in the last decade. Especially, small molecule-based approaches depict an accessible strategy to modulate RBP-related pathways to better understand RNA biology and to develop novel therapeutics. The aim of the thesis is the discovery and structural evaluation of small-molecule inhibitors targeting three distinct and disease-related RBPs that have been found to influence different RNA species: The miRNA-binding protein LIN28, the m^{6}A methyltransferase METTL16 and the m^{6}A recognizing protein YTHDF2.

The first part aims to investigate LIN28, an RBP which represses the tumor-suppressive miRNA *let-7* and thereby promotes the expression of various oncogenic proteins. LIN28 was shown to be overexpressed in numerous cancers acting as a key driver of tumorigenesis. To date, there are several efforts to identify small-molecule LIN28 inhibitors which already show significant impact by restoring levels of mature *let-7*. However, most of the small molecules are poorly characterized in terms of their inhibitory mode. Additionally, no inhibitor reached the submicromolar potency at this stage, leading to only minor effects in mouse models or LIN28-dependent cancer cells. Therefore, improvement of potency *in vitro* and *in cellulo* might be beneficial to develop improved LIN28-targeting small molecules. Consequently, in this chapter of the thesis, the aim is to identify potent LIN28 inhibitors via a scaffold-based approach and to discover novel LIN28-inhibiting small molecules by using a screening-based approach.

The second part of the thesis focuses on modulation of the m^{6}A RNA network which was proven to be crucial in all aspects of RNA biology. In this complex network, the m^{6}A writer METTL16 was found to be responsible for the methylation of specific mRNA transcripts, including *MAT2A*. By catalyzing the m^{6}A transfer for *MAT2A*, the writer can induce degradation of the transcript and thus controls SAM homeostasis throughout the cell. Depending on its localization, METTL16 was also found to facilitate translation-initiation, promoting the protein expression of several thousand transcripts including oncogenes. With this intricate dual functionality, METTL16 not only depicts a key player in the m^{6}A pathway but also makes METTL16 a promising target for small-molecule inhibition, independent of its methyltransferase activity. A small-molecule inhibitor could serve as a chemical tool to further elaborate the function of the methyltransferase and might act as a starting point for drug development targeting METTL16-associated cancers. Thus, this part of the work aims to identify the first experimentally validated METTL16-inhibiting small molecule via a screening-based approach.

Another RMP, acting as a key player in the m^{6}A network, is the m^{6}A reader YTHDF2 which has been found to control the stability of all kinds of RNA in a multilayered and dynamic fashion. By recruitment of different protein complexes, YTHDF2 can induce the decay of RNA via deadenylation, endoribonucleolytic cleavage, or decapping. The fact that YTHDF2 recognizes m^{6}A globally results in a dual functionality of the reader in many human cancers by altering the proliferation and migration of tumor cells. Although it has been demonstrated to function as an oncogene in most cancers, there is also evidence for YTHDF2 acting as a tumor suppressor.[217] This prominent effect of YTHDF2 generally demonstrates the therapeutic value of the m^{6}A reader and highlights the need for developing effective modulators to provide further insights into its function. The final aim of this work is therefore to identify small-molecular entities that can interfere with the PRI of m^{6}A RNA and YTHDF2. Both a scaffold-based and a screening-based approach are used to either rationally design a YTHDF2-inhibiting small molecule or to identify novel YTHDF2 inhibitors.

3 Results and discussion

3.1 Identification and evaluation of LIN28-inhibiting small molecules

Parts of this section were done in cooperation with L. Borgelt, L. Hohnen, P. Hommen, X. Qiu, F. Huang, J.S. Pallesen, F. Bosica, Y. Liu, J. Hwang, F. Li, G. O'Mahony, P. Lampe, H. Lightfoot or were part of my master's thesis.[234] *Contributions are indicated below the respective figures and tables.*

Small molecules disrupting the PRI of LIN28 and *let-7* hold great potential to develop new anticancer therapeutics and serve as chemical probes which should help to better understand the complex pathways and mechanisms in which LIN28 is involved. Since the miRNA-binding protein has been identified as a key driver of many cancers and today is a well-validated oncogene, a reverse chemical genomics approach depicts a reasonable strategy to perturb the LIN28-*let-7* interaction causing a restoration of the *let-7* biogenesis and thus a potential inhibition of cancer progression. In this work, inhibitors of the LIN28-*let-7* interaction were first synthesized and then evaluated in biochemical or cellular assays. To achieve this, two strategies were pursued: A scaffold-based approach and a screening-based approach. The starting point for the scaffold-based approach was a reported LIN28 inhibitor which I extensively investigated with regard to its structure-activity relationship. In contrast, the screening-based approach involved developing an assay capable of medium to high throughput to identify new LIN28 inhibitors, which were subsequently also structurally investigated.

3.1.1 Scaffold-derived LIN28 inhibitors

Results from this section were published as "Small molecules with tetrahydroquinoline-containing Povarov scaffolds as inhibitors disrupting the Protein–RNA interaction of LIN28–let-7".[235]

Most of the previously reported LIN28-inhibiting small molecules are poorly validated and characterized without a clear mode of inhibition. Additionally, cellular data involving treatment with LIN28 inhibitors mostly suggests a lack of potency or is missing entirely. Among the best-characterized compounds are the tetrahydroquinoline LI71 (**8**) and the chromenopyrazole SB1301 (**3**). The chromenopyrazole scaffold of SB1301 (**3**) allowed for the exploration of multiple positions, which has been summarized in several publications by our research group.[236–239] Part of this work was the in-depth characterization of the tetrahydroquinoline scaffold of LI71 (**8**) by chemical derivatization to identify a more potent analog and provide a systematic analysis of structural features required for LIN28 inhibition (Figure 11).

3.1.1.1 Initial SAR of tetrahydroquinoline LIN28 inhibitors

LI71 (**8**) and its enantiomer were reported as weak inhibitors of the LIN28 CSD with moderate IC_{50} values of 50 µM and 40 µM, respectively (Figure 9). The compound shows a tetrahydroquinoline (THQ) core scaffold accessible through a Povarov reaction which was initially reported in 1965 as an

efficient, acid-catalyzed, multicomponent reaction involving an aniline, an aldehyde, and an olefin component to form a cyclic product with three new stereocenters.[240] Two distinct mechanistic scenarios were proposed to explain the reactivity of each component: The first proposal consists of a concerted [4+2] cycloaddition process while another mechanistic hypothesis involves a sequential Mannich-Pictet Spengler ionic transformation with a subsequent electrophilic attack of the olefin component to give a cationic intermediate. The activated iminium ion is subsequently trapped by the aryl group and finally yields the THQ adduct upon re-aromatization. Generally, the involvement of three components allows for efficient variations of individual substituents, making the Povarov reaction an optimal procedure for diversity-oriented synthesis (DOS) (Figure 11A).[241] To investigate the structure-activity relationship (SAR) of LI71 (**8**) I therefore evaluated the impact of different substituents on the phenyl moiety of the THQ core, the benzoic acid substituent, and the fused cyclopentene ring (Figure 11B).

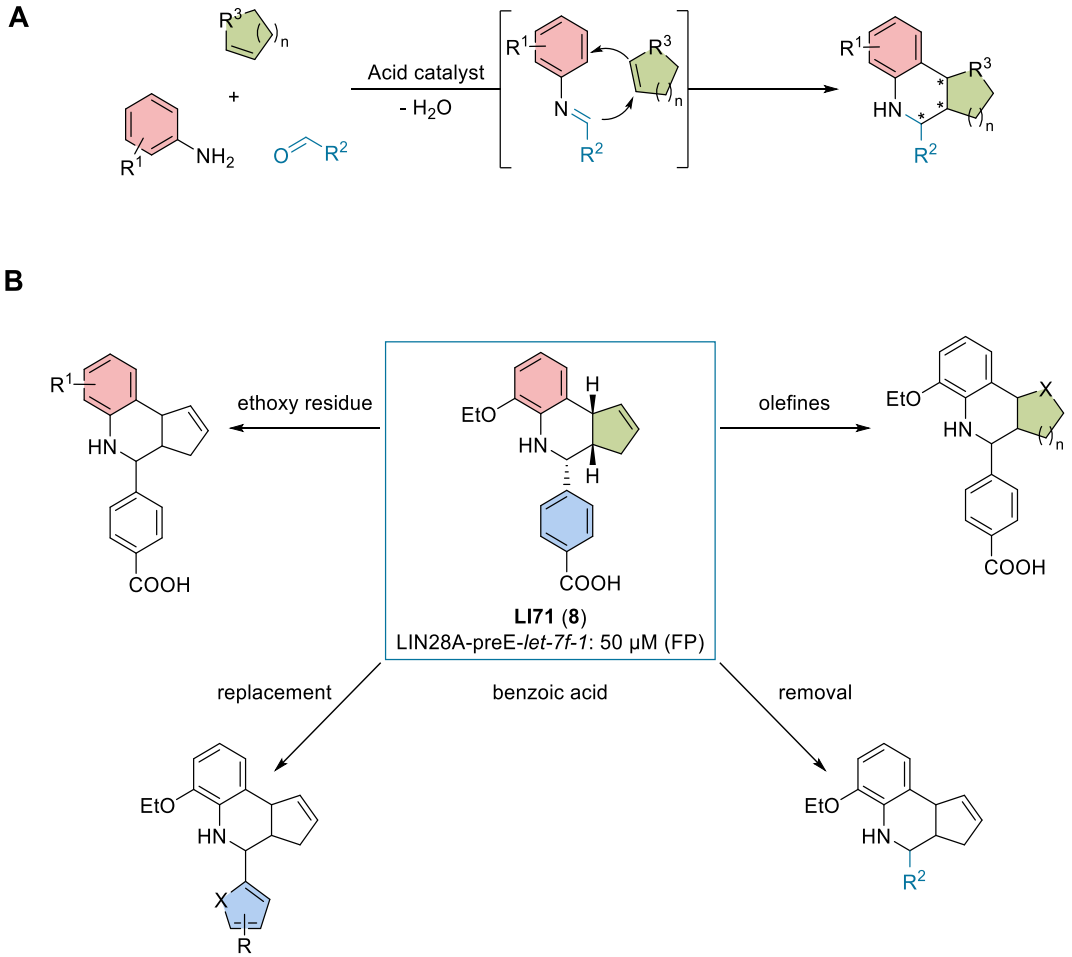

Figure 11: Structural investigation of Povarov-derived tetrahydroquinolines (THQs) as LIN28 inhibitors. (A) Scheme of multi-component Povarov reaction involving an aniline, an aldehyde, and a cyclic olefin to form the THQ core scaffold. (B) Strategy to investigate the structure-activity relationship (SAR) of the reported LIN28 inhibitor LI71 (**8**).

To start the first extensive SAR study of LI71 (**8**), the reported compound was initially synthesized and biochemically evaluated in-house to confirm its inhibitory effect against LIN28. Consequently, 2-ethoxyaniline, 4-formylbenzoic acid, and cyclopenta-1,3-diene were treated with the Lewis acid

ytterbium triflate to form the desired THQ-containing compound (**8**) which was isolated in good yield and an excellent diastereomeric ratio (d.r. > 99:1) measured by NOESY NMR. After obtaining LI71 (**8**), the compound was subjected to an electrophoretic mobility shift assay (EMSA) using Cy3-labeled preE-*let-7f-1* and LIN28A (residues 16-187) to evaluate the LIN28-inhibitory potency. Single-dose treatment with LI71 (**8**) at 75 µM revealed 53% inhibition of the LIN28-*let-7* interaction and thus confirmed its ability to moderately disrupt the PRI. To improve the inhibitory potency, initially, a systematic investigation of the phenyl moiety of the THQ core was performed while maintaining the 4-carboxyphenyl moiety. This approach was primarily selected because Wang *et al.* claimed in their initial publication that the carboxylic acid moiety was crucial for the interaction with LIN28.[128] Therefore, several anilines, with different electronic characteristics, were converted into THQ-containing compounds under Povarov conditions and subsequently tested in single-dose EMSAs to investigate their respective inhibitory effects. Next to the synthesis of electron-rich, aliphatic ether moiety-containing compounds (2-methoxy (**27**), 2-*iso*-propoxy (**28**) or 3,4,5-trimethoxy (**29**)), additional electron-withdrawing compounds were synthesized (4-cyano (**30**), 2,4-dichloro (**31**), 4-acetyl (**32**) and 3-acetyl (**33**)). Subsequent evaluation in the established mobility shift assay indicated no significant inhibitory effects of the compounds against LIN28-*let-7*, except compound **31** which only showed limited activity against the PRI (34% inhibition at 75 µM) (Table 1; Figure 12). Consequently, it was discovered that the 2-ethoxy residue of LI71 (**8**) not only provided previously claimed benefits but was deemed crucial for the interaction with LIN28.[128]

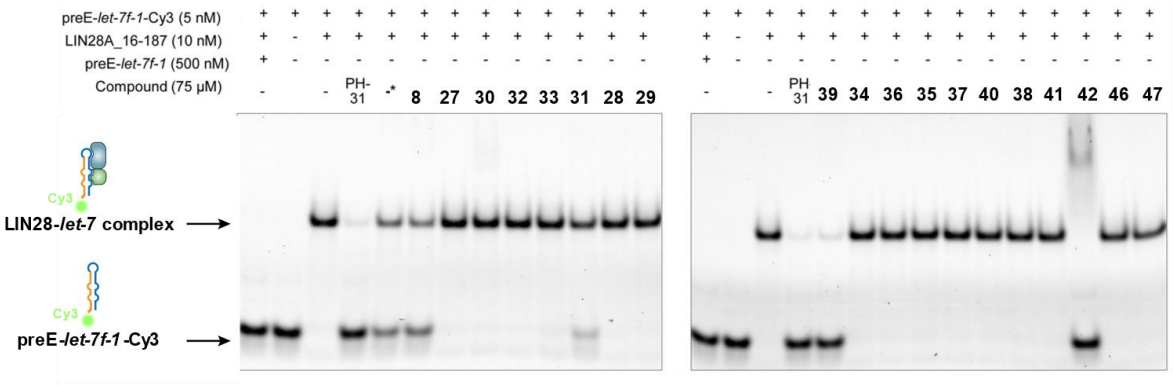

Figure 12: Inhibitory activity of synthesized compounds in electrophoretic mobility shift assay (EMSA). EMSA was performed using Cy3-labeled preE-let-7f-1 and LIN28A (residues 16-187). THQ compounds were tested in single concentration of 75 µM. PH-31 represents a LIN28 inhibitor that was previously identified in an FP-based screening and was used as a small-molecule positive control (-* diastereomer of LI71 (**8**)). The experiment was performed by Lisa Hohnen as part of her master's thesis.

In another SAR perspective, the essential effect of the carboxylic acid moiety should be further evaluated. Therefore, the aldehyde component of the Povarov reaction was varied while maintaining the aniline and the olefin component. Due to the electron-withdrawing nature of the carboxylic acid and its previously exhibited importance for LIN28 inhibition, we only used alternative electron-withdrawing components for the synthesis of LI71 analogs (**34**-**40**). A change of the carboxylic acid to a methyl ester

(**34**) or a nitro group (**35**) led to a complete loss of activity as indicated by EMSA matching with the reported data (Figure 12).[128] Similar trends were observed for a cyano group in para position (**36**), a trifluoromethyl group (**37**), or a pyridine-3-yl group (**38**). A change of the carboxylic acid position from para to meta (**39**), however, showed improved inhibitory activity against LIN28 compared to LI71 (**8**), and thus compound **39** was the subject of further investigations. Additionally, we incorporated a 3-hydroxy group (**40**) which could serve as an improved LIN28 inhibitor with better cell permeability, metabolic stability, and less potential idiosyncratic toxicity.[242] However, in a single-dose EMSA no disruptive effect on the LIN28-*let-7* interaction was observed for **40**. For compounds without a benzoic acid moiety, it was intriguing to observe the improved potency of carboxy-containing compound **42** compared to LI71 (**8**). The compound was synthesized using ethyl glyoxylate as an aldehyde component for the Povarov reaction to form a compound with an ethyl ester directly attached to the THQ core. After ester hydrolysis, the carboxy-containing compound **42** was tested at 75 µM showing 86% inhibition of the LIN28-*let-7* complex, thus depicting a promising hit candidate for further investigations (Table 1). Altogether, variations on the 4-carboxyphenyl moiety of LI71 (**8**) might be considered beneficial to improve the inhibitory activity against the LIN28-*let-7* complex.

Lastly, the olefin component was exchanged to investigate the impact of the respective cyclic moiety of LI71 (**8**). Thus, 2,3-dihydrofurane, 3,4-dihydropyran, and boc-protected tetrahydropyridine were used as electron-rich alkenes to be individually converted into the respective THQ compounds **43**, **44,** and **45**. Subsequent hydrolysis of the individual esters, and boc-deprotection under acidic conditions, gave compounds **46**-**49** which were then biologically evaluated in a single-dose EMSA (Scheme 1). Here, a complete loss of activity against LIN28 was observed for each compound, emphasizing the necessity of the original cyclic moiety of LI71 (**8**) to inhibit the PRI of LIN28 and *let-7* (Table 1).

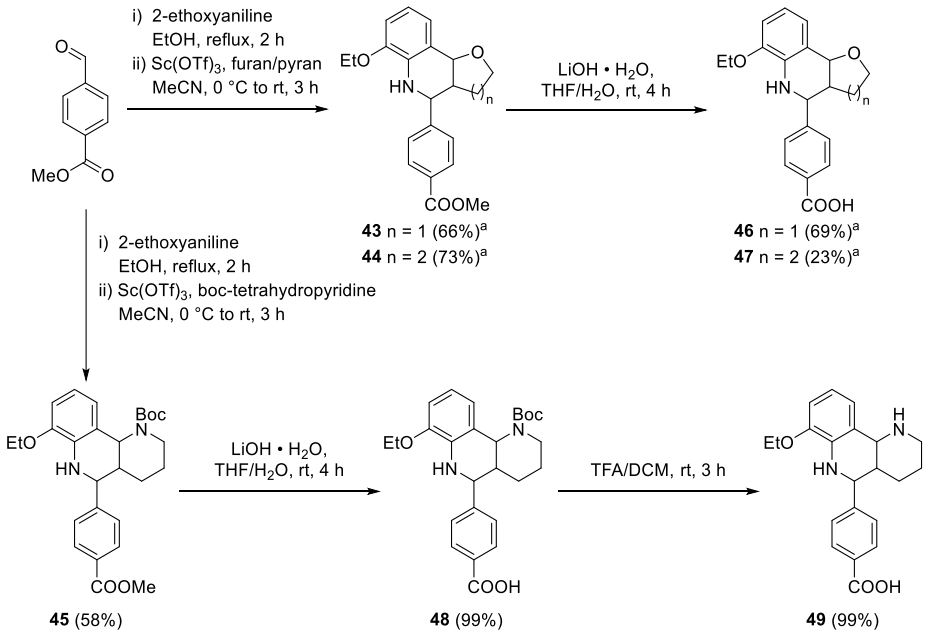

Scheme 1: Synthesis of the THQ compounds **43**-**49**. [a]The synthesis was performed as part of my master's thesis and is included to give a complete SAR study.[234]

Table 1: THQ-containing Povarov compounds and their respective inhibitory activity against the PRI of LIN28–*let-7*.

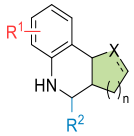

Compound ID	R^1	R^2	Olefin	Yield (%)	Inhibition at 75 µM (%)[b]
LI71 (**8**)	2-ethoxy	4-carboxy-phenyl	cyclopentadiene	68[a]	53
variation of R^1					
27	2-methoxy	4-carboxyphenyl	cyclopentadiene	40[a]	<5
28	2-*iso*-propoxy	4-carboxyphenyl	cyclopentadiene	70[a]	<5
29	3,4,5-trimethoxy	4-carboxyphenyl	cyclopentadiene	62[a]	<5
30	4-cyano	4-carboxyphenyl	cyclopentadiene	21[a]	<5
31	2,4-dichloro	4-carboxyphenyl	cyclopentadiene	47[a]	34
32	4-acetyl	4-carboxyphenyl	cyclopentadiene	23[a]	<5
33	3-acetyl	4-carboxyphenyl	cyclopentadiene	50[a]	<5
variation of R^2					
34	2-ethoxy	4-methoxy-carbonylphenyl	cyclopentadiene	94[a]	<5
35	2-ethoxy	4-nitrophenyl	cyclopentadiene	77[a]	<5
36	2-ethoxy	4-cyano	cyclopentadiene	76[a]	<5
37	2-ethoxy	4-trifluoromethyl	cyclopentadiene	76[a]	<5
38	2-ethoxy	pyridine-3-yl	cyclopentadiene	43[a]	<5
39	2-ethoxy	3-carboxyphenyl	cyclopentadiene	59[a]	92
40	2-ethoxy	3-hydroxyphenyl	cyclopentadiene	62[a]	<5
41	2-ethoxy	ethoxycarbonyl	cyclopentadiene	36[a]	<5
42	2-ethoxy	carboxyl	cyclopentadiene	71[a]	86

variation of olefins					
43	2-ethoxy	4-methoxy-carbonylphenyl	2,3-dihydrofuran	66[a]	<5
44	2-ethoxy	4-methoxy-carbonylphenyl	3,4-dihydropyran	73[a]	<5
45	2-ethoxy	4-methoxy-carbonylphenyl	boc-tetrahydropyridine	58	<5
46	2-ethoxy	4-carboxyphenyl	2,3-dihydrofuran	69[a]	<5
47	2-ethoxy	4-carboxyphenyl	3,4-dihydropyran	23[a]	<5
48	2-ethoxy	4-carboxyphenyl	boc-tetrahydropyridine	99	<5
49	2-ethoxy	4-carboxyphenyl	1,2,3,4-tetrahydropyridine	99	<5

[a]The synthesis was performed as part of my master's thesis and is included to give a complete SAR study.[234]

[b]EMSAs were performed in duplicates by Lisa Hohnen as part of her master's thesis.[243]

Taken together, initial SAR investigations of the LIN28 inhibitor LI71 (**8**) could show that replacement of the 2-ethoxy group with other substituents on the phenyl moiety or replacement of the cyclopentene with heterocyclic, five- or six-membered rings led to reduced- or a complete loss of activity. Only the 2,4-dichlorophenyl-containing compound **31** showed 34% inhibition of the RNP complex at 75 µM. Nevertheless, many other cyclic and acyclic olefins still can be incorporated in the Povarov reaction to obtain additional compounds with different THQ scaffolds that may present opportunities to identify other LIN28-inhibiting compounds. In contrast, variations of the 4-carboxyphenyl moiety resulted in the identification of two additional compounds (**39**, **42**) capable of disrupting the PRI of LIN28 and *let-7 in vitro* with improved potencies. Therefore, the two compounds, together with LI71 (**8**) were used in a second round of structural modifications to further explore structural features required for LIN28 inhibition.

3.1.1.2 Second SAR of tetrahydroquinoline LIN28 inhibitors

With the identification of two additional potential LIN28 inhibitors, a second round of structural modification was performed which focused on three different aspects: i) the modification of the secondary amine of the THQ core; ii) the replacement of hydrogens with bioisosteric groups at crucial moieties of the LIN28 inhibitors and iii) the use of different heterocyclic, aromatic rings to replace the original carboxyphenyl moiety (Figure 13). The modification of the secondary amine residue of the quinoline core should help to prevent redox cycling and thus trapping the mesomeric structure of the original hit compound. Therefore, the THQ compounds **8**, **39,** and **42** were acetylated at the NH of the

THQ core resulting in the incorporation of an oxygen as alternative hydrogen bond acceptor to be involved with LIN28 binding. For practical reasons, the acetylation of the THQ compounds was performed on methyl ester containing THQ analogs which reduced polarity and allowed for a more efficient purification by silica gel column chromatography of intermediates **50**-**52**. After purification, the acetylated analogs **50**-**52** were hydrolyzed using lithium hydroxide to give the desired carboxylic acid and acetyl-containing analogs **53**-**55** (Scheme 2). All intermediates and final compounds were subsequently investigated in the established mobility shift assay in which no inhibitory effect on the RNP complex could be observed for any of the compounds (Figure 14). This loss of activity led to the assumption that the original amino group of LI71 (**8**) may also essentially contribute to LIN28 binding by donating and accepting hydrogen bonds. The acetyl group, on the other side, might be sterically more demanding compared to the original proton and thus might clash with amino acid residues of the RBD resulting in no inhibitory effect.

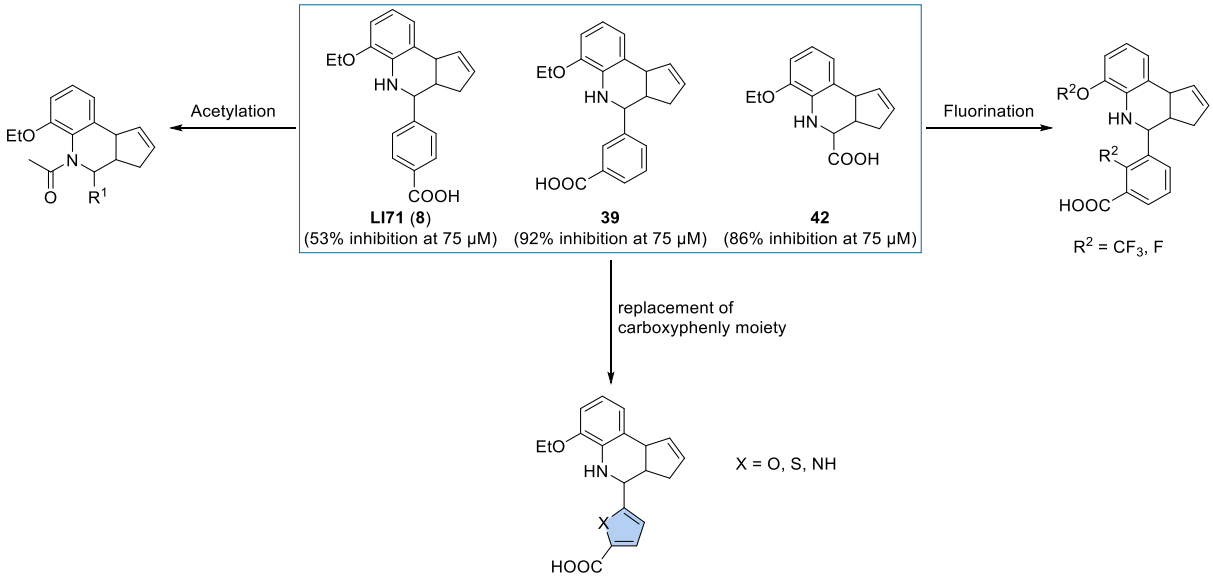

Figure 13: Second round of SAR investigation of THQ compounds as potential LIN28 inhibitors. Three distinct strategies were pursued to extend the understatement of the inhibitory mode of LI71 (**8**).

Another strategy that was intended to help increase the inhibitory potency of previously identified THQ compound incorporating additional fluorine atoms to the moieties that are assumed to contribute to LIN28 inhibition. Fluorinated compounds have a wide-ranging effect on molecular properties and thus are frequently used in chemical drug design. Among the reported effects of fluorine incorporation are the enhancement of potency or specificity, the improvement of cell permeability, and the creation of higher-order bioisosteres that offer context-dependent advantages.[244] To fluorinate **39**, which showed the highest potency against LIN28 *in vitro*, I used 2-fluoro-3-formylbenzoic acid, 3-formyl-2-(trifluoromethyl)benzoic acid or 2-(trifluoromethoxy)aniline in individual Povarov reactions to form compounds **56**-**59** (Scheme 2). While compounds **58** and **59** were synthesized to investigate the effect of fluoride atoms on the 3-carboxyphenyl moiety, **56** and **57** should help to explore the impact of a fluorinated, aliphatic ether moiety. After the successful isolation of the desired compounds, testing in

single-dose EMSA was conducted which revealed a complete loss of activity (Figure 14). These negative results might be attributed to the potential of fluorinated compounds to be destabilized under specific assay conditions thus causing the formation of fluoride anions that interfere with LIN28 inhibition.[245]

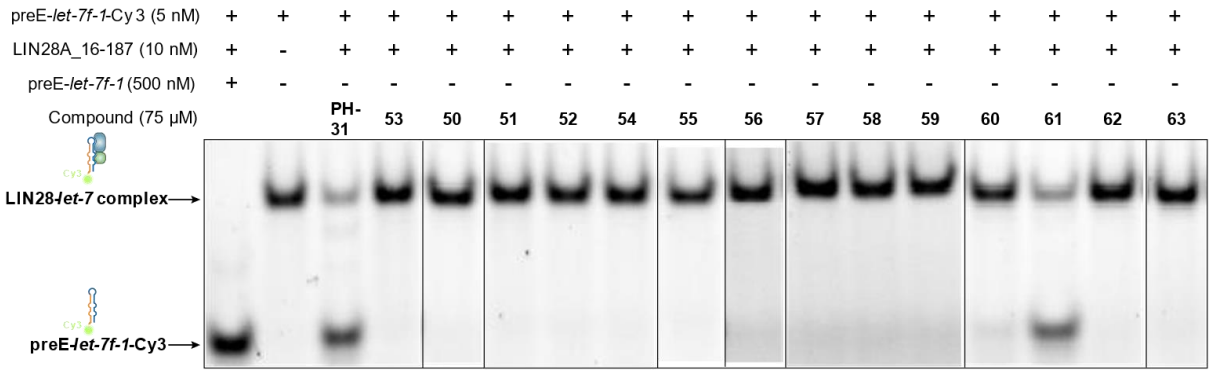

Figure 14: Inhibitory activity of synthesized compounds in electrophoretic mobility shift assay (EMSA). EMSA was performed using Cy3-labeled preE-*let-7f-1* and LIN28A (residues 16-187). THQ compounds were tested in single concentration of 75 uM. PH-31 represents a LIN28 inhibitor which was previously identified in an FP-based screening and was used as a small-molecule positive control. The experiment was performed by Lisa Hohnen as part of her master's thesis.

The last strategy pursued to optimize the inhibitory potency of **39**, was to replace the original carboxyphenyl moiety with alternative heterocyclic, aromatic rings which should increase the number of hydrogen bond acceptors or donors, respectively. Therefore, 5-formylfuran-2-carboxylic acid, 5-formylthiophene-2-carboxylic acid, and 5-formyl-1*H*-pyrrole-2-carboxylate were used as aldehyde components to be converted into the desired LI71 (**8**) analogs **60**-**63** under Povarov conditions (Scheme 2). The methyl-pyrrole-2-carboxylate (**62**) was hydrolyzed to obtain the desired carboxylic acid-containing compound upon which all compounds were subjected to EMSA analysis. Although pyrrole **63** and furan **60** led to a complete loss of inhibitory activity against LIN28, the thiophene **61** interestingly showed slightly reduced potencies compared to **39** (Figure 12). The observed 60% inhibitory activity of **61** might be explained by the sulfur atom of the thiophene moiety which contributes to the interaction with backbone oxygens of LIN28 amino acids. In these interactions, despite its electronegativity, the sulfur atom can function as Lewis acid to form σ-hole bonds with different oxygens which are likely motivated by HOMO–LUMO and electrostatic interactions.[246] Alternatively, the sulfur could function as a chalcogen atom to form σ-hole interactions with LIN28.[247]

Collectively, the performed structural investigations of the previously identified LIN28 inhibitors **8**, **39,** and **42** showed a limited extent of tolerability for the crucial functional groups of the THQ core scaffold. Neither the acetylation nor the fluorination approach resulted in the identification of LIN28 inhibiting small molecules. Only the exchange of the carboxyphenyl ring with a thiophene carboxylate led to a moderate disruptive effect of the LIN28–*let-7* interaction. Since attempts to enhance the potency of compound **39** were unsuccessful, subsequent biochemical and cellular investigations were conducted exclusively with the most effective LIN28 inhibitors.

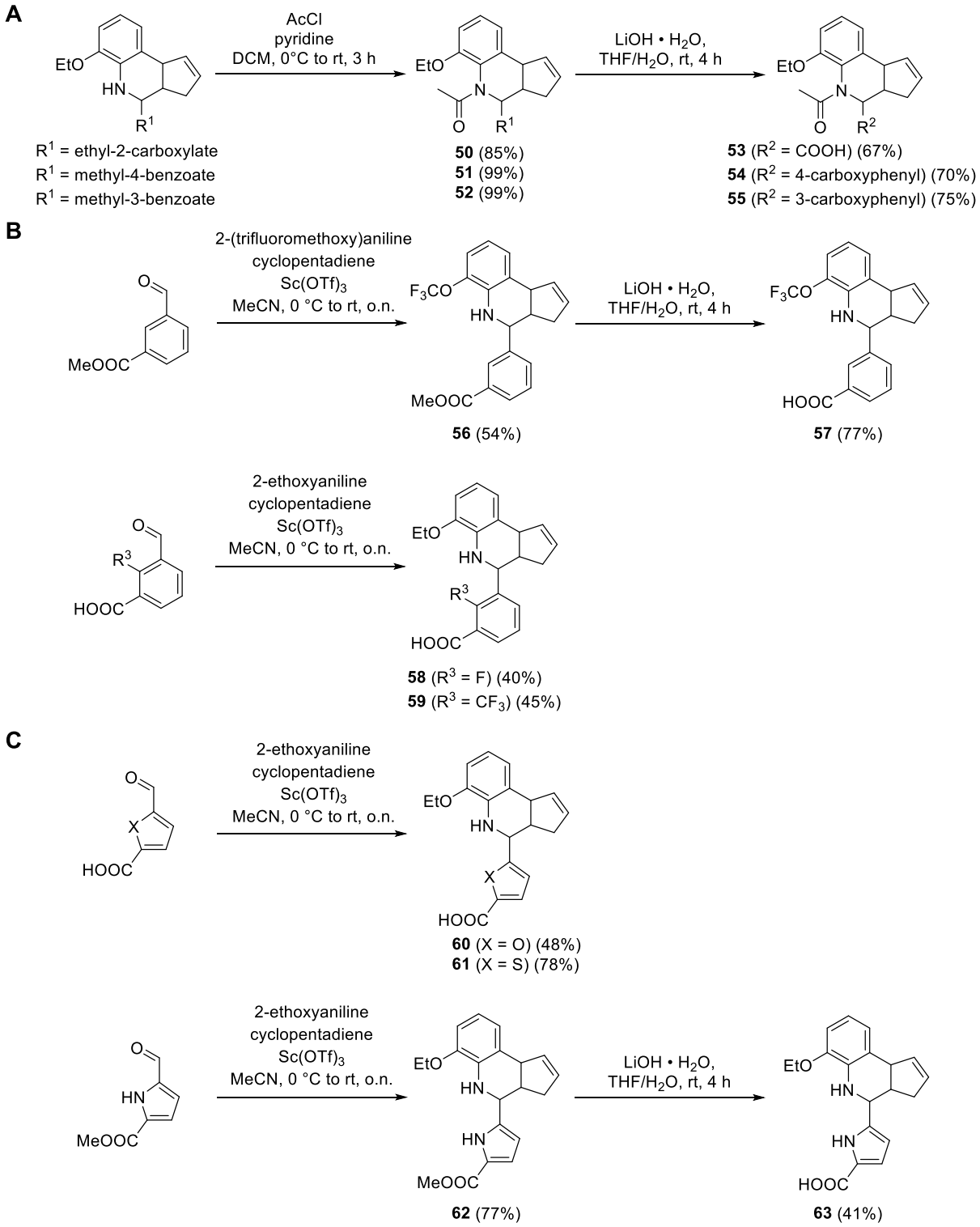

Scheme 2: Synthesis of the THQ compounds **50**-**63**. (A) Acetylation of THQ compounds **8**, **39,** and **42** (B) Incorporation of fluorine atoms, or a trifluoromethyl group to compound **39**. (C) Replacement of the carboxyphenyl moiety of compound **39** with aromatic heterocycles.

3.1.1.3 Validation of tetrahydroquinolines in orthogonal assays

To further confirm the inhibitory activity of the most active LIN28 inhibitors identified via the single-dose EMSA, the compounds were tested in a dose-dependent EMSA for the determination of IC_{50} values. Therefore, the compounds were individually titrated against LIN28 with increasing concentrations up to 75 µM. The inhibitory activity, measured by dose-dependent EMSA, matched with that of the reported IC_{50} value thus proofing the LIN28-inhibiting effect of LI71 (**8**) (Figure 15A).[128]

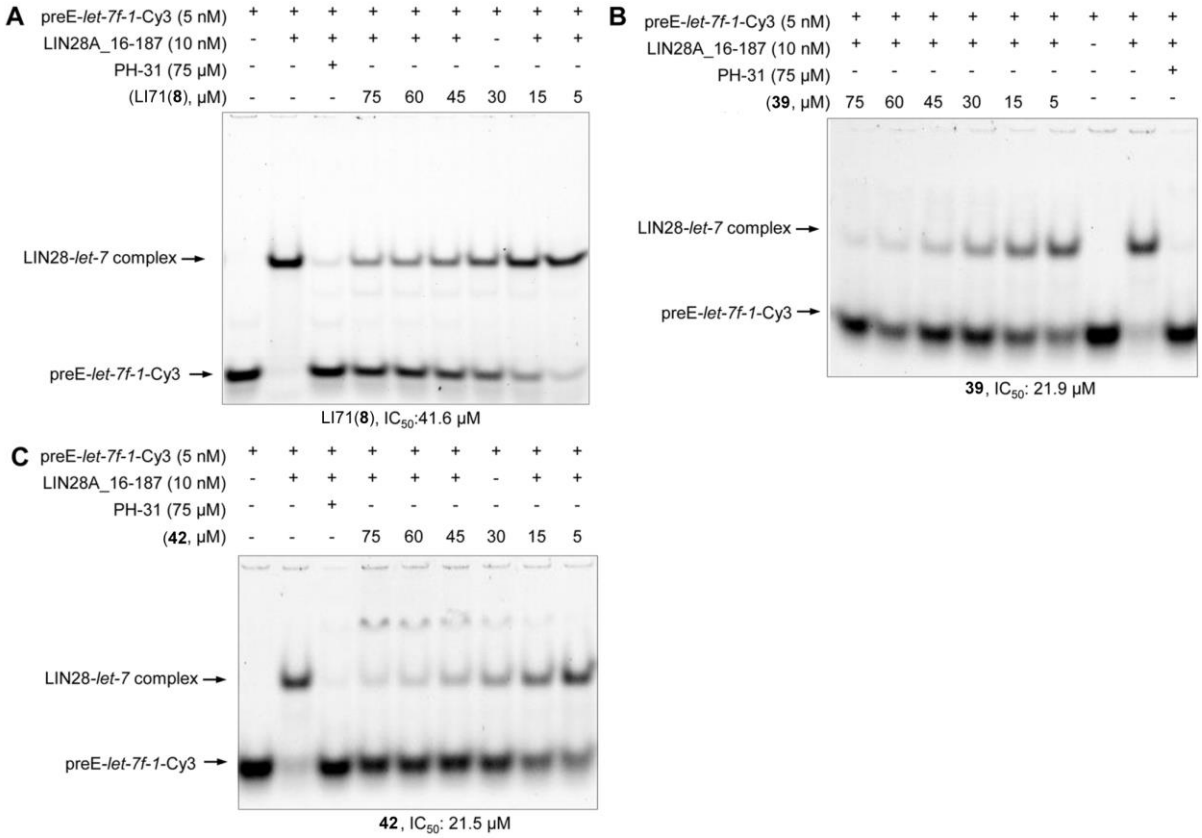

Figure 15: Dose-dependent inhibition of selected THQ compounds measured by EMSA. (A) Inhibitory effect of LI71 (**8**) on LIN28-*let-7* (IC_{50} = 41.6 µM). (B) Compound **39**, the 3-carboxyphenyl analog of the reported LI71 (**8**), showed an improved IC_{50} of 21.9 µM. (C) Compound **42**, the carboxy-THQ analog of the reported LI71 (**8**), showed an improved IC_{50} of 21.5 µM. The experiment was performed by Lisa Hohnen as part of her master's thesis.

Investigations of compounds **39** and **42** in the dose-dependent experiment resulted in improved IC_{50} values compared to that of inhibitor **8**, validating the previous findings (Figure 15B, C). Surprisingly, compound **42** exhibited an even stronger inhibitory effect against LIN28 compared to compound **39**. To further evaluate the activity of the potential LIN28 inhibitors, an orthogonal fluorescence polarization (FP) assay was performed. This technique is widely used to monitor binding events in solution by measuring the degree of polarization of a fluorophore which is inversely related to its molecular rotation. Thereby, the rotation is largely driven by Brownian motion, allowing the identification of diverse molecular interactions and enzymatic activities.[248] In our case, a FAM (6-carboxyfluorescein)-fluorophore-labeled preE-*let-7f-1* was used together with human LIN28A (residues 16-187) to monitor inhibitory effects of the best-performing compounds **39** and **42** against the

LIN28-*let-7* interaction. Prior to the evaluation of the LIN28 inhibiting small molecules, the assay was performed using unlabeled preE-*let-7f* as control (Figure 16A). Similar to dose-dependent EMSAs, the established FP assay requires a titration of compounds against LIN28 allowing for the determination of half-maximal inhibitory concentrations. Testing compound **39** via FP assay could further validate its improved potency against LIN28-*let-7* showing an IC_{50} value of 4 µM (Figure 16B). The IC_{50} value of compound **42** however, could not be accurately determined in the FP assay due to observed autofluorescence of the compound interfering with the readout of the assay (Figure 16C).

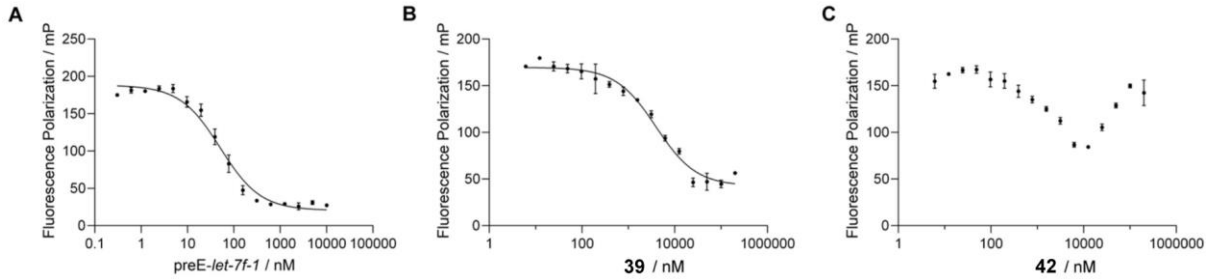

Figure 16: FP assay of compounds **39** and **42** using human LIN28A (residues 16-187) and FAM-labeled preE-*let-7f-1*. (A) Unlabeled preE-*let-7f-1* was used as a control and showed an IC_{50} value of 55 nM. (B) The most active compound **39** showed IC_{50} of 4 µM. (C) The IC_{50} of compound **42** could not be accurately measured in FP. The experiment was performed by Lisa Hohnen as part of her master's thesis.[243]

This discrepancy of the inhibitory effect observed for compound **39** in the two different assays is a commonly observed phenomenon that can be explained for various reasons. While the EMSA relies on the mobility of a fluorophore-labeled miRNA in a native polyacrylamide gel, the FP assay depicts a method that allows for the investigation of PRIs in solution. Additionally, the choice of different fluorophores may lead to varied results. Nevertheless, the LIN28-inhibiting activity of **39** could be confirmed via FP assay and thus a more potent small-molecule inhibitor was identified.

Furthermore, we continued to test the antiproliferation activity of synthesized THQ compounds (**8**, **39**, **42**) against JAR cells. However, none of the tested compounds showed an inhibitory rate of more than 50% at a single concentration of 10 µM as measured in a 3-(4,5-dimethylthiazol-2-yl)-2,5-diphenyltetrazolium bromide (MTT) assay. The fact that the rather potent LIN28 inhibitors **8**, **39**, and **42** barely showed any inhibitory activity indicated that the antiproliferation activity against JAR cells did not correlate with LIN28 inhibition. Altogether, testing of the most potent LI71 analogs (**39** and **42**) in a dose-dependent EMSA and an orthogonal FP assay resulted in the identification of **39** as the most active THQ compound which disrupts the LIN28-*let-7* interaction with low micromolar potency. On the other hand, Compound **42** needs further scrutiny with additional assays, as it exhibited autofluorescence in the FP assay, preventing the accurate calculation of an IC_{50} value using the methods employed here.

3.1.1.4 Binding mode prediction for THQ LIN28 inhibitors

To predict a binding mode between synthesized inhibitors and LIN28, we performed a molecular docking study for the most potent compound **39**. LI71 (**8**) was found to interact with the CSD of LIN28 as indicated by a saturation transfer difference (STD) analysis. In the original publication, an additional HSQC titration of LI71 and STD analysis of a mutant protein LIN28Δ_{K102} treated with the inhibitor showed that K102 contributes mainly to the binding.[128] Therefore, we chose the G9-A10 binding site of LIN28 to perform the docking of compound **39** into the RBD (Figure 17).

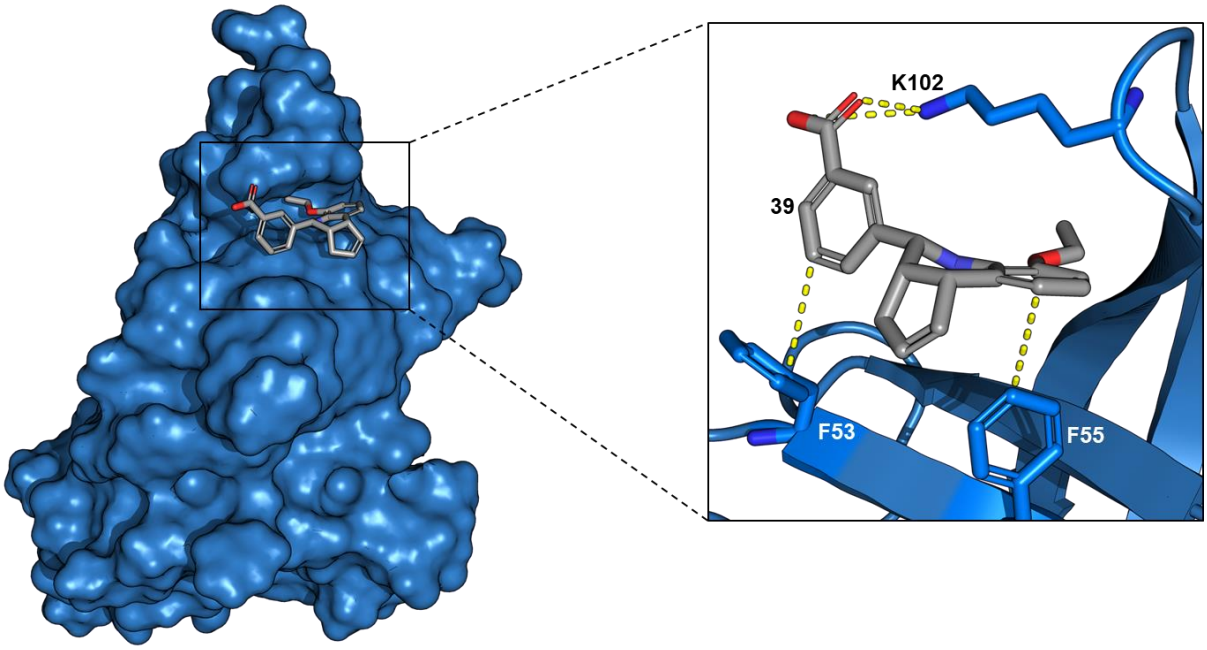

Figure 17: Molecular docking analysis to predict the binding mode of the most potent THQ inhibitor **39** to the CSD of LIN28 (PDB: 5UDZ). Compound **39** bound to the G9-A10 binding site with the Lys102 forming a salt bridge with the 3-carboxyphenyl moiety.

In the most optimal binding configuration, compound **39** fits into the RBD of LIN28 and forms a salt bridge between the 3-carboxyphenyl moiety and K102 similar to the reported LI71 (**8**).[128] Additionally, extensive π-π stackings could be identified involving F53, F55, and F73 which were found to interact with the phenyl moiety of the THQ core and the 3-carboxyphenyl moiety. Moreover, this visualization might explain the greatly reduced activity of other synthesized THQ compounds, which could be attributed to the additional substituents on the phenyl moiety creating steric clashes or displacing the carboxylic acid, which in turn cannot form the crucial salt bridge with K102.

Altogether, the prediction of a binding mode for compound **39** revealed reasonable interactions with the CSD of LIN28 matching with reported data and our own experimental data. However, the analysis relies on static crystal structure models of LIN28 or even fully predicted configurations of the small molecule and thus requires careful evaluation. Hence, further experimental evidence is necessary to validate the mode of action of compound **39**. For example, co-crystallization or cryo-EM analysis, as being the most reliable techniques for elucidating biomolecular structures, might be considered.

Alternatively, molecular dynamics (MD) simulations to capture the behavior of LIN28 and **39** in full atomic detail and at fine temporal resolution could be performed to create a more realistic and accurate model.[249]

3.1.2 Screening-derived LIN28 inhibitors

Results from this section were published as "Trisubstituted Pyrrolinones as Small-Molecule Inhibitors Disrupting the Protein–RNA Interaction of LIN28 and Let-7" and "N-Biphenyl Pyrrolinones and Dibenzofuran Analogues as RNA-Binding Protein LIN28 Inhibitors Disrupting the LIN28–Let-7 Interaction."[250, 251]

To identify a new class of LIN28 inhibitors with scaffolds that are amenable to further structural optimization, a screening-based approach was designed. The aim was to establish an assay capable of medium-to-high throughput which should help to identify small molecules interfering with LIN28-*let-7* binding. After the hit identification and validation in orthogonal assays, a structural evaluation and optimization of potential LIN28 inhibitors was performed, which should allow for the discovery of compounds with increased activity, and potentially reduced toxicity.

3.1.2.1 Identification and validation of a new LIN28 inhibiting small molecule

For the identification of new LIN28 inhibitors, an FP assay was established to measure the binding between truncated human LIN28A containing the CSD (residues 16-187) and a FAM-labeled preE-*let-7f-1* miRNA. In the FP assay, unlabeled preE-*let-7f-1* was used as a positive control showing an IC_{50} value of 55 nM, equivalent to the reported value (Figure 18C).[128] To further proof the robustness of the assay the reported LIN28 inhibitor SB1301 (**3**) was used as a small-molecule positive control which also showed an IC_{50} consistent with the reported value (Figure 18D).[125] Consequently, the assay was deemed suitable for small-molecule screening which was executed using a natural-product-inspired collection of 1,400 compounds. As a result, compound **64** could be identified as a potential CSD-binding LIN28 inhibitor showing micromolar inhibitory activity (Figure 18E).

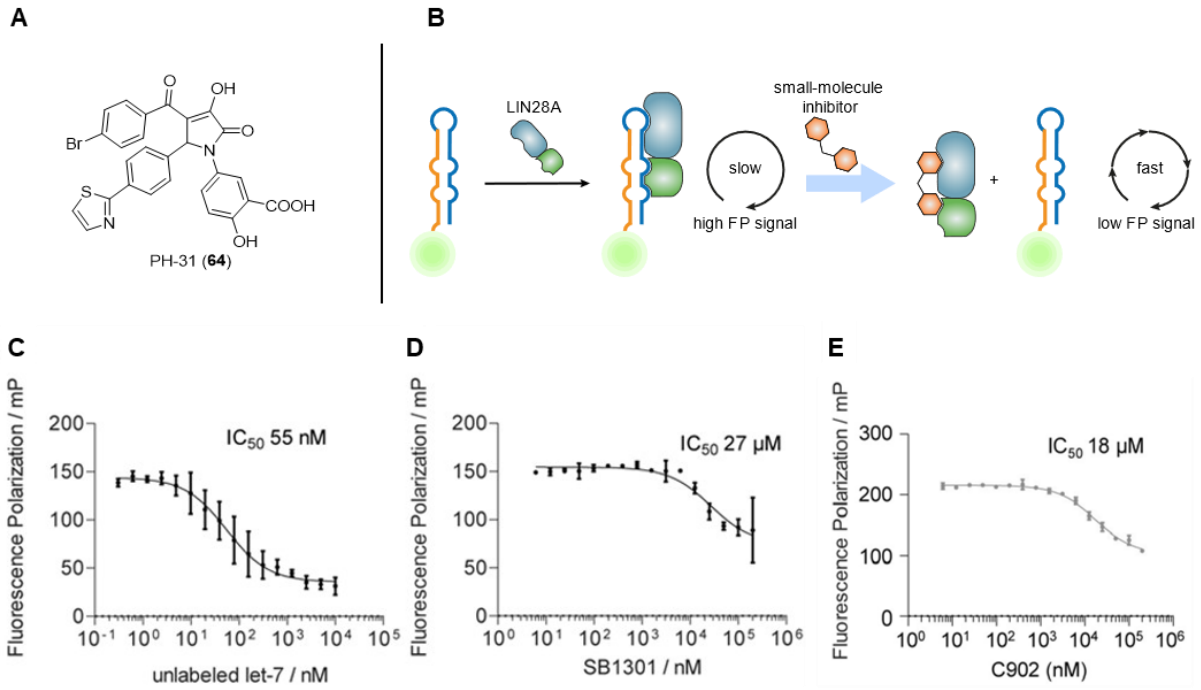

Figure 18: FP assay to identify new LIN28 inhibitors. (A) Structure of the re-synthesized hit compound PH-31 (**64**). Re-synthesis of **64** was performed by Pascal Hommen. (B) Principle of the established FP assay. (C) Inhibition of the LIN28–*let-7* interaction using unlabeled preE-*let-7f-1* (IC_{50} = 55 nM). (D) Inhibition of the LIN28 using the reported inhibitor SB1301 (**3**) (IC_{50} = 27 µM). (E) Inhibitory activity of C902 (**64**) showing a disruptive effect on the LIN28-*let-7* interaction. The FP assay was adapted, optimized, and performed by Lydia Borgelt and Philipp Lampe.

To validate the activity of **64**, the hit compound was re-synthesized (as PH-31 (**64**)) by using a three-component Doebner condensation-type reaction. This reaction was first described in 1887 and involves an aniline, an aldehyde, and pyruvic acid.[252] Although the exact mechanism for the reaction has not yet been elucidated entirely, there are two possible scenarios to occur: The first involves an aldol condensation between the aldehyde and pyruvic acid forming a β,γ-unsaturated α-keto-carboxylic acid. This intermediate subsequently reacts with the aniline in an addition to the γ-position and lastly undergoes a ring-closing condensation followed by re-aromatization (Scheme 3A). An alternative pathway describes the formation of a Schiff base instead of the aldol condensation, which then forms the same addition product with the keto-enol tautomerizing pyruvic acid and lastly undergoes the same condensation reaction (Scheme 3B).[253] After isolating the desired pyrrolinone **64**, the compound was tested in a dose-response FP assay as well as an EMSA (Figure 19A). Here, the inhibitory activity could be verified and **64** was identified as a new inhibitor that is able to disrupt the formation of the LIN28–*let-7* complex. To furthermore show the inhibitory effects of pyrrolinone **64** *in cellulo*, levels of mature *let-7* miRNA family members *let-7a* and *let-7g* were measured in JAR cells using reverse transcription-quantitative polymerase chain reaction (RT-qPCR). Treatment with 5 µM or 20 µM of **64**, respectively upregulated the mature miRNA levels twofold thus indicating cellular LIN28 inhibition mediated by the small molecule (Figure 19B).

Altogether, the screening-based approach involving the investigation of 1,400 compounds in an established FP assay resulted in the identification of a trisubstituted pyrrolinone (**64**) as a new LIN28-inhibiting scaffold which diversifies the limited number of available LIN28 inhibitors. Additionally, compound **64** served as a lead structure to guide follow-up SAR investigations of the structural features required for LIN28 inhibition.

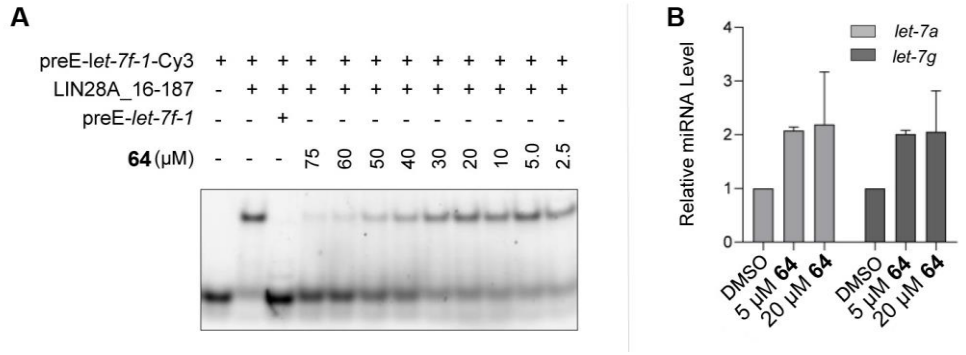

Figure 19: (A) In EMSA **64** showed dose-dependent inhibition of the LIN28−let-7 interaction. (B) Treatment of JAR cells with **64** led to increased levels of mature *let-7a* and *let-7g* quantified by RT-qPCR. Error bars indicate standard deviations of two independent measurements. The assays were performed by Lydia Borgelt.

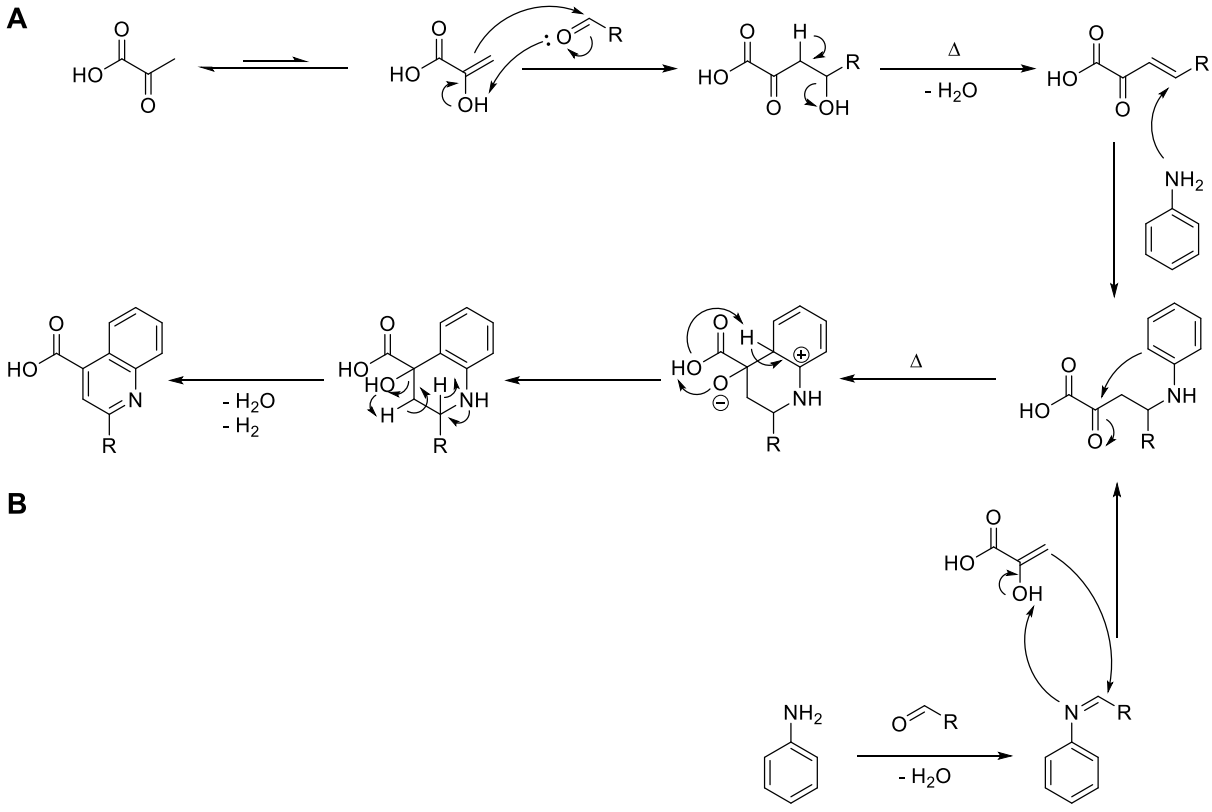

Scheme 3: Proposed mechanisms for the three-component Doebner reaction. (A) The pathway involves an aldol condensation, followed by the addition of an aniline and recovery of aromaticity. (B) The pathway involves the formation of an imine, followed by a reaction with keto-enol tautomerizing pyruvic acid.

3.1.2.2 Initial SAR of the LIN28-inhibiting trisubstituted pyrrolinone

After identifying the trisubstituted pyrrolinone **64** as LIN28 inhibitor interfering with *let-7* binding to the CSD, our group focused on structural investigations of the initial compound by varying substituents at each of the 1-, 4-, and 5- positions. Here, the importance of the *N*-salicylic acid substituent on the pyrrolinone core scaffold was highlighted and claimed essential for LIN28 inhibition while other substituents of the pyrrolinone core scaffold allowed for modifications to a variable extent.[250] However, the carboxylic acid is not always an optimal residue for potential lead candidates, as it has been linked with issues such as poor membrane permeability and metabolic toxicity.[242] So, we continued to investigate the SAR of the original pyrrolinone **64**, in cooperation with O'Mahony and colleagues, to identify more potent and less toxic LIN28 inhibitors. By synthesizing several pyrrolinones, we were able to build up a focused compound library containing 60 analogs of **64** featuring a variety of modifications at the 1-, 3-, 4-, and 5-positions of the core scaffold.[254] Thereby, the substituent variations can be subdivided into three different strategies: i) A change of the carboxyphenyl residue; ii) Variations of the thiazole moiety, and iii) a change of the salicylic acid moiety (Figure 20).

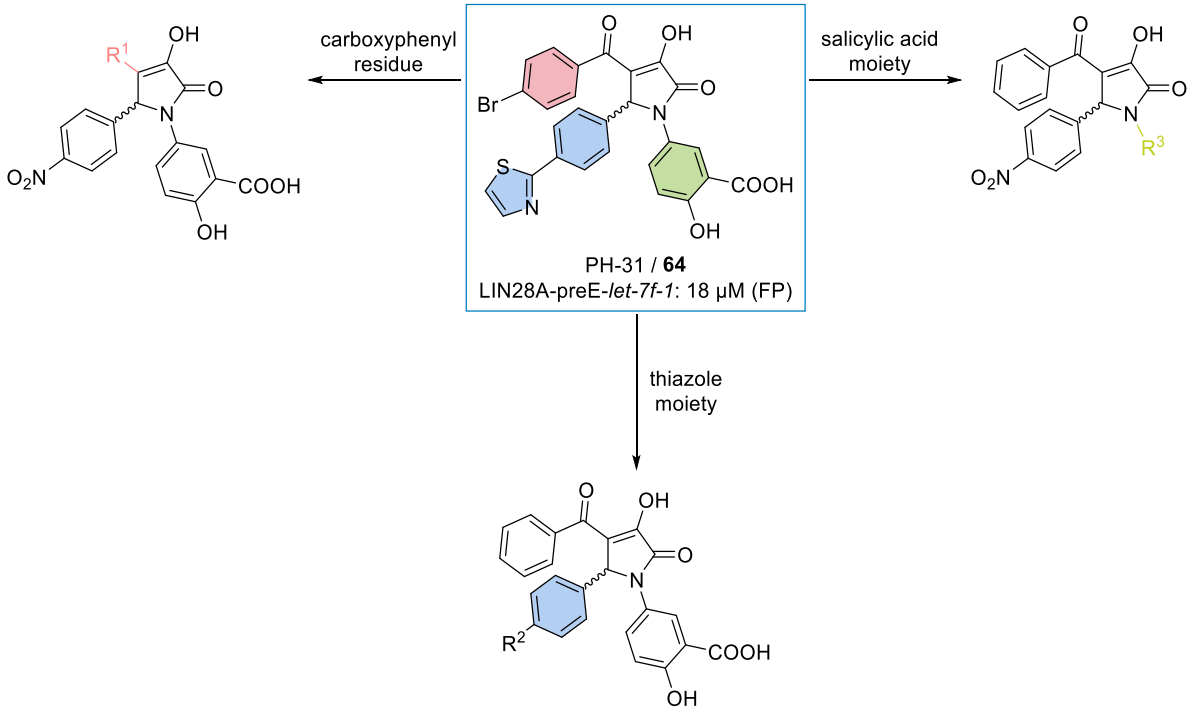

Figure 20: Structural investigation of trisubstituted pyrrolinones as potential LIN28 inhibitors. The strategy to investigate the structure-activity relationship (SAR) of the LIN28 inhibitor PH-31 (**64**) consisted of individual changes in the carboxyphenyl residue, the thiazole moiety, and the salicylic acid moiety. Synthesis of the focused library of 60 pyrrolinone analogs was performed by Jakob S. Pallesen and Francesco Bosica.

Upon isolation, all 60 analogues were tested in single-dose EMSAs at 75 µM, to identify potential inhibitory effects against the LIN28-*let-7* complex. Here, a total of twelve compounds showed at least 60% inhibition of the RNP complex formation. Generally, most of the active small molecules still harbored a salicylic acid moiety underlining the importance for LIN28 inhibition. Among the most

potent analogs of **64** were compounds with *N*-heterocycles either at the 5-position or the 4-position of the pyrrolinone core, possibly forming additional hydrogen bonds with amino acids of LIN28. Although modifications of the 1-position commonly confirmed the observed trend that exchanging the salicylic acid leads to a complete loss of activity, compound **66** showed a promising inhibition rate of 84%. This inhibitory effect against LIN28 was of particular interest since pyrrolinone **66** shows a biphenyl moiety at the 1-position and thus potentially depicts a small molecule with better bioavailability and less toxicity.[255] Therefore, **66** was re-synthesized using the previously established three-component Doebner condensation reaction involving ethyl 2,4-dioxo-4-phenylbutanoate, 4-nitrobenzaldehyde and a [1,1'-biphenyl]-3-amine (Scheme 4). After validating the inhibitory activity of **66**, the compound was chosen as an alternative lead candidate to investigate the structural features required to disrupt the LIN28-*let-7* interaction.

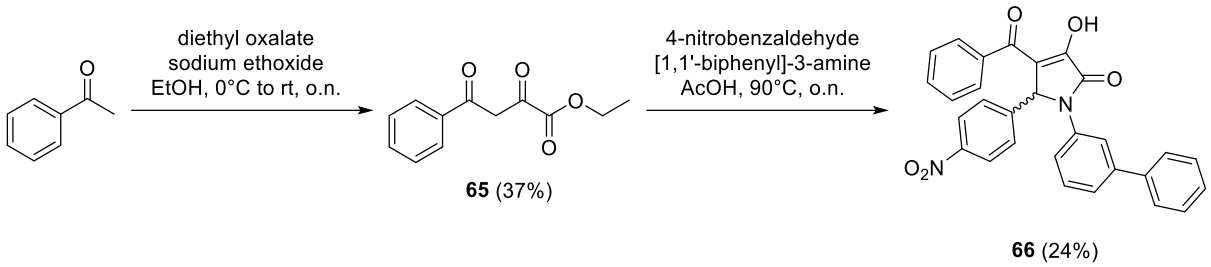

Scheme 4: Synthetic procedure to obtain the LIN28-inhibiting, trisubstituted pyrrolinone **66** as a racemic mixture.

First, biolayer interferometry was measured to evaluate the direct binding of **66** to LIN28, in which it showed dose-dependent binding to the CSD (Figure 21B). Since all synthesized pyrrolinones have a stereocenter at the 5-position of the core scaffold, **66** underwent purification by chiral high-performance liquid chromatography (HPLC) to separate both the (*S*)- and (*R*)-enantiomer, namely **66S** and **66R** respectively. Both enantiomers were then tested for their inhibitory potency against LIN28 in a dose-dependent EMSA and nano differential scanning fluorimetry (DSF) (Figure 21C, D). While dose-response EMSA revealed that **66R** was slightly more active than **66S** with IC_{50} values of 24 µM and 37 µM, respectively which indicates that the (*R*)-enantiomer has a slightly favorable geometry, nanoDSF could show a similar LIN28-stabilizing effect of both enantiomers by ~1.9°C at 75 µM. Furthermore, **66**, as a racemic mixture, was tested *in cellulo* by measuring the relative mature *let-7d* and *let-7i* levels in JAR cells. Here, the biogenesis of both *let-7* family members was affected by dose-dependent compound treatment of **66**. To note, a comparison with the alteration of mature *let-7* levels induced by compound **64** revealed a 2- to 3-fold increase in potency of the biphenyl analog **66**, indicating that the exchange of the salicylic acid moiety led to increased cell permeability (Figure 21E).

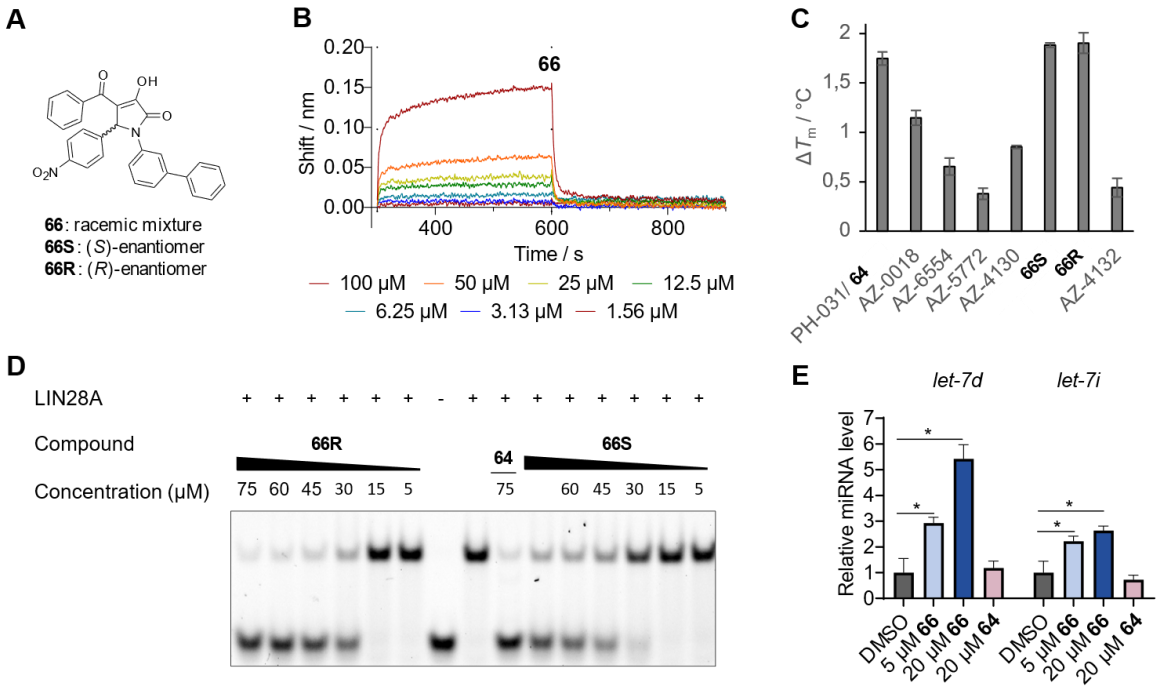

Figure 21: Validation of pyrrolinone **66** as LIN28 inhibitor. (A) Structure of re-synthesized trisubstituted pyrrolinone **66** as a racemic mixture. Separation via chiral HPLC afforded the individual enantiomers **66S** and **66R** and was performed by Jakob S. Pallesen and Francesco Bosica. (B) Concentration-dependent biolayer interferometry (BLI) of **66**. (C) Melting temperature of the CSD of LIN28 treated with 75 µM pyrrolinones measured by nanoDSF. Compounds AZ-0018, -6554, -5772, -4130, and -4132 depict compounds of the focused library whose structure is not disclosed in this thesis. (D) Dose-dependent inhibition of the LIN28-*let-7* interaction by **66R** and **66S** measured by EMSA. (E) RT-qPCR measurement to monitor relative mature *let-7d* and *let-7i* levels in JAR cells after treatment with compounds **64** and **66**; error bars indicate the standard deviation. All biophysical, and cellular assays were performed by Lydia Borgelt; The dose-dependent EMSA was performed by Lisa Hohnen.

In summary, we performed a structural investigation of the original trisubstituted pyrrolinone **64** by evaluating different substitution patterns at the 1-, 3- 4- and 5-position of the pyrrolinone core. Most of the LIN28-inhibiting compounds harbored a salicylic acid moiety except for the promising hit candidate **66**. The biphenyl moiety-containing analog thus was chosen to be further evaluated in biophysical-, biochemical, and cellular assays. To our delight, we identified **66** as being able to inhibit the LIN28-*let-7* interaction in a dose-dependent manner, to interact with the CSD of LIN28, and to show improved cellular activity in comparison with the original compound **64**. To continue with these promising results, we furthermore extended the SAR study of pyrrolinone **66** to identify more potent analogs.

3.1.2.3 Binding mode prediction for trisubstituted pyrrolinone LIN28 inhibitors

To predict a binding mode between synthesized inhibitors and LIN28, we performed a molecular docking study for the biphenyl-substituted pyrrolinone **66**. Since all the previously performed experiments indicated binding of the inhibitor to the CSD of LIN28, we used the G9-A10 binding site to dock compound **66** into the RBD (Figure 22).

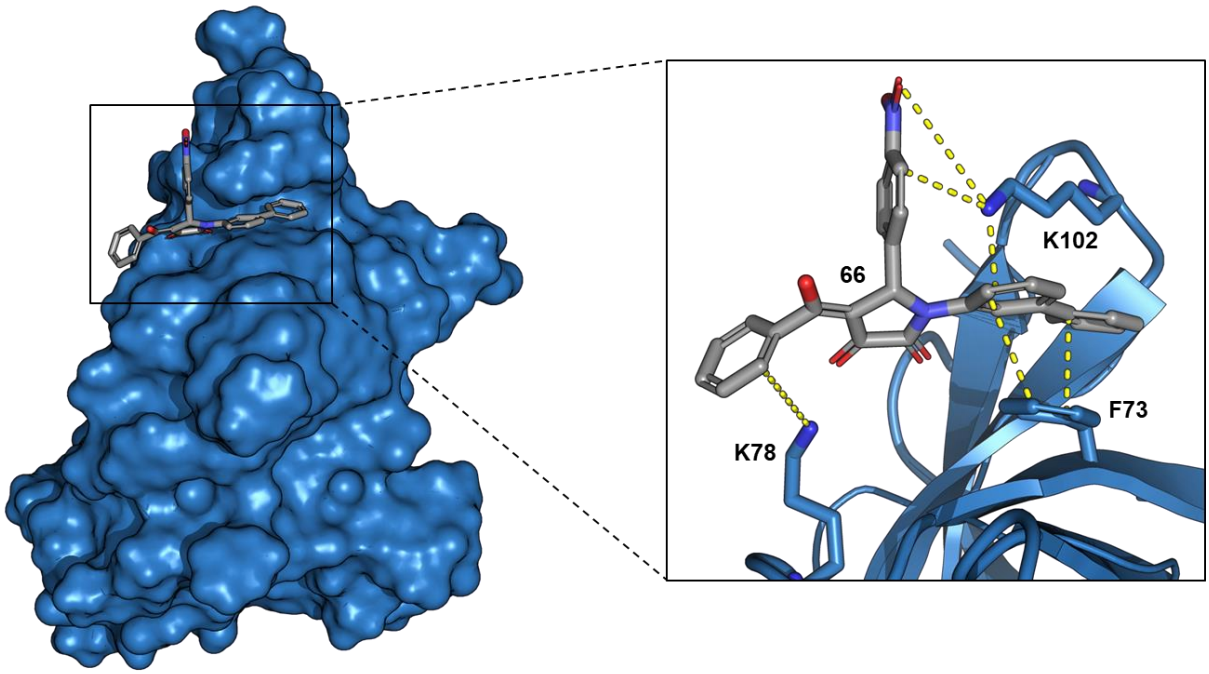

Figure 22: Molecular docking analysis to predict the binding mode of pyrrolinone **66** to the CSD of LIN28 (PDB: 5UDZ). Surface structure of LIN28A (sky blue) and **66** in gray carbon backbone (left) and the enlarged visualization of the ribbon structure of LIN28A with **66** (right). Selected key interacting residues are depicted as sticks.

In our model, docking analysis indicated the formation of a salt bridge between the nitro group of **66** and K102 of LIN28, as well as extensive π–cation and π–π stacking interactions involving the aromatic moieties of **66** and LIN28 residues K102, K78, and F73. Altogether, the prediction of a binding mode for compound **66** revealed reasonable interactions with the CSD of LIN28 in line with reported- as well as experimental data.[250]

3.1.2.4 Second SAR of trisubstituted pyrrolinone LIN28 inhibitors

We next aimed to improve the moderate micromolar potency of compound **66** and thus synthesized an additional 16 analogs. These analogs included variations specifically at the 4-position of the pyrrolinone core, such as cycloalkyls (**67**-**69**), fluorophenyls (**75**, **76**), or furan-2-yls (**78**, **79**). A general trend we could observe after testing the individual compounds in single-dose EMSA was the decrease in activity for cycloalkyl substituents (**67**-**69**) and certain substituents at the phenyl ring (**70**-**72**, **77**, and **81**). Additionally, aromatic five-membered heterocycles with hydrogen bond acceptors such as furan-2-yl (**78**) and *N*-methyl-pyrrole (**80**) led to slightly decreased activities compared to the original **66**. Only compound **76** with a 2-fluorophenyl group indicated more potent LIN28 inhibition. (Table 2). To further extend the SAR study, we picked the most active pyrrolinones obtained from the previous variation of the 4-position and focused on changes in the biphenyl moiety. Therefore, we used dibenzo[*b*,*d*]furan-3-amine and dibenzo[*b*,*d*]furan-2-amine, respectively, to synthesize ten more derivatives with an additional hydrogen bond acceptor and a rigidified scaffold (Table 2). With the incorporation of a dibenzofuran moiety, the idea was to reduce the conformational entropy penalty upon small-molecule

binding to LIN28. Upon isolation, the analogs (**83-92**) were tested for their ability to disrupt the interaction of LIN28 and *let-7* in single-dose EMSA at 75 µM. All of the dibenzofuran-containing analogs inhibited LIN28 with similar activities compared to the original compound **66**. Compounds with a dibenzofuran-3-yl instead of dibenzofuran-2-yl moiety generally showed higher potencies and compounds **88** and **92** even exhibited better LIN28-inhibiting activities than **66**. The 4-phenyl- (**88**) and 4-furan-2-yl (**92**) containing compounds subsequently were subjected to dose-dependent EMSA in which the best inhibitory activities among all evaluated small molecules could be observed (Figure 22).

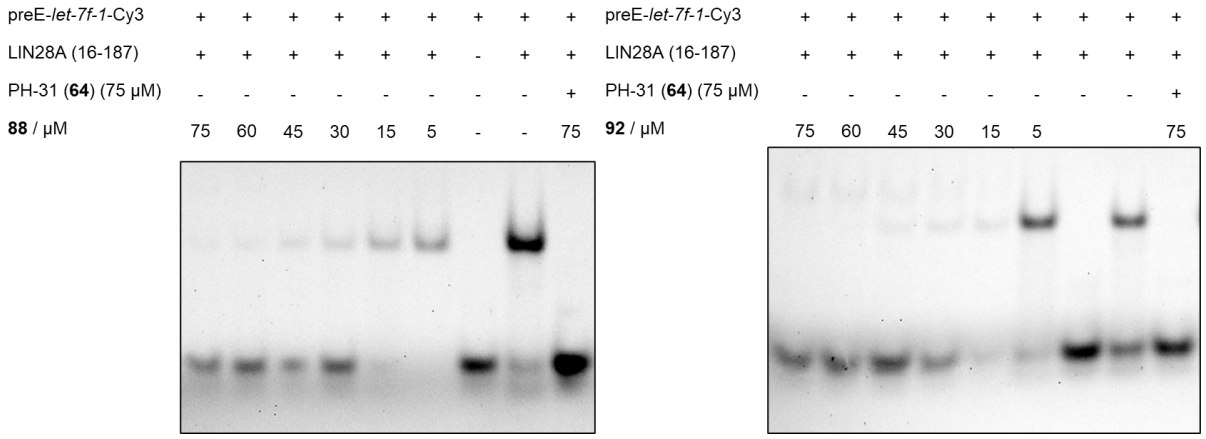

Figure 23: Concentration-dependent inhibition of the LIN28−*let-7* interaction in EMSA for the most potent dibenzo[*b*,*d*]furan-3-yl pyrrolinones **88** and **92** The dose-dependent EMSAs were performed by Lisa Hohnen.

Table 2*:* Trisubstituted pyrrolinone compounds and their respective inhibitory activity against the PRI of LIN28–*let-7*.

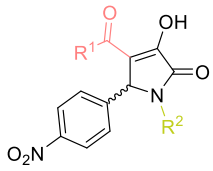

Compound ID	R^1	R^2	Yield (%)	Inhibition at 75 µM (%)[b]
66	Phenyl	[1,1'-biphenyl]-3-ylbiphenyl	24	95
		Variation of R^1		
67	Cyclohexyl	[1,1'-biphenyl]-3-ylbiphenyl	74[a]	49
68	Cyclopropyl	[1,1'-biphenyl]-3-ylbiphenyl	9[a]	<5
69	Cyclobutyl	[1,1'-biphenyl]-3-ylbiphenyl	58[a]	8
70	4-fluoro-2-hydroxyphenyl	[1,1'-biphenyl]-3-ylbiphenyl	4[a]	<5
71	methylsulfonyl-phenyl	[1,1'-biphenyl]-3-ylbiphenyl	26[a]	<5

72	3,4-dimethoxyphenyl	[1,1'-biphenyl]-3-ylbiphenyl	49[a]	<5
73	4-bromophenyl	[1,1'-biphenyl]-3-ylbiphenyl	22	73
74	4-methoxyphenyl	[1,1'-biphenyl]-3-ylbiphenyl	30 [a]	87
75	4-fluorophenyl	[1,1'-biphenyl]-3-ylbiphenyl	52	76
76	2-fluorophenyl	[1,1'-biphenyl]-3-ylbiphenyl	48	98
77	4-nitro-3-hydroxyphenyl	[1,1'-biphenyl]-3-ylbiphenyl	2[a]	49
78	Furanyl	[1,1'-biphenyl]-3-ylbiphenyl	50	87
79	5-methyl furanyl	[1,1'-biphenyl]-3-ylbiphenyl	33	83
80	*N*-methyl-pyrrole	[1,1'-biphenyl]-3-ylbiphenyl	14[a]	75
81	thiazolyl	[1,1'-biphenyl]-3-ylbiphenyl	60[a]	8
82	4-trifluoromethyl-phenyl	[1,1'-biphenyl]-3-ylbiphenyl	25[a]	40
		Variation of R^2		
83	Phenyl	dibenzo[*b*,*d*]furan-2-yl	39[a]	94
84	4-bromophenyl	dibenzo[*b*,*d*]furan-2-yl	23[a]	53
85	4-methoxyphenyl	dibenzo[*b*,*d*]furan-2-yl	15[a]	74
86	4-fluorophenyl	dibenzo[*b*,*d*]furan-2-yl	19[a]	60
87	Furanyl	dibenzo[*b*,*d*]furan-2-yl	61[a]	90
88	Phenyl	dibenzo[*b*,*d*]furan-3-yl	27	97
89	4-bromophenyl	dibenzo[*b*,*d*]furan-3-yl	26	86
90	4-methoxyphenyl	dibenzo[*b*,*d*]furan-3-yl	29	87
91	4-fluorophenyl	dibenzo[*b*,*d*]furan-3-yl	32	93
92	Furanyl	dibenzo[*b*,*d*]furan-3-yl	47	95

[a]Compounds **66**-**71**, **73**, **76,** and **79**-**86** were synthesized by Pascal Hommen.

[b]Two independent replicates of the EMSAs were performed by Lisa Hohnen as part of her Master thesis.

In a last synthetic effort, we aimed to investigate the inhibitory impact of a spirocyclic pyrrolinone scaffold. This strategy should help to further rigidify the original scaffold while simultaneously adding three-dimensionality which finally should increase the binding affinity and LIN28 inhibitory potency

of the compounds. Therefore, we synthesized six spirocyclic pyrrolinones harboring either -phenyl, -biphenyl, or dibenzofuranyl substituents at the 1-position of the pyrrolinone core scaffold (Scheme 5). It is noteworthy to mention, that the prior formation of imine intermediates (**94**, **95**, **98**, **101,** and **103**) seemed beneficial for the ring-closing condensation to occur, which suggests that the reaction may follow the pathway involving the formation of a Schiff base, rather than the aldol condensation pathway (Scheme 3A, B). After isolation of the desired compounds (**96**-**97**, **99**-**100**, **102**, and **104**) we performed single-dose EMSA with compound concentrations at 75 µM. However, none of the spirocyclic pyrrolinones could disrupt the LIN28-*let-7* interaction leading to no further efforts in synthesizing additional spirocycles.

In summary, we performed an extensive SAR study of LIN28-inhibiting trisubstituted pyrrolinones by analyzing a collection of a total of 95 analogs of the original inhibitor **64**. Contrary to our first assumption, that a salicylic acid moiety is required to obtain optimal inhibitory activity against LIN28, we identified a biphenyl-containing pyrrolinone **66** showing equivalent potency *in vitro* and improved activity *in cellulo*. Further structural investigations revealed dibenzofuranyl-containing compounds (**88** and **92**) as another generation of pyrrolinone LIN28 inhibitors, exhibiting the best inhibitory activities among all evaluated compounds. In a final diversification, we used a spirocyclization approach to rigidify the pyrrolinone scaffold while simultaneously adding three-dimensionality. However, the spirocyclic compounds did not show any inhibitory effect against the PRI of LIN28 and *let-7*. Taken together, this work represents one of the most extensive structural investigations performed so far for small molecules targeting the LIN28−*let-7* interaction and paves the way for the development of next-generation LIN28 inhibitors.

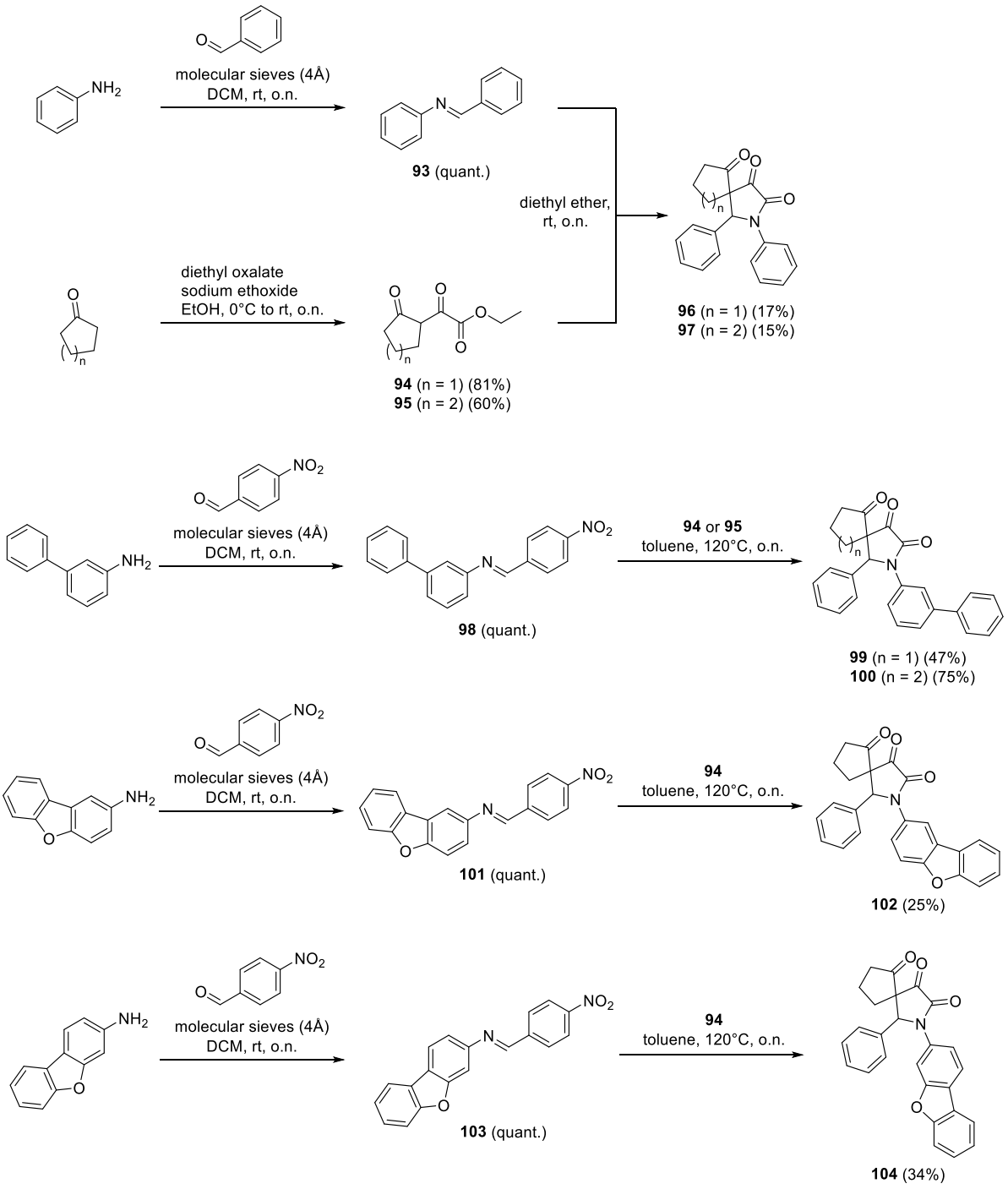

Scheme 5: Spirocyclization of trisubstituted pyrrolinones.

3.1.3 Conclusions from the scaffold- and screening-based approach to identify LIN28 inhibitors

Using two different strategies resulted in the identification of THQ compound **39** and a trisubstituted pyrrolinone **64** as new LIN28 inhibitors. For both compounds, extensive SAR analyses were performed which led to improved potencies against the miRNA-binding protein LIN28 and helped to understand the inhibitory mode of the individual compounds.

For the scaffold-based approach, the reported LIN28 inhibitor LI71 (**8**) was used as a fundamental compound for a systematic structural exploration leading to 34 analogs which were subsequently

investigated in orthogonal assays allowing for visualization of LIN28-*let-7* disruption upon compound treatment. Among the most active THQ compounds was **39**, which included a carboxylic acid residue that seemed to be crucial for its inhibitory effect. This general trend for LIN28 inhibitors might be explained by the negative charge of the carboxylic acid which mimics the phosphate backbone of RNA and thus interacts preferably with the rather positively charged RBD of LIN28.[125,128,237] In general, the SAR study around the reported LI71 (**8**) did not yield many new LIN28-inhibiting small molecules but could expand the knowledge about a potential inhibitory mode of the THQ-containing compound class of LIN28 inhibitors. Despite the rather positive findings, however, there is growing evidence that THQ compounds are likely interfering with assay readouts due to reactive byproducts.[256] To exclude potential degradation and false positive results obtained from our assays, the stability of the THQ compounds should be investigated using different buffers or conditions.

In a screening-based approach, we were able to identify a new class of LIN28-inhibiting small molecules. The trisubstituted pyrrolinone **64** showed consistent activity against LIN28-*let-7* in orthogonal biochemical assays and *in cellulo* and thus was chosen as a lead structure to guide follow-up SAR investigations. In this SAR study another equipotent pyrrolinone **66** was identified which lacks the salicylic acid moiety and instead likely interacts with amino acids of LIN28 via π-π interactions. The absence of the carboxylic acid residue additionally led to improved effects of **66** in cellular assays which might be due to an improved cell permeability. Further structural optimization of the biphenyl moiety revealed dibenzofuranyl-containing pyrrolinones as next-generation LIN28 inhibitors showing improved potency. However, further orthogonal assays and cellular experiments are required to support these findings.

Generally, the LIN28 inhibitors reported here along with those from previous reports, have not yet achieved nanomolar potencies. This limitation hinders the development of chemical probes to understand cellular contexts of the LIN28-*let-7* interaction or the discovery of therapeutics for LIN28-related diseases. A major challenge to overcome this problem is the competition with the high-affinity interaction with *let-7* miRNAs and the absence of a well-defined and deep pocket of LIN28 which might be targeted by rationally designed small molecules. A feasible approach might involve the discovery of strong allosteric binders which could be used as proximity-inducing bifunctional molecules, such as PROTACs to initiate the proteasomal degradation of LIN28 and the release of *let-7*.

3.2 Identification and evaluation of METTL16-inhibiting small molecules

Parts of this section were done in cooperation with Y. Liu, L. Kanis, C. Kemker, O. Hastürk, L. Wagner and COMAS. Contributions are indicated below the respective figures and tables.

*N*6-methyladenosine has been described as the most abundant chemical RNA modification in nature which can have significant impacts on key molecular signaling pathways. The installation of m^6A on *MAT2A* is primarily mediated by the methyltransferase METTL16 and results in the decay of the mRNA. In turn, no translation into the SAM synthetase occurs leading to a negative feedback loop showing decreased SAM levels in the cell and alterations of numerous SAM-dependent processes. Additionally, METTL16 was shown to have a distinct function in the cytosol. Here, the recruitment of eIF3a/b, ribosomes, and respective mRNAs is mediated by METTL16 and results in a translational promotion. Once METTL16 recruits oncogenes, it was shown to promote tumorigenesis making the RMP a key driver of several cancers. Therefore, METTL16 inhibition via small molecules depicts a promising new anticancer strategy. To date, there is no experimental report of METTL16 inhibitors nor has there been an efficient discovery approach, underlining the unmet need to develop such small molecules to elucidate the METTL16-involved regulatory network. Within this work, a screening was performed to identify first-in-class, small-molecule METTL16 inhibitors, which were subsequently structurally optimized. The resulting compounds furthermore could be useful probes to elucidate the biological function of METTL16 and might evaluate the therapeutic potential of METTL16 inhibition.

3.2.1 Identification of aminothiazolones as METTL16 inhibitors

Results from this section were published as "Aminothiazolone Inhibitors Disrupt the Protein−RNA Interaction of METTL16 and Modulate the m^6A RNA Modification."[257]

To identify small-molecule inhibitors of METTL16, we initially established an FP assay involving the methyltransferase domain (MTD) of METTL16 (residues 1-291) and its natural binding partner *MAT2A*. The interaction between METTL16 and the FAM-labeled RNA results in the formation of a larger complex, leading to a higher fluorescence polarization (FP) signal compared to unbound RNA (Figure 24A). Titrations were conducted with varying concentrations of FAM-labeled RNA and protein to determine the optimal assay conditions, which were found to be reached at a concentration of 80 nM METTL16 and 2 nM FAM-*MAT2A* RNA, along with assessment of different incubation times. As a control inhibitor, unlabeled *MAT2A* RNA was used, disrupting the interaction between METTL16 and FAM-labelled *MAT2A* dose-dependently with an IC_{50} value of 60 nM. This approximately matches with reported affinities of *MAT2A* towards the MTD of METTL16 and thus proofed the assay to be robust.[146] In the following, a compound library of ~25,000 small molecules was screened using the established FP assay to identify potential METTL16 inhibitors. One hit compound, which showed an IC_{50} value of 16.3 µM, was the 5-(2-oxoindolin-3-ylidene)thiazol-4(5*H*)-one (**105**) (Figure 24B, C). To validate the inhibitory effect against the METTL16-*MAT2A* interaction, a re-synthesis of the potential hit compound

was performed, which involved a two-step synthetic route. In the first step, 4-methoxybenzenesulfonyl chloride was used in a nucleophilic substitution reaction with pseudothiohydantoin to form the desired intermediate **106** in good yields. In the following, a Knoevenagel condensation reaction involving **106** and 5-chloroisatin afforded the desired hit compound **105** in moderate yields (Scheme 6).[258] Subsequently, the re-synthesized compound was tested in the FP assay as well as a dose-dependent EMSA. In both assays, the inhibitory effect of compound **105** could be validated, thus confirming the METTL16-inhibiting hit molecule (Figure 24D).

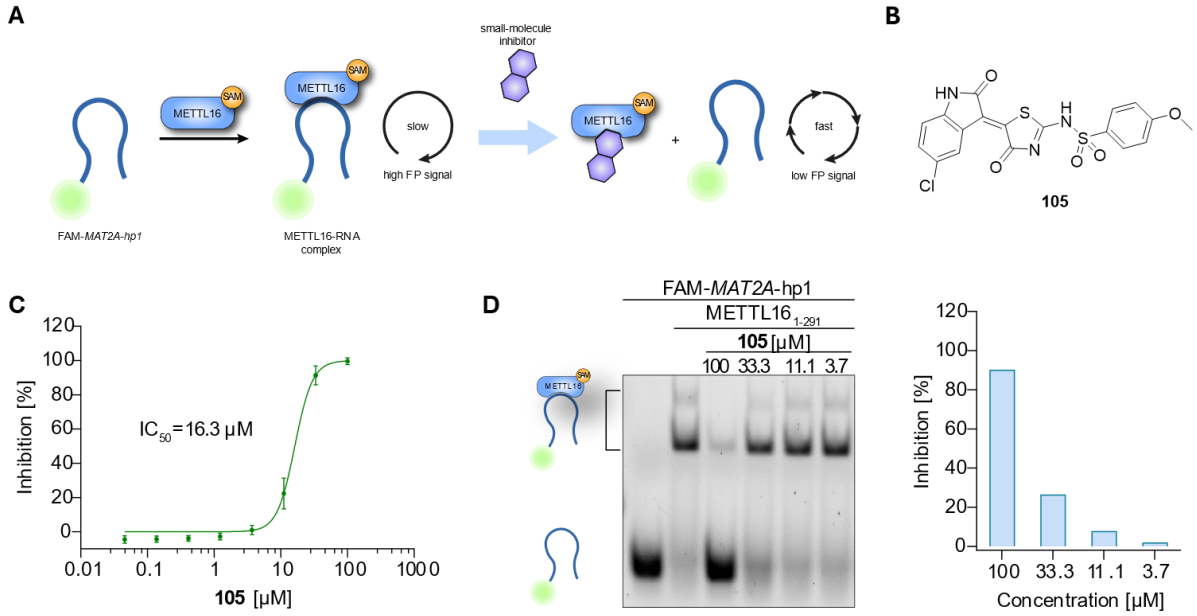

Figure 24: Identification of aminothiazolone **105** as METTL16 inhibitor. (A) Principle of the established FP assay which measures the disruption of the interaction between METTL16 and *MAT2A*. Small-molecule inhibitors disrupting the interaction lead to weaker FP signals. (B) Structure of the identified hit compound **105**. (C) **105** inhibited the PRI with an IC_{50} value of 16.3 µM in the FP assay. Data are shown as mean ± SEM, n = 4. (D) **105** disrupted the RNP complex of METTL16 and *MAT2A* in EMSA in a dose-dependent manner. The experiments were adapted, optimized, and conducted by Yang Liu.

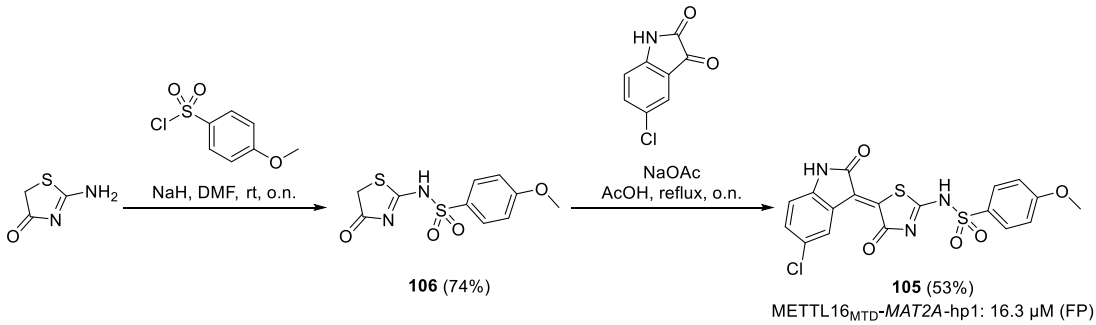

Scheme 6: Synthetic procedure to obtain the METTL16-inhibiting, aminothiazolone **105**. Yields are indicated in brackets as well as the inhibitory effect against METTL16 measured by FP.

After confirming the ability of aminothiazolone **105** to disrupt the protein–RNA interaction of METTL16 and *MAT2A* in a dose-dependent manner, we next aimed to investigate the structural features of the hit compound required for METTL16 inhibition.

3.2.1.1 Initial SAR of the METTL16-inhibiting aminothiazolone

To explore structural features contributing to the inhibitory effect of compound **105**, we performed structural modifications on the oxindole moiety (R^1), the sulfonamide moiety (R^2), and the thiazolone core scaffold (Figure 25).

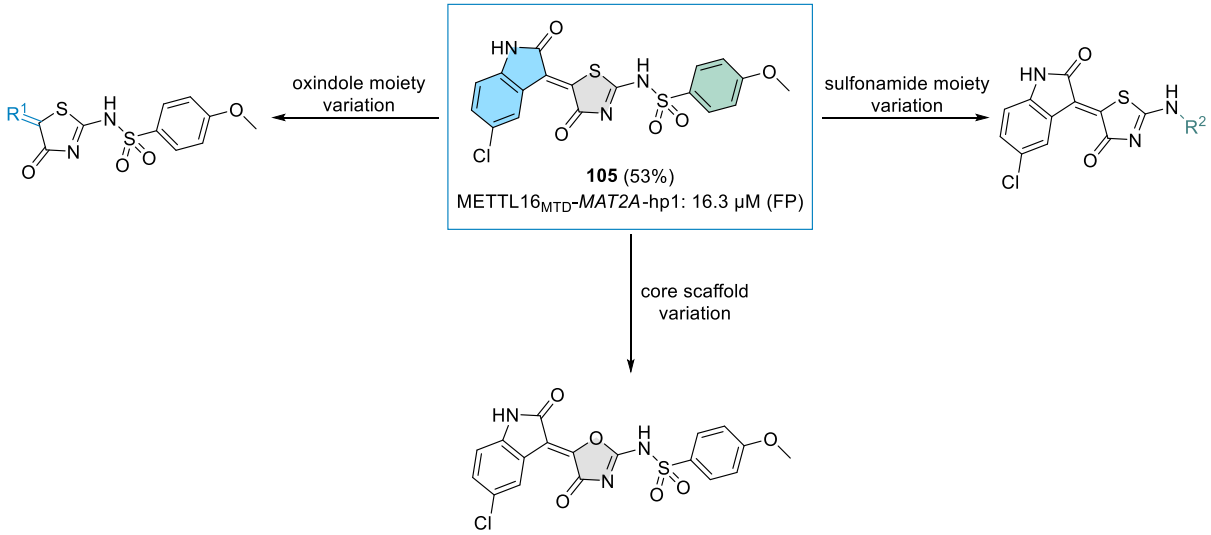

Figure 25: Structural investigation of aminothiazolones as potential METTL16 inhibitors. The strategy to investigate the structure-activity relationship (SAR) of the METTL16 inhibitor **105** consisted of individual changes in the oxindole moiety, the sulfonamide moiety, and the core scaffold.

Therefore, we synthesized 38 derivatives of the original aminothiazolone showing a variety of substituents characterized by either electron-donating groups (**108**, **133**), electron-withdrawing groups (**109**, **110**, **127**, **132**, **135**, **137**) or hydrophobic and bulky groups (**115**, **124**, **128**, **130**, **131**, **136**). Additionally, we introduced a methyl group at the *N*-1 position of the oxindole moiety (**110**, **112**, **114**, **121**, **122**) and exchanged the aminothiazolone core with an oxazole core scaffold (**143**) (Table 3). Upon isolation of the desired compounds, inhibitory potencies against METTL16-*MAT2A* were measured in the established FP assay, as well as the dose-response EMSA. Here, the following trend was observed: Changes in substituents on the oxindole group (R^1) were generally accepted to varying extents. The corresponding changes included the variation of halide groups (**113**, **114**, **116**, **118-122**), hydrophobic residues (**107**, **112**), electron-donating (**108**) or electron-withdrawing groups (**109**), and methylation at the *N*-1 position (**110**, **114**, **121**, **122**) of the previously modified oxindole. The introduction of a phenyl ring to the *N*-1 position of the oxindole however led to a complete loss of activity similar to the exchange of the aminothiazolone core scaffold with an oxazole core. Also, the exchange of the oxindole with an indole moiety led to decreasing inhibition against METTL16 (Table 3). In a separate investigation, variations of the sulfonamide moiety revealed alternative trends. The introduction of hydrophobic and

bulky sulfonamides (**128**, **130**, **131**, **134**) for example led to decreased activities or even the complete loss of activity against METTL16. This phenomenon could be explained by the size of the substituents which might cause steric clashes with amino acids of METTL16 and therefore cannot compete with the RNA. Variation of the methoxy residue of **105** to a carboxylic acid (**132**) revealed the most potent inhibition against the PRI with an IC_{50} value of 2.7 µM. This recurring effect can probably be attributed to the ionic interactions formed between the positively charged RNA-binding site of the RBP and the negatively charged carboxylic acid of **132**. Contrarily, changes in the sulfonamide moiety to amides (**139**-**142**) resulted in a complete loss of activity against METTL16 (Table 3).

Table 3: Aminothiazolone compounds and their respective inhibitory activity against the PRI of METTL16–*MAT2A*.

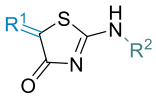

Compound ID	R^1	R^2	Yield (%)	Inhibition / IC_{50} (µM)
105	5-chlorooxindole	4-methoxybenzenesulfonamide	53	16.3±2.2
		Variation of R^1		
107	5-methyloxindole	4-methoxybenzenesulfonamide	71	24.3.3±5.3
108	5-methoxyoxindole	4-methoxybenzenesulfonamide	47	23.8±5.5
109	5-nitrooxindole	4-methoxybenzenesulfonamide	71	8.2±0.76
110	*N*-methyl-5-nitrooxindole	4-methoxybenzenesulfonamide	70[a]	6.8±1.0
111	oxindole	4-methoxybenzenesulfonamide	68	39.4±11.5
112	*N*-methyloxindole	4-methoxybenzenesulfonamide	59	25.2±3.4
113	5-bromooxindole	4-methoxybenzenesulfonamide	85	12.4±2.8
114	*N*-methyl-5-bromooxindole	4-methoxybenzenesulfonamide	82	6.8±0.45
115	*N*-phenyloxindole	4-methoxybenzenesulfonamide	71	inactive
116	7-fluorooxindole	4-methoxybenzenesulfonamide	65	28.9±5.8
117	6-fluorooxindole	4-methoxybenzenesulfonamide	52	Inactive
118	5-fluorooxindole	4-methoxybenzenesulfonamide	83	26.9±5.8

119	7-chlorooxindole	4-methoxybenzenesulfonamide	85	57.6±1.3
120	6-chlorooxindole	4-methoxybenzenesulfonamide	85	26.4±5.0
121	*N*-methyl-5-fluorooxindole	4-methoxybenzenesulfonamide	81[a]	15.0±1.0
122	*N*-methyl-6-fluorooxindole	4-methoxybenzenesulfonamide	67[a]	22.8±2.3
123	indole	4-methoxybenzenesulfonamide	32	23.2±2.7
		Variation of R^2		
124	5-chlorooxindole	4-methylbenzenesulfonamide	48	13.5±1.7
125	5-chlorooxindole	benzenesulfonamide	64	15.7±1.6
126	5-chlorooxindole	3,5-difluorobenzenesulfonamide	51	13.6±1.7
127	5-chlorooxindole	3-nitrobenzenesulfonamide	76	12.0±2.0
128	5-chlorooxindole	4-*tert*-butylbenzenesulfonamide	79	Inactive
129	5-chlorooxindole	2-chloro-4-fluorobenzenesulfonamide	81	14.0±1.5
130	5-chlorooxindole	4-cyclohexylbenzenesulfonamide	80	Inactive
131	5-chlorooxindole	[1,1'-biphenyl]-4-sulfonamide	82	Inactive
132	5-chlorooxindole	4-carboxybenzenesulfonamide	82	2.7±0.7
133	5-chlorooxindole	2-methoxy-5-bromobenzenesulfonamide	79	9.8±0.6
134	5-chlorooxindole	methanesulfonamide	74	36.2±2.8
135	5-chlorooxindole	4-trifluoromethylbenzenesulfonamide	88	13.6±3.6
136	5-chlorooxindole	naphthalene-2-sulfonamide	88	9.9±1.3
137	5-chlorooxindole	4-cyanobenzenesulfonamide	85	38.9±22.2
138	5-chlorooxindole	4-fluorobenzenesulfonamide	81	30.4±10.5
139	5-chlorooxindole	4-methylamide	79	Inactive
140	5-chlorooxindole	4-methoxyamide	85	Inactive
141	5-chlorooxindole	3,4-dimethoxyamide	69	Inactive

142	5-chlorooxindole	4-fluoroamide	76	Inactive

[a]Compounds **110**, **121**, and **122** were synthesized by Laurin Kanis as part of his Master thesis.

[b]FP assays as well as orthogonal EMSAs were performed by Yang Liu.

To further proof the necessity of the sulfonamide moiety contributing to the activity, we evaluated compounds lacking the moiety entirely. Therefore, one-pot condensation reactions were performed to synthesize six derivatives of **105** (**147-152**) (Scheme 6) which were then tested in the established FP assay and EMSA to investigate their ability to disrupt the PRI of METTL16 and *MAT2A*. Most of the compounds did not show an inhibitory effect, except for compound **150** that showed a decreased activity (IC_{50} = 26.9 µM) compared to the original hit compound **105**. Potentially, the compound (**150**) forms an alternative interaction mediated by the 5-nitrooxindole moiety. Nevertheless, concluding the results from the evaluation of amide moiety-containing compounds and derivatives that lack the moiety completely, it can be assumed that the sulfonamide moiety is beneficial for METTL16 inhibition.

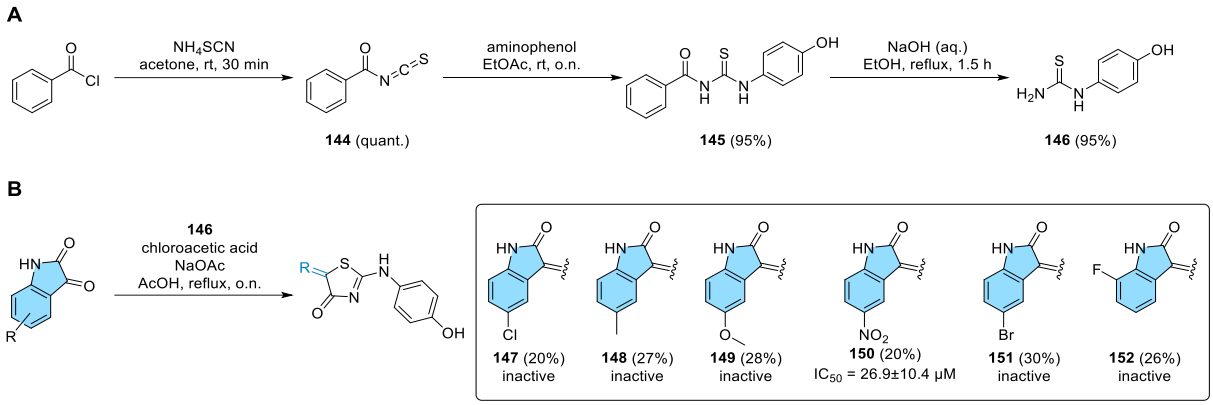

Scheme 7: Synthesis of aminothiazolones lacking the sulfonamide moiety. (A) Synthesis of thiourea intermediate **146**. (B) Synthesis of six derivatives of **105** lacking the sulfonamide moiety which showed decreased inhibitory activity against METTL16. FP assays as well as orthogonal EMSAs were performed by Yang Liu.

In summary, we established an FP assay suitable for medium to high throughput and screened a compound collection of ~25,000 small molecules with regard to their ability to disrupt the PRI of METTL16 and *MAT2A*. The screening resulted in the identification of several hit compounds among which the aminothiazolone **105** showed robust activity, which was confirmed for the re-synthesized compound. After the validated inhibition of METTL16, we systematically investigated the structural features required for METTL16 inhibition by varying substituents of either the oxindole- or the sulfonamide moiety. Here, we identified analogs **110**, **113**, **114**, and **132** showing the best METTL16-inhibiting activity, which should be investigated in another SAR to identify more potent inhibitors. Additionally, the sulfonamide moiety was identified to be beneficial for METTL16 inhibition that could be attributed to additional hydrogen bond acceptors formed by the oxygen atoms of the moiety.

3.2.1.2 Second SAR of aminothiazolone METTL16 inhibitors

After identifying the three aminothiazolones **110**, **113**, **114**, and **132** as the most potent METTL16 inhibitors, we continued with the synthesis of another collection of modified analogs by combining the structural key features of the three analogs, which resulted in compounds **154**, **155**, and **156** (Scheme 8A). Dose-response FP assays revealed the most potent METTL16 inhibitor **154** with an IC_{50} value of 1.7 µM and equipotent analogs **155** and **156** with IC_{50} values of 2.0 and 2.1 µM, respectively (Figure 26A, C). Given the obtained results from previous studies, we next investigated the impact of the carboxylic acid residue and synthesized a methyl ester-containing analog (**159**) which was subsequently tested regarding its ability to inhibit METTL16.[235,237,250] In addition to the methyl ester analog (**159**), we also changed the carboxylic acid group from *para*- to *meta* position, which has been proven to significantly increase the potency of an RBP inhibitor (Scheme 8B).[235] However, the synthesized analog (**160**) did not show improved METTL16 inhibition (IC_{50} = 3.0 µM) (Figure 26B, C).

Altogether, through extensive structural optimization based on the original aminothiazolone scaffold of **105**, we were able to identify a series of compounds that revealed single-digit micromolar potency against METTL16. In the following, we focused on probing the inhibition mechanism of the newly identified METTL16 inhibitors via various binding assays.

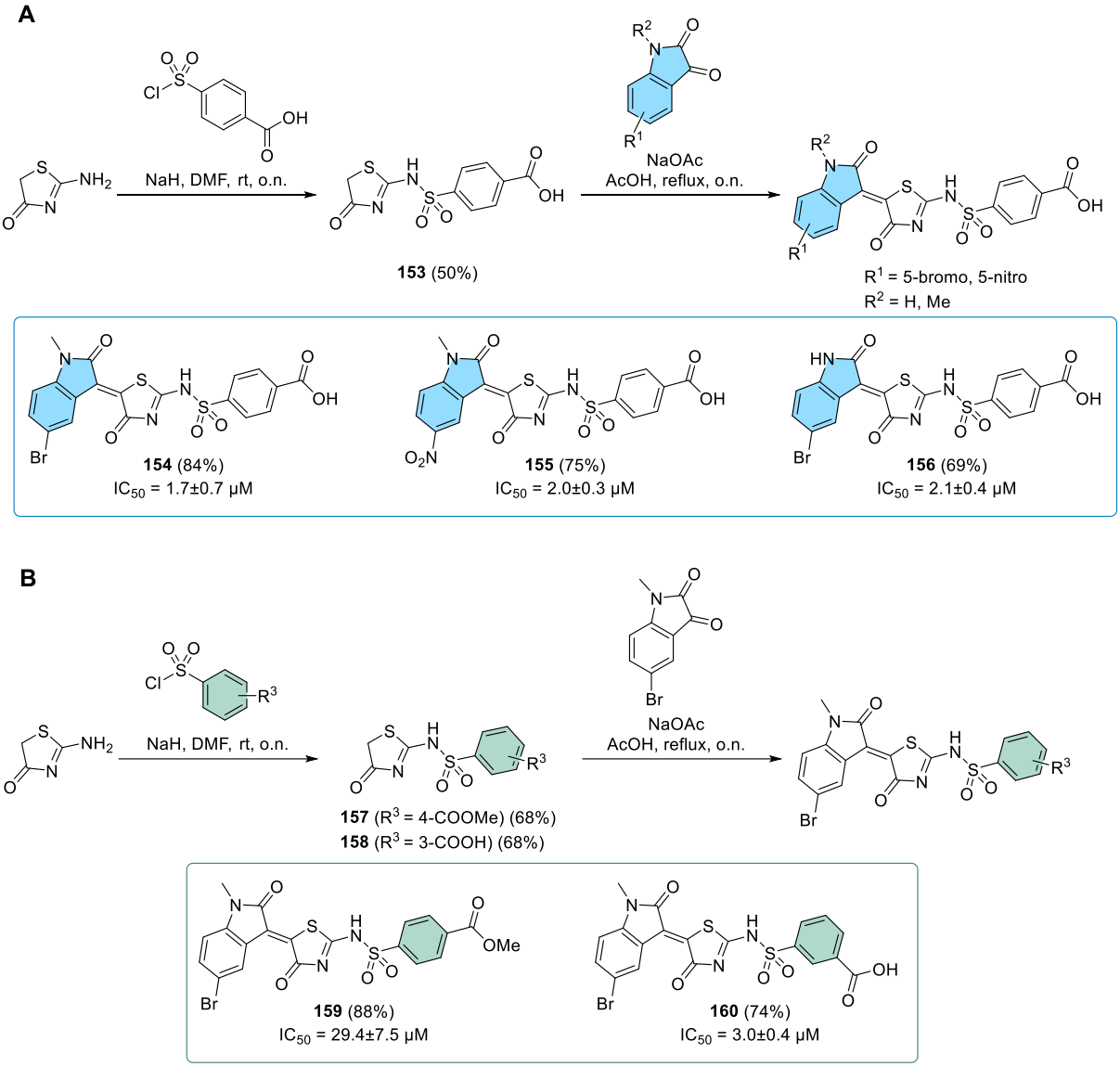

Scheme 8: Synthesis of the most potent aminothiazolone-based METTL16 inhibitors. (A) Variations of the oxindole moiety resulted in the most potent compounds **154**, **155**, **156**. Compound **156** was synthesized by Laurin Kanis as part of his master's thesis. (B) Variation of the carboxylic acid position slightly decreased the activity against METTL16, while methyl ester containing analogue **159** significantly decreased the activity against METTL16. FP assays as well as orthogonal EMSAs were performed by Yang Liu.

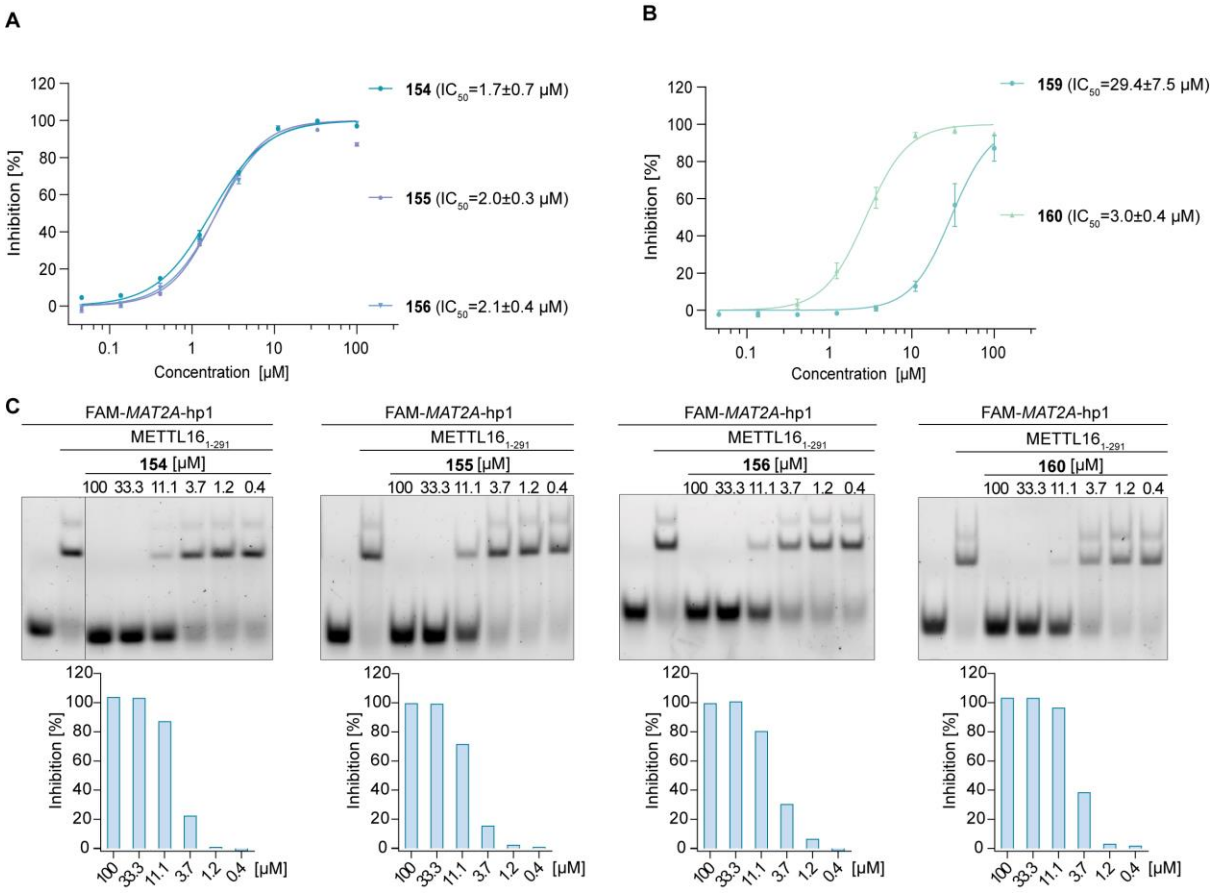

Figure 26: Biochemical evaluation of aminothiazolones. (A) Combination of the most potent aminothiazolones yielded potent inhibitors **154**, **155**, **156**. (B) Evaluation of carboxylic acid residue and methyl ester analog **159** decreased the activity, while meta-position carboxylic acid analog **160** maintained the activity. (F) EMSA results and gel quantification data for compounds **154-156**, and **160**. FP assays as well as orthogonal EMSAs were performed by Yang Liu.

3.2.1.3 Biological evaluation of aminothiazolones

To probe the inhibitory mechanism of the optimized aminothiazolones, we investigated the direct binding of the inhibitors to METTL16 with a DSF experiment which shows the protein unfolding by monitoring changes in fluorescence as a function of temperature.[259] Therefore, we measured the thermal stability of METTL16 MTD upon treatment with the four most active compounds (**132**, **154**, **155,** and **156**). The treatment generally showed a dose-dependent stabilization of METTL16 upon binding of the compounds (Figure 27A). To confirm this binding event and to determine binding affinities, a switchSENSE biosensor assay was performed which allows for the detection of molecular interactions through changes in fluorescence intensity. Here, especially compounds **154** and **156** could be confirmed as METTL16 binders and showed K_D values of 1.35 and 1.76 µM, respectively. For compound **156** the binding affinity could be further validated by isothermal titration calorimetry (ITC) measurements, giving a K_D value of 5.12 µM (Figure 27B, C).

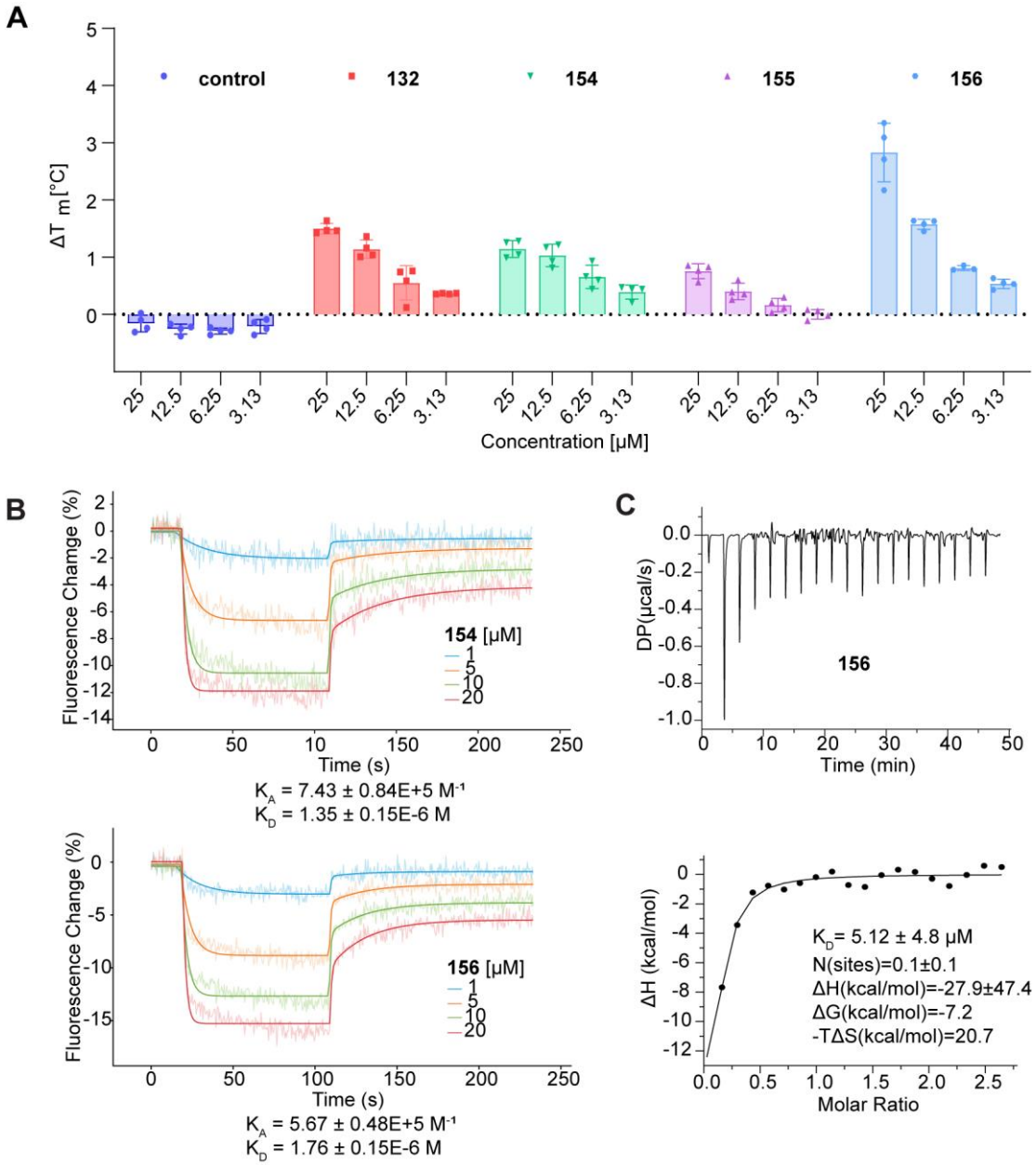

Figure 27: Biophysical assays to confirm binding of the aminothiazolones to METTL16. (A) DSF measurement shows stabilization of METTL16 upon dose-dependent compound treatment. (B) switchSENSE biosensor assay could confirm the binding of **154** and **156** to METTL16 and allowed for the determination of K_A and K_D values. (C) Confirmation of **156** binding to METTL16 in an orthogonal ITC measurement. All assays were performed by Yang Liu.

As the performed assays only confirm the general binding of the small molecules to the MTD of METTL16, we next evaluated the mode of inhibition by monitoring the methyltransferase activity of METTL16 using the MTase-Glo assay kit (Promega). With this assay, it is possible to measure a SAM-dependent methyl transfer based on the formation of *S*-adenosyl homocysteine which is converted into adenosine diphosphate (ADP) by the MTase-Glo reagent, resulting in visualization via luciferase reaction. In our case, especially the aminothiazolones **132**, **155,** and **156** showed potent inhibitory activity against the methyltransferase activity of METTL16 toward *MAT2A* in a dose-dependent manner (Figure 28A). These results indicated that the aminothiazolones bind to the RBD of METTL16 to inhibit

the PRI with *MAT2A*. However, binding to the SAM binding pocket with an extended part reaching the RNA binding site would also cause this effect. To exclude this possibility, we performed a competitive FP assay by incubating METTL16 together with different concentrations of SAM before compound treatment. In the case of competition between SAM and the aminothiazolones, this would result in a decreasing inhibitory effect of the aminothiazolones. However, the inhibitory activity of our compounds did not vary in the presence of SAM confirming the IC_{50} values for compounds **154**, **155,** and **156** (Figure 28B).

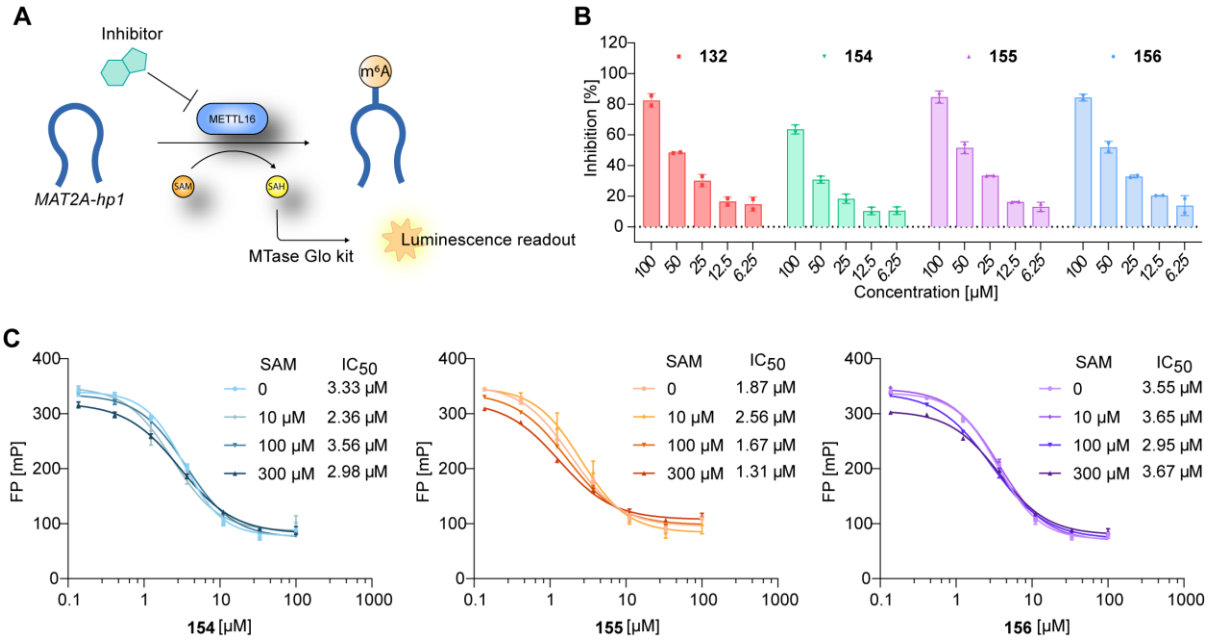

Figure 28: Inhibitory mechanism of the aminothiazolones. (A) Principle of the MTase Glo assay which allows to monitor methyltransferase activity. (B) Results of the MTase Glo assay showed dose-dependent methyl transfer inhibition mediated by the aminothiazolones. (C) Competitive FP assay using excessive SAM concentrations did not alter the inhibitory activity of the aminothiazolones. MTase Glo assay as well as FP assays were performed by Yang Liu.

The structure of the different aminothiazolones exhibits an unsaturated double bond connecting the oxindole moiety with the aminothiazolone core which could cause a covalent bond formation between the compound and reactive amino acids of METTL16. To rule out this possibility, we performed LC-MS analysis of METTL16 after incubating the protein with the most active aminothiazolones for 30 and 150 min, respectively. In the case of a covalent interaction, the formation of mass adducts could be observed which would accrue over time. However, in our case, no such adduct with a mass value shift was observed indicating that the aminothiazolones are non-covalent or potentially reversible covalent METTL16 binders (Figure 29).

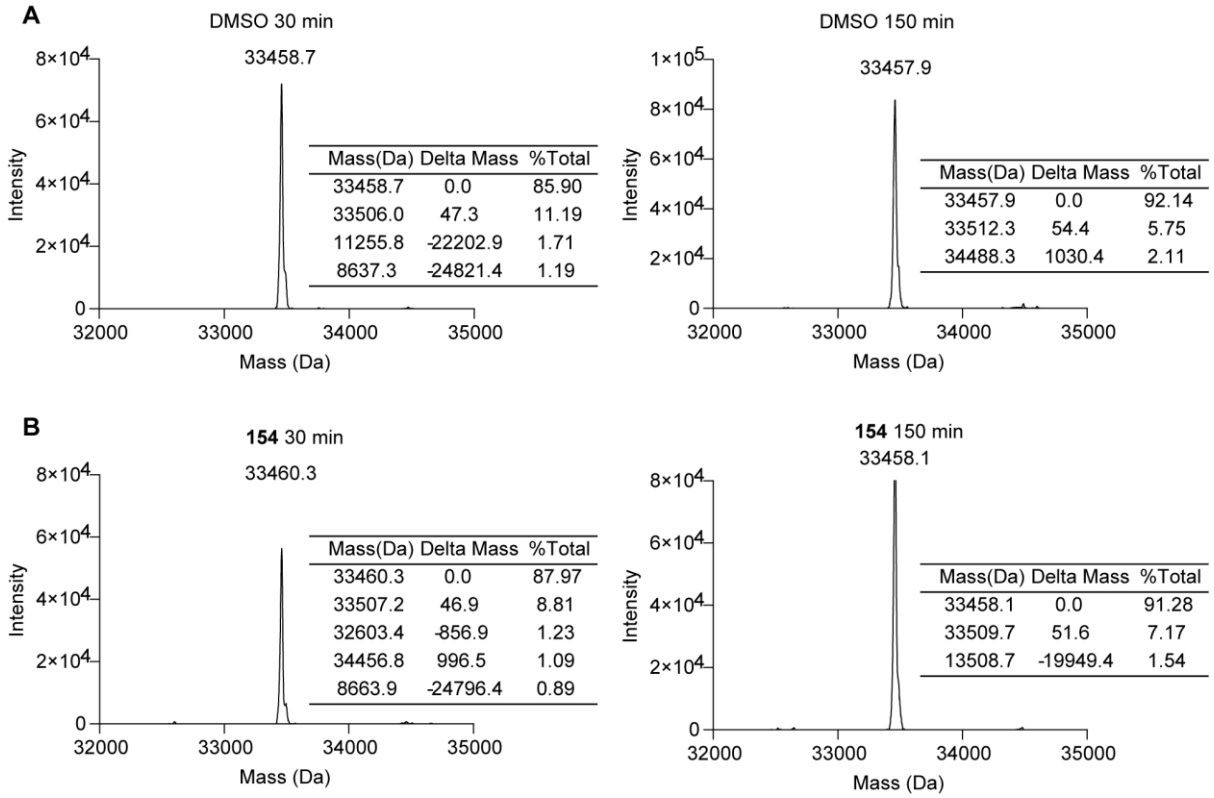

Figure 29: LC-MS analysis to probe for covalent binding of the aminothiazolones to METTL16. (A) Mass spectrum of 30 µM METTL16 (1-291) incubated with 1% DMSO for 30 min (left) and 150 min (right). (B) Representative mass spectrum of 30 µM METTL16 (1-291) incubated with 100 µM **154** for 30 min (left) and 150 min (right). Expected Mass for METTL16 (1-291), 33,455.7 Da. LC-MS analysis was performed by Yang Liu.

In conclusion, the aminothiazolones **132**, **154**, **155,** and **156** were investigated in several binding- and activity assays which should help to understand the inhibition mechanism of the compounds toward the METTL16-*MAT2A* interaction. After confirming general binding by DSF, biosensor assays, and ITC, we continued to narrow down the binding site where the compounds might interfere with RNA binding and thus performed a methyltransferase activity monitoring MTase Glo assay. Dose-dependent inhibition of the methyl transfer suggested the binding of the aminothiazolones to the RNA pocket or the SAM binding pocket. Competitive FP assays involving excessive amounts of SAM however could rule out the possibility of SAM binding pocket occupation by the aminothiazolones. A covalent interaction of the compound with METTL16 was also disproved via LC-MS monitoring.

3.2.1.4 Binding mode prediction for aminothiazolone METTL16 inhibitors

Based on the findings of the previously mentioned binding assays, we studied the potential binding mode of the aminothiazolones via molecular docking analysis based on the complex structure of METTL16 MTD and *MAT2A*-hp1. An optimal binding pose between aminothiazolone **154** and the RNA binding site of METTL16 revealed some key interactions consistent with our experimental observations. For example, the carboxylic acid of **154** forms a stable salt bridge with K251 and an additional hydrogen bond with N198 which could explain the beneficial effect on the inhibitory

potency. Additionally, the sulfonamide moiety is involved in hydrogen bonding with R204 echoing the results obtained from previous SAR studies. Compounds lacking the moiety (**147-152**) either showed decreased activity or a complete loss of activity.

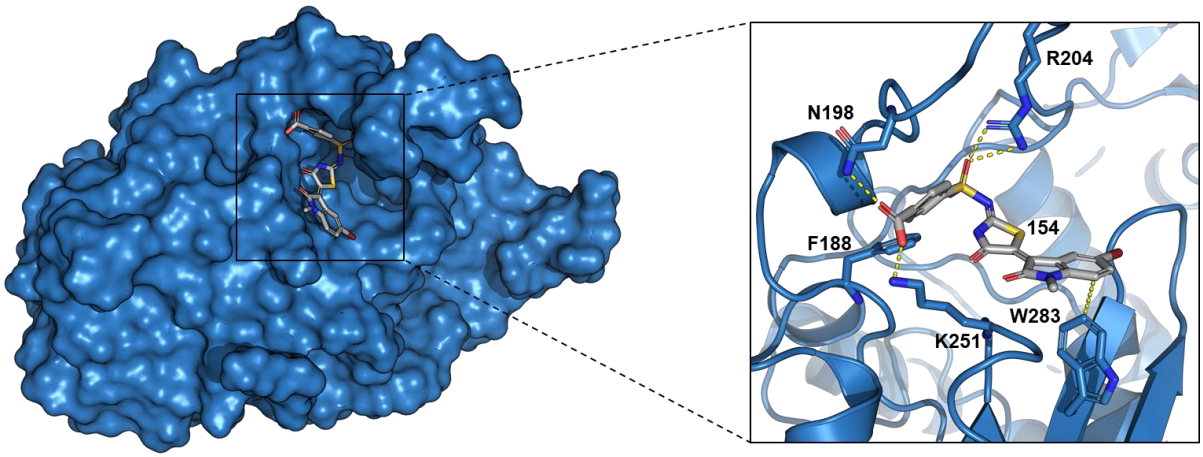

Figure 30: Molecular docking analysis to predict the binding mode of aminothiazolone **154** to the MTD of METTL16 (PDB: 6DU5). Surface structure of $METTL16_{MTD}$ (sky blue) and **154** in gray carbon backbone (left) and the enlarged visualization of the ribbon structure of METTL16 with **154** (right). Selected key interacting residues are depicted as sticks.

Furthermore, the phenyl ring of the oxindole group is engaged in a π–π stacking interaction with W283. Another potential π–π interaction might form between the sulfonamide moiety and F188 upon rotation of the amino acid which brings the phenyl ring of **154** in closer proximity to enable the binding.

Generally, the proposed binding mode of compound **154** provides a plausible explanation for its inhibitory effect on METTL16, as it involves amino acids close to the conserved $_{185}NPPF_{188}$ catalytic motif (R204, F188). Consequently, the interaction of compound **154** with METTL16 has the potential to obstruct the RNA binding site, thereby disrupting the protein−RNA interaction between METTL16 and *MAT2A*-hp1.

3.2.1.5 Evaluation of aminothiazolones as METTL16 inhibitors in cellular assays

To further elucidate the potential of our hit compounds, we proceeded to evaluate the potential anticancer activity of the synthesized aminothiazolones (**132**, **154**, **155,** and **156**) against human cancer cells. Therefore, we treated different cancer cell lines to monitor the effect of our compounds on their viability. Only mild antiproliferative effects in triple-negative breast cancer cells MDA-MB-231 could be observed after treatment with **132** (Figure 31B), while in HAP1 cells the compounds did not show any effect (Figure 31A). Subsequently, we evaluated the colony formation inhibition for the aminothiazolone inhibitors against MDA-MB-231, which showed varied results for different compounds. For example, compounds **154** and **155** did not show an inhibitory effect on colony formation while **132** and **156** demonstrated mild inhibition in all three tested concentrations (Figure 31C). The discrepancy observed in anticancer activities between cellular data and *in vitro* results for the inhibitors suggests that other physicochemical properties, such as cellular permeability, likely play significant roles in translating biochemical activity into cellular activity. Consequently, additional *in*

cellulo experiments could be performed using compounds, such as the methyl ester containing analog **159** to act as a prodrug that is hydrolyzed by esterases upon entering the cell. This strategy is often used in drug development to overcome deficiencies in physicochemical properties with the final goal of improving all LADME (Liberation, Absorption, Distribution, Metabolism, and Excretion) properties of a compound.[258] Additionally, the exchange of the carboxylic acid residue with bioisosteres could lead to improved cellular activity of the METTL16 inhibitors.[260]

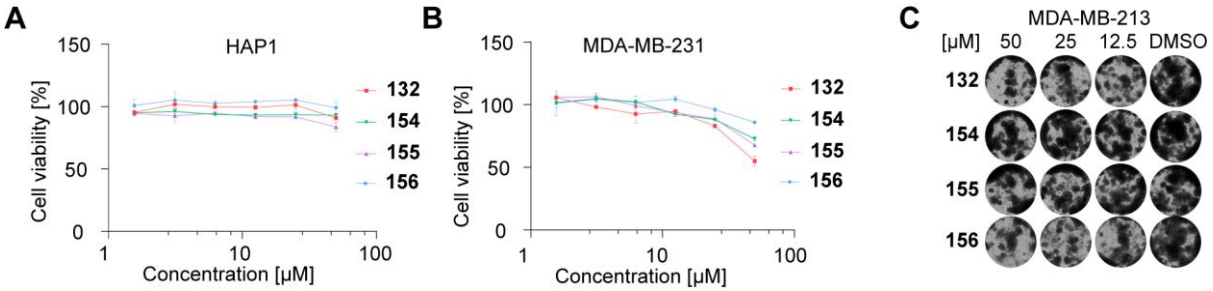

Figure 31: Cellular effects of the selected aminothiazolone METTL16 inhibitors **132**, **154**, **155**, **156**. (A) Antiproliferation assay involving the aminothiazolones did not show significant suppressive effects on cell viability in HAP1 cells. (B) Slight suppression of cell viability in MDA-MB-231 cells upon treatment with **132**. (C) Inhibition of colony formation by **132** and **156** in MDA-MB-231 cells. The assays were performed by Yang Liu.

Next, we investigated the impact of the aminothiazolones on global m^6A levels (Figure 32A) and *MAT2A* splicing (Figure 32B). The methylation of *MAT2A* was shown to cause the decay of the mRNA, thus disrupting the translation into the SAM synthetase. Consequently, SAM levels decrease in the cell and less methyl transfer processes occur leading to lower m^6A levels (Figure 32C (black arrows)). However, once METTL16 is inhibited, splicing of *MAT2A* is promoted, leading to protein synthesis and thus higher cellular SAM- and m^6A levels (Figure 32C (red arrows)). Treatment of MDA-MB-231 cells with our aminothiazolone **154** could show this effect, by significantly upregulating spliced *MAT2A* levels along with increasing m^6A levels in a dose-dependent manner (Figure 32A, B). Nevertheless, the underlying mechanism requires further investigation to unravel the dynamic m^6A methylation network and the effects of METTL16-inhibiting small molecules.

Altogether, the cellular evaluation of the best-performing aminothiazolones obtained after structural optimization of the initial hit compound **105** did not show obvious anti-viability effects in different cancer cell lines. However, monitoring of METTL16-related levels of spliced *MAT2A* and global levels of m^6A could show a significant effect of aminothiazolone **154**, which increased levels of spliced *MAT2A* and concurrently global m^6A levels, giving evidence about the crucial role of METTL16 as a global SAM level regulator.[180]

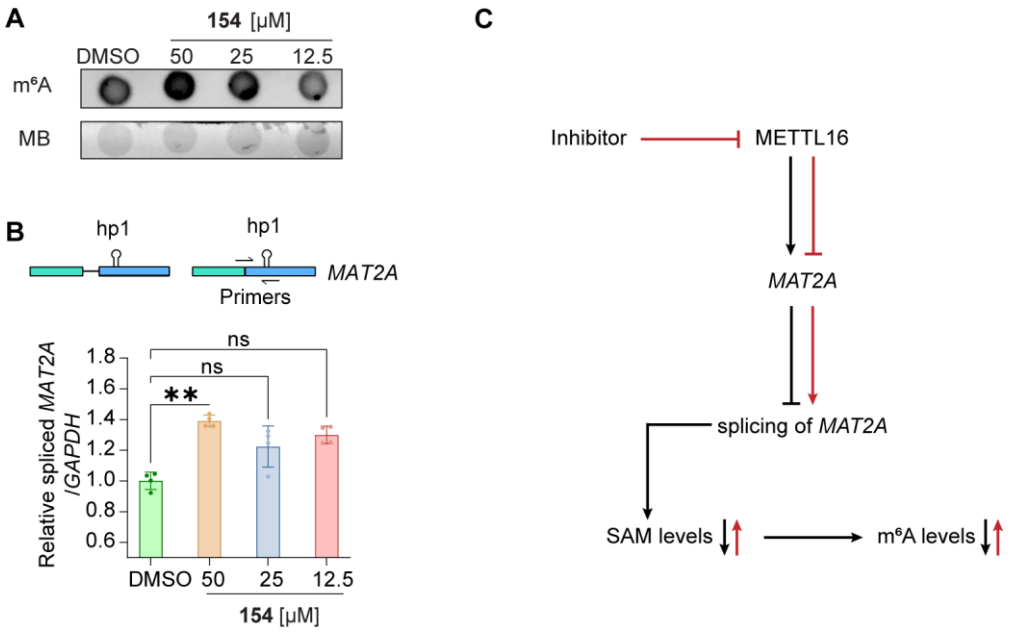

Figure 32: Impact of aminothiazolones on *MAT2A* splicing and m^{6}A levels. (A) Compound **154** treatment increases the global m^{6}A levels in MDA-MB-231 cells. (B) Compound **154** treatment concurrently increases levels of spliced *MAT2A* in MDA-MB-231 cells. The assays were performed by Yang Liu. (C) Assumed effect of METTL16 inhibitors on the m^{6}A methylation network.

3.2.2 Identification of hydantoins and pseudothiohydantoins as METTL16 inhibitors

Next to the previously investigated aminothiazolones acting as METTL16 inhibitors, our screening revealed two alternative hit compounds (**164** and **170**) with IC_{50} values of 4.0 µM, and 3.3 µM, respectively. Similar to previous investigations, a re-synthesis of both compounds was performed to confirm their inhibitory effects against METTL16. In the case of **164**, the hydantoin core (**163**) was synthesized in a sequence of substitution reactions, followed by a coupling reaction with the aryl furane building block (**161**) in a Knoevenagel condensation (Scheme 9A). For **170**, a similar strategy was pursued by initially synthesizing two building blocks, which were subsequently used to form the desired hit compound (Scheme 9B). After purification both potential hit compounds were tested in the established FP assay, to confirm the METTL16-inhibiting activities. Both compounds showed disruptive effects on the METTL16-*MAT2A* interaction (Figure 33A, B) and thus were identified as alternative hit compounds which should be further investigated regarding their structure-activity relationships.

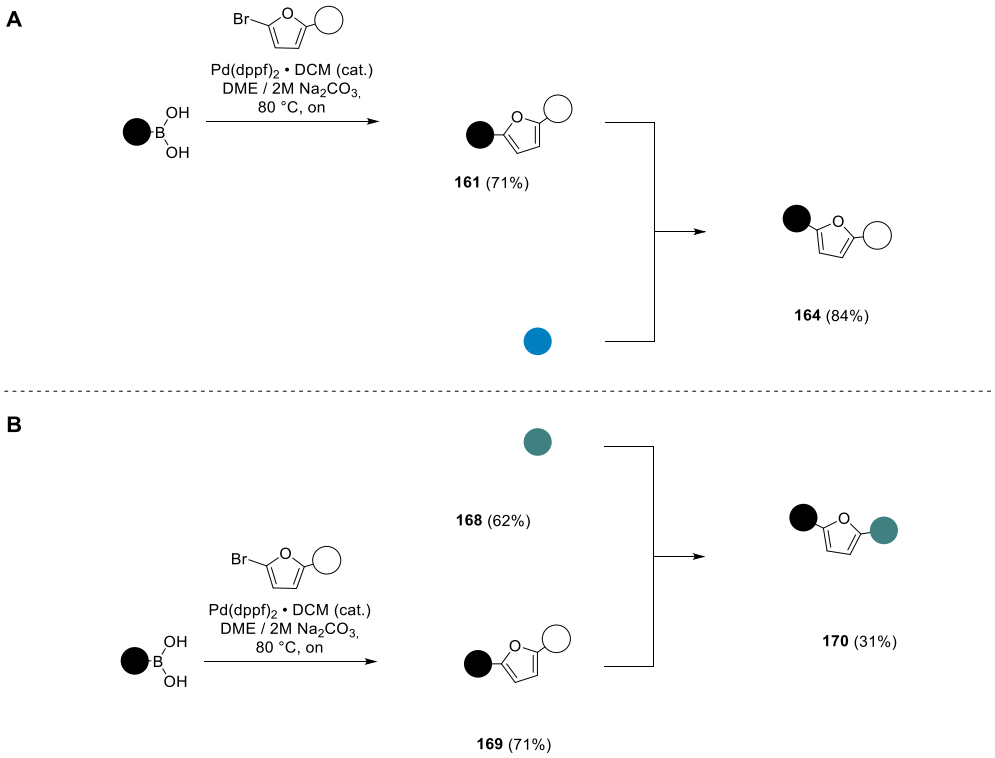

Scheme 9: Synthesis of potential METTL16 inhibitors **164** and **170**. (A) The synthesis of **164** involved a Suzuki coupling reaction. (B) The synthesis of **170** involved a Suzuki coupling reaction to form the aryl furane moiety. Lastly, a condensation of both building blocks afforded the desired hit compound in poor yield. The synthesis of **166**-**170** was performed by Claus Kemker as part of his master's thesis.

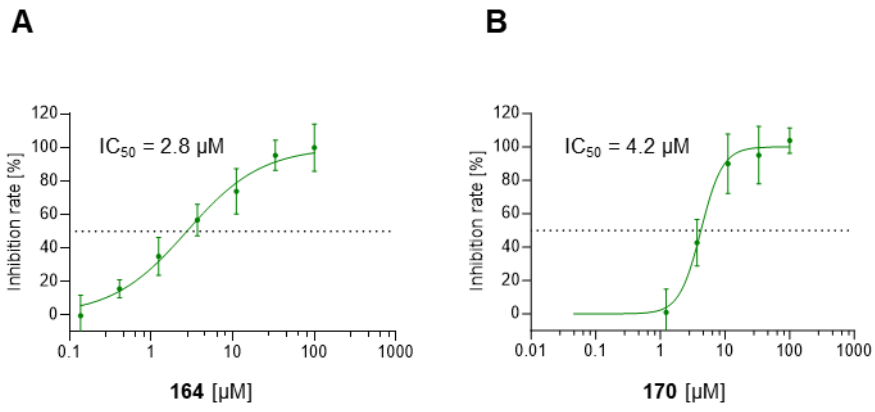

Figure 33: Hydantoin **164** and pseudothiohydantoin **170** both inhibit the METTL16-RNA interaction. (A) The inhibitory effect of **164** with an IC_{50} value of 2.8 µM. (B) The inhibitory effect of **170** with an IC_{50} value of 4.2 µM. FP assays were performed by Leon Wagner as part of his master's thesis.

3.2.2.1 SAR analysis of METTL16-inhibiting small molecules

Since both compounds (**164** and **170**) share the same aryl furan moiety, a simultaneous investigation of structural features contributing to the inhibitory activity against METTL16 was performed. Therefore, several aryl furans containing an aldehyde residue were synthesized by using Suzuki coupling conditions. The intermediates showed a variety of substituents characterized by either electron-withdrawing groups (**171**-**175** and **179**), electron-donating groups (**178**, **180**, **181**), or *N*-heterocycles

(**182-185**). Subsequently, the isolated intermediates were either converted into hydantoin-containing compounds (**171-185**) or pseudothiohydantoins (**186-197**), respectively, which should allow for the simultaneous investigation of features required for the core scaffold to inhibit METTL16 (Figure 34).

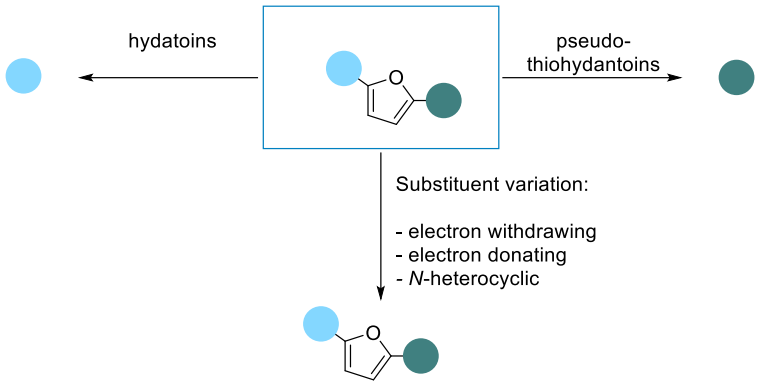

Figure 34: Simultaneous structural investigation of hydantoins and pseudothiohydantoins as potential METTL16 inhibitors. The strategy to investigate the structure-activity relationship (SAR) of the METTL16 inhibitors **164** and **170** included individual changes of the aryl furan moiety and the core scaffold.

For both core scaffolds Knoevenagel condensation conditions afforded the individually desired compounds in poor to excellent yields (Table 4). After the isolation of the hydantoins and pseudothiohydantoins, the individual compounds were tested in the established FP assay as well as orthogonal EMSAs. The biological evaluation only revealed compounds **175** and **186** to act as METTL16-inhibiting small molecules with IC_{50} values of 12.9 µM and 3.4 µM, respectively. All other analogs did not show any effect on the METTL16-*MAT2A* interaction. Compound **175** contains two carboxylic acid residues, which likely decrease cell permeability and increase cell toxicity. Therefore, we did not further investigate this compound. The pseudothiohydantoin **186** showed slightly improved activity against METTL16 compared to the original **170**, however, the potency still did not match with the hydantoin **164**. Thus, additional experiments were only conducted with the original hit compound **164**.

Table 4: Hydantoin- and Pseudothiohydantoin compounds and their respective inhibitory activity against the PRI of METTL16–*MAT2A*.

Compound ID	Yield (%)	Inhibition / IC_{50} (µM)[b]
164	84	2.8
171	60	inactive
172	42	inactive
173	73	inactive
174	35	inactive

175	21	12.9
176	39	inactive
177	27	inactive
178	57	inactive
179	52	inactive
180	60	inactive
181	50	inactive
182	54	inactive
183	24	inactive
184	55	inactive
185	13	inactive
170	31	4.2
186	37[a]	3.4
187	64[a]	inactive
188	46[a]	inactive
189	66[a]	inactive
190	69[a]	inactive
191	63[a]	inactive
192	66[a]	inactive
193	53[a]	inactive
194	72[a]	inactive
195	59[a]	inactive
196	25[a]	inactive
197	37[a]	inactive

[a]Compounds **186**-**197** were synthesized by Claus Kemker as part of his master's thesis.

[b] IC_{50} values were determined based on FP assays. The FP assay as well as orthogonal EMSAs were performed by Leon Wagner as part of his master's thesis.

To further probe the inhibitory activity of **164**, we focused on the disruptive effects of the compound toward METTL16-U6 dTS3 RNA labeled with a Cyanine 5 (Cy5) fluorophore. Our group has previously reported that this RNA containing an UACAGAGAA motif similarly interacts with METTL16 to *MAT2A*.[257] Furthermore, the incorporation of the Cy5 fluorophore was expected to minimize any potential interference from autofluorescence emitted by our compounds, thereby ensuring the reliability of our data (Figure 35A). Since the hydantoin **164** has an unsaturated double bond which might act as a Michael acceptor to form covalent adducts with METTL16, we additionally investigated potentially occurring covalent interactions. Hence, we initially increased the incubation time of the compound together with METTL16 (Figure 35B). Surprisingly, we observed a significantly increased potency of **164** after 4 h incubation time which might be attributed to covalent binding to the MTD of METTL16 of the compound.

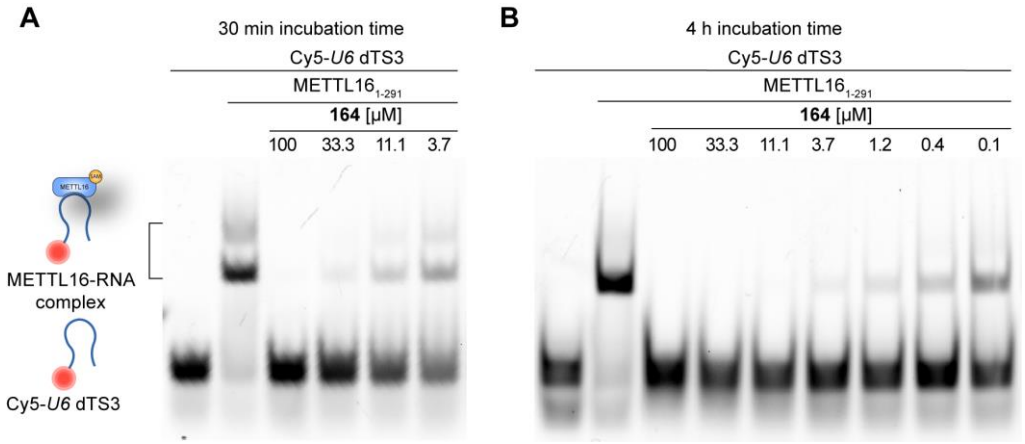

Figure 35: (A) **164** inhibited the PRI of METTL16 and Cy5-U6 dTS3 RNA after 30 minutes of incubation with METTL16. (B) The potency of **164** increased significantly after prolonging the incubation time with METTL16 up to 4 h.

To further validate the possibility of covalent inhibition, we tested for adduct formation via LC-MS analysis that should reveal a mass value shift for METTL16. As anticipated, upon incubation with compound **164**, we detected a mass shift indicative of a covalent adduct formation, likely representing a METTL16-compound complex. This observation supports a mechanism of covalent inhibition (Figure 36).

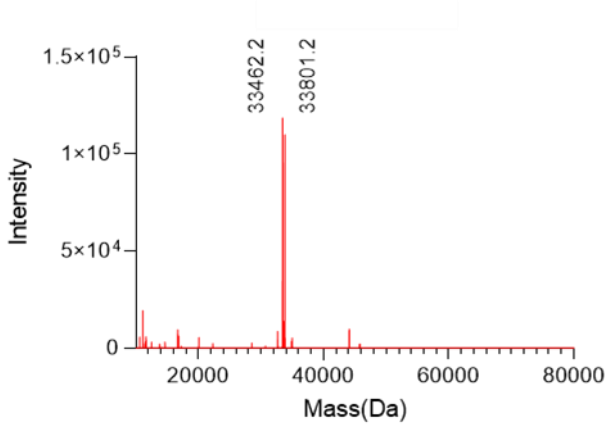

Figure 36: LC-MS analysis to probe for covalent binding of the hydantoin **164** to METTL16. Mass spectrum of 30 µM METTL16 (1-291) incubated with 100 µM **164** for 150 min indicates the formation of an adduct with a mass shift of 339 Da. The expected Mass for METTL16 (1-291) is 33,455.7 Da. LC-MS analysis was performed by Leon Wagner as part of his master's thesis.

In summary, we identified two potential METTL16 inhibitors in a screening approach and performed extensive SAR analyses involving the simultaneous investigation of hydantoins and pseudothiohydantoins which shared similar aryl furan moieties. After testing the 27 analogs in the established FP assay and dose-dependent EMSA, no improvement in inhibitory potency could be observed. Therefore, we continued to only investigate the original hit compound **164** in an alternative dose-dependent EMSA involving the PRI of METTL16 and U6 dTS3 RNA. A prolonged incubation time indicated significantly improved potency of **164** leading to the assumption that the compound might covalently interact with METTL16. This hypothesis could be validated via LC-MS analysis in the first instance; however, the underlying inhibition mechanism requires further investigation to understand the exact binding of **164**. Generally, additional studies are necessary to investigate the inhibitory mechanism of compound **164** and assess its potential as a METTL16 inhibitor.

3.2.3 Conclusions from the screening-based approach to identify METTL16 inhibitors

Using a screening-based approach resulted in the identification of aminothiazolones and hydantoins as first-in-class METTL16 inhibitors. Multiple derivatizations of both hit substances coupled with activity profiling of the resulting compound library led to the identification of more potent METTL16 inhibitors and helped to understand their mode of action towards the target protein.

The aminothiazolone **105** showed robust activity against METTL16-*MAT2A* in orthogonal biochemical assays and thus was chosen as a lead structure to guide follow-up structural investigations. In this SAR study, several equipotent compounds could be identified, as well as four compounds showing improved inhibitory potency. In a synthetic effort, the key structural features of the best-performing aminothiazolones **110**, **113**, **114,** and **132** were combined and the resulting compounds **154**, **155**, and **156** were tested in FP assays as well as dose-response EMSAs. The biological evaluation revealed single-digit micromolar potency for those compounds, thus justifying further biophysical and

cellular characterization of the inhibitors. To proof the binding of the compounds **132 154**, **155**, and **156** to METTL16, several binding assays were performed that indicated interactions of the aminothiazolones with the protein. Furthermore, the mode of inhibition was investigated by using an MTase Glo assay, which revealed the inhibition of the methyltransferase activity of METTL16 upon compound treatment. To exclude the possibility of a SAM binding site occupation of the aminothiazolones, competitive FP assays, involving excessive SAM concentrations, were conducted for each of the best-performing compounds **154**, **155**, and **156**. In the case that the aminothiazolones bind to the SAM binding site of METTL16, the high SAM concentration would interfere with the inhibitory activity of the compounds. As this effect was not observed, we assumed that the inhibitory mechanism relies on the binding of the aminothiazolones to the RNA binding site of METTL16. A potential interaction of **154** was visualized by molecular docking analysis which matches with experimental observations. Nevertheless, further structural investigations are required to fully comprehend the interaction of the METTL16-inhibiting aminothiazolones. In a last effort, the most potent compounds **132**, **154**, **155**, and **156** were evaluated with regard to their anticancer potential. Here, mild cell viability inhibition was observed for **132** which was confirmed in an additional colony formation assay. The disparity between the anticancer activities in cells and *in vitro* data for the involved inhibitors indicated that other physicochemical properties such as cellular permeability, likely played non-negligible roles in the translation from biochemical to cellular activity. Alternatively, inhibition of METTL16 alone could be insufficient to induce lethality in the used cancer cells. While anti-viability effect of compound **154** was not obvious in both cellular assays, the compound could demonstrate upregulation of *MAT2A* splicing in MDA-MB-231 cells and a concomitant increase of global m^6A levels. This trend helped to understand the m^6A methylation network together with the role of METTL16 and thus underscores the significant impact resulting from METTL16 inhibition. However, more analyses are required to fully understand the dynamical regulation network among METTL16, *MAT2A* splicing, SAM levels, and m^6A levels.

Alternative hit compounds identified from the screening were the hydantoin **164** and the pseudothiohydantoin **170**, which were re-synthesized in-house and then evaluated in FP assays and dose-response EMSAs. After confirming their inhibitory activity against METTL16-*MAT2A*, we performed a simultaneous investigation of structural features required for the inhibition of both compounds (**164** and **170**). Therefore, a synthesis of a total 27 analogs was performed containing different substituents on the shared aryl furan moiety. *In vitro* assays only revealed hydantoin **175** and pseudothiohydantoin **186** to act as potential METTL16 inhibitors with similar potencies compared to the original hit compounds. Thus, additional investigations were performed with the most active substance **164**. In a time-dependent, dose-response EMSA, potential covalent binding of the unsaturated compound **164** was observed which was further investigated in LC-MS analysis of METTL16. Upon incubation with the compound, a mass shift was observed indicating a covalent interaction of **164** with METTL16. To validate this inhibitory mode, additional experiments such as Michaelis Menten's

kinetics studies should be performed allowing for the determination of a k_{inact} / K_I rate that describes the efficiency of a covalent bond formation.[261] Also established assays such as DSF, biosensor, or ITC would provide important clarification on the binding mode of the compound. Lastly, cellular assays are needed to probe the potential anticancer effect of hydantoin **164**.

3.3 Identification and evaluation of YTHDF2-targeting small molecules and bifunctional molecules

Parts of this section were done in cooperation with X. Qiu, C. Kemker, N. Giannino, J. Schloßhauer, Y. Liu, L. Borgelt, R. Gasper, N. Wallis, D. Schiller, J. Imig, G. Yeo and COMAS. Contributions are indicated below the respective figures and tables.

Once the dynamic and reversible m^{6}A modification is installed onto RNA, it can be recognized by a variety of reader proteins determining the function and fate of the transcript. YT521-B homology domain family 2 (YTHDF2) is an m^{6}A reader that was shown to initiate the decay of RNA by recruiting different RNA-degrading protein complexes. The *N*-terminal domain of YTHDF2 for example can interact with the CCR4-NOT complex and thereby brings two deadenylases in close proximity to the m^{6}A RNA, thus initiating its decay.[211] Alternatively, endonucleolytic cleavage of m^{6}A RNA was shown to be mediated by YTHDF2 after recruitment of the RNase P-/ MRP complex.[215] In more recent studies, it was also discovered that YTHDF2 mediates an additional level of m^{6}A RNA stability regulation by recruiting UPF1, which triggers decapping and subsequent RNA decay.[216] The fact that YTHDF2 creates this multilayered stability arrangement of m^{6}A RNA throughout the cell, highlights its crucial role in multiple biological processes such as cell viability, differentiation, proliferation, and inflammation. Therefore, it is not surprising that YTHDF2 was shown to play a significant role in multiple diseases such as cancer.[218] While in most cases, the reader protein was shown to act as an oncogene, there are examples in which YTHDF2 plays a tumor suppressive role, highlighting the unmet need to clarify the exact function of the m^{6}A reader. Generally, the development of effective modulators of YTHDF2 may provide novel strategies for the treatment of a variety of cancers in the future. To date, only very few examples of YTHDF2 inhibitors have been reported which describe rather poorly validated and characterized compounds lacking either in potency or selectivity. This underlines the importance of discovering such small molecules able to inhibit YTHDF2 to better understand the regulatory network in which the m^{6}A reader is involved in. Within this work, several approaches were performed to target YTHDF2: Initially, a targeted protein degradation (TPD) approach was utilized to initiate the UPS-mediated decay of the reader. In another attempt, rationally designed small-molecule inhibitors should be identified based on YTHDF2's natural ligand, *N*6-methyladenosine. Lastly, a screening-based approach was performed to identify new YTHDF2-inhibiting small molecules. One hit compound identified from the screening was further investigated regarding its structure-activity relationship to YTHDF2, leading to the identification of an inhibitor being three times more potent. The resulting bifunctional molecules and small molecules depict useful chemical probes to unravel the exact biological function of YTHDF2 and might evaluate the therapeutic potential of the m^{6}A reader.

3.3.1 Identification of YTHDF2 degraders based on multitargeted kinase inhibitors

Results from this section were published as "Profiling Cellular Morphological Changes Induced by Dual-targeting PROTACs of Aurora Kinase and RNA-binding Protein YTHDF2."[262]

While in 2021, no report about YTHDF2-targeting small molecules existed, the work of Donovan *et al.* was found to provide notable insights about targeted degradation across entire gene families which should help to understand TPD beyond the kinome. In their report, multitargeted kinase degraders were used to comprehend the efficiency and selectivity of proteome-wide degradation events which should finally help to accelerate the development of chemical probes as well as clinically relevant lead compounds improving the prediction of degradation activity.[263]

Cereblon (CRBN) was found to form an E3 ubiquitin ligase complex with damaged DNA binding protein 1 (DDB1), Cullin-4A (CUL4A), and the regulator of cullins 1 (ROC1) which adds polyubiquitin chains to proteins and thus marks them for proteasomal degradation.[264] The recruitment of the CRBN complex by thalidomide- or pomalidomide analogs was found exceptionally useful for TPD and today several PROTACs using CRBN recruiters are being investigated in clinical trials.[265] One PROTAC, used in their study, was SK-3-91 (**198**) which, among several proteins, was found to significantly degrade YTHDF2 and thus in our case depicted a promising starting point to identify YTHDF2 inhibitors. Additionally, the potential degrader represents an alternative strategy to target the disease-related m^6A reader allowing the investigation of the therapeutic potential of YTHDF2-degradation. To verify the degradational effect of SK-3-91 (**198**), we initially re-synthesized the compound and subsequently investigated YTHDF2 levels in western blot analysis upon compound treatment (Scheme 10).

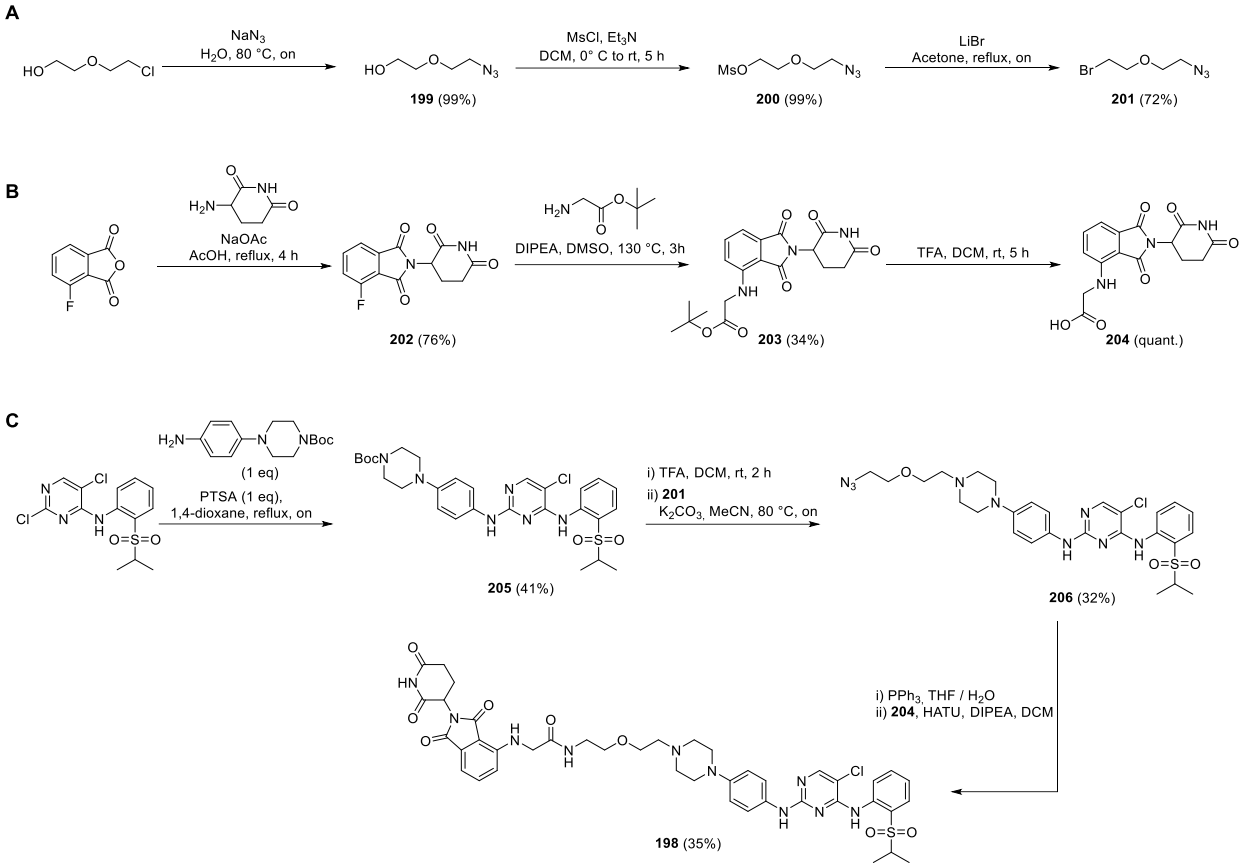

Scheme 10: Synthesis of SK-3-91 (**198**). (A) Synthesis of ethylene glycol linker moiety **201**. (B) Synthesis of cereblon (CRBN)-recruiting small molecule (**204**). (C) Kinase inhibitor-containing and CRBN-recruiting PROTAC SK-3-91 (**198**).

The synthesis of the bifunctional molecule consisted of forming three individual building blocks which were finally combined to obtain SK-3-91 (**198**). First, a functionalized ethylene glycol linker was synthesized in three nucleophilic substitution reactions to get the electrophilic and azide-containing compound (**201**) (Scheme 10A). Another building block was the functionalized pomalidomide analog (**204**) which depicts the CRBN-recruiting moiety to induce close proximity between CRBN and a protein of interest (Scheme 10B). The last building block of the potential YTHDF2 degrader SK-3-91 (**198**) was the multi-kinase inhibiting small molecule TL13-87 (**212**) which was synthesized in a nucleophilic aromatic substitution reaction (S_NAr) to form the *N*-boc protected analog of TL13-87 (**205**) (Scheme 10C).[266] After deprotection, the azide linker **201** was connected to the small-molecule moiety, which was then further functionalized under Staudinger reaction conditions to give a primary amine. In the final step, the resulting amine reacted with a prior formed active ester of carboxylic acid **204** to give the desired PROTAC (**198**).

With the establishment of a synthetic route for SK-3-91 (**198**), I next synthesized two additional compounds showing different linker moieties. Instead of the ethylene glycol linker, I incorporated a short alkyl linker or removed the linker moiety completely to directly attach pomalidomide (**204**) to the piperidine moiety of **207** (Scheme 11). Here, the strategy was to form more rigid and drug-like PROTACs with improved potencies against YTHDF2.

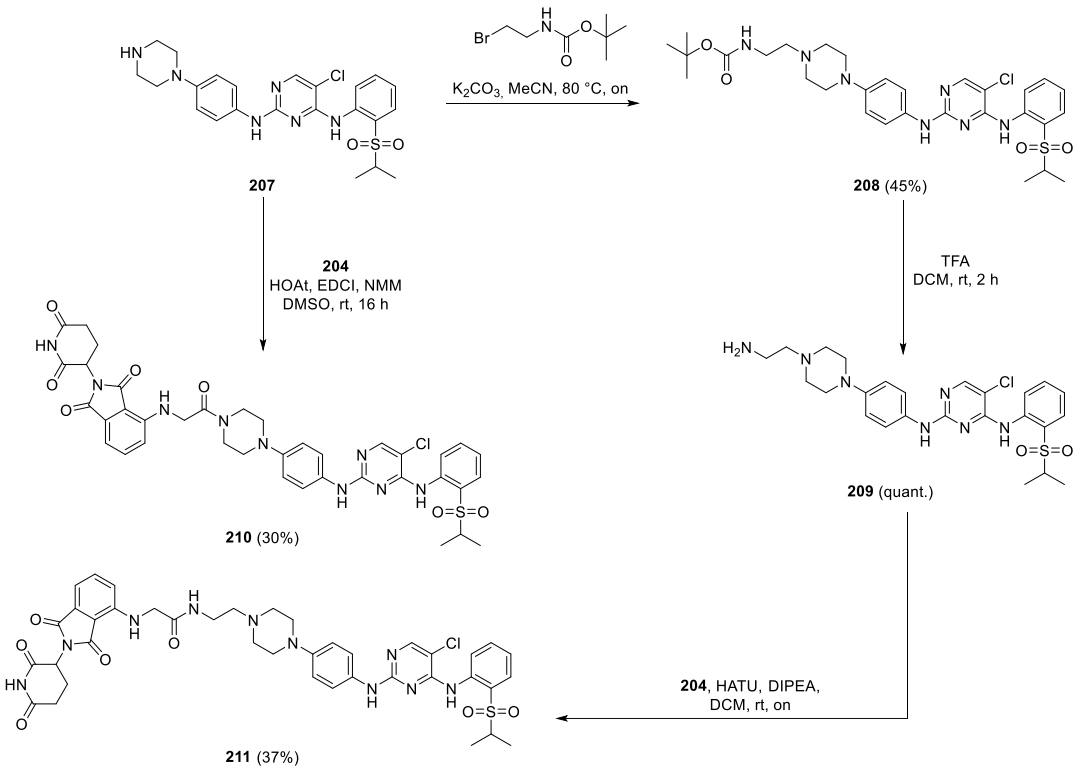

Scheme 11: Synthesis of potential YTHDF2 degraders based on SK-3-91 (**198**). The small-molecule moiety **207** either directly was converted into the bifunctional molecule **210** or underwent alkyl linker attachment and final conversion into **211** using coupling conditions.

After isolating the desired bifunctional molecules, we tested the potential YTHDF2 degraders in western blot analysis to monitor protein levels after compound treatment. As previously demonstrated, compound **198** indeed could show significant degradational effects on the m^6A RNA-binding protein YTHDF2 with low micromolar potency in K562 cells (Figure 37A). The corresponding analogs **210** and **211** with shorter linker moieties also demonstrated consistent potent degrading activity against YTHDF2 (Figure 37). For dose-response western blot analysis, the hook effect was observed underlining an effective binding of the PROTACs to both the POI and CRBN. The hook effect is a reoccurring phenomenon describing squelching activity at high concentrations of degraders which is caused by the unproductive binary interaction of a PROTAC with substrates or ubiquitin ligases rather than a productive ternary complex of both target and E3 ligase.[267]

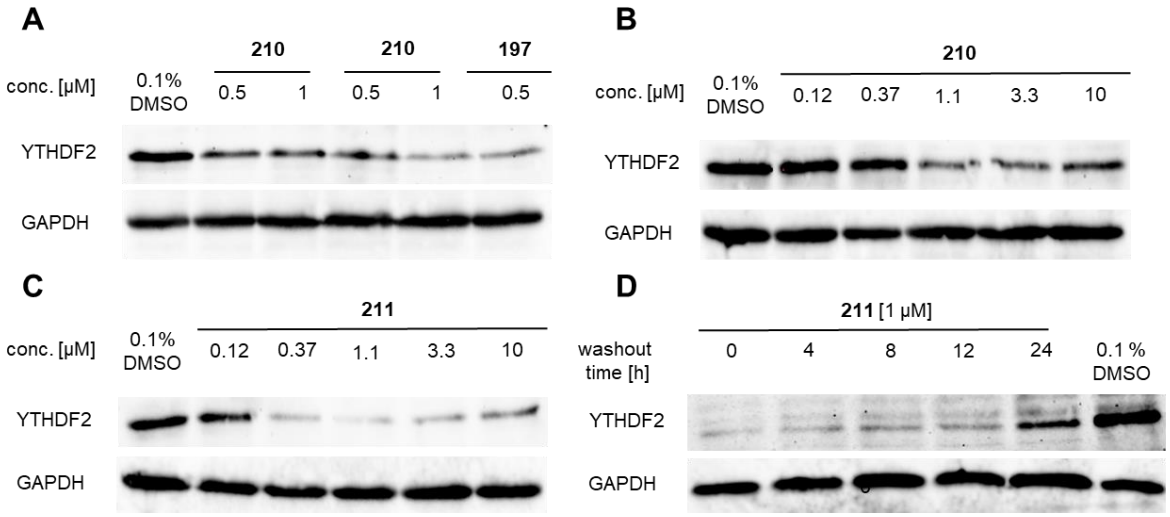

Figure 37: PROTACs degrading the m^{6}A RNA-binding protein YTHDF2. (A) PROTACs **198**, **210**, and **211** recruit the E3 ligase cereblon to achieve YTHDF2 degradation via the UPS. (B) PROTAC **209** degraded YTHDF2 in the low micromolar potency in the K562 cells, with the hook effect showing at the higher concentration of 10 µM. (C) PROTAC **211** degraded YTHDF2 in the low micromolar potency in the K562 cells, with the hook effect showing at the higher concentration of 10 µM. (D) Washout of **211** demonstrated YTHDF2 recovery after 24 h. Western Blot analyses were performed by Xiaqiu Qiu.

Given the scarcity of small molecules targeting YTHDF2 and no degrader of the m^{6}A reader is currently available, the revealed potent YTHDF2 degrading activity of PROTACs **198** and **211** served as a feasible foundation for our ongoing efforts in developing YTHDF2-selective degraders.

In addition to degradation, we next tested the ability of **198**, **210,** and **211** to disrupt the interaction between YTHDF2 and a FAM-labeled m^{6}A RNA probe in a fluorescence polarization assay. Despite the double-digit micromolar inhibitory activity of **198** (IC_{50} = 10.1 µM) and **211** (IC_{50} = 28.9 µM), the inhibitory activity of **210** was less significant (Figure 38). To investigate whether the small-molecule components of the degraders are crucial structural features required for YTHDF2 inhibition, we also synthesized the corresponding compounds without the pomalidomide ligand (**209**, **212,** and **214**) (Scheme 12) and tested their potential inhibitory effects. For all small-molecule components, no disruptive activity was observed which may be explained by an allosteric binding of the compounds to YTHDF2. In the case of PROTACs **198**, **210**, and **211** the additional pomalidomide moiety potentially reaches into the RBD of YTHDF2 and thus interferes with RNA-binding. However, this hypothesis needs to be investigated in more detail by using alternative binding assays which could allow for the identification of an exact binding site of the PROTACs.

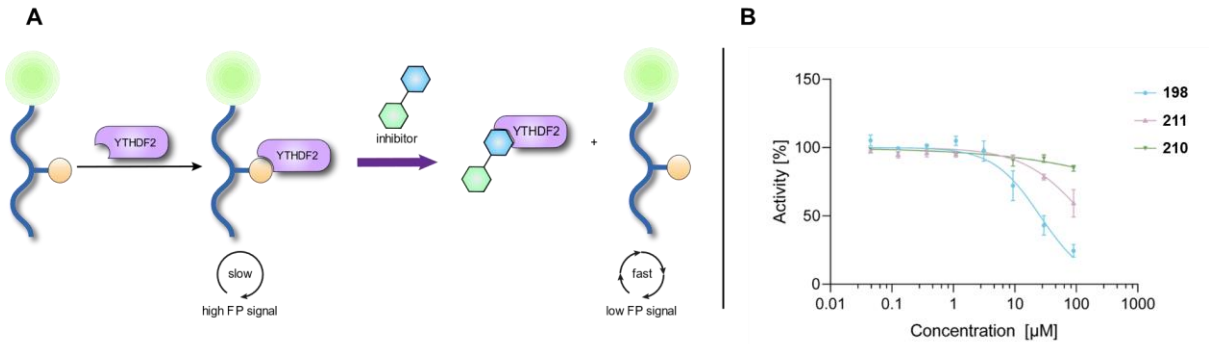

Figure 38: Principle of the established FP assay which measures the disruption of the interaction between YTHDF2 and FAM-labelled m^{6}A RNA. Inhibitors disrupting the interaction lead to weaker FP signals. (B) **198** inhibited the PRI with an IC_{50} value of 10.1 µM in the FP assay while PROTACs 210 and 211 showed weaker inhibitory effects.

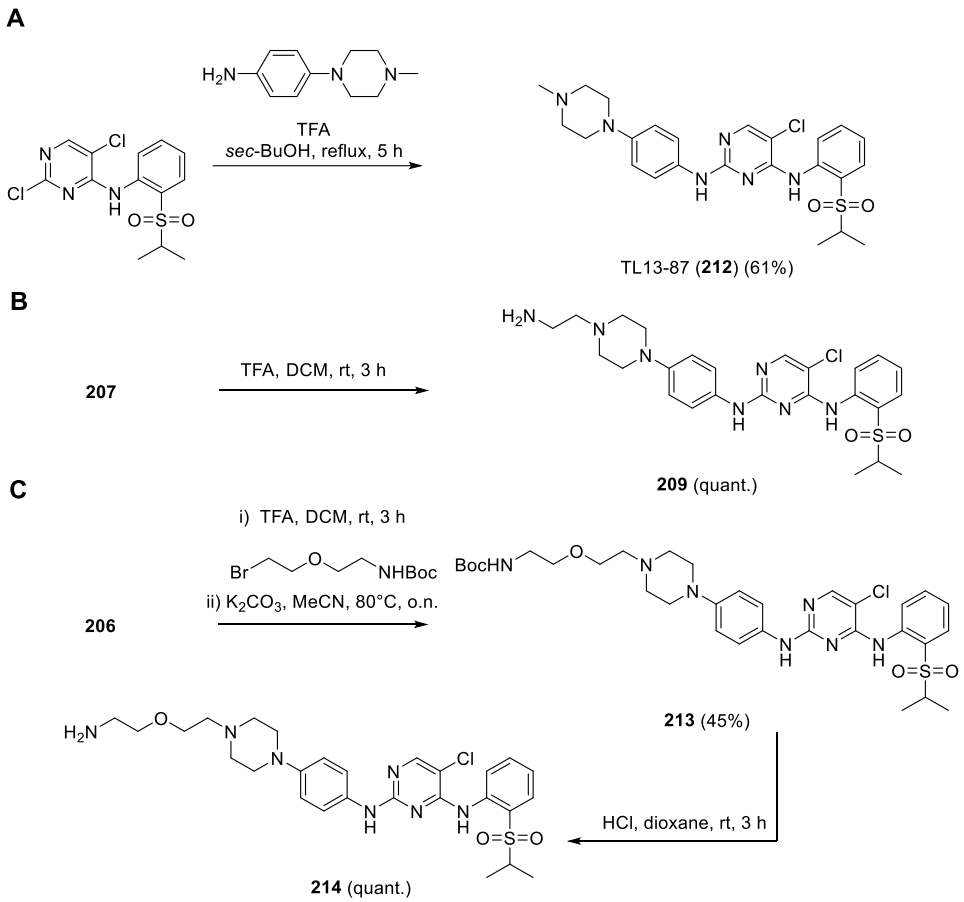

Scheme 12: Synthesis of the kinase inhibiting small molecules. (A) Synthesis of reported kinase inhibitor TL13-87 (**212**). (B) Synthesis of kinase inhibitor connected with a short alkyl linker (**209**). (C) Synthesis of kinase inhibitor connected with an ethylene glycol linker (**214**).

Nevertheless, the observed YTHDF2 degrading effect and YTHDF2–RNA inhibitory activity of **198** and **211** gave feasible candidates to be developed as more selective YTHDF2-targeting PROTACs, although it may be challenging and daunting to attenuate the multitargeting kinase inhibitory- and degrading effect of the PROTACs while at the same time maintain or even improve the YTHDF2-targeting activity. A strategy for future studies might involve an extensive variation of linker moieties

which previously has been proved to increase the selectivity against numerous POIs.[120] Alternatively, the PROTACs could be employed to compare YTHDF2 degradation with knockdown experiments or the inhibitory effects of more potent small molecule inhibitors, providing a detailed overview of YTHDF2 modulation effects.

3.3.2 Identification of small-molecule YTHDF2 inhibitors

Next to the emerging event-driven pharmacology mediated by proximity-inducing bifunctional molecules, there is also potential in the traditional approach of occupancy-driven pharmacology mediated by small-molecule inhibitors of specific target proteins.[268] Due to their numerous advantages e.g. low molecular weight, oral bioavailability, cell permeability, or target specificity, small molecules depict attractive candidates for drug development across a wide range of therapeutic areas.[269]

Disrupting PRIs of YTHDF2 and m^{6}A RNA by using small-molecule inhibitors holds great potential to develop new anticancer therapeutics and enables better understatement of the complex pathways and mechanisms in which YTHDF2 is involved. In this work, inhibitors of YTHDF2 should be identified and then evaluated in biochemical or cellular assays. To achieve this, two strategies were pursued: First, rationally designed inhibitors were synthesized based on the structure of the natural ligand *N*6-methyladenosine and reported, co-crystallized fragments in complex with YTHDF2. Secondly, a screening-based approach was performed to identify new YTHDF2 inhibitors which subsequently were assessed for structural features necessary for inhibiting the m^{6}A reader.

3.3.2.1 Rationally designed small-molecule YTHDF2 inhibitors

Due to the limited reports of YTHDF2-targeting small molecules, we initially focused on the natural binding partner of the reader. M^{6}A RNA has been reported to bind YTHDF2 with a moderate affinity, characterized by a K_D value of 2.54 µM, making it suitable for investigating compounds that can outcompete the protein–RNA interaction.[213] Besides studies on m^{6}A RNA recognition, another report by Nai *et al.* focused on binding affinities of m^{6}A-based fragments identified from an HTRF-based assay. Upon identification of the fragments, the authors investigated the small molecules in co-crystal structure analyses with YTHDF2$_{YTH}$, which revealed similar binding modes compared to m^{6}A (Figure 39).[230] In addition to YTHDF2, most of the fragments were found to also interact with YTHDC1, which was neglected for their initial study. With this structural foundation, I aimed to rationally design small molecules, capable of inhibiting YTHDF2–m^{6}A RNA interactions. Thus, I synthesized m^{6}A-based fragments (**218**-**221**) (Scheme 13) which subsequently were tested regarding their ability to interfere with m^{6}A RNA binding to YTHDF2. The synthesis of the four adenine analogs consisted of an alkylation of the *N*6- and the *N*9 position of the purine core scaffold. To form compounds **218** and **219**, 6-chloropurine was converted via two individual methylation or alkylation reactions. Contrarily, 9-cyclopropylpurines **220** and **221** initially underwent an S_NAr using cyclopropylamine and subsequently were treated with triethyl orthoformate under acidic conditions to form the purine core scaffold. In the last step, the 6-chloride was substituted with methylamine or cyclopropylamine, respectively.

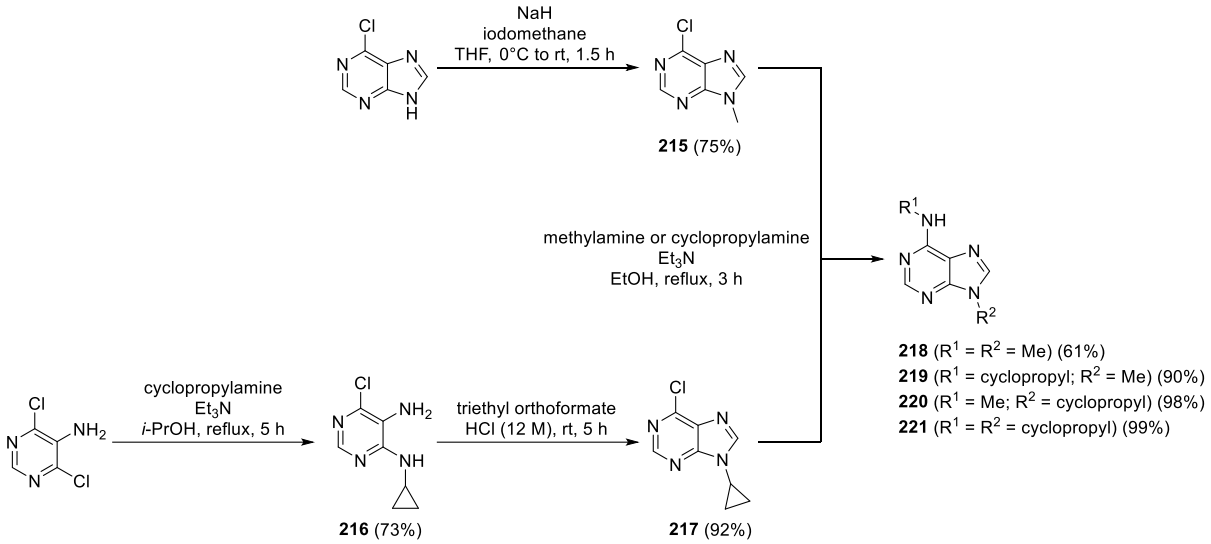

Scheme 13: Synthesis of m^{6}A-based fragments with alkylation patterns of the *N*6- and the *N*9 positions.

After the isolation of the fragments, we tested their ability to disrupt the interaction between YTHDF2 and a FAM-labeled m^{6}A RNA probe in an established FP assay. However, none of the m^{6}A-based fragments showed inhibitory activity against the PRI at 100 µM which is not surprising considering that the compounds are small fragments lacking in reactive residues to form stable interactions with the RBP. Additionally, the report of Nai *et al.* demonstrated that *N*6-adenine derivatives did not show inhibitory effects at concentrations of 1 mM.[230] To further increase the affinity of the fragments, we therefore investigated alternative, reported co-crystallized fragments binding to YTHDF2. Here, fragment **222** was identified and should serve as a fundament for further functionalization (Figure 39C). The fact that the phenyl moiety did not sterically clash with the aromatic cage of YTHDF2, especially represented a promising starting point to incorporate additional moieties to improve the binding affinity to the RBP.

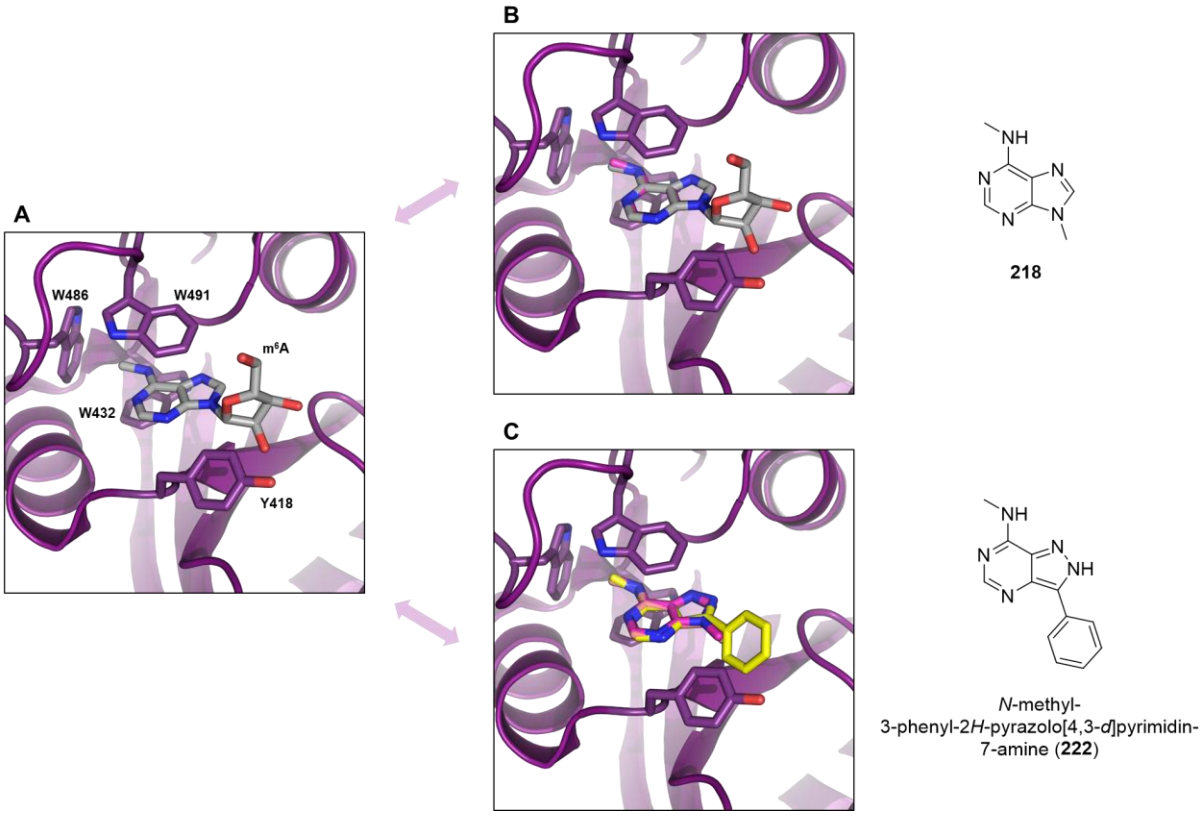

Figure 39: Co-crystal structures of YTHDF2 and m^{6}A or m^{6}A-based fragments. (A) M^{6}A in complex with the aromatic cage of the YTH domain of YTHDF2. (B) Structural overlap of m^{6}A and fragment **218** in complex with the YTH domain of YTHDF2. (C) Structural overlap of fragments **218** and **222** in complex with the YTH domain of YTHDF2.

To synthesize compounds based on the co-crystallized fragment **222**, I started with the substitution of the *N*9-position of a purine core scaffold with a methyl-4-phenylcarboxlyate moiety allowing for further functionalization upon hydrolysis (Scheme 14). The pyrazolo core scaffold of **222** was exchanged due to the reactive secondary amine which might interfere with further reactions. Additionally, the pyrazolo scaffold was described to bind YTHDC1 with a higher affinity compared to YTHDF2 and thus does not depict an optimal starting point for selective compounds.[230] Therefore, I chose the hydrolyzed aryl purine **223** as a key intermediate allowing for the synthesis of different derivatives showing variations either at the *N*6-position or a terminal, rather drug-like piperazine moiety. Additionally, a first attempt to exchange the core scaffold with a pyrimidine heterocycle was performed (Figure 40; Scheme 14C)

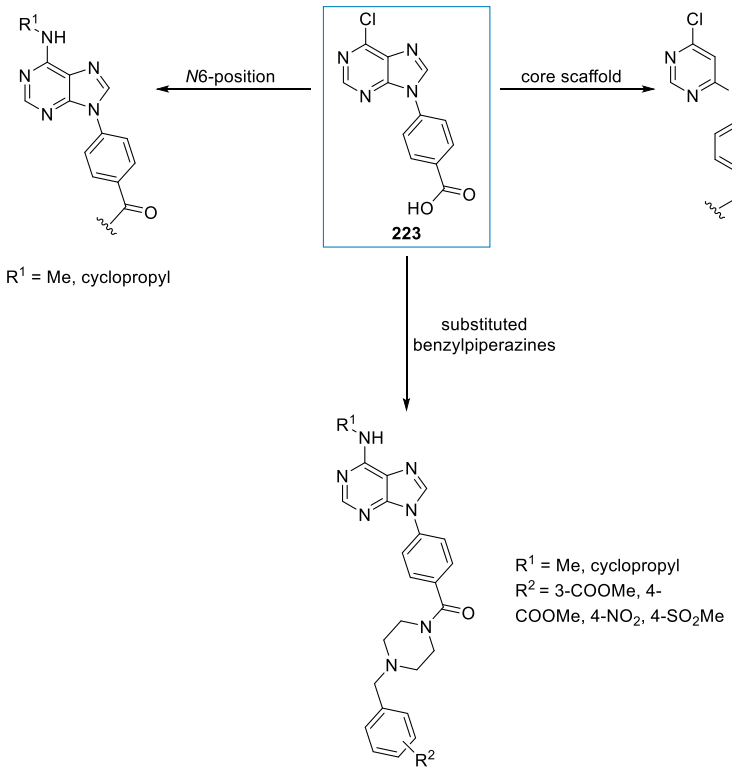

Figure 40: Structural variations of the key intermediate **223** including different substitution patterns of the *N*6-position, differently substituted benzylpiperazines, and a change of the core scaffold.

The analysis of the reported YTHDF2 crystal structure revealed a shallow and positively charged pocket which depicts an optimal structural feature that might be targetable with rather negatively charged residues of rationally designed small molecules. Therefore, I coupled the carboxylic acid residue of **233** with benzylpiperazine moieties exhibiting different electron-withdrawing residues such as carboxylic acids, a methylsulfonyl residue, or a nitro group to form the desired aryl purines (**237-240**) (Scheme 14A). For compounds showing variations at the *N*6-position (**244**) or at the core scaffold (**247**), I only incorporated a 4-(piperazin-1-ylmethyl)benzoic acid moiety (Scheme 14B, C).

After isolating the desired compounds, we tested the potential disruptive effects against the PRI of YTHDF2 and m^{6}A RNA in the FP assay. Unfortunately, none of the rationally designed m^{6}A-based compounds showed significant inhibitory activity. Only compounds **239** and **240** showed minor inhibition rates at 100 µM (24% and 49% respectively), however, the mechanism of inhibition appeared rather unclear, as none of the other derivatives exhibited any activity against YTHDF2. Additionally, no activity was observed in an orthogonal EMSA leading to no further efforts of rationally synthesized compounds. To improve the binding affinities of the compounds, structural clarification of a potential binding site is required to optimally design residues that tightly interact with YTHDF2. Alternatively, other fragments could be used as a starting point to successively build up a small molecule inhibitor.

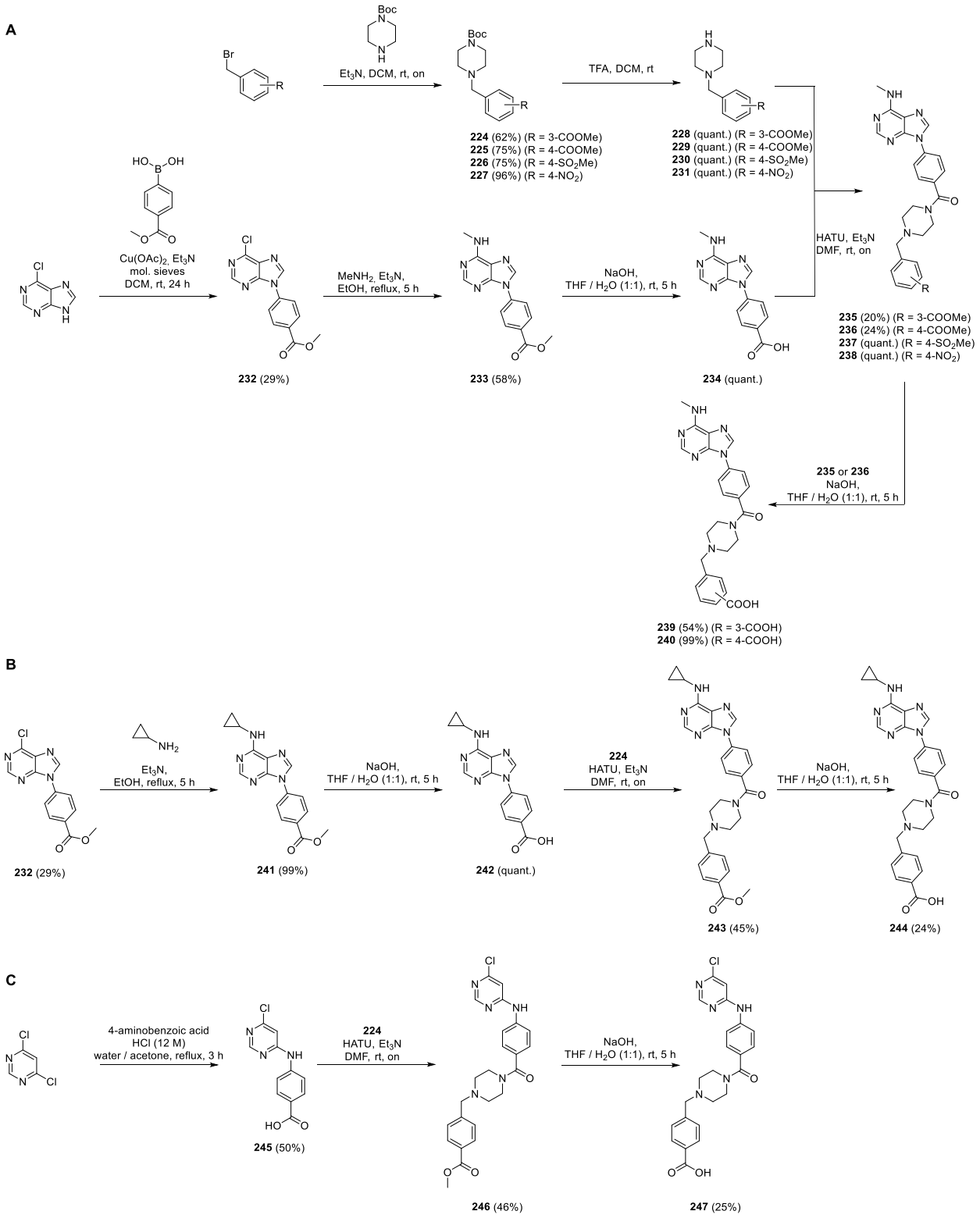

Scheme 14: Synthesis of rationally designed, potential YTHDF2 inhibitors. (A) Variations of the benzylpiperazine moiety using different electron-withdrawing substituents. (B) Variation of the *N*6-position. (C) Exchange of the core scaffold starting with dichloropyrimidine.

3.3.2.2 Identification of phenyl pyrazoles as YTHDF2 inhibitors

Besides the numerous advantages of rationally designed protein inhibitors such as specificity, versatility, improved drug-like properties, or the use for precision medicine, there are drawbacks that hinder the process of developing optimal hit- or lead candidates.[270] Especially, limited structural elucidation of the target protein and its inherent complexity can be particularly daunting, presenting significant challenges in optimizing the binding affinities of small-molecule inhibitors.[271] To circumvent these problems of the top-down approach, we performed an alternative strategy to identify potential YTHDF2 inhibitors by using a bottom-up screening approach. Therefore, we used the established FP assay involving the YTH domain of YTHDF2 and a FAM-labelled 17mer m^{6}A RNA (Figure 38A). After proving the assay to be robust, which showed a low background and high signal-to-noise ratio, we screened an in-house library of ~15,000 synthetic small molecules using single concentrations of 30 µM. Among several hit candidates, we identified 3-(3-(2-hydroxybenzoyl)-1*H*-pyrazol-1-yl)benzoic acid (**248**) to act as a moderate YTHDF2 inhibitor showing an IC_{50} value of 13.64 µM. After re-synthesizing and confirming the activity of the compound in the FP assay, we next tested the hit candidate in an amplified luminescent proximity homogenous assay (AlphaScreen). Here, an inhibition rate of ~31% at 100 µM could be observed, confirming the disruptive effect against the PRI of YTHDF2 and m^{6}A RNA. To further optimize the inhibitory effect of the phenyl pyrazole **248**, we subsequently focused on synthesizing a collection of 36 structural analogs featuring various residues at the phenyl moiety or the hydroxyphenon moiety (Scheme 15, Table 5).

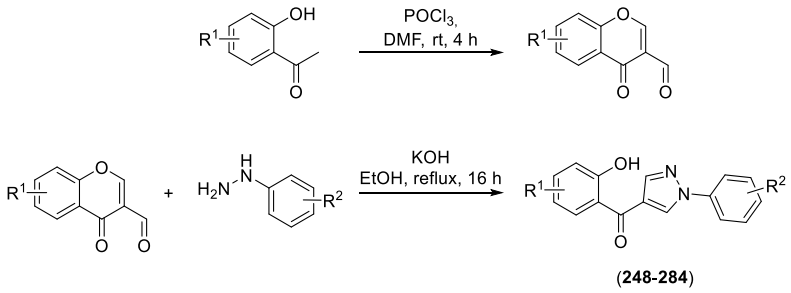

Scheme 15: Synthesis of substituted 3-formylchromones intermediates which were subsequently converted into phenyl pyrazoles in a ring-opening ring-closing condensation reaction involving nucleophilic hydrazines.

For the phenyl moiety either electron withdrawing (**250-251**, **263-266**), electron donating (**257-262**), or a variety of halogen residues (**252-256**) were incorporated and initially tested for YTHDF2 inhibition. Testing of the compounds (**250-266**) in AlphaScreen revealed that most of the small molecules showed decreased activity, and only five compounds (**251**, **261**, **262**, **264-265**) showed equipotent or improved potencies against YTHDF2. For the next round of structural optimization, we, therefore, chose compound **251** as the fundamental compound to separately investigate the hydroxyphenon moiety of the phenyl pyrazole. The additional 18 analogs of **251** included an incorporation of hydrophobic residues (**267-270**, **284**), varieties of halogen residues (**271-279**), and electron donating residues (**280-281**) as well as one nitro group-containing analog (**282**). Especially, hydrophobic residues at the 5-

position of the hydroxyphenon moiety seemed to be well tolerated as indicated by improved inhibitory effects against YTHDF2 (Table 5). Among the best-performing phenyl pyrazoles was **284** containing a 1-napthoyl moiety which increased the potency up to 89% inhibition at 100 µM.

Table 5: Phenyl pyrazoles and their respective inhibitory activity against the PRI of YTHDF2–m^{6}A RNA.

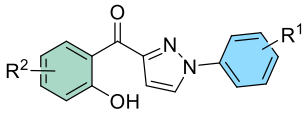

Compound ID	R^1	R^2	Yield (%)[a]	Inhibition at 100 µM (%)[b]
248	3-COOH	H	33	30.7 ± 4.9
		Phenyl moiety		
249	H	H	58	10.8 ± 9.0
250	2-COOH	H	60	5.1 ± 6.4
251	4-COOH	H	33	30.9 ± 4.0
252	2-fluoro	H	33	4.8 ± 3.4
253	4-fluoro	H	64	23.4 ± 2.2
254	2-chloro	H	60	25.0 ± 9.0
255	4-chloro	H	19	2.9 ± 3.4
256	4-bromo	H	13	19.9 ± 8.0
257	2-methyl	H	45	3.3 ± 8.3
258	4-methyl	H	58	22.2 ± 5.0
259	2-methoxy	H	<10	5.4 ± 4.2
260	4-methoxy	H	49	11.9 ± 3.6
261	6-methoxypyridin-3-yl	H	38	30.5 ± 5.2
262	4-trifluoromethoxy	H	48	31.7 ± 3.5
263	4-trifluoromethyl	H	61	3.5 ± 4.8
264	4-cyano	H	81	31.9 ± 7.2
265	4-methylsulfonyl	H	66	48.5 ± 5.6

266	4-sulfonamide	H	56	15.8 ± 8.5
		Hydroxyphenon moiety		
267	4-COOH	5-methyl	60	35.5 ± 6.9
268	4-COOH	4-methyl	27	61.9 ± 6.9
269	4-COOH	5-ethyl	61	71.3 ± 7.6
270	4-COOH	5-*iso*propyl	54	84.9 ± 2.6
271	4-COOH	5-fluoro	35	55.3 ± 3.5
272	4-COOH	4-fluoro	47	53.1 ± 1.7
273	4-COOH	3,5-difluoro	36	42.1 ± 3.1
274	4-COOH	5-chloro	47	81.9 ± 5.7
275	4-COOH	4-chloro	46	46.0 ± 3.8
276	4-COOH	3-chloro	14	29.6 ± 6.6
277	4-COOH	3,5-dichloro	62	88.2 ± 4.2
278	4-COOH	5-bromo	11	44.6 ± 6.1
279	4-COOH	4-bromo	63	40.5 ± 1.5
280	4-COOH	5-methoxy	33	88.4 ± 1.7
281	4-COOH	6-methoxy	8	57.7 ± 5.6
282	4-COOH	5-nitro	63	36.0 ± 6.9
283	4-COOH	4-methyl-5-chloro	47	36.6 ± 5.0
284	4-COOH	1-naphtoyl	43	89.4 ± 2.1

[a]All phenyl pyrazoles **247**-**283** were synthesized by Claus Kemker as part of his master's thesis.

[b]Inhibition rates of the compounds at 100 µM were determined via AlphaScreen. Data represent average values ± s.d. The assay was performed by Xiaqiu Qiu.

3.3.2.3 Biological evaluation of phenyl pyrazoles

After identifying several phenyl pyrazoles with improved potency against YTHDF2 according to AlphaScreen investigations, we next validated the compounds in a pipeline of orthogonal assays. Initially, a single-dose EMSA was performed using a FAM-labeled m^6A RNA probe together with $YTHDF2_{YTH}$ and compound concentrations of 100 µM. The best-performing compounds **277**, **283,** and

284 were then subjected to dose-dependent EMSAs allowing for approximate determinations of IC_{50} values. Here, especially compound **284** could be confirmed as a potent YTHDF2 inhibitor showing 100% inhibition at 25 µM, echoing the AlphaScreen results (Figure 41)

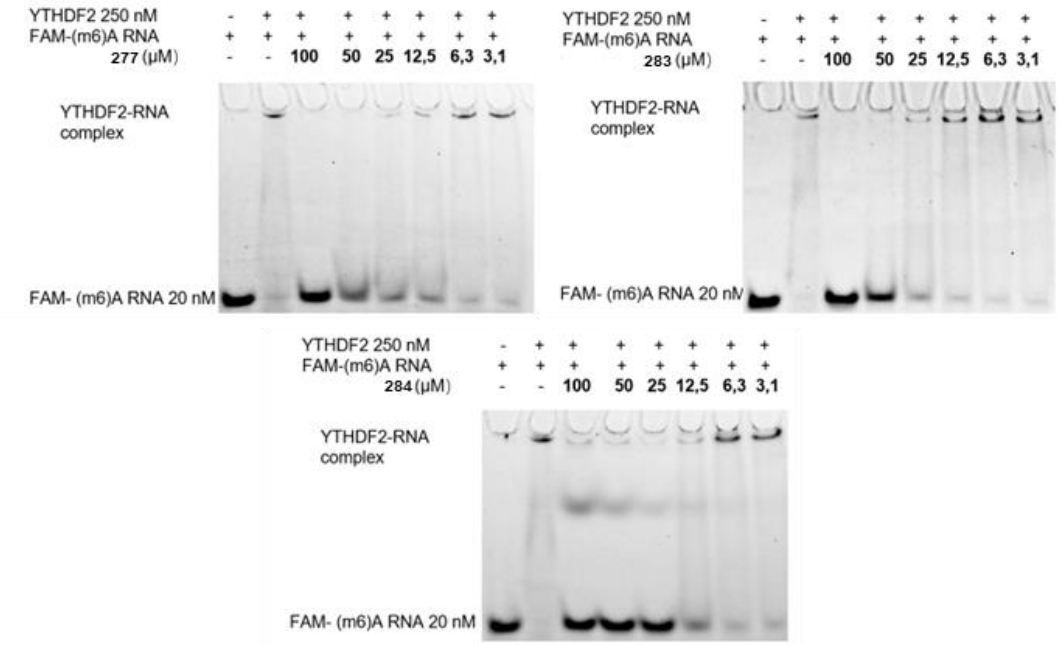

Figure 41: Phenyl pyrazoles **277**, **283** and **284** dose-dependently inhibit the YTHDF2–m^{6}A RNA interaction as indicated by EMSA. The most potent compound **284** fully inhibited the PRI at a concentration of 25 µM. The assay was performed by Xiaqiu Qiu.

Due to the promising inhibitory effects against YTHDF2, we selected compound **284** for evaluating a direct binding to the reader protein in a nano-differential scanning fluorimetry thermal shift assay (nanoDSF). Matching with the previous findings, the phenyl pyrazole showed significant stabilizing effects at increasing concentrations inducing a thermal shift of ~2°C. This phenomenon can probably be explained by increasing intramolecular interactions caused by the aggregation of YTHDF2. To further proof the binding of **284** to YTHDF2, we next investigated the effect of the compound on the cellular protein–RNA complex by using a cellular thermal shift assay (CETSA). Hereby, changes in the aggregation temperature (T_{agg}), describing the temperature of protein unfolding, can be modified by the binding of small molecules that causes a thermal shift. To optimally visualize such an effect of **284**, we used K562 cells, showing high expression levels of YTHDF2. Similar to the *in vitro* findings, treatment of the cells with **284** (50 µM) significantly increased the T_{agg} of YTHDF2 by 2.4°C after 24 h, indicating the binding of the small molecule to YTHDF2 (Figure 42).

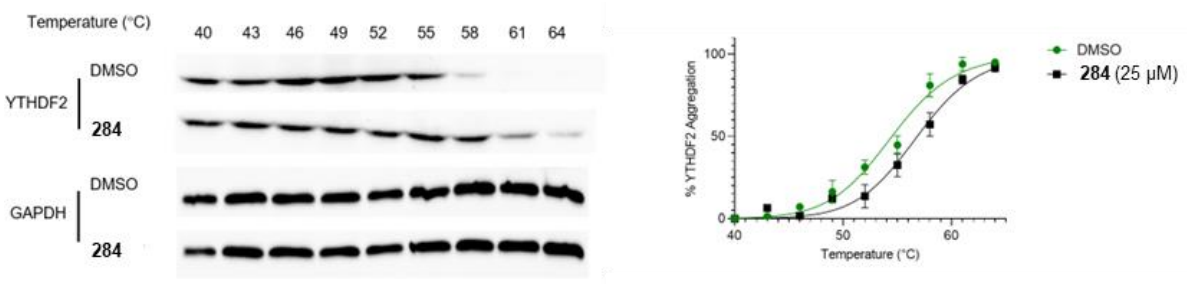

Figure 42: Stabilizing effect of **284** against YTHDF2 measured by CETSA (left: Western blot results; right: T_{agg} curves representing the results of the Western blot results). The assay was performed by Xiaqiu Qiu.

Altogether, compound **284** depicts a promising YTHDF2-binding small molecule indicating not only effects *in vitro* but also *in cellulo*. To further demonstrate this effect alternative cellular assays were performed, such as flow cytometry-based experiments. Initially, we evaluated the effect of **284** on cell cycle changes of K562 cells. Treatment of the cells with either 10 µM or 25 µM of **284** induced a strong increase in the G0/ G1 stage of the cell cycle, indicating the formation of apoptotic cells (Figure 43A). Given the fact that overexpression of YTHDF2 has been reported to inhibit apoptosis in ovarian cancer cells, the effect of **284** to induce apoptosis was delightful to observe.[272] However, the exact mechanism remains unclear and may be triggered by entirely different factors. In another flow cytometry-based assay, we continued to investigate the apoptotic effect on K562 cells and found that 27% of the cells underwent apoptosis after treatment with 25 µM of **284**. It is noteworthy to mention that the effect occurred with slight dose-dependency, as 5 µM treatment only showed 23% apoptosis and 10 µM 24% (Figure 43B). Concomitantly, we could demonstrate a moderate micromolar inhibitory effect against the proliferation of human cancer cells (K562, IC_{50} = 29.7 µM, HCT116, IC_{50} = 33.3 µM; JAR, IC_{50} = 47.5 µM). Generally, these results confirmed the effect of **284** against human cancer cell lines, but the exact apoptotic mechanism remains unclear and needs to be further clarified.

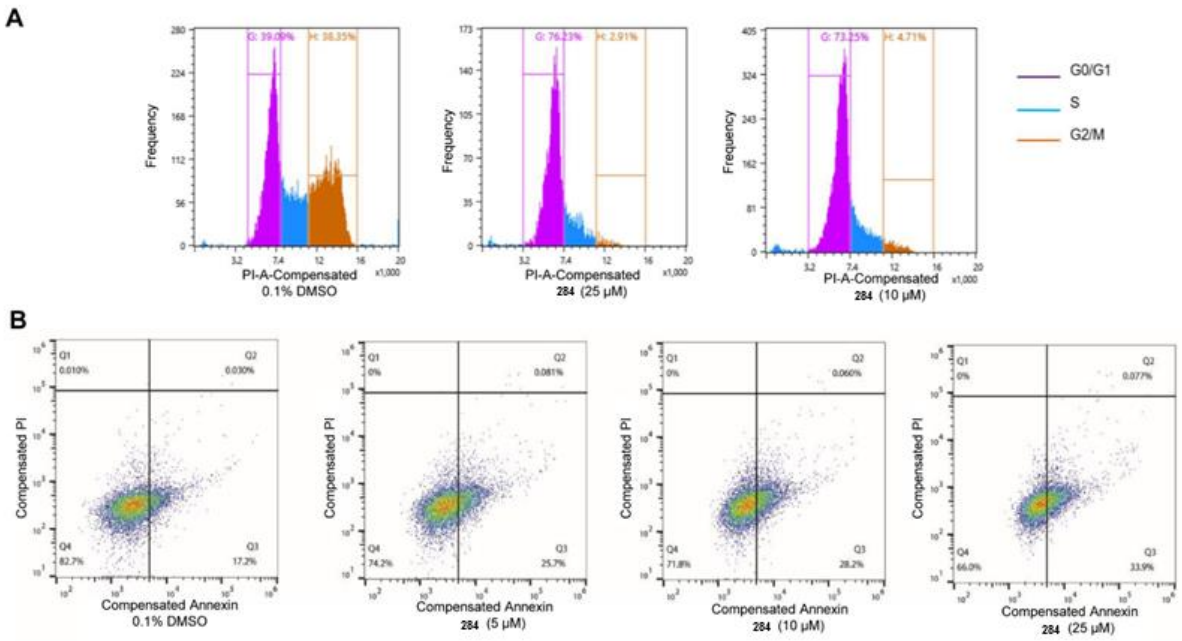

Figure 43: **284** induced cell cycle arrest and apoptosis in K562. (A) Cell cycle changes upon treatment with **284**. The compound induced a significant arrest at the G0/ G1 stage measured in flow cytometry. (B) The dose-dependent, apoptotic effect of **284** as measured in flow cytometry. The assays were performed by Damian Schiller.

3.3.2.4 Binding mode prediction for phenyl pyrazole YTHDF2 inhibitors

Next, a molecular docking analysis was performed to provide a plausible binding mode of the best-performing phenyl pyrazole **284**. Therefore, the crystal structure of the *C*-terminal YTH domain in complex with m^6A served as a fundament for the model. An optimal binding pose between **284** and the RNA binding site revealed several key interactions consistent with the previous findings of *in vitro* and *in cellulo* studies. For example, the 1-naphtoyl moiety of **284** optimally fits into the m^6A binding site forming a π–π interaction with Y418, one of the amino acids forming the prominent aromatic cage of YTHDF2. The fact that the hydrophobic moiety occupies the aromatic cage of the protein could also explain the similar potencies of other hydrophobic compounds. For further structural optimizations, the hydrophobic character of the hydroxyphenon moiety generally should be maintained. The phenyl moiety or the pyrazole core scaffold on the other side could be rather extensively varied to improve the potency of the YTHDF2 inhibitor.

Furthermore, K490 forms a stable salt bridge with the carboxylic acid residue of the **284** which might also explain the moderate affinities of phenyl pyrazoles **264** and **265**. Here, the cyano- or the methylsulfonyl residue might form similar interactions with K490. Another hydrogen bond is formed by D528 and the hydroxyl residue of **284**, potentially also increasing the binding affinity towards YTHDF2.

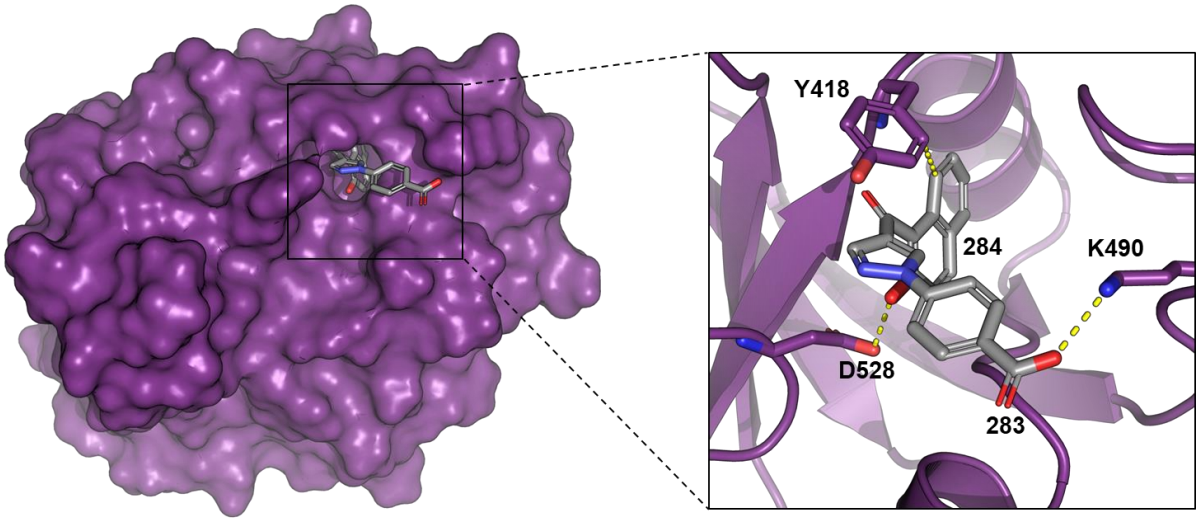

Figure 44*:* Molecular docking analysis to predict the binding mode of phenyl pyrazole **284** to the YTH domain of YTHDF2 (PDB: 4RDN). Surface structure of YTHDF2$_{YTH}$ (violet purple) and **284** in gray carbon backbone (left) and the enlarged visualization of the ribbon structure of YTHDF2 with **284** (right). Selected key interacting residues are depicted as sticks.

Generally, the proposed binding mode of compound **284** provides a plausible explanation for its inhibitory effect on YTHDF2, as it involves amino acids of the aromatic cage (Y418) and other residues of the RBD. Consequently, the interaction of **284** with YTHDF2 has the potential to obstruct the RNA-binding site, thereby disrupting the PRI between YTHDF2 and m^{6}A RNA.

3.3.3 Conclusions from the identification of YTHDF2 degraders and small-molecule inhibitors

Due to lacking reports of YTHDF2-inhibiting small molecules or -degrading bifunctional molecules, there is a great need for discovering such modalities in order to understand and modulate the pathogenic pathways of the RBP. To initiate the discovery of novel YTHDF2-targeting modalities, we pursued two different strategies: First, the report of Donovan *et al.* provided helpful insights about a polypharmacological PROTAC SK-3-91 (**198**), capable of degrading YTHDF2 significantly. This PROTAC initially was resynthesized and tested in western blot analysis to validate the degradation of YTHDF2. After confirming the decrease of YTHDF2 levels upon compound treatment, we next installed different linkers to the small-molecule moiety and investigated the changes in degradational efficacy. PROTAC **211** showed equipotent degradation of YTHDF2 and thus was further investigated in dose-dependent western blot analysis as well as a washout experiment, revealing a full recovery of YTHDF2 levels after 24 h. Generally, the YTHDF2 degrading activity of PROTACs **198** and **211** serves as a feasible foundation for our ongoing efforts in developing YTHDF2-selective degraders. To test whether the PROTACs or the small molecules functionalized with amine linker moieties are also capable of disrupting the PRI of YTHDF2 and m^{6}A RNA, we furthermore subjected the compounds to an FP assay. However, only PROTACs **198** and **211** moderately inhibited YTHDF2, providing evidence for allosteric binding of the small-molecule moiety to the RBP. Altogether, the compounds **198** and **211**

depict a promising starting point to identify alternative and more selective YTHDF2 degraders, however, for the discovery of YTHDF2-inhibiting small molecules another strategy is required.

To discover novel inhibitors of the m^{6}A reader, two different approaches were performed. One attempt was to rationally design a small-molecule inhibitor based on m^{6}A and m^{6}A-derived fragments. Alternatively, a bottom-up screening approach should provide a variety of synthetic small molecules capable of disrupting the PRI of YTHDF2 and m^{6}A RNA. For the rational design of a YTHDF2 inhibitor, initially, alkylated purine fragments were synthesized and tested against the m^{6}A reader. Unfortunately, none of the fragments showed an inhibitory effect at 100 µM, however, the report of Nai *et al.* demonstrated an interaction of fragment **218** with the m^{6}A binding site of YTHDF2, justifying further functionalization of the purine core scaffold.[230] To expand the structure of the purine core scaffold, a benzyl piperazine moiety was installed, which should reach into a rather positively charged pocket of the YTH domain. Alternative variations of rationally designed molecules consisted of *N*6-alkylation or an exchange of the core scaffold with a pyrimidine heterocycle. After isolating a total amount of eight different small molecules, we tested their ability to inhibit the YTHDF2–m^{6}A RNA interaction. However, none of the compounds showed significant inhibitory effects, outlining the importance of clarifying a specific binding mode and structural features required for inhibiting a protein of interest. To improve the potency of the rationally designed small molecules, other fragments binding to the RBD of YTHDF2 could serve as fundamental compounds. Additionally, a detailed structural investigation of the compounds binding to the m^{6}A reader is required to fully comprehend the structural features involved in interactions with the protein.

Due to the missing success in identifying selective and rationally designed YTHDF2 inhibitors, next a screening approach was carried out involving a compound collection of ~15,000 compounds. The treatment of YTHDF2–m^{6}A RNA with the different synthetic small molecules revealed the phenyl pyrazole **248** as a moderate YTHDF2 inhibitor. Subsequent to its identification, we next investigated the structure-activity relationship of the **248** which not only should help to understand the binding mode of the compound to YTHDF2 but also should provide more potent analogs. To our delight, we identified several phenyl pyrazoles that showed over 50% inhibition against the YTHDF2–m^{6}A RNA interaction in a bead-based AlphaScreen. In particular, compound **284** showed promising anti-YTHDF2 activity, as indicated in orthogonal, dose-dependent EMSA analysis, or cellular thermal shift analysis. Consequently, the 1-napthoyl containing compound was further evaluated in flow cytometry-based cellular assays. Here, **284** was found to induce a cell cycle arrest in the G0/ G1 stage of K562 cells. Additionally, moderate apoptosis induction was observed after treating the cells with the phenyl pyrazole. Although the exact mechanism of apoptosis induction and cell cycle arrest mediated by **284** needs to be further investigated, the small molecule depicts a promising tool compound that could be utilized to study the m^{6}A reader YTHDF2 in more detail. Next to our attempt to provide a plausible binding mode via molecular docking analysis, it might be reasonable to investigate the binding mode of **284** in more detail, e.g. by using X-ray crystallography or cryo-EM. This should help to identify

structural features required for YTHDF2 binding and thus could support the optimization of the compound's rather moderate potency.

4 Conclusion and perspectives

The interaction between proteins and RNA is critical for various cellular activities, and its dysregulation can lead to a variety of human diseases. Therefore, targeting disease-related RBPs using small molecules or proximity-inducing bifunctional molecules represents a promising strategy to elucidate the cellular functions of RBPs and could help in the development of new therapeutic approaches. In this work, the miRNA-binding protein LIN28, the m^6A writer METTL16, and the m^6A reader YTHDF2 were targeted using small molecules. While LIN28 depicts an ncRNA-binding protein specifically interacting with tumor-suppressive *let-7*, METTL16, and YTHDF2 represent RNA-modifying proteins binding to a variety of coding- and ncRNAs. The strategies to target the individual RBPs varied from scaffold-based approaches that focused on optimizing specific RBP-targeting scaffolds, to screening-based efforts aiming for the identification of small-molecule inhibitors of new scaffolds. Additionally, we initiated the first efforts to identify bifunctional molecules that degrade YTHDF2, representing an alternative strategy to address the disease-related protein.

To target LIN28, we applied two complementary strategies which allowed for the successful identification of alternative and more potent LIN28 inhibitors. In a scaffold-based approach, one of the first systematic SAR studies surrounding the reported LIN28-inhibiting tetrahydroquinoline LI71 (**8**) led to the identification of a 2-fold more potent analog (**39**) expanding the knowledge about its potential inhibitory mode. The biological evaluation data obtained from the THQ scaffold-containing compounds however must be carefully scrutinized, as compounds of such scaffolds are likely to interfere with assay readouts due to reactive byproducts. The alternative screening-based approach led to the identification of a trisubstituted pyrrolinone (**64**) showing a micromolar potency, adding a new scaffold to the small-molecule collection of LIN28 inhibitors. Follow-up efforts included an extensive structural investigation of the original pyrrolinone (**64**) resulting in the synthesis and evaluation of a total 95 analogues. Among the tested compounds, a biphenyl moiety-containing analogue (**66**) depicted a promising hit compound with improved cellular activity and equivalent potency *in vitro* and thus the hit was further optimized by changing the biphenyl moiety to a dibenzofuranyl moiety. A resulting compound **88** represented the most potent LIN28 inhibitor among the trisubstituted pyrrolinone series.

Epitranscriptomic modifications, such as m^6A, have a profound impact on regulating RNA stability and gene expression. Installation of the chemical modification can be mediated by METTL16 which was found to actively contribute to tumor progression once aberrantly active, highlighting the need for identifying METTL16-inhibiting small molecules. Due to the lack of such inhibitors, a screening-based approach led to the identification of compound series that showed significant disruptive effects on the METTL16-*MAT2A* interaction. Among the aminothiazolone series, the inhibitor **105** was initially investigated through an extensive SAR study, resulting in more potent tool compounds **132**, **154**, **155,** and **156**. These compounds were tested in binding assays demonstrating the direct binding to

METTL16. Furthermore, cellular assays revealed effective modulation of m^{6}A RNA levels as well as spliced *MAT2A* levels upon treatment with compound **154**, thus providing new insights into the regulatory network among METTL16, *MAT2A* splicing, SAM levels, and m^{6}A levels. In addition to the aminothiazolones, a small collection of hydantoin- and pseudothiohydantoin compounds (**164** and **170**) were identified as potential METTL16 inhibitors. The shared aryl furan moiety of both hit compounds allowed for a simultaneous SAR analysis comprising the synthesis of 16 hydantoin- and 11 pseudothiohydantoin analogs. As none of the analogs showed improved potencies against METTL16, the original hit candidate **164** was further investigated in dose- and time-dependent EMSAs that revealed nanomolar potencies potentially mediated through a covalent interaction with the RMP. The formation of a covalent adduct was further confirmed in an LC-MS-based analysis of METTL16 treated with **164**. The newly identified inhibitors in this work represent one of the first examples of METTL16-inhibiting small molecules, which could serve as tool compounds to explore the m^{6}A-regulatory role of METTL16 in pathogenic scenarios.

In addition to the m^{6}A writer, another strategy to comprehend and manipulate pathways involving the m^{6}A modification was to target m^{6}A readers including YTHDF2, which acts as an oncogene in many cancers and has thus recently emerged as a promising drug target. Among very few reports about YTHDF2-targeting chemical modalities, the polypharmacological PROTAC SK-3-91 (**198**) was demonstrated to degrade cellular YTHDF2 significantly. After confirming the degradational activity of **198**, additional analogues were synthesized showing shorter linker moieties that were also identified as YTHDF2-degrading PROTACs. However, testing the ability of the degraders to disrupt the YTHDF2–m^{6}A RNA interaction demonstrated only weak- to no inhibitory effects suggesting an allosteric binding mode of the compounds. Although further confirmation is needed to prove this assumption, another strategy was required to identify potential small-molecule YTHDF2 inhibitors. First, a rational design strategy based on m^{6}A and m^{6}A-like fragments was performed leading to eight compounds among which only **239** and **240** showed weak inhibitory effects. To identify more potent and novel YTHDF2 inhibitors, another screening approach was conducted, leading to the discovery of a phenyl pyrazole (**248**) with moderate potency. This hit compound was successively investigated in a SAR analysis providing not only meaningful insights into the inhibitory mode of the compound but also leading to the identification of the more potent 4-(4-(2-hydroxy-1-naphthoyl)-1*H*-pyrazol-1-yl)benzoic acid **284**, which was tested in a pipeline of orthogonal assays and showed promising cellular activities measuring cell cycle changes and induction of apoptosis. Although the exact apoptotic mechanism remains to be further clarified, **284** depicts one of the first examples of YTHDF2-inhibiting tool compounds that can be utilized to manipulate m^{6}A RNA decay.

Targeting RBPs with small molecules is generally considered challenging due to the high affinities of RNAs, which result from extensive surface- and electrostatic interactions with the RNA-binding site. This fact is also echoed by the identified RBP inhibitors mentioned in this work, which mostly showed low micromolar potencies. For LIN28 particularly, more potent small-molecule inhibitors are difficult

to be discovered as the RBP consists of two distinct domains contributing to tight interactions with *let-7*. If only one of these domains is targeted, the miRNA can potentially still bind to the protein and thus remains blocked for Drosha- or Dicer-mediated cleavage. In this context, new modalities covering both RNA-binding sites need to be sought after to efficiently target the miRNA-binding protein. The RMPs METTL16 and YTHDF2 depict emerging targets in the field of epitranscriptomics that were studied within this thesis via small-molecule inhibition. While the potencies of most compounds lay within the micromolar range, the identified inhibitors represent some of the first-in-class or best-in-class RMP modulators. Taken together, these findings paved the way for the development of small-molecule therapeutic agents aimed at disrupting the function of m^6A regulators.

5 Experimental

5.1 General Chemistry Information

Unless stated otherwise, all commercially available reagents and solvents were used without any further purification. The solvents used for silica gel column chromatography were laboratory grade. Dry solvents were bought from Fischer Scientific, Acros, and/or VWR, and were employed without any additional processing. Moisture and/or oxygen-sensitive solutions were transferred in an inert gas atmosphere using cannulas and syringes.

Analytical thin-layer chromatography (TLC) was conducted on silica-coated aluminum plates (Merck 60 F254) and visualization of synthetic products proceeded with UV irradiation (254 nm and/or 356 nm), potassium permanganate stain (1.5 g $KMnO_4$, 10 g K_2CO_3 in 1.25 mL of 10% aq. NaOH and 200 mL demineralized water) or phosphomolybdic acid (PMA) stain (phosphomolybdic acid in 100 mL absolute ethanol).

Analytical uHPLC-MS and LC-MS were performed and evaluated either on an Agilent 1290 Infinity system equipped with a mass detector (column: Zorbax Eclipse C18 Rapid Resolution 2.1x50 mm 1.8µm) (flow rate: 0.5 mL/min) or an Agilent Infinity HPLC system with 3x50 mm, 1.8 µm Macherey-Nagel Nucleodur C18 Gravity column (flow rate: 0.56 mL/min). To analyze intermediates and final products, a gradient was applied starting from 10% acetonitrile (+0.1% TFA) in water (+0.1% TFA) up to 99.9% acetonitrile (+0.1% TFA).

Purification of crude products was performed by using silica gel column chromatography (Merck 60, particle size 0.040-0.063 mm) or automated medium-pressure liquid chromatography (Büchi Pure C-810 Flash or Pure C-850 Flash/Prep) using indicated solvents.

NMR spectra were recorded either with a Bruker AV 400 Avance III HD (NanoBay), Agilent Technologies DD2, Bruker AV 500 Avance III HD (Prodigy), Bruker Avance NEO – 500 MHz, Bruker AV 600 Avance III HD (CryoProbe) or a Bruker AV 700 Avance III HD (CryoProbe) spectrometer. Data is reported in parts per million (ppm) with reference to the deuterated solvent ($CDCl_3$: 7.26 ppm, 77.16 ppm; DMSO-d_6: 2.50 ppm, 39.52 ppm). Multiplicities are abbreviated as follows: s = singlet, d = doublet, t = triplet, dd = double doublet, and m = multiplet, and coupling constant values are given in Hz. Signals were assigned to their corresponding hydrogens or carbons based on 2D NMR correlations ($^1H/^1H$ COSY, $^1H/^1H$ NOESY, $^1H/^{13}C$ HSQC, $^1H/^{13}C$ HMBC). To facilitate accurate analysis of fluoride-containing compounds, ^{19}F NMR analysis without $\{^1H\}$ decoupling was conducted.

High-resolution mass spectrometry (HRMS) was measured using an LTQ Orbitrap mass spectrometer coupled to an Accela HPLC-system (HPLC column: Hypersyl GOLD, 50 mm x 1 mm, particle size 1.9 µm, ionization method: electron spray ionization (ESI)).

5.2 Synthetic procedures and compound characterizations

5.2.1 LIN28

5.2.1.1 Tetrahydroquinolines (THQs)

General Procedure A (Povarov reaction):

In a two-neck round bottom flask, a catalytic amount of scandium trifluoromethane sulfonate (0.05 mmol, 0.10 equiv.) in anhydrous acetonitrile (3.00 mL) was added to a mixture of an aldehyde (0.50 mmol, 1.00 equiv.) and an aniline derivative (0.50 mmol, 1.00 equiv.) under an argon atmosphere. Then, freshly distilled cyclopentadiene (2.00 mmol, 4.00 equiv.) was added slowly to the stirring solution. The reaction mixture was stirred at room temperature for a further 16 h. Afterwards, the solvent was evaporated and purification of the crude material by silica gel flash chromatography afforded the corresponding tricyclic tetrahydroquinoline product.[273]

General Procedure B (acetylation):

Tetrahydroquinoline derivative (1 equiv.) was dissolved in 3 ml dichloromethane, and pyridine (1.3 equiv.) was added dropwise at 0°C. While maintaining the temperature, acetyl chloride (1.5 equiv.) was added dropwise. Afterward, the cooling bath was removed, and the solution was allowed to stir at room temperature for an additional 3 h. Upon completion, the reaction was quenched with a saturated solution of ammonium chloride, and the organic layer was extracted with dichloromethane (3 x 15 mL). The combined organic layer was dried over anhydrous $MgSO_4$ and concentrated under reduced pressure. Purification of the crude via silica gel column chromatography afforded the desired acetylated tetrahydroquinoline product as a diastereomeric mixture.

General Procedure C (hydrolysis):

To a suspension of an ester (1.0 equiv.) in a THF water mixture (1:1), lithium hydroxide monohydrate (2.5 equiv.) was added. The mixture was stirred for 3 h and upon completion of the reaction, the mixture was acidified with a 1 M HCl solution and extracted with EtOAc (2 x 30 mL). The organic layer was washed with 20 mL of saturated aqueous NaCl solution, dried, and concentrated under reduced pressure. The resulting crude mixture was purified by using silica gel column chromatography applying an appropriate gradient.

tert-Butyl (4aR,10bR)-7-ethoxy-5-(4-(methoxycarbonyl)phenyl)-3,4,4a,5,6,10b-hexahydrobenzo[h][1,6]naphthyridine-1(2H)-carboxylate (**45**).

A catalytic amount of scandium trifluoromethane sulfonate (24.6 mg, 0.05 mmol, 0.10 eq) and 4 Å molecular sieves were added to a stirring mixture of 4-formylbenzoate (82.10 mg, 0.50 mmol, 1.00 eq) and 2-ethoxyaniline (65.10 µL, 0.50 mmol, 1.00 eq) in anhydrous acetonitrile (3 mL). The resulting solution was allowed to stir for 5 min and then *tert*-butyl 3,4-dihydropyridine-1(2*H*)-carboxylate (89.00 µL, 0.50 mmol, 1.00 eq) was added *via* syringe. The reaction mixture was stirred overnight

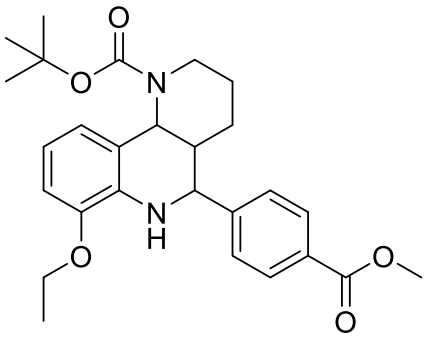

under an argon atmosphere and then quenched with a saturated $NaHCO_3$ solution. After extracting with EtOAc (3x 50 mL) the combined organic layer was dried using anhydrous $MgSO_4$ and the solvent was evaporated under reduced pressure. The crude material was purified using silica gel flash column chromatography with an elution of 6% EtOAc in petroleum ether to afford the desired tricyclic tetrahydroquinoline compound as a white foam (133.20 mg, 0,29 mmol, 58%). $\mathbf{R_f}$ = 0.35 (petroleum ether / EtOAc = 4:1). **^{1}H NMR** (600 MHz, DMSO-d_6) δ 7.92 (d, *J* = 8.4 Hz, 2H), 7.33 (d, *J* = 7.9 Hz, 2H), 6.75 (d, *J* = 7.9 Hz, 1H), 6.52 (t, *J* = 8.1 Hz, 1H), 6.32 (dd, *J* = 51.0, 7.8 Hz, 1H), 5.89 (d, *J* = 5.1 Hz, 1H), 4.81 – 4.71 (m, 1H), 4.48 (d, *J* = 4.2 Hz, 1H), 4.10 (h, *J* = 6.7 Hz, 1H), 4.06 – 3.99 (m, 1H), 3.83 (s, 3H), 2.43 (t, *J* = 12.8 Hz, 1H), 1.98 (d, *J* = 14.5 Hz, 1H), 1.77 (s, 1H), 1.56 (dt, *J* = 12.9, 3.2 Hz, 1H), 1.47 – 1.23 (m, 12H), 1.15 (s, 3H). **^{13}C NMR** (151 MHz, DMSO-d_6) δ 166.60, 155.10, 151.90, 144.80, 134.20, 129.80, 128.50, 126.40, 118.40, 116.40, 115.30, 110.40, 79.40, 64.10, 57.80, 52.50, 47.00, 40.50, 37.70, 28.50, 28.10, 26.30, 25.50, 15.30.

4-((4aR,10bR)-1-(tert-Butoxycarbonyl)-7-ethoxy-1,2,3,4,4a,5,6,10b-octahydrobenzo[h][1,6]naphthyridin-5-yl)benzoic acid (**48**).

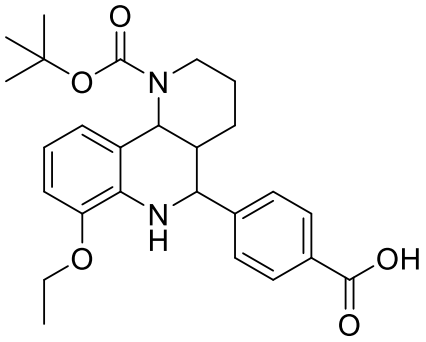

To a suspension of tetrahydroquinoline **45** (100.00 mg, 0.21 mmol, 1.00 eq) in 4 mL of THF was added 2 mL of water and lithium hydroxide monohydrate (22.48 mg, 0.54 mmol, 2.50 eq). The mixture was stirred and heated at 50°C overnight before treatment with 1 M aqueous HCl solution and extraction with DCM (3 x 15 mL). The organic layer was dried with anhydrous $MgSO_4$ and the solvent was removed *in vacuo*. Recrystallization using petroleum ether (4 mL) and EtOAc (0.2 mL) afforded the pure acid as white crystals (95.0 mg, 0.21 mmol, 99%). $\mathbf{R_f}$ = 0.2 (petroleum ether / EtOAc = 1:1). **^{1}H NMR** (600 MHz, DMSO-d_6) δ 12.84 (s, 1H), 7.89 (d, *J* = 8.1 Hz, 2H), 7.30 (d, *J* = 8.0 Hz, 2H), 6.75 (d, *J* = 7.9 Hz, 1H), 6.52 (t, *J* = 7.9 Hz, 1H), 6.32 (dd, *J* = 50.5, 7.8 Hz, 1H), 5.88 (t, *J* = 7.1 Hz, 1H), 4.78 (dd, *J* = 30.0, 5.0 Hz, 1H), 4.47 (s, 1H), 4.10 (h, *J* = 6.9 Hz, 1H), 4.03 (q, *J* = 7.1 Hz, 2H), 3.87 – 3.65 (m, 1H), 1.99 (s, 1H), 1.94 (d, *J* = 33.9 Hz, 1H), 1.81 – 1.72 (m, 1H), 1.56 (dq, *J* = 12.9, 3.2 Hz, 1H), 1.40 – 1.33 (m, 9H), 1.19 – 1.14 (m, 4H). **^{13}C NMR** (151 MHz, DMSO-d_6) δ 167.70, 155.10, 151.40, 144.80, 134.20, 129.90, 126.20, 118.40, 116.40, 115.30, 110.40, 79.40, 64.10, 60.20, 57.80, 48.70, 47.10, 38.50, 37.70, 28.50, 28.10, 26.40, 25.50, 21.20, 15.30, 14.60.

4-((4aS,10bR)-7-Ethoxy-1,2,3,4,4a,5,6,10b-octahydrobenzo[h][1,6]naphthyridin-5-yl)benzoic acid (**49**).

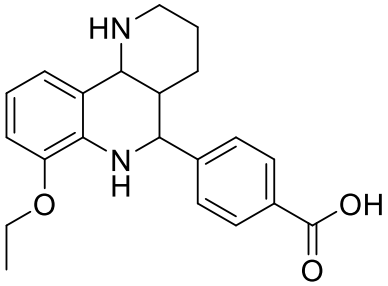

To a stirred solution of *N*-Boc protected tetrahydroquinoline **47** (45.00 mg, 0.10 mmol, 1.00 eq) in dry dichloromethane (1 mL), cooled to 0 °C, trifluoracetic acid (76.60 μL, 1.00 mmol, 10.00 eq) was added. After 30 min the mixture was allowed to warm to room temperature and stirred for an additional 2.5 h. The mixture was concentrated under reduced pressure to afford the desired tetrahydroquinoline as a TFA salt (35.24 mg, 0.10 mmol, 99%).[36] $\mathbf{R}_f$ = 0.01 (petroleum ether / EtOAc and 0.1% AcOH = 1:1). **^{1}H NMR** (700 MHz, DMSO-d_6) δ 12.97 (s, 1H), 9.17 – 9.05 (m, 1H), 8.82 (d, *J* = 9.6 Hz, 1H), 7.97 (d, *J* = 8.1 Hz, 2H), 7.46 (d, *J* = 7.9 Hz, 2H), 6.93 (dd, *J* = 8.1, 1.2 Hz, 1H), 6.87 (dd, *J* = 8.1, 1.2 Hz, 1H), 6.64 (t, *J* = 7.9 Hz, 1H), 5.66 (s, 1H), 4.69 (d, *J* = 8.8 Hz, 1H), 4.35 (s, 1H), 4.08 (dq, *J* = 9.8, 7.0 Hz, 1H), 4.01 (dq, *J* = 9.8, 7.0 Hz, 1H), 3.16 – 3.03 (m, 2H), 2.38 (dt, *J* = 9.3, 4.5 Hz, 1H), 1.73 – 1.61 (m, 2H), 1.32 (t, *J* = 7.0 Hz, 3H), 1.24 (qd, *J* = 6.3, 3.2 Hz, 1H). **^{13}C NMR** (176 MHz, DMSO-d_6) δ 167.60, 158.50, 158.30, 145.50, 135.20, 130.70, 130.10, 127.80, 118.50, 116.70, 116.20, 111.90, 64.10, 36.00, 23.30, 15.20.

Ethyl (3aS,9bR)-5-acetyl-6-ethoxy-3a,4,5,9b-tetrahydro-3H-cyclopenta[c]quinoline-4-carboxylate (**50**)

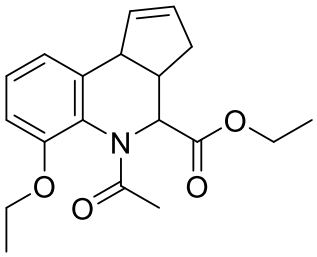

Following the general procedure B, the product was obtained as a yellow solid using an elution system of 50% EtOAc in petroleum ether which afforded the desired acetylated tetrahydroquinoline as a diastereomeric mixture (dr = 4:1) (487.10 mg, 1.48 mmol, 85%). $\mathbf{R}_f$ = 0.15 (petroleum ether / EtOAc = 1:1 +0.1% AcOH). **^{1}H NMR** (400 MHz, Chloroform-*d*) δ 7.14 (t, *J* = 8.0 Hz, 1H), 6.87 (dt, *J* = 7.7, 1.2 Hz, 1H), 6.81 (dt, *J* = 8.3, 1.1 Hz, 1H), 5.96 (dq, *J* = 5.8, 2.2 Hz, 1H), 5.81 (dq, *J* = 5.9, 2.4 Hz, 1H), 5.77 (d, *J* = 8.8 Hz, 1H), 4.16 – 4.01 (m, 2H), 3.91 (qd, *J* = 7.2, 2.9 Hz, 2H), 3.81 (d, *J* = 8.5 Hz, 1H), 3.25 (qd, *J* = 8.5, 5.1 Hz, 1H), 2.56 (ddq, *J* = 16.5, 8.4, 2.3 Hz, 1H), 2.41 (dtd, *J* = 16.4, 4.4, 2.2 Hz, 1H), 2.07 (s, 3H), 1.41 (t, *J* = 7.0 Hz, 3H), 1.06 (t, *J* = 7.1 Hz, 3H). **LC-MS** (**ESI**) (*m/z*) calculated for $C_{19}H_{23}NO_4$ $[M+H]^+$ = 330.1; found: 330.0.

Methyl 4-((3aS,9bR)-5-acetyl-6-ethoxy-3a,4,5,9b-tetrahydro-3H-cyclopenta[c]quinolin-4-yl)benzoate (**51**)

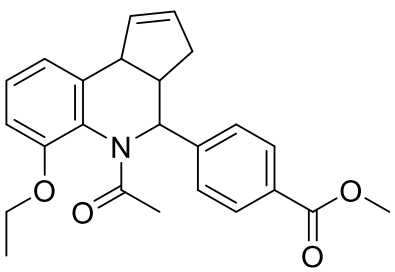

Following the general procedure B, the product was obtained as a yellow oil using an elution system of 20% EtOAc in petroleum ether which afforded the desired acid as a diastereomeric mixture (dr = 4:1) (233.1 mg, 0.6 mmol, 99%). $\mathbf{R}_f$ = 0.1 (petroleum ether / EtOAc = 3:1). **^{1}H NMR** (400 MHz, Chloroform-*d*) δ 7.69 (d, *J* =

8.4 Hz, 2H), 7.15 (t, *J* = 8.0 Hz, 1H), 6.96 (d, *J* = 15.6 Hz, 3H), 6.85 (d, *J* = 8.7 Hz, 1H), 6.65 (d, *J* = 8.2 Hz, 1H), 6.41 (d, *J* = 9.0 Hz, 1H), 6.22 (d, *J* = 12.9 Hz, 1H), 5.82 (d, *J* = 12.8 Hz, 1H), 4.01 (d, *J* = 10.8 Hz, 1H), 3.83 (s, 3H), 3.60 (s, 1H), 3.45 (s, 1H), 2.49 (d, *J* = 29.4 Hz, 1H), 2.04 (s, 3H), 1.96 (d, *J* = 25.7 Hz, 1H), 1.08 (t, *J* = 7.0 Hz, 3H). **LC-MS** (**ESI**) (*m/z*) calculated for $C_{24}H_{25}NO_4$ $[M+H]^+$ = 392.2; found: 392.0.

Methyl 3-((3aS,9bR)-5-acetyl-6-ethoxy-3a,4,5,9b-tetrahydro-3H-cyclopenta[c]quinolin-4-yl)benzoate (**52**)

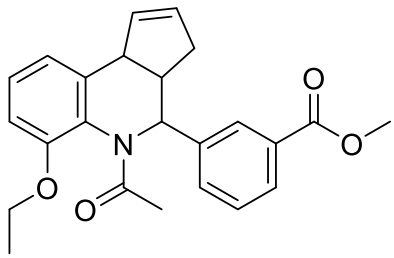

Following the general procedure B, the product was obtained as a yellow oil using an elution system of 50% EtOAc in petroleum ether which afforded the desired acetylated tetrahydroquinoline as a diastereomeric mixture (dr = 78:22) (233.1 mg, 0.6 mmol, 99%). $\mathbf{R_f}$ = 0.6 (petroleum ether / EtOAc = 1:1). **^{1}H NMR** (400 MHz, Chloroform-*d*) δ 7.74 (dt, *J* = 7.5, 1.5 Hz, 1H), 7.63 (d, *J* = 2.0 Hz, 1H), 7.19 – 7.12 (m, 1H), 7.10 – 6.95 (m, 3H), 6.66 (dt, *J* = 8.2, 1.1 Hz, 1H), 6.42 (d, *J* = 9.0 Hz, 1H), 6.23 (d, *J* = 12.8 Hz, 1H), 5.83 (d, *J* = 12.8 Hz, 1H), 4.00 (d, *J* = 10.9 Hz, 1H), 3.82 (s, 3H), 3.65 (d, *J* = 35.8 Hz, 1H), 3.50 (d, *J* = 30.5 Hz, 1H), 2.47 (d, *J* = 33.6 Hz, 1H), 2.05 (s, 3H), 1.91 (s, 1H), 1.06 (t, *J* = 7.0 Hz, 3H).

(3aS,9bR)-5-Acetyl-6-ethoxy-3a,4,5,9b-tetrahydro-3H-cyclopenta[c]quinoline-4-carboxylic acid (**53**)

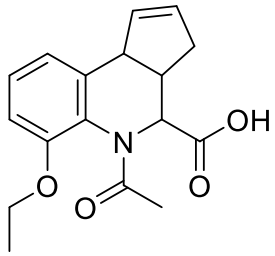

Following the general procedure C, the product was obtained as a yellow solid using an elution system of 75% EtOAc in petroleum ether (233.10 mg, 0.77 mmol, 67%). **R_f:** 0.15 (EtOAc). **^{1}H NMR** (700 MHz, DMSO-d_6) δ 12.41 (s, 1H), 7.13 (t, *J* = 7.9 Hz, 1H), 6.92 (dd, *J* = 8.4, 1.3 Hz, 1H), 6.86 (dd, *J* = 7.8, 1.2 Hz, 1H), 5.69 (dq, *J* = 4.8, 2.4 Hz, 1H), 5.51 (dq, *J* = 4.8, 2.3 Hz, 1H), 5.47 (d, *J* = 1.2 Hz, 1H), 4.10 (dq, *J* = 9.7, 7.0 Hz, 1H), 4.06 – 3.96 (m, 2H), 3.44 (tdd, *J* = 9.6, 5.0, 1.3 Hz, 1H), 2.74 (dddd, *J* = 17.2, 9.8, 4.2, 2.2 Hz, 1H), 2.30 (ddq, *J* = 17.2, 5.1, 2.5 Hz, 1H), 1.86 (s, 3H), 1.30 (t, *J* = 7.0 Hz, 3H). **^{13}C NMR** (176 MHz, DMSO-d_6) δ 152.90, 136.30, 133.60, 130.20, 127.90, 127.30, 120.80, 111.80, 64.40, 59.50, 47.70, 40.50, 38.80, 21.70, 15.10. **LC-MS** (**ESI**) (*m/z*) calculated for $C_{17}H_{19}NO_4$ $[M+H]^+$ = 302.1; found: 302.0.

4-((3aS,9bR)-5-Acetyl-6-ethoxy-3a,4,5,9b-tetrahydro-3H-cyclopenta[c]quinolin-4-yl)benzoic acid (**54**).

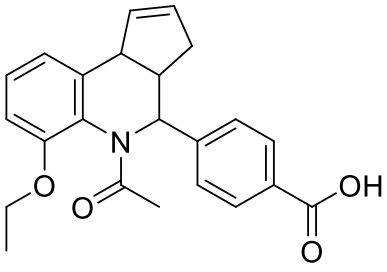

Following the general procedure C, the product was obtained as a yellow solid using an elution system of 50% EtOAc in petroleum ether which afforded the desired acid as a diastereomeric mixture (dr = 85:15) (135,88 mg, 0,36 mmol, 70%). $\mathbf{R_f}$ **=** 0.15 (petroleum ether / EtOAc = 1:1 and 0.1% AcOH). **^{1}H NMR** (600 MHz, DMSO-d_6) δ 12.82 (s, 1H), 7.65 – 7.61 (m, 2H), 7.20 (t, *J* = 8.0 Hz, 1H), 7.03 (dt, *J* = 7.8, 1.2 Hz, 1H), 7.00 – 6.95 (m, 2H), 6.89 (dt, *J* = 8.3, 1.2 Hz, 1H), 6.40 – 6.29 (m, 1H), 6.24 (d, *J* = 9.4 Hz, 1H), 5.78 (dt, *J* = 5.8, 2.2 Hz, 1H), 3.97 – 3.92 (m, 2H), 3.73 (dq, *J* = 9.9, 7.0 Hz, 1H), 3.52 (qd, *J* = 9.7, 6.7 Hz, 1H), 2.41 – 2.33 (m, 1H), 1.90 (s, 3H), 1.67 (ddq, *J* = 17.0, 7.2, 2.5 Hz, 1H), 1.05 (t, *J* = 6.9 Hz, 3H). **^{13}C NMR** (151 MHz, DMSO-d_6) δ 169.70, 167.50, 152.70, 144.50, 138.10, 132.50, 132.20, 129.70, 129.00, 128.60, 127.60, 126.90, 119.40, 111.70, 64.20, 54.90, 45.20, 41.80, 35.50, 22.10, 14.80.

3-((3aS,9bR)-5-Acetyl-6-ethoxy-3a,4,5,9b-tetrahydro-3H-cyclopenta[c]quinolin-4-yl)benzoic acid (**55**).

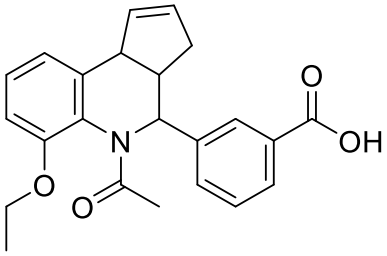

Following the general procedure C, the product was obtained as a yellow solid using an elution system of 50% EtOAc in petroleum ether which afforded the desired acid as a diastereomeric mixture (dr = 78:22) (144.37 mg, 0.38 mmol, 75%). $\mathbf{R_f}$ = 0.1 (petroleum ether / EtOAc = 1:1). **^{1}H NMR** (700 MHz, DMSO-d_6) δ 12.81 (s, 1H), 7.67 (dt, *J* = 7.7, 1.5 Hz, 1H), 7.60 (dt, *J* = 10.5, 1.9 Hz, 1H), 7.17 (dt, *J* = 20.5, 7.8 Hz, 2H), 7.01 (ddt, *J* = 17.1, 7.8, 1.4 Hz, 2H), 6.87 (dt, *J* = 8.3, 1.1 Hz, 1H), 6.34 (dq, *J* = 4.7, 2.3 Hz, 1H), 6.25 (d, *J* = 9.4 Hz, 1H), 5.79 (dq, *J* = 6.2, 2.2 Hz, 1H), 3.97 – 3.92 (m, 2H), 3.66 (dq, *J* = 9.8, 7.0 Hz, 1H), 3.53 (qd, *J* = 9.7, 6.8 Hz, 1H), 2.35 (ddq, *J* = 16.9, 9.6, 2.0 Hz, 1H), 1.99 (s, 3H), 1.68 (ddq, *J* = 17.0, 7.2, 2.5 Hz, 1H), 1.18 (t, *J* = 7.1 Hz, 3H). **^{13}C NMR** (176 MHz, DMSO-d_6) δ 170.80, 169.60, 167.60, 152.80, 140.00, 138.20, 132.40, 129.80, 128.00, 127.60, 126.90, 119.30, 111.70, 64.30, 60.20, 54.90, 45.20, 41.80, 35.60, 24.60, 22.10, 21.20, 14.60.

Methyl 3-((3aS,9bR)-6-(trifluoromethoxy)-3a,4,5,9b-tetrahydro-3H-cyclopenta[c]quinolin-4-yl)benzoate (**56**)

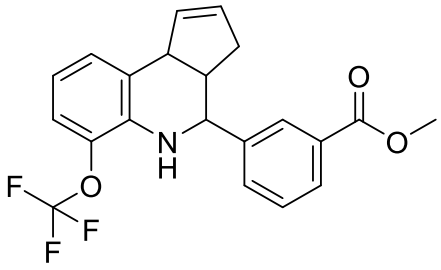

Following the general procedure A, the product was obtained as a pale grey solid using a silica gel flash chromatography elution system of 4% EtOAc in petroleum ether which afforded the product as diastereomeric mixture (dr = 94:6) (106.80 mg, 0.27 mmol, 54%). $\mathbf{R_f}$ = 0.65 (petroleum ether / EtOAc = 4:1) **^{1}H NMR** (400 MHz, Chloroform-*d*) δ 8.10 (tdt, *J* = 2.0, 1.4, 0.7 Hz, 1H), 8.00 (dq, *J* = 7.7, 1.4 Hz, 1H), 7.67 (dddd, *J* = 7.8, 2.0, 1.2, 0.6 Hz, 1H), 7.48 (td, *J* = 7.8,

1.1 Hz, 1H), 7.01 – 6.96 (m, 2H), 6.72 (td, *J* = 7.9, 1.1 Hz, 1H), 5.85 (dtt, *J* = 5.6, 2.7, 1.2 Hz, 1H), 5.67 (dh, *J* = 5.9, 1.4 Hz, 1H), 4.70 (d, *J* = 3.3 Hz, 1H), 4.18 – 4.10 (m, 1H), 3.94 (s, 3H), 3.07 – 2.97 (m, 1H), 2.66 – 2.53 (m, 1H), 1.77 (dddt, *J* = 16.5, 8.7, 2.8, 1.3 Hz, 1H).

3-((3aS,9bR)-6-(Trifluoromethoxy)-3a,4,5,9b-tetrahydro-3H-cyclopenta[c]quinolin-4-yl)benzoic acid (**57**).

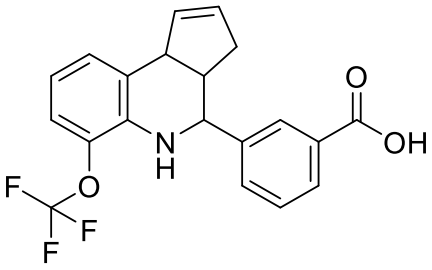

Following the general procedure C, the product was obtained as a gray solid elution system of 11% EtOAc in petroleum ether which afforded the product as diastereomeric mixture (dr = 95:5) (64.80 mg, 0.17 mmol, 77%). $\mathbf{R_f}$ = 0.2 (petroleum ether / EtOAc = 1:1). **^{1}H NMR** (700 MHz, DMSO-d_6) δ 12.95 (s, 1H), 8.03 (t, *J* = 1.8 Hz, 1H), 7.88 (dt, *J* = 7.7, 1.4 Hz, 1H), 7.68 (dt, *J* = 7.7, 1.5 Hz, 1H), 7.52 (t, *J* = 7.7 Hz, 1H), 7.06 (d, *J* = 7.7 Hz, 1H), 7.00 (dt, *J* = 8.2, 1.7 Hz, 1H), 6.70 (t, *J* = 7.9 Hz, 1H), 5.93 (dtd, *J* = 5.9, 2.9, 1.3 Hz, 1H), 5.61 (ddt, *J* = 5.8, 2.9, 1.3 Hz, 1H), 5.41 (s, 1H), 4.68 (d, *J* = 3.5 Hz, 1H), 4.10 (dd, *J* = 7.7, 2.5 Hz, 1H), 2.97 – 2.90 (m, 1H), 2.36 (ddq, *J* = 16.6, 9.8, 2.4 Hz, 1H), 1.60 (dddd, *J* = 16.1, 8.5, 2.7, 1.4 Hz, 1H). **^{13}C NMR** (176 MHz, DMSO-d_6) δ 167.90, 143.70, 138.70, 136.20, 134.80, 131.50, 131.20, 130.40, 128.90, 128.40, 128.10, 127.90, 118.60, 117.80, 56.10, 45.50, 45.30, 31.50.

3-((3aS,9bR)-6-Ethoxy-3a,4,5,9b-tetrahydro-3H-cyclopenta[c]quinolin-4-yl)-5-fluorobenzoic acid (**58**).

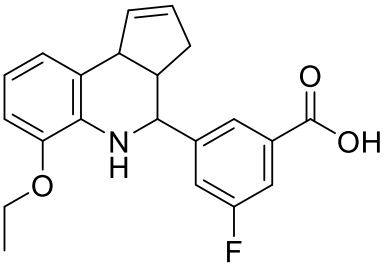

Following the general procedure A, the product was obtained as a greenish solid using a silica gel flash chromatography elution system of 4% EtOAc 0.1% AcOH in petroleum ether which afforded the product as diastereomeric mixture (dr = 97:3) (55.30 mg, 0.16 mmol, 40%). $\mathbf{R_f}$ = 0.3 (petroleum ether / EtOAc and 0.1% AcOH = 1:1). **^{1}H NMR** (700 MHz, DMSO-d_6) δ 13.16 (s, 1H), 7.90 (s, 1H), 7.64 – 7.50 (m, 2H), 6.66 (dp, *J* = 15.2, 8.5, 7.7 Hz, 3H), 5.88 (p, *J* = 2.9 Hz, 1H), 5.58 (d, *J* = 5.6 Hz, 1H), 4.65 – 4.58 (m, 2H), 4.06 (dq, *J* = 9.7, 6.9 Hz, 2H), 4.01 – 3.93 (m, 1H), 3.08 – 2.85 (m, 1H), 2.43 – 2.36 (m, 1H), 1.69 – 1.56 (m, 1H), 1.34 (t, *J* = 6.9 Hz, 3H). **^{13}C NMR** (176 MHz, DMSO-d_6) δ 166.80, 163.10, 161.70, 147.30, 146.60, 135.10, 133.60, 129.80, 126.00, 123.80, 121.00, 118.50, 118.30, 114.70, 108.70, 63.90, 56.50, 45.90, 45.30, 31.50, 15.20.

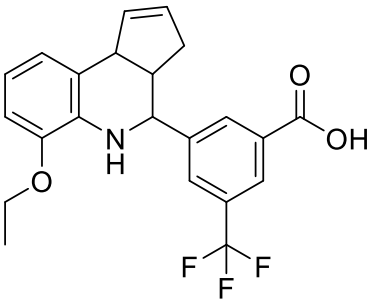

3-((3aS,9bR)-6-Ethoxy-3a,4,5,9b-tetrahydro-3H-cyclopenta[c]quinolin-4-yl)-5-(trifluoromethyl)benzoic acid (**59**).

Following the general procedure A, the product was obtained as a pale greenish solid using a silica gel flash chromatography elution system of 4% EtOAc 0.1% AcOH in petroleum ether which afforded the product as diastereomeric mixture (dr = 98:2) (74.10 mg, 0.18 mmol, 45%). $\mathbf{R_f}$ = 0.3 (petroleum ether / EtOAc and 0.1% AcOH = 1:1). **^{1}H NMR** (700 MHz, DMSO-d_6) δ 13.49 (s, 1H), 8.32 (d, *J* = 1.7 Hz, 1H), 8.11 (d, *J* = 1.7 Hz, 1H), 8.04 (d, *J* = 1.8 Hz, 1H), 6.70 – 6.61 (m, 3H), 5.90 (ddq, *J* = 5.8, 2.9, 1.4 Hz, 1H), 5.60 – 5.54 (m, 1H), 4.78 (s, 1H), 4.72 (d, *J* = 3.4 Hz, 1H), 4.10 – 4.03 (m, 2H), 3.98 (dq, *J* = 9.7, 7.0 Hz, 1H), 2.97 (qdd, *J* = 8.7, 3.6, 1.8 Hz, 1H), 2.43 – 2.35 (m, 1H), 1.60 (ddt, *J* = 15.8, 8.8, 2.2 Hz, 1H), 1.33 (t, *J* = 6.9 Hz, 3H). **^{13}C NMR** (176 MHz, DMSO-d_6) δ 166.60, 146.70, 146.30, 135.10, 135.00, 132.50, 131.60, 129.80, 127.90, 125.90, 124.70, 121.10, 118.50, 108.80, 63.90, 56.40, 45.80, 45.20, 31.40, 15.20.

5-((3aS,9bR)-6-Ethoxy-3a,4,5,9b-tetrahydro-3H-cyclopenta[c]quinolin-4-yl)furan-2-carboxylic acid (**60**).

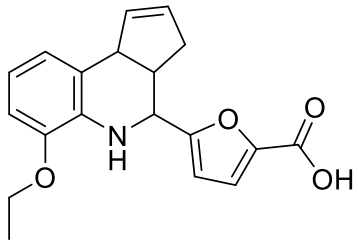

Following the general procedure A, the product was obtained as a yellow solid using a silica gel flash chromatography elution system of 10% EtOAc +0.1% AcOH in petroleum ether which afforded the product as diastereomeric mixture (dr = 24:1) (78.70 mg, 0.24 mmol, 48%). $\mathbf{R_f}$ = 0.15 (petroleum ether / EtOAc = 1:1 +0.1% AcOH). **^{1}H NMR** (700 MHz, DMSO-d_6) δ 12.98 (s, 1H), 7.20 (d, *J* = 3.5 Hz, 1H), 6.72 – 6.62 (m, 3H), 6.53 (dd, *J* = 3.4, 0.9 Hz, 1H), 5.83 (dtd, *J* = 5.7, 2.8, 1.6 Hz, 1H), 5.62 – 5.58 (m, 1H), 4.65 (s, 1H), 4.56 (d, *J* = 3.4 Hz, 1H), 4.02 (ddtd, *J* = 33.3, 14.0, 7.0, 3.2 Hz, 3H), 3.11 (qdd, *J* = 8.9, 3.5, 1.8 Hz, 1H), 2.46 (ddq, *J* = 16.2, 8.8, 2.4 Hz, 1H), 2.08 (ddt, *J* = 16.3, 8.9, 2.2 Hz, 1H), 1.35 (t, *J* = 6.9 Hz, 3H). **^{13}C NMR** (176 MHz, DMSO-d_6) δ 160.40, 159.80, 146.50, 144.20, 135.00, 134.40, 129.80, 126.10, 121.10, 119.10, 118.70, 108.80, 108.50, 63.90, 52.00, 45.60, 42.20, 32.60, 15.20.

5-((3aS,9bR)-6-Ethoxy-3a,4,5,9b-tetrahydro-3H-cyclopenta[c]quinolin-4-yl)thiophene-2-carboxylic acid (**61**).

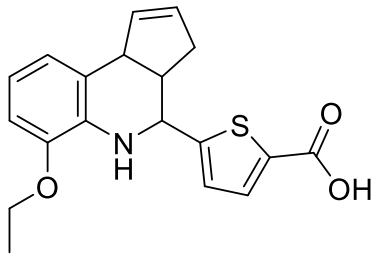

Following the general procedure A, the product was obtained as a yellow solid using a silica gel flash chromatography elution system of 10% EtOAc +0.1% AcOH in petroleum ether which afforded the product as diastereomeric mixture (dr = 24:1) (126.30 mg, 0.39 mmol, 78%). $\mathbf{R_f}$ = 0.25 (petroleum ether / EtOAc = 1:1 +0.1% AcOH). **^{1}H NMR** (600 MHz, DMSO-d_6) δ 12.43 (s, 1H), 7.66 (d, *J* = 3.8 Hz, 1H), 7.19 (dd, *J* = 3.8, 0.8 Hz, 1H), 6.70 – 6.63 (m, 3H), 5.88 (dtd, *J* = 5.8, 2.8, 1.5 Hz, 1H),

5.64 – 5.53 (m, 1H), 4.83 (d, *J* = 3.5 Hz, 1H), 4.67 (s, 1H), 4.04 (dq, *J* = 9.6, 7.0 Hz, 2H), 3.97 (dq, *J* = 9.6, 6.9 Hz, 1H), 2.99 (qdd, *J* = 8.9, 3.5, 1.8 Hz, 1H), 1.91 (s, 2H), 1.33 (t, *J* = 7.0 Hz, 3H). **^{13}C NMR** (151 MHz, DMSO-d_6) δ 172.50, 163.40, 154.70, 146.50, 135.00, 134.40, 133.50, 132.80, 129.80, 125.30, 121.00, 118.90, 108.80, 63.90, 53.90, 45.60, 32.30, 21.50, 15.20.

Methyl 5-((3aS,9bR)-6-ethoxy-3a,4,5,9b-tetrahydro-3H-cyclopenta[c]quinolin-4-yl)-1H-pyrrole-2-carboxylate (**62**)

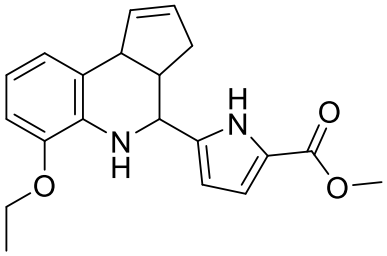

Following the general procedure A, the product was obtained as a yellow solid using an elution system of 4% EtOAc in petroleum ether which afforded the product as diastereomeric mixture (dr = 96:4) (64.80 mg, 0.17 mmol, 77%). **R_f** = 0.3 (petroleum ether / EtOAc = 4:1). **^{1}H NMR** (600 MHz, DMSO-d_6) δ 11.91 (s, 1H), 6.77 (dd, *J* = 3.7, 2.4 Hz, 1H), 6.66 (s, 3H), 6.18 – 6.14 (m, 1H), 5.80 (d, *J* = 12.9 Hz, 1H), 5.58 (d, *J* = 12.7 Hz, 1H), 4.52 (d, *J* = 3.3 Hz, 1H), 4.40 (s, 1H), 3.99 (d, *J* = 60.7 Hz, 3H), 3.75 (s, 3H), 3.10 – 3.02 (m, 1H), 2.89 (s, 1H), 2.73 (d, *J* = 0.7 Hz, 1H), 1.90 (d, *J* = 29.6 Hz, 1H), 1.32 (t, *J* = 6.9 Hz, 3H). **^{13}C NMR** (151 MHz, DMSO-d_6) δ 161.29, 146.36, 140.30, 134.99, 130.05, 126.22, 121.42, 121.05, 118.40, 115.91, 108.61, 107.01, 63.84, 51.70, 51.43, 45.94, 43.61, 40.52, 32.41, 15.19.

5-((3aS,9bR)-6-Ethoxy-3a,4,5,9b-tetrahydro-3H-cyclopenta[c]quinolin-4-yl)-1H-pyrrole-2-carboxylic acid (**63**).

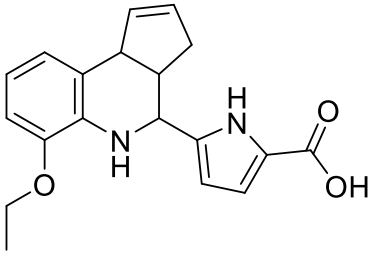

Following the general procedure C, the product was obtained as a yellow solid using an elution system of 11% EtOAc in petroleum ether which afforded the product as diastereomeric mixture (dr = 24:1) (32.10 mg, 0,09 mmol, 41%). **R_f** = 0.2 (petroleum ether / EtOAc = 1:1). **^{1}H NMR** (600 MHz, DMSO-d_6) δ 12.14 (s, 1H), 11.74 (t, *J* = 2.4 Hz, 1H), 6.71 (dd, *J* = 3.7, 2.4 Hz, 1H), 6.68 – 6.56 (m, 3H), 6.15 – 6.11 (m, 1H), 5.80 (dtd, *J* = 5.7, 2.8, 1.5 Hz, 1H), 5.62 – 5.53 (m, 1H), 4.51 (d, *J* = 3.2 Hz, 1H), 4.38 (d, *J* = 1.9 Hz, 1H), 4.09 – 3.89 (m, 3H), 3.06 (qdd, *J* = 9.0, 3.4, 1.9 Hz, 1H), 1.98 – 1.88 (m, 1H), 1.32 (t, *J* = 6.9 Hz, 3H). **^{13}C NMR** (151 MHz, DMSO-d_6) δ 162.40, 146.40, 139.60, 135.20, 135.00, 130.10, 126.20, 122.50, 121.10, 118.40, 115.50, 108.60, 106.70, 63.80, 51.70, 46.00, 43.60, 32.40, 15.20.

5.2.1.2 Pyrrolinones

General Procedure D (Butanoate synthesis)

Butanoates (**65**, **I-VI**) (1 equiv.) followed by diethyl oxalate (1 equiv.) were added to a solution of sodium ethoxide (1.0 M, 1.1 equiv.) in EtOH (3.5 mL) at 0°C. The resulting suspension was warmed to room temperature and subsequently stirred overnight, at room temperature. After completion of the

reaction, the mixture was added to ice water and acidified by the addition of 1 M HCl. The aqueous solution was extracted with dichloromethane (3 × 15 mL), washed with water and brine, dried over anhydrous $MgSO_4$, and evaporated under reduced pressure. The resulting residue was then purified by using flash column chromatography using appropriate gradients to afford the desired butanoates.[274]

General Procedure E (Doebner Condensation)

Benzaldehyde (1 equiv.) followed by aniline (1 equiv.) were added to a suspension (0.06 M) of the corresponding dioxobutanoates (1 equiv.) in acetic acid. The reaction mixture was stirred, overnight at 90°C. After the mixture was cooled to room temperature, it was diluted with Et_2O. The resulting residue was washed with additional Et_2O and then dried under reduced pressure to give the desired pyrrolinone derivative. In the case that precipitation did not yield a pure product, the precipitate was further purified with an appropriate gradient on a preparative HPLC system.[275]

Ethyl-4-(4-fluorophenyl)-2,4-dioxobutanoate (**65**).

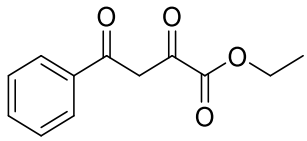

Ethyl 2,4-dioxo-4-phenylbutanoate (200.00 µL, 1.71 mmol 1.00 equiv.) was used according to the general procedure D (petroleum ether / ethyl acetate = 5:1) (460.20 mg, 37%) **^{1}H NMR** (600 MHz, Chloroform-*d*) δ 15.30 (s, 1H), 8.05 – 7.96 (m, 2H), 7.61 (ddt, *J* = 8.7, 7.0, 1.3 Hz, 1H), 7.53 – 7.48 (m, 2H), 7.08 (s, 1H), 4.40 (q, *J* = 7.2 Hz, 2H), 1.42 (t, *J* = 7.2 Hz, 3H). **^{13}C NMR** (151 MHz, Chloroform-*d*) δ 190.76, 169.81, 162.23, 133.81, 128.92, 127.91, 97.97, 62.64, 14.11. **LC-MS** (**ESI**) (*m/z*) calculated for $C_{12}H_{12}O_4$ $[M+H]^+$ = 221.1; found:221.0.

Ethyl-4-(4-fluorophenyl)-2,4-dioxobutanoate (**I**).

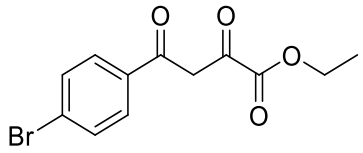

4-Bromo-acetophenone (403.09 mg, 3.33mmol 1.00 equiv.) was used according to the general procedure D and was used without further purification (460.20 mg, 37%). **^{1}H NMR** (600 MHz, Chloroform-*d*) δ 15.41 (s, 1H), 8.12 – 8.05 (m, 2H), 7.91 – 7.83 (m, 2H), 7.26 (s, 1H), 4.63 (q, *J* = 7.1 Hz, 2H), 1.64 (t, *J* = 7.1 Hz, 3H). **^{13}C NMR** (151 MHz, Chloroform-*d*) δ 189.70, 170.34, 162.25, 133.94, 132.48, 129.52, 97.95, 62.95, 14.31. **LC-MS** (**ESI**) (*m/z*) calculated for $C_{12}H_{11}BrO_4$ $[M+H]^+$ = 299.0; found: 299.0.

Ethyl-4-(furan-2-yl)-2,4-dioxobutanoate (**II**).

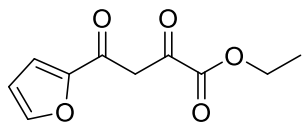

2-Acetylfuran (111.31 µL, 1.11 mmol, 1.00 equiv.) was used according to the general procedure D and purified by flash column chromatography to yield the desired product as a white powder (151.00 mg, 65%). **^{1}H NMR** (600 MHz, Chloroform-*d*) δ 14.41 (s, 1H), 7.60 (dd, *J* = 1.7, 0.7 Hz, 1H), 7.26 (dd, *J* = 3.6, 0.8 Hz, 1H), 6.86 (s, 1H), 6.54 (dd, *J* = 3.6, 1.7 Hz, 1H), 4.31 (q, *J* = 7.1 Hz, 2H), 1.32 (t, *J* = 7.2 Hz, 3H). **^{13}C NMR** (151 MHz, Chloroform-*d*) δ 181.24, 162.21, 151.12, 147.88, 118.68, 113.34, 99.21, 62.79, 14.29. **LC-MS** (**ESI**) (*m/z*) calculated for $C_{10}H_{10}O_5$ $[M+H]^+$ = 211.1; found:211.1.

Ethyl-4-(4-methoxyphenyl)-2,4-dioxobutanoate (**III**).

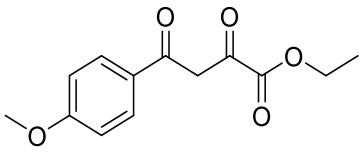

4-Methoxy-Acetophenone (500.00 mg, 3.33 mmol, 1.00 equiv.) was used according to the general procedure D and purified by flash column chromatography to yield the desired product as a white powder (318.00 mg, 21%). **^{1}H NMR** (600 MHz, Chloroform-*d*) δ 15.39 (s, 1H), 7.95 – 7.89 (m, 2H), 6.96 (s, 1H), 6.94 – 6.89 (m, 2H), 4.33 (q, *J* = 7.1 Hz, 2H), 3.83 (s, 3H), 1.34 (t, *J* = 7.1 Hz, 3H). **^{13}C NMR** (151 MHz, Chloroform-*d*) δ 190.37, 168.11, 164.34, 162.50, 130.33, 127.75, 114.24, 97.76, 62.52, 55.61, 14.13. **LC-MS** (**ESI**) (*m/z*) calculated for $C_{13}H_{14}O_5$ $[M+H]^+$ = 251.1; found:251.0.

Ethyl-4-(4-fluorophenyl)-2,4-dioxobutanoate (**IV**).

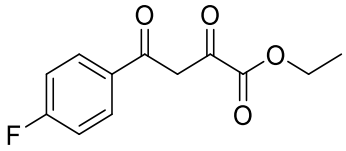

4-Fluoro-acetophenone (403.09 mg, 3.33mmol 1.00 equiv.) was used according to the general procedure D and was used without further purification (460.20 mg, 37%). **^{1}H NMR** (500 MHz, Chloroform-*d*) δ 15.16 (s, 1H), 8.00 – 7.94 (m, 2H), 7.15 – 7.09 (m, 2H), 6.96 (s, 1H), 4.33 (q, *J* = 7.1 Hz, 2H), 1.35 (t, *J* = 7.1 Hz, 3H). **^{13}C NMR** (126 MHz, Chloroform-*d*) δ 189.74, 169.20, 167.25, 165.21, 162.15, 130.59 (d, *J* = 9.5 Hz), 116.18 (d, *J* = 21.9 Hz), 97.83, 63.16, 62.69, 14.10, 13.94. **LC-MS** (**ESI**) (*m/z*) calculated for $C_{12}H_{11}FO_4$ $[M+H]^+$ = 239.1; found: 239.3.

Ethyl-4-(5-methylfuran-2-yl)-2,4-dioxobutanoate (**V**).

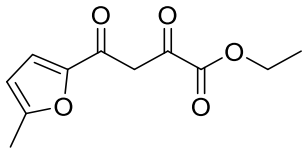

5-Methyl-2-acetylfuran (387.06 µl, 3.33mmol, 1.00 equiv.) according to the general procedure D and was used without further purification (672.20 mg, 72%). **^{1}H NMR** (600 MHz, Chloroform-*d*) δ 14.51 (s, 1H), 6.80 (s, 1H), 6.18 (dd, *J* = 3.5, 1.0 Hz, 1H), 4.32 (q, *J* = 7.1 Hz, 2H), 2.37 (s, 3H), 2.32 (s, 1H), 1.33 (t, *J* = 7.1 Hz, 3H). **^{13}C NMR** (151 MHz, Chloroform-*d*) δ 179.59, 161.21, 158.52, 148.66, 119.61, 109.09, 107.90, 98.05, 61.47, 24.65, 13.08. **LC-MS** (**ESI**) (*m/z*) calculated for $C_{11}H_{12}O_5$ $[M+H]^+$ = 225.0; found: 224.8.

Ethyl-4-(2-fluorophenyl)-2,4-dioxobutanoate (**VI**).

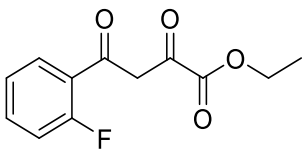

2-Fluoroacetophenone (404.58 µl, 3.33mmol 1.00 equiv.) according to the general procedure D and was used without further purification (669.60 mg, 59%) **^{1}H NMR** (600 MHz, Chloroform-*d*) δ 15.04 (s, 1H), 7.89 (td, *J* = 7.7, 1.9 Hz, 1H), 7.52 – 7.45 (m, 1H), 7.23 – 7.20 (m, 1H), 7.11 (ddd, *J* = 11.5, 8.4, 1.1 Hz, 1H), 7.05 (d, *J* = 1.4 Hz, 1H), 4.33 (q, *J* = 7.1 Hz, 2H), 1.34 (t, *J* = 7.1 Hz, 3H). **^{13}C NMR** (151 MHz, Chloroform-*d*) δ 187.55, 187.53, 170.15, 162.52, 162.02, 160.81, 135.17, 135.10, 130.50, 130.49, 124.74, 124.72, 116.90 (d, *J* = 23.3 Hz), 102.33 (d, *J* = 13.0 Hz), 62.65, 14.08. **LC-MS** (**ESI**) (*m/z*) calculated for $C_{12}H_{11}FO_4$ $[M+H]^+$ = 239.1; found: 239.2.

1-([1,1'-Biphenyl]-3-yl)-4-benzoyl-3-hydroxy-5-(4-nitrophenyl)-1,5-dihydro-2H-pyrrol-2-one (**66**).

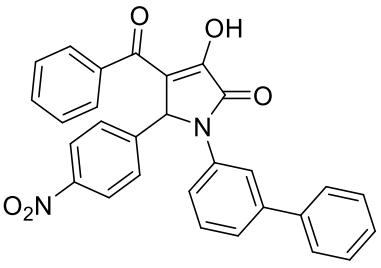

4-Nitrobenzaldehyde (44.65 mg, 0.30 mmol, 1.00 equiv.) followed by the 3-Aminobiphenyl (50.00 mg, 0.30 mmol, 1.00 equiv.) were added to a suspension (6.0 mL, 0.06 M) of Ethyl 2,4-dioxo-4-phenylbutanoate (65.07 mg, 0.30 mmol, 1.00 equiv.) in acetic acid following the general procedure E to give the desired product as a yellow solid (38.6 mg, 24%). **^{1}H NMR** (700 MHz, DMSO-d_6) δ 8.08 – 8.05 (m, 2H), 7.96 (t, *J* = 1.9 Hz, 1H), 7.82 – 7.79 (m, 2H), 7.75 – 7.73 (m, 2H), 7.66 (dt, *J* = 7.4, 1.9 Hz, 1H), 7.65 – 7.62 (m, 2H), 7.50 – 7.45 (m, 5H), 7.44 – 7.40 (m, 3H), 6.68 (s, 1H). **^{13}C NMR** (176 MHz, DMSO-d_6) δ 189.53, 165.21, 147.64, 145.17, 141.28, 139.77, 138.34, 137.12, 133.22, 129.94, 129.74, 129.50, 129.46, 129.22, 128.67, 128.29, 128.01, 127.22, 127.11, 127.04, 126.96, 124.44, 123.96, 122.17, 121.21, 119.76, 60.83. **HRMS**-ESI (*m/z*) calculated for $C_{29}H_{21}N_2O_5$ $[M+H]^+$ 477.1445; found, 477.1447.

1-([1,1'-Biphenyl]-3-yl)-4-(4-bromobenzoyl)-3-hydroxy-5-(4-nitrophenyl)-1,5-dihydro-2H-pyrrol-2-one (**73**):

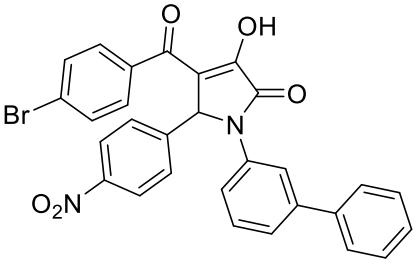

4-Nitrobenzaldehyde (44.65 mg, 0.30 mmol, 1.00 equiv.) followed by the 3-Aminobiphenyl (50.00 mg, 0.30 mmol, 1.00 equiv.) were added to a suspension (6.0 mL, 0.06 M) of Ethyl 4-(4-bromophenyl)-2,4-dioxobutanoate (88.38 mg, 0.30 mmol, 1.00 equiv.) in acetic acid following the general procedure E to give the desired product as a yellow solid (40.4 mg, 22%). **^{1}H NMR** (600 MHz, DMSO-d_6) δ 8.94 (s, 1H), 8.04 (d, *J* = 8.9 Hz, 2H), 7.98 (s, 1H), 7.88 (d, *J* = 8.5 Hz, 2H), 7.83 (d, *J* = 8.5 Hz, 2H), 7.66 (d, *J* = 8.9 Hz, 2H), 7.65 – 7.59 (m, 2H), 7.47 (t, *J* = 7.7 Hz, 2H), 7.38 (d, *J* = 7.4 Hz, 2H), 7.35 (d, *J* = 7.3 Hz, 2H), 6.25 (s, 1H). **^{13}C NMR** (176 MHz, DMSO-d_6) δ 189.51, 165.06, 147.66, 145.12, 141.29, 139.75, 137.44, 137.06, 132.70, 132.29, 131.76, 131.17, 130.38, 129.95, 129.92, 129.76, 129.50, 129.46, 128.30, 127.22, 127.11, 126.96, 124.50, 123.95, 122.19, 121.22, 60.73. **HRMS**-ESI (*m/z*) calculated for $C_{29}H_{20}N_2O_5Br$ $[M+H]^+$ 555.0550; found, 555.0553.

1-([1,1'-Biphenyl]-3-yl)-3-hydroxy-4-(4-methoxybenzoyl)-5-(4-nitrophenyl)-1,5-dihydro-2H-pyrrol-2-one (**74**).

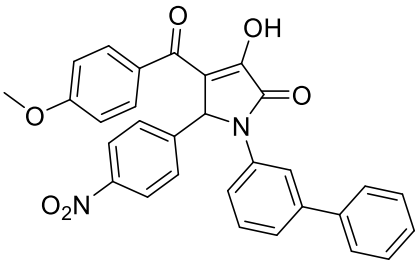

4-Nitrobenzaldehyde (44.65 mg, 0.30 mmol, 1.00 equiv.) followed by the 3-Aminobiphenyl (50.00 mg, 0.30 mmol, 1.00 equiv.) were added to a suspension (5 mL, 0.06 M) of Ethyl-4-(4-methoxyphenyl)-2,4-dioxobutanoate (**95d**) (123.23 mg, 0.30 mmol, 1.00 equiv.) in acetic acid following the general procedure E to give the desired product as a yellow solid (50.7 mg, 30%). **^{1}H NMR** (700 MHz, DMSO-d_6) δ 12.04 (s, 1H), 8.03 (d, *J* = 8.4 Hz, 2H), 7.96 (s, 1H), 7.80 (d, *J* = 8.3

Hz, 2H), 7.74 (d, *J* = 8.4 Hz, 2H), 7.68 – 7.64 (m, 1H), 7.61 (d, *J* = 7.6 Hz, 2H), 7.46 (t, *J* = 7.6 Hz, 2H), 7.42 – 7.34 (m, 3H), 6.94 (d, *J* = 8.4 Hz, 2H), 6.55 (s, 1H), 3.81 (s, 3H). **^{13}C NMR** (176 MHz, DMSO-d_6) δ 186.87, 166.69, 162.93, 147.31, 146.81, 141.18, 139.90, 137.63, 131.67, 129.95, 129.85, 129.55, 129.43, 128.21, 127.19, 126.96, 124.02, 123.74, 121.80, 120.92, 114.28, 113.59, 60.86, 55.87. **HRMS**-ESI (*m/z*) calculated for $C_{30}H_{23}N_2O_6$ $[M+H]^+$ 507.1551; found, 507.1557.

1-([1,1'-Biphenyl]-3-yl)-4-(4-fluorobenzoyl)-3-hydroxy-5-(4-nitrophenyl)-1,5-dihydro-2H-pyrrol-2-one (**75**):

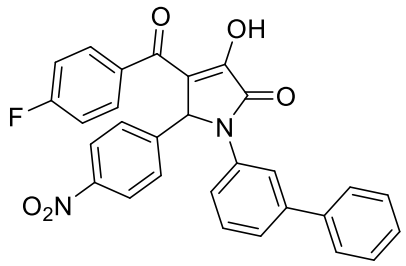

4-Nitrobenzaldehyde (44.65 mg, 0.30 mmol, 1.00 equiv.) followed by the 3-Aminobiphenyl (50.00 mg, 0.30 mmol, 1.00 equiv.) were added to a suspension (5 mL, 0.06 M) of Ethyl-4-(4-fluorophenyl)-2,4-dioxobutanoate (**95h**) (125.19 mg, 0.30 mmol, 1.00 equiv.) in acetic acid following the general procedure E to give the desired product as a yellow solid (84.4 mg, 58%). **^{1}H NMR** (700 MHz, DMSO-d_6) δ 7.99 (s, 2H), 7.90 (s, 2H), 7.61 (dd, *J* = 23.3, 10.4 Hz, 6H), 7.46 (t, *J* = 7.6 Hz, 3H), 7.37 (t, *J* = 7.0 Hz, 3H), 7.10 (t, *J* = 8.3 Hz, 2H), 6.36 (s, 1H). **^{13}C NMR** (176 MHz, DMSO-d_6) δ 183.83, 170.33, 164.33, 162.94, 162.77, 150.17, 146.69, 141.09, 140.06, 138.27, 137.51, 131.62, 129.75, 129.42, 129.22, 128.16, 127.18, 123.67, 123.33, 121.25, 120.51, 115.45, 114.35, 114.22, 60.85. **HRMS**-ESI (*m/z*) calculated for $C_{29}H_{20}N_2O_5F$ $[M+H]^+$ 495.1351; found, 495.1354.

1-([1,1'-Biphenyl]-3-yl)-4-(2-fluorobenzoyl)-3-hydroxy-5-(4-nitrophenyl)-1,5-dihydro-2H-pyrrol-2-one (**76**):

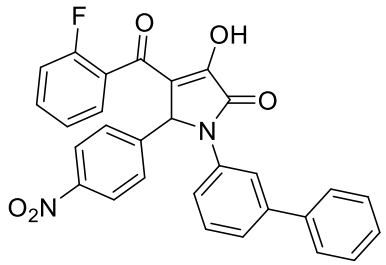

4-Nitrobenzaldehyde (44.65 mg, 0.30 mmol, 1.00 equiv.) followed by the 3-Aminobiphenyl (50.00 mg, 0.30 mmol, 1.00 equiv.) were added to a suspension (5 mL, 0.06 M) of Ethyl-4-(2-fluorophenyl)-2,4-dioxobutanoate (**95o**) (87.98 mg, 0.30 mmol, 1.00 equiv.) in acetic acid following the general procedure E to give the desired product as a yellow solid (70.8 mg, 48%). **^{1}H NMR** (700 MHz, DMSO-d_6) δ 8.13 – 8.08 (m, 2H), 7.95 (t, *J* = 2.0 Hz, 1H), 7.77 – 7.74 (m, 2H), 7.65 – 7.62 (m, 3H), 7.55 (dddd, *J* = 8.5, 7.1, 5.2, 1.8 Hz, 1H), 7.49 – 7.46 (m, 2H), 7.46 – 7.42 (m, 3H), 7.42 – 7.37 (m, 2H), 7.28 – 7.23 (m, 2H), 6.65 (s, 1H). **^{13}C NMR** (176 MHz, DMSO-d_6) δ 164.93, 160.55, 159.13, 147.64, 145.25, 141.30, 139.72, 136.94, 133.64, 130.75, 130.07, 129.96, 129.75, 129.46, 128.64, 128.30, 127.22, 127.12, 124.87, 124.63, 123.93, 122.28, 121.35, 119.99, 116.35, 116.23, 60.36. **HRMS**-ESI (*m/z*) calculated for $C_{29}H_{20}N_2O_5F$ $[M+H]^+$ 495.1351; found, 495.1355.

1-([1,1'-Biphenyl]-3-yl)-4-(furan-2-carbonyl)-3-hydroxy-5-(4-nitrophenyl)-1,5-dihydro-2H-pyrrol-2-one (**78**):

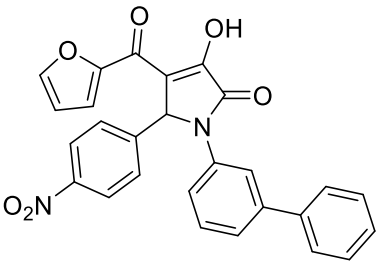

4-Nitrobenzaldehyde (44.65 mg, 0.30 mmol, 1.00 equiv.) followed by the 3-Aminobiphenyl (50.00 mg, 0.30 mmol, 1.00 equiv.) were added to a suspension (5 mL, 0.06 M) of Ethyl-4-(furan-2-yl)-2,4-dioxobutanoate (**95c**) (77.63 mg, 0.30 mmol, 1.00 equiv.) in acetic acid following the general procedure E to give the desired product as a yellow solid (77.9 mg, 50%). **^{1}H NMR** (700 MHz, DMSO-d_6) δ 8.07 – 8.03 (m, 2H), 7.97 (dd, *J* = 1.7, 0.7 Hz, 1H), 7.94 (t, *J* = 2.0 Hz, 1H), 7.74 – 7.70 (m, 2H), 7.67 – 7.66 (m, 1H), 7.66 – 7.63 (m, 2H), 7.62 (t, *J* = 1.1 Hz, 1H), 7.50 – 7.46 (m, 3H), 7.43 – 7.37 (m, 3H), 6.72 (dd, *J* = 3.6, 1.7 Hz, 1H), 6.67 (s, 1H). **^{13}C NMR** (176 MHz, DMSO-d_6) δ 174.69, 165.04, 151.99, 150.59, 148.52, 147.64, 145.05, 141.28, 139.74, 137.01, 129.93, 129.73, 129.44, 128.28, 127.22, 127.10, 127.04, 124.47, 123.94, 122.22, 121.25, 120.98, 119.42, 112.92, 60.66. **HRMS**-ESI (*m/z*) calculated for $C_{27}H_{18}N_2O_6$ $[M+H]^+$ 467.1165; found, 467.1241.

1-([1,1'-Biphenyl]-3-yl)-3-hydroxy-4-(5-methylfuran-2-carbonyl)-5-(4-nitrophenyl)-1,5-dihydro-2H-pyrrol-2-one (**79**):

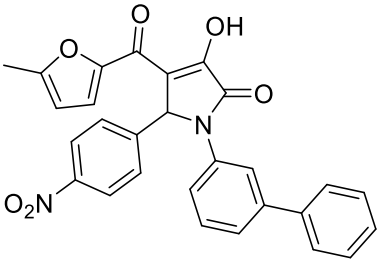

4-Nitrobenzaldehyde (44.65 mg, 0.30 mmol, 1.00 equiv.) followed by 3-Aminobiphenyl (50.00 mg, 0.30 mmol, 1.00 equiv.) were added to a suspension (5 mL, 0.06 M) of Ethyl-4-(5-methylfuran-2-yl)-2,4-dioxobutanoate (**95m**) (82.81 mg, 0.30 mmol, 1.00 equiv.) in acetic acid following the general procedure E to give the desired product as a yellow solid (46.7 mg, 33%). **^{1}H NMR** (700 MHz, DMSO-d_6) δ 8.05 (d, *J* = 8.9 Hz, 2H), 7.94 (t, *J* = 2.0 Hz, 1H), 7.70 (d, *J* = 8.9 Hz, 2H), 7.65 – 7.62 (m, 3H), 7.60 (d, *J* = 3.5 Hz, 1H), 7.47 (t, *J* = 7.7 Hz, 3H), 7.42 (t, *J* = 1.6 Hz, 1H), 7.40 – 7.38 (m, 2H), 6.66 (s, 1H), 6.37 (dd, *J* = 3.5, 1.1 Hz, 1H), 2.33 (s, 3H). **^{13}C NMR** (176 MHz, DMSO-d_6) δ 173.84, 165.13, 158.79, 150.94, 147.62, 145.08, 141.26, 139.75, 137.06, 129.92, 129.72, 129.49, 129.47, 129.44, 129.29, 128.28, 127.21, 127.10, 126.98, 124.40, 123.92, 123.08, 122.19, 121.22, 60.69, 14.10. **HRMS**-ESI (*m/z*) calculated for $C_{28}H_{20}N_2O_6$ $[M+H]^+$ 481.1321; found, 481.1398.

4-Benzoyl-1-(dibenzo[b,d]furan-3-yl)-3-hydroxy-5-(4-nitrophenyl)-1,5-dihydro-2H-pyrrol-2-one (**88**):

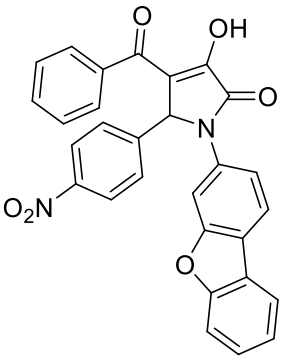

4-Nitrobenzaldehyde (34.30 mg, 0.23 mmol, 1.00 equiv.) followed by the dibenzo[*b*,*d*]furan-3-amine (41.60 mg, 0.23 mmol, 1.00 equiv.) were added to a suspension (3 mL, 0.06 M) of ethyl 3-oxo-3-phenylpropanoate (50.00 mg, 0.23 mmol, 1.00 equiv.) in acetic acid following the general procedure E to give the desired product as a pale yellow solid (30.10 mg, 0.06 mmol, 27%).

^{1}H NMR (700 MHz, DMSO-d_6) δ 11.66 (d, *J* = 421.9 Hz, 1H), 8.10 – 8.01 (m, 5H), 7.82 (d, *J* = 8.9 Hz, 2H), 7.75 (d, *J* = 6.8 Hz, 2H), 7.72 (dd, *J* = 8.3,

1.9 Hz, 1H), 7.67 (d, *J* = 8.2 Hz, 1H), 7.59 (d, *J* = 17.6 Hz, 1H), 7.48 (dt, *J* = 13.5, 7.5 Hz, 3H), 7.38 (t, *J* = 7.5 Hz, 1H), 6.68 (s, 1H). **^{13}C NMR** (176 MHz, DMSO-d_6) δ 189.56, 165.18, 156.34, 155.77, 147.62, 144.97, 138.31, 135.95, 133.27, 130.24, 129.77, 129.23, 128.68, 128.00, 124.57, 123.92, 123.80, 123.51, 121.65, 121.50, 121.47, 119.80, 118.46, 112.06, 106.53, 104.67, 61.23. **HRMS**-ESI (*m/z*) calculated for $C_{29}H_{19}N_2O_6$ $[M+H]^+$ 490.1165; found, 491.1243.

4-(4-Bromobenzoyl)-1-(dibenzo[b,d]furan-3-yl)-3-hydroxy-5-(4-nitrophenyl)-1,5-dihydro-2H-pyrrol-2-one (**89**):

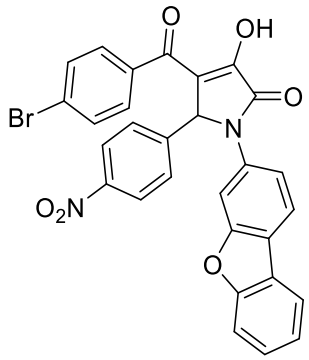

4-Nitrobenzaldehyde (25.30 mg, 0.17 mmol, 1.00 equiv.) followed by the dibenzo[*b,d*]furan-3-amine (30.60 mg, 0.17 mmol, 1.00 equiv.) were added to a suspension (3 mL, 0.06 M) of ethyl 3-(4-bromophenyl)-3-oxopropanoate (50.00 mg, 0.17 mmol, 1.00 equiv.) in acetic acid following the general procedure E to give the desired product as a yellow solid (24.70 mg, 0.04 mmol, 26%). **^{1}H NMR** (600 MHz, DMSO-d_6) δ 12.49 (s, 1H), 8.10 – 8.02 (m, 5H), 7.84 – 7.80 (m, 2H), 7.73 – 7.64 (m, 6H), 7.49 (ddd, *J* = 8.4, 7.2, 1.4 Hz, 1H), 7.38 (td, *J* = 7.5, 0.9 Hz, 1H), 6.66 (s, 1H). **^{13}C NMR** (176 MHz, DMSO-d_6) δ 188.50, 165.06, 156.35, 155.76, 152.04, 147.64, 144.94, 137.42, 135.89, 131.77, 131.19, 129.80, 128.01, 127.15, 123.91, 123.81, 123.50, 121.66, 121.52, 119.32, 118.48, 112.07, 106.55, 61.13. **HRMS**-ESI (*m/z*) calculated for $C_{29}H_{18}N_2O_6Br$ $[M+H]^+$ 569.0270; found, 569.0350.

1-(Dibenzo[b,d]furan-3-yl)-3-hydroxy-4-(4-methoxybenzoyl)-5-(4-nitrophenyl)-1,5-dihydro-2H-pyrrol-2-one (**90**):

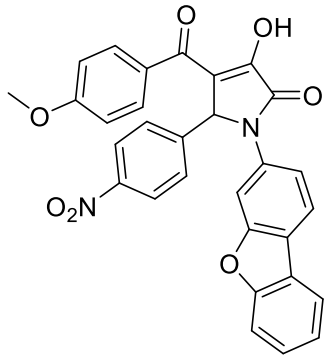

4-Nitrobenzaldehyde (30.2 mg, 0.2 mmol, 1.0 equiv.) followed by the dibenzo[*b,d*]furan-3-amine (36.6 mg, 0.2 mmol, 1.0 equiv.) were added to a suspension (3 mL, 0.06 M) of ethyl 3-(4-methoxyphenyl)-3-oxopropanoate (**95d**) (50.0 mg, 0.2 mmol, 1.0 equiv.) in acetic acid following the general procedure E to give the desired product as a yellow solid (33.30 mg, 0.06 mmol, 32%). **^{1}H NMR** (700 MHz, DMSO-d_6) δ 11.97 (s, 1H), 8.10 (s, 1H), 8.08 – 7.99 (m, 2H), 7.93 (dd, *J* = 15.2, 8.4 Hz, 3H), 7.73 (d, *J* = 8.6 Hz, 2H), 7.63 (d, *J* = 8.3 Hz, 1H), 7.58 (d, *J* = 8.4 Hz, 1H), 7.51 – 7.44 (m, 1H), 7.36 (t, *J* = 7.5 Hz, 1H), 7.04 – 6.70 (m, 3H), 6.41 (s, 1H), 3.75 (s, 3H). **^{13}C NMR** (176 MHz, DMSO-d_6) δ 184.61, 171.09, 161.34, 156.26, 155.89, 150.17, 146.58, 137.26, 133.57, 131.18, 129.21, 127.71, 123.70, 123.65, 123.21, 121.51, 121.38, 121.37, 121.32, 120.69, 117.72, 113.65, 112.78, 112.30, 111.98, 105.60, 61.52, 55.59. **HRMS**-ESI (*m/z*) calculated for $C_{30}H_{21}N_2O_7$ $[M+H]^+$ 521.1271; found, 521.1348.

1-(Dibenzo[b,d]furan-3-yl)-4-(4-fluorobenzoyl)-3-hydroxy-5-(4-nitrophenyl)-1,5-dihydro-2H-pyrrol-2-one (**91**):

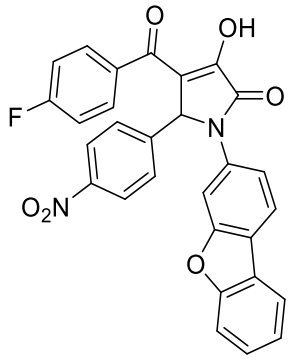

4-Nitrobenzaldehyde (31.70 mg, 0.21 mmol, 1.00 equiv.) followed by the dibenzo[*b,d*]furan-3-amine (38.50 mg, 0.21 mmol, 1.00 equiv.) were added to a suspension (3 mL, 0.06 M) of ethyl 3-(4-fluorophenyl)-3-oxopropanoate (**95h**) (50.00 mg, 0.17 mmol, 1.00 equiv.) in acetic acid following the general procedure E to give the desired product as a yellow solid (34.20 mg, 0.07 mmol, 32%). **^{1}H NMR** (600 MHz, DMSO-d_6) δ 12.36 (s, 1H), 8.09 – 8.02 (m, 5H), 7.87 – 7.80 (m, 4H), 7.71 (dd, *J* = 8.5, 1.8 Hz, 1H), 7.67 (d, *J* = 8.2 Hz, 1H), 7.49 (ddd, *J* = 8.4, 7.2, 1.4 Hz, 1H), 7.38 (td, *J* = 7.5, 1.0 Hz, 1H), 7.34 – 7.27 (m, 2H), 6.67 (s, 1H). **^{13}C NMR** (151 MHz, DMSO-d_6) δ 188.04, 166.10, 165.11, 164.43, 156.35, 155.77, 151.51, 147.64, 144.93, 135.92, 134.90, 132.23, 132.17, 129.79, 128.00, 123.92, 123.80, 123.50, 121.65, 121.50, 121.49, 119.58, 118.47, 115.84, 115.70, 112.06, 106.53, 61.21. **HRMS**-ESI (*m/z*) calculated for $C_{29}H_{17}N_2O_6$ $[M+H]^+$ 509.1071; found, 509.1148.

1-(Dibenzo[b,d]furan-3-yl)-4-(furan-2-carbonyl)-3-hydroxy-5-(4-nitrophenyl)-1,5-dihydro-2H-pyrrol-2-one (**92**):

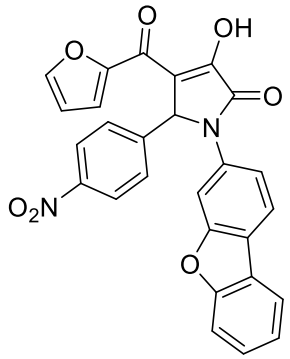

4-Nitrobenzaldehyde (35.90 mg, 0.24 mmol, 1.00 equiv.) followed by the dibenzo[*b,d*]furan-3-amine (43.60 mg, 0.24 mmol, 1.00 equiv.) were added to a suspension (3 mL, 0.06 M) of ethyl 3-(furan-2-yl)-3-oxopropanoate (**95c**) (50.00 mg, 0.24 mmol, 1.00 equiv.) in acetic acid following the general procedure E to give the desired product as a yellow solid (39.00 mg, 0.08 mmol, 34%). **^{1}H NMR** (700 MHz, DMSO-d_6) δ 11.96 (s, 1H), 8.61 (d, *J* = 41.1 Hz, 1H), 8.30 – 7.95 (m, 4H), 7.94 – 7.76 (m, 2H), 7.75 – 7.69 (m, 1H), 7.65 (s, 1H), 7.58 (d, *J* = 8.8 Hz, 2H), 7.47 (s, 1H), 7.40 – 7.31 (m, 1H), 6.99 – 6.60 (m, 1H), 6.59 – 6.27 (m, 1H). **^{13}C NMR** (176 MHz, DMSO-d_6) δ 172.48, 162.78, 156.29, 155.85, 154.12, 152.54, 146.94, 146.53, 144.87, 137.31, 136.29, 129.66, 129.38, 128.03, 127.69, 123.70, 123.07, 121.39, 120.62, 117.73, 116.24, 112.90, 112.01, 111.73, 111.53, 105.58, 46.08. **HRMS**-ESI (*m/z*) calculated for $C_{27}H_{16}N_2O_7$ $[M+H]^+$ 481.0958; found, 481.1033.

Ethyl 2-oxo-2-(2-oxocyclopentyl)acetate (**94**).

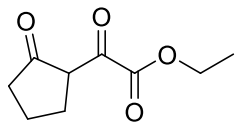

A solution of sodium ethoxide was freshly prepared by the cautious addition of sodium (316.17 mg, 13.75 mmol, 1.1 equiv.) to 10.0 mL of anhydrous ethanol in a 100.0 mL two-necked flask equipped with a dropping funnel. Once the sodium was fully dissolved the flask was immersed in an ice bath and a cold solution (1.11 mL, 12.5 mmol, 1.0 equiv.) of cyclohexanone in (1,70 mL, 12.5 mmol, 1.0 equiv.) of diethyl oxalate was added from the dropping funnel over a period of about 15 min. When the addition was complete, the ice bath was

retained for 30 min, and then the mixture was stirred at room temperature for another 16 h. The reaction mixture was added to ice water and acidified by the addition of aqueous 1 M HCl. The aqueous solution was extracted with dichloromethane (3 × 40.0 mL), washed with brine, and dried over anhydrous $MgSO_4$. Then, the resulting residue was purified by flash column chromatography on silica gel to afford the desired enol form of the product (1.86 g, 10.1 mmol, 81%) as a yellow oil. **^{1}H NMR** (400 MHz, Chloroform-*d*) δ 12.87 (s, 1H), 4.34 – 4.23 (m, 2H), 2.90 (t, *J* = 7.3 Hz, 2H), 2.44 – 2.38 (m, 2H), 1.98 – 1.87 (m, 2H), 1.31 (td, *J* = 7.1, 0.5 Hz, 3H). **LC-MS** (**ESI**) (*m/z*) calculated for $C_9H_{12}O_4$ $[M+H]^+$ = 184.1; found: 184.0.

Ethyl 2-oxo-2-(2-oxocyclohexyl)acetate (**95**).

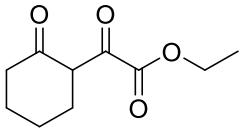

A solution of cyclohexanone (517.60 µL, 5.00 mmol, 1.00 equiv.) in abs. EtOH (10 mL) was cooled to 0°C, then sodium ethoxide (21% wt solution in EtOH, 2.05 mL, 5.50 mmol, 1.10 equiv.) was added. To this mixture diethyl oxalate (679.1 µL, 5.0 mmol, 1.0 equiv.) was added and the mixture was allowed to warm to room temperature. After stirring the beige solution overnight ice water and 2 M HCl (aq.) were added to acidify the crude mixture. The aqueous solution was extracted with dichloromethane (3 x 50 mL), washed with brine, dried over anhydrous $MgSO_4$, and evaporated under reduced pressure. The resulting crude residue was purified by silica gel column chromatography (eluent system: Petroleum ether/ EtOAc = 6:1) to give the desired product as a yellow oil (594.60 mg, 3.0 mmol, 60%). **^{1}H NMR** (400 MHz, Chloroform-*d*) δ 4.34 (qd, *J* = 7.1, 1.2 Hz, 2H), 2.50 – 2.41 (m, 4H), 2.25 – 1.82 (m, 1H), 1.79 – 1.64 (m, 4H), 1.37 (td, *J* = 7.2, 1.2 Hz, 3H). **LC-MS** (**ESI**) (*m/z*) calculated for $C_{10}H_{14}O_4$ $[M+H]^+$ = 199.2; found: 199.2.

1,2-Diphenyl-2-azaspiro[4.4]nonane-3,4,6-trione (**96**).

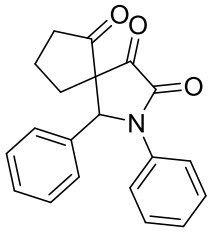

A mixture containing the imine (36.8 mg, 0.2 mmol, 1.0 equiv.), intermediate **94** (36.2 mg, 0.2 mmol, 1.0 equiv.), and benzaldehyde (42.4 mg, 0.4 mmol, 2.0 equiv.) was dissolved in diethyl ether. A solid formed almost at once which was collected via filtration after stirring the suspension at room temperature for 24 h. The solid was then thoroughly washed with diethyl ether and water to afford the desired spirocyclic product as a beige solid (10.80 mg, 0.03 mmol, 17%). **^{1}H NMR** (400 MHz, DMSO-d_6) δ 7.67 (d, *J* = 7.8 Hz, 2H), 7.41 – 7.20 (m, 8H), 5.87 (s, 1H), 2.52 (d, *J* = 15.4 Hz, 2H), 2.17 – 1.97 (m, 1H), 1.95 – 1.80 (m, 2H), 1.44 – 1.33 (m, 1H). **LC-MS** (**ESI**) (*m/z*) calculated for $C_{20}H_{17}NO_3$ $[M+H]^+$ = 320.4; found: 320.4.

1,2-Diphenyl-2-azaspiro[4.5]decane-3,4,6-trione (**97**).

A mixture containing the imine (36.8 mg, 0.2 mmol, 1.0 equiv.), intermediate **95** (36.2 mg, 0.2 mmol, 1.0 equiv.), and benzaldehyde (42.4 mg, 0.4 mmol, 2.0 equiv.) was dissolved in diethyl ether. A solid formed almost at once which was collected via filtration after stirring the suspension at room

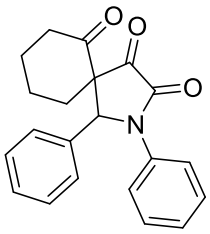

temperature for 24 h. The solid was then thoroughly washed with diethyl ether and water to afford the desired spirocyclic product as a beige solid. (10.00 mg, 0.03 mmol, 15%). **^{1}H NMR** (400 MHz, DMSO-d_6) δ 7.61 (d, *J* = 14.2 Hz, 2H), 7.55 – 7.15 (m, 8H), 6.24 (s, 1H), 2.64 (dd, *J* = 8.0, 5.2 Hz, 2H), 1.92 (d, *J* = 39.8 Hz, 2H), 1.67 (d, *J* = 34.4 Hz, 2H), 1.49 (d, *J* = 18.2 Hz, 1H), 1.15 – 1.03 (m, 1H). **LC-MS** (**ESI**) (*m/z*) calculated for $C_{21}H_{19}NO_3$ $[M+H]^+$ = 334.4; found: 334.2.

2-([1,1'-Biphenyl]-3-yl)-1-(4-nitrophenyl)-2-azaspiro[4.4]nonane-3,4,6-trione (**99**).

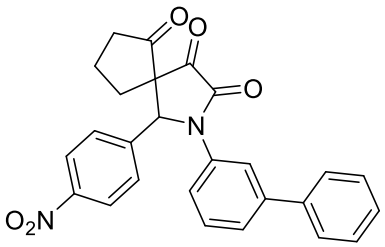

Intermediate **94** (27.60 mg, 0.15 mmol, 1.00 equiv.) and imine **98** (45.30 mg, 0.15 mmol, 1.0 equiv.) were suspended in toluene (2 mL) and the mixture was stirred at 120°C overnight. After completion of the reaction as monitored by TLC and LC-MS, water was added to the solution, and it was extracted with EtOAc (3 x 10 mL). After drying the combined organic layer using $MgSO_4$, the solvent was removed under reduced pressure. Purification using silica gel column chromatography afforded the desired spirocyclic trione as a yellow solid (41.4 mg, 0.09 mmol, 47%). ^{1}H NMR (500 MHz, Chloroform-*d*) δ 8.09 (d, *J* = 8.8 Hz, 2H), 7.57 (d, *J* = 4.0 Hz, 1H), 7.24 (s, 10H), 5.52 (s, 1H), 2.28 (s, 2H), 1.25 – 1.18 (m, 4H). **LC-MS** (**ESI**) (*m/z*) calculated for $C_{26}H_{20}N_2O_5$ $[M+H]^+$ = 441.4; found: 441.2.

2-([1,1'-Biphenyl]-3-yl)-1-(4-nitrophenyl)-2-azaspiro[4.5]decane-3,4,6-trione (**100**).

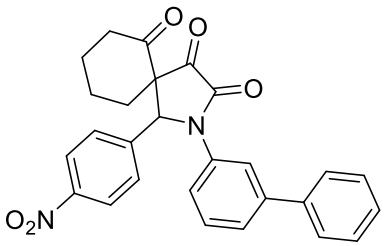

Intermediate **95** (39.6 mg, 0.2 mmol, 1.0 equiv.) and imine **98** (60.5 mg, 0.2 mmol, 1.0 equiv.) were suspended in toluene (2 mL) and the mixture was stirred at 120°C overnight. After completion of the reaction as monitored by TLC and LC-MS, water was added to the solution, and it was extracted with EtOAc (3 x 10 mL). After drying the combined organic layer using $MgSO_4$, the solvent was removed under reduced pressure. Purification using silica gel column chromatography afforded the desired spirocyclic trione as a yellow solid (46.4 mg, 0.1 mmol, 51%). **^{1}H NMR** (500 MHz, Chloroform-*d*) δ 8.09 (d, *J* = 8.8 Hz, 2H), 7.57 (d, *J* = 4.0 Hz, 1H), 7.24 (s, 10H), 5.52 (s, 1H), 2.28 (s, 2H), 1.24 – 1.15 (m, 6H). **^{13}C NMR** (126 MHz, Chloroform-*d*) δ 178.49, 167.34, 148.07, 143.38, 142.35, 142.29, 140.25, 136.68, 129.57, 128.87, 128.25, 127.75, 127.13, 125.85, 124.49, 124.45, 120.35, 120.31, 64.03, 33.17, 29.73, 26.81, 24.10, 24.02, 14.22. **LC-MS** (**ESI**) (*m/z*) calculated for $C_{27}H_{22}N_2O_5$ $[M+H]^+$ = 455.4; found: 455.4.

2-(Dibenzo[b,d]furan-2-yl)-1-(4-nitrophenyl)-2-azaspiro[4.4]nonane-3,4,6-trione (**102**).

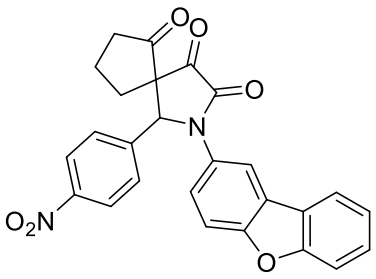

Intermediate **94** (36.8 mg, 0.2 mmol, 1.0 equiv.) and imine **101** (63.2 mg, 0.2 mmol, 1.0 equiv.) were suspended in toluene (2 mL) and the mixture was stirred at 120°C overnight. After completion of the reaction as monitored by TLC and LC-MS, water was added to the solution, and it was extracted with EtOAc (3 x 10 mL). After drying the combined organic layer using $MgSO_4$, the solvent was removed under reduced pressure. Purification using silica gel column chromatography afforded the desired spirocyclic trione as a yellow solid (22.7 mg, 0.05 mmol, 25%). **^{1}H NMR** (700 MHz, DMSO-d_6) δ 8.16 – 8.11 (m, 2H), 8.06 – 7.98 (m, 3H), 7.71 – 7.57 (m, 3H), 7.55 – 7.43 (m, 2H), 7.41 – 7.33 (m, 1H), 2.45 – 2.28 (m, 2H), 1.92 (s, 1H), 1.91 – 1.72 (m, 2H), 1.45 – 1.40 (m, 1H), 1.29 – 1.23 (m, 1H). **^{13}C NMR** (176 MHz, DMSO-d_6) δ 170.80, 166.52, 147.69, 145.49, 143.04, 139.56, 137.23, 129.02, 127.04, 126.29, 124.49, 123.69, 121.50, 120.91, 120.14, 118.96, 116.79, 115.10, 111.90, 104.61, 102.32, 60.22, 41.22, 24.57, 21.23, 14.56. **LC-MS** (**ESI**) (*m/z*) calculated for $C_{26}H_{18}N_2O_6$ $[M+H]^+$ = 455.4; found: 455.4.

2-(Dibenzo[b,d]furan-3-yl)-1-(4-nitrophenyl)-2-azaspiro[4.4]nonane-3,4,6-trione (**104**).

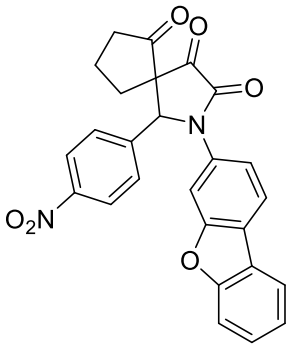

Intermediate **94** (36.8 mg, 0.2 mmol, 1.0 equiv.) and imine **103** (63.2 mg, 0.2 mmol, 1.0 equiv.) were suspended in toluene (2 mL) and the mixture was stirred at 120°C overnight. After completion of the reaction as monitored by TLC and LC-MS, water was added to the solution and it was extracted with EtOAc (3 x 10 mL). After drying the combined organic layer using $MgSO_4$, the solvent was removed under reduced pressure. Purification using silica gel column chromatography afforded the desired spirocyclic trione as a yellow solid (30.9 mg, 0.07 mmol, 34%). **^{1}H NMR** (700 MHz, DMSO-d_6) δ 10.05 (s, 1H), 9.82 (s, 1H), 8.41 (d, *J* = 2.2 Hz, 1H), 8.31 (d, *J* = 2.3 Hz, 1H), 8.13 – 8.10 (m, 1H), 8.07 – 8.02 (m, 1H), 7.73 (dd, *J* = 8.9, 2.3 Hz, 1H), 7.67 (ddt, *J* = 8.1, 7.2, 0.9 Hz, 1H), 7.63 (dd, *J* = 8.9, 3.1 Hz, 2H), 7.56 (dd, *J* = 8.9, 2.2 Hz, 1H), 7.52 (dddd, *J* = 8.4, 7.2, 4.0, 1.4 Hz, 1H), 7.38 (dtd, *J* = 25.8, 7.5, 1.0 Hz, 1H), 6.20 (s, 1H), 2.45 – 2.31 (m, 2H), 1.92 – 1.74 (m, 2H). **^{13}C NMR** (176 MHz, DMSO-d_6) δ 171.18, 170.81, 166.40, 156.42, 152.73, 151.95, 147.69, 145.48, 143.13, 135.33, 133.14, 129.14, 128.06, 125.84, 124.45, 123.43, 122.39, 121.42, 120.20, 114.86, 62.28, 60.22, 21.23, 14.56. **LC-MS** (**ESI**) (*m/z*) calculated for $C_{26}H_{18}N_2O_6$ $[M+H]^+$ = 455.4; found: 455.4.

5.2.2 METTL16

5.2.2.1 Aminothiazolones

General Procedure F (thiazolidinonesulfonamide formation):

An excess of pseudothiohydantoin or 2-imino-4-oxazolidinone (3 equiv) was suspended in anhydrous DMF and sodium hydride (3 equiv; 60% dispersion in mineral oil) was added portion-wise. After

stirring for 30 min at room temperature, the corresponding sulfonyl chloride was added to the milky solution and the reaction mixture was stirred for an additional 16 h. Then, 1 M HCl was slowly added to form a precipitate, which was isolated *via* vacuum filtration by using a sintered glass funnel. The solid was washed with 1 M HCl, water, ethanol, and finally diethyl ether. Subsequently, the solid was dried under high vacuum to afford the desired sulfonamides. In case no precipitate formed after adding 1 M HCl, the solution was extracted using EtOAc. The organic layer was collected and dried over anhydrous $MgSO_4$, and the solvent was removed under reduced pressure. The crude product was then purified via silica gel column chromatography using the indicated solvent gradient.[276]

General Procedure G (thiazolidinoneamide formation):

An excess of pseudothiohydantoin (3 equiv) was suspended in anhydrous DMF and sodium hydride (3 equiv; 60% dispersion in mineral oil) was added thereto portion-wise. After stirring for 30 min at room temperature, benzoyl chloride was added to the milky solution and the reaction mixture was stirred for an additional 16 h. Then 1 M HCl was slowly added to form a precipitate which was isolated via vacuum filtration by using a sintered glass funnel. The solid was washed with 1 M HCl, water, ethanol, and finally diethyl ether. Subsequently, the solid was dried under high vacuum to afford the desired sulfonamides. In case no precipitate formed after adding 1 M HCl, the solution was extracted using EtOAc. The organic layer was collected, and dried over anhydrous $MgSO_4$ and the solvent was removed under reduced pressure. The crude product was then purified via silica gel column chromatography using indicated solvent gradients.[276]

General Procedure H (Knoevenagel condensation):

A mixture of a(n) ketone/aldehyde (1 equiv.), corresponding sulfonamide/benzoyl chloride (1 equiv.), and sodium acetate (3 equiv.) in glacial acetic acid (0.06 M) was heated to reflux and then stirred for 16 h. After cooling to room temperature, the resulting precipitate was filtered and washed with water, ethanol, and diethyl ether to afford the desired product.

General Procedure I (One-pot condensation)

A solution of 1-(4-hydroxyphenyl)thiourea (**146**) (1 equiv.), chloroacetic acid (1 equiv.), isatin (1 equiv.), and sodium acetate (1 equiv.) in acetic acid (0.12 M) was stirred under reflux for 16 h. After cooling to room temperature, the red-brownish solid was filtered off, and washed with water, ethanol, and diethyl ether in sequence to afford the desired 4-thiazolidinones.

4-Methoxy-N-(4-oxo-4,5-dihydrothiazol-2-yl)benzenesulfonamide (**106**):

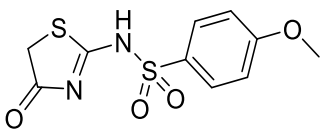

Following the general procedure F, the product was obtained as a beige solid after filtration and washing using 1 M HCl, water, ethanol, and diethyl ether (770.00 mg, 2.69 mmol, 74%). **^{1}H NMR** (700 MHz, DMSO-d_6) δ 12.46 (s, 1H), 7.81 – 7.77 (m, 2H), 7.16 – 7.11 (m, 2H), 4.04 (s, 2H), 3.85 (s, 3H). **^{13}C NMR** (176 MHz, DMSO-d_6) δ 174.20, 172.46, 163.24, 132.67, 129.16, 114.94, 56.23, 35.36.

N-(4-Oxo-4,5-dihydrothiazol-2-yl)benzenesulfonamide (**VII**):

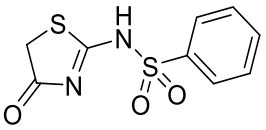

Following the general procedure F, the product was obtained as a beige solid after filtration and washing using 1 M HCl, water, ethanol, and diethyl ether (143.70 mg, 0.56 mmol, 99%). **^{1}H NMR** (700 MHz, DMSO-d_6) δ 12.54 (s, 1H), 7.92 – 7.83 (m, 2H), 7.73 – 7.67 (m, 1H), 7.67 – 7.58 (m, 2H), 4.06 (s, 2H). **^{13}C NMR** (176 MHz, DMSO-d_6) δ 174.24, 173.42, 141.02, 133.68, 129.81, 126.86, 35.48.

4-Methyl-N-(4-oxo-4,5-dihydrothiazol-2-yl)benzenesulfonamide (**VIII**):

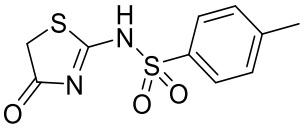

Following the general procedure F, the product was obtained as a beige solid after filtration and washing using 1 M HCl, water, ethanol, and diethyl ether (36.20 mg, 0.13 mmol, 51%). **^{1}H NMR** (600 MHz, DMSO-d_6) δ 12.50 (s, 1H), 7.79 – 7.71 (m, 2H), 7.43 (d, *J* = 8.0 Hz, 2H), 4.05 (s, 2H), 2.40 (s, 3H). **^{13}C NMR** (151 MHz, DMSO-d_6) δ 174.22, 173.00, 144.12, 138.19, 130.20, 126.94, 40.53, 35.42, 21.51.

3,5-Difluoro-N-(4-oxo-4,5-dihydrothiazol-2-yl)benzenesulfonamide (**IX**):

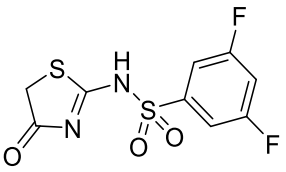

Following the general procedure F, the product was obtained as a yellow solid after filtration and washing using 1 M HCl, water, ethanol, and diethyl ether (82.20 mg, 0.28 mmol, 64%). **^{1}H NMR** (600 MHz, DMSO-d_6) δ 12.69 (s, 1H), 7.69 (tt, *J* = 9.2, 2.3 Hz, 1H), 7.60 – 7.53 (m, 2H), 4.08 (s, 2H). **^{13}C NMR** (151 MHz, DMSO-d_6) δ 175.50, 174.36, 163.49 (d, *J* = 12.2 Hz), 161.82 (d, *J* = 12.2 Hz), 144.28 (t, *J* = 8.6 Hz), 111.23 – 110.27 (m), 109.49 (t, *J* = 25.7 Hz), 35.82.

3-Nitro-N-(4-oxo-4,5-dihydrothiazol-2-yl)benzenesulfonamide (**X**):

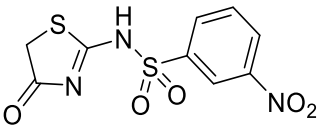

Following the general procedure F, the product was obtained as a yellow solid after filtration and washing using 1 M HCl, water, ethanol, and diethyl ether (92.50 mg, 0.31 mmol, 69%). **^{1}H NMR** (700 MHz, DMSO-d_6) δ 12.71 (s, 1H), 8.54 (ddd, *J* = 8.2, 2.3, 1.0 Hz, 1H), 8.52 (t, *J* = 2.0 Hz, 1H), 8.30 (ddd, *J* = 7.8, 1.8, 1.0 Hz, 1H), 7.94 (t, *J* = 8.0 Hz, 1H), 4.08 (s, 2H). **^{13}C NMR** (151 MHz, DMSO-d_6) δ 175.32, 174.32, 148.31, 142.51, 132.89, 132.06, 128.28, 121.48, 35.84.

4-(tert-Butyl)-N-(4-oxo-4,5-dihydrothiazol-2-yl)benzenesulfonamide (**XI**):

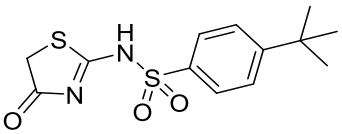

Following the general procedure F, the product was obtained as a white solid after filtration and washing using 1 M HCl, water, ethanol, and diethyl ether (123.60 mg, 0.4 mmol, 92%). **^{1}H NMR** (600 MHz, DMSO-d_6) δ 12.49 (s, 1H), 7.81 – 7.76 (m, 2H), 7.67 – 7.61 (m, 2H), 4.05 (s, 2H), 1.31 (s, 9H). **^{13}C NMR** (151 MHz, DMSO-d_6) δ 174.24, 173.02, 156.76, 138.21, 126.81, 126.64, 40.53, 35.42, 35.41, 31.24.

2-Chloro-4-fluoro-N-(4-oxo-4,5-dihydrothiazol-2-yl)benzenesulfonamide (**XII**):

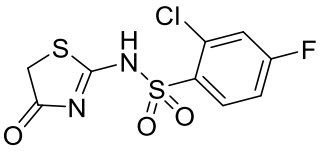

Following the general procedure F, the product was obtained as a yellow solid after filtration and washing using 1 M HCl, water, ethanol, and diethyl ether (107.40 mg, 0.35 mmol, 79%). **^{1}H NMR** (600 MHz, DMSO-d_6) δ 12.67 (s, 1H), 8.14 (dd, *J* = 8.9, 5.9 Hz, 1H), 7.76 (dd, *J* = 8.9, 2.6 Hz, 1H), 7.47 (ddd, *J* = 8.9, 8.0, 2.6 Hz, 1H), 4.10 (s, 2H). **^{13}C NMR** (151 MHz, DMSO-d_6) δ 174.79, 174.30, 165.44, 163.75, 134.99 (d, *J* = 3.3 Hz), 133.84 (d, *J* = 11.6 Hz), 132.68 (d, *J* = 10.3 Hz), 119.97 (d, *J* = 26.2 Hz), 115.41 (d, *J* = 21.9 Hz), 35.78.

4-Cyclohexyl-N-(4-oxo-4,5-dihydrothiazol-2-yl)benzenesulfonamide (**XIII**):

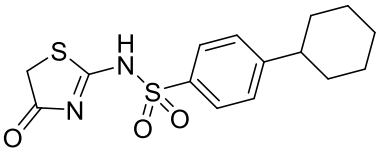

Following the general procedure F, the product was obtained as a yellow solid after filtration and washing using 1 M HCl, water, ethanol, and diethyl ether (78.00 mg, 0.23 mmol, 59%). **^{1}H NMR** (700 MHz, DMSO-d_6) δ 12.48 (s, 1H), 7.77 (d, *J* = 8.0 Hz, 2H), 7.47 (d, *J* = 8.0 Hz, 2H), 4.05 (s, 2H), 2.60 (d, *J* = 11.6 Hz, 1H), 1.79 (d, *J* = 11.6 Hz, 4H), 1.71 (d, *J* = 13.4 Hz, 1H), 1.40 (tt, *J* = 13.4, 12.4 Hz, 4H), 1.23 (t, *J* = 12.4 Hz, 1H). **^{13}C NMR** (176 MHz, DMSO-d_6) δ 174.22, 172.95, 153.65, 138.52, 128.07, 127.04, 44.12, 35.40, 33.97, 26.61, 25.90.

N-(4-Oxo-4,5-dihydrothiazol-2-yl)-[1,1'-biphenyl]-4-sulfonamide (**XIV**):

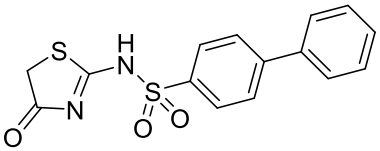

Following the general procedure F, the product was obtained as a yellow solid after filtration and washing using 1 M HCl, water, ethanol, and diethyl ether (86.40 mg, 0.26 mmol, 65%). **^{1}H NMR** (700 MHz, DMSO-d_6) δ 12.56 (s, 1H), 7.92 (p, *J* = 10.3 Hz, 4H), 7.74 (t, *J* = 10.3 Hz, 2H), 7.60 – 7.39 (m, 3H), 4.07 (s, 2H). **^{13}C NMR** (176 MHz, DMSO-d_6) δ 174.25, 173.46, 145.19, 139.72, 138.90, 129.64, 129.12, 128.02, 127.62, 127.58, 55.82, 35.51.

4-(N-(4-Oxo-4,5-dihydrothiazol-2-yl)sulfamoyl)benzoic acid (**153**):

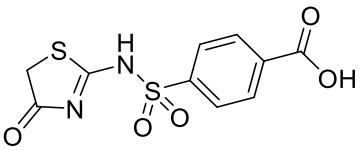

Following the general procedure F, the product was obtained as an orange solid after filtration and washing using 1 M HCl, water, and diethyl ether (130.40 mg, 0.43 mmol, 50%). **^{1}H NMR** (700 MHz, DMSO-d_6) δ 13.39 (s, 1H), 12.62 (s, 1H), 8.31-8.13 (m, 2H), 8.07-7.96 (m, 2H), 4.07 (s, 2H). **^{13}C NMR** (176 MHz, DMSO-d_6) δ 174.25, 166.58, 144.40, 135.22, 130.67, 130.49, 127.29, 127.21, 35.63.

5-Bromo-2-methoxy-N-(4-oxo-4,5-dihydrothiazol-2-yl)benzenesulfonamide (**XV**):

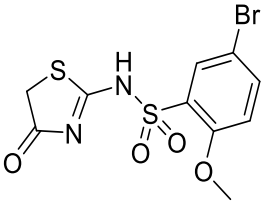

Following the general procedure F, the product was obtained as a yellow solid after filtration and washing using 1 M HCl, water, ethanol, and diethyl ether (87.40 mg, 0.24 mmol, 68%). **^{1}H NMR** (700 MHz, DMSO-d_6) δ 12.55 (s, 1H), 7.92 – 7.79 (m, 2H), 7.24 (d, *J* = 8.8 Hz, 1H), 4.10 (s, 2H), 3.89 (s, 3H). **^{13}C NMR** (176 MHz, DMSO-d_6) δ 174.43, 174.35, 156.70, 137.99, 130.99, 130.20, 116.26, 111.42, 57.19, 35.35.

N-(4-Oxo-4,5-dihydrothiazol-2-yl)methanesulfonamide (**XVI**):

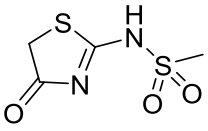

Following the general procedure F, the product was obtained as a yellow solid after filtration and washing using 1 M HCl, water, and diethyl ether (112.40 mg, 0.58 mmol, 89%). **^{1}H NMR** (600 MHz, DMSO-d_6) δ 12.44 (s, 1H), 4.05 (s, 2H), 3.07 (s, 3H). **^{13}C NMR** (151 MHz, DMSO-d_6) δ 174.34, 172.05, 41.75, 35.30.

N-(4-Oxo-4,5-dihydrothiazol-2-yl)-4-(trifluoromethyl)benzenesulfonamide (**XVII**):

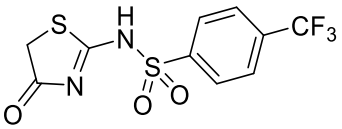

Following the general procedure F, the product was obtained as a yellow solid after filtration and washing using 1 M HCl, water, ethanol, and diethyl ether (152.00 mg, 0.47 mmol, 77%). **^{1}H NMR** (600 MHz, DMSO-d_6) δ 12.67 (s, 1H), 8.08 (d, *J* = 8.3 Hz, 2H), 8.02 (d, *J* = 8.3 Hz, 2H), 4.07 (s, 2H). **^{13}C NMR** (151 MHz, DMSO-d_6) δ 174.91, 174.28, 162.77, 144.80, 133.24 (q, *J* = 32.3 Hz), 127.92, 127.07 (q, *J* = 3.7 Hz), 123.89 (q, *J* = 272.9 Hz), 35.74.

N-(4-Oxo-4,5-dihydrothiazol-2-yl)naphthalene-2-sulfonamide (**XVIII**):

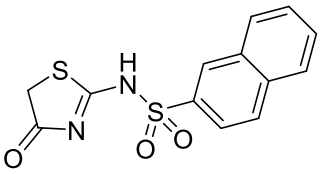

Following the general procedure F, the product was obtained as a beige solid after filtration and washing using 1 M HCl, water, ethanol, and diethyl ether (162.90 mg, 0.53 mmol, 81%). **^{1}H NMR** (700 MHz, DMSO-d_6) δ 12.56 (s, 1H), 8.56 (s, 1H), 8.22 (d, *J* = 8.2 Hz, 1H), 8.16 (d, *J* = 9.1 Hz, 1H), 8.07 (d, *J* = 8.2 Hz, 1H), 7.85 (d, *J* = 9.1 Hz, 1H), 7.71 (m, 2H), 4.07 (s, 2H). **^{13}C NMR** (176 MHz, DMSO-d_6) δ 174.23, 173.53, 137.96, 134.90, 132.08, 129.95, 129.87, 129.57, 128.34, 128.21, 127.78, 122.59, 35.53.

4-Cyano-N-(4-oxo-4,5-dihydrothiazol-2-yl)benzenesulfonamide (**XIX**):

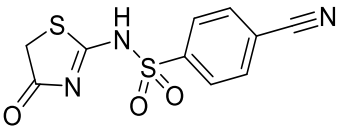

Following the general procedure F, the product was obtained as a yellow solid after filtration and washing using 1 M HCl, water, ethanol, and diethyl ether (45.40 mg, 0.16 mmol, 32%). **H NMR** (700 MHz, DMSO-d_6) δ 12.69 (s, 1H), 8.11 (d, *J* = 8.4 Hz, 2H), 8.03 (d, *J* = 8.4 Hz, 2H), 4.07 (s, 2H). **^{13}C NMR** (176 MHz, DMSO-d_6) δ 175.14, 174.31, 144.93, 134.03, 127.63, 118.11, 116.01, 35.78.

4-Fluoro-N-(4-oxo-4,5-dihydrothiazol-2-yl)benzenesulfonamide (**XX**):

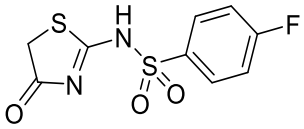

Following the general procedure F, the product was obtained as a yellow solid after filtration and washing using 1 M HCl, water, ethanol, and diethyl ether (95.70 mg, 0.35 mmol, 68%). **^{1}H NMR** (600 MHz, DMSO-d_6) δ 12.56 (s, 1H), 7.93 (dd, *J* = 8.9, 5.1 Hz, 2H), 7.47 (t, *J* = 8.9 Hz, 2H), 4.06 (s, 2H). **^{13}C NMR** (151 MHz, DMSO-d_6) δ 174.24, 173.69, 165.84, 164.17, 137.45 (d, *J* = 3.1 Hz), 130.00 (d, *J* = 9.5 Hz), 117.01 (d, *J* = 22.8 Hz), 35.55.

Methyl 4-(N-(4-oxo-4,5-dihydrothiazol-2-yl)sulfamoyl)benzoate (**156**):

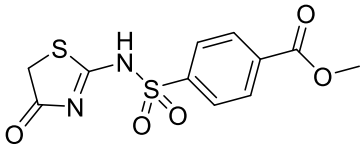

Following the general procedure F, the product was obtained as a yellow solid after filtration and washing using 1 M HCl, water, ethanol, and diethyl ether (85.30 mg, 0.27 mmol, 68%). **^{1}H NMR** (700 MHz, DMSO-d_6) δ 12.64 (s, 1H), 8.17 (d, *J* = 8.4 Hz, 2H), 8.00 (d, *J* = 8.4 Hz, 2H), 4.07 (s, 2H), 3.90 (s, 3H). **^{13}C NMR** (176 MHz, DMSO-d_6) δ 174.45, 174.26, 165.56, 144.86, 133.93, 130.61, 127.36, 53.17, 35.67.

3-(N-(4-Oxo-4,5-dihydrothiazol-2-yl)sulfamoyl)benzoic acid (**157**):

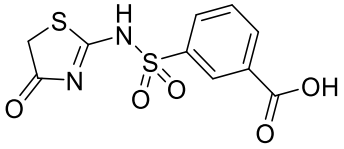

Following the general procedure F, the product was obtained as a yellow solid after purification using silica gel column chromatography (eluent system: MeOH in DCM (0-4%)) (85.30 mg, 0.27 mmol, 68%). **^{1}H NMR** (500 MHz, DMSO-d_6) δ 12.63 (s, 2H), 8.64 (t, *J* = 1.8 Hz, 1H), 8.37 (dt, *J* = 7.8, 1.6 Hz, 1H), 8.10 (dt, *J* = 7.8, 1.6 Hz, 1H), 7.80 (t, *J* = 7.8 Hz, 1H), 4.07 (s, 2H). **^{13}C NMR** (126 MHz, DMSO-d_6) δ 174.35, 174.08, 141.54, 133.95, 131.05, 130.53, 127.56, 49.07, 35.69, 35.11.

4-Methoxy-N-(4-oxo-4,5-dihydrooxazol-2-yl)benzenesulfonamide (**XXI**):

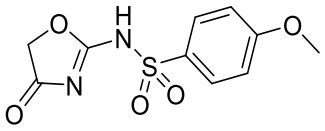

Following the general procedure F, the product was obtained as a white solid after filtration and washing using 1 M HCl, water, and diethyl ether (102.5 mg, 0.4 mmol, 79%). **^{1}H NMR** (600 MHz, DMSO-d_6) δ 12.53 (s, 1H), 7.85 – 7.74 (m, 2H), 7.15 – 7.03 (m, 2H), 4.91 (s, 2H), 3.84 (s, 3H). **^{13}C NMR** (151 MHz, DMSO-d_6) δ 173.55, 162.71, 161.57, 134.20, 129.21, 114.53 71.86, 56.12.

4-Methyl-N-(4-oxo-4,5-dihydrothiazol-2-yl)benzamide (**XXII**):

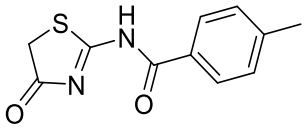

Following the general procedure G, the product was obtained as a yellow solid after filtration and washing using 1 M HCl, water, ethanol, and diethyl ether (154.60 mg, 0.66 mmol, 100%). **^{1}H NMR** (600 MHz, DMSO-d_6) δ 12.48 (s, 1H), 8.03 (d, *J* = 8.2 Hz, 2H), 7.34 (d, *J* = 8.2 Hz, 2H), 3.96 (s, 2H), 2.39 (s, 3H). **^{13}C NMR** (151 MHz, DMSO-d_6) δ 167.77, 165.84, 143.96, 130.29, 130.21, 129.79, 129.67, 128.61, 98.18, 35.10, 21.69.

4-Methoxy-N-(4-oxo-4,5-dihydrothiazol-2-yl)benzamide (**XXIII**):

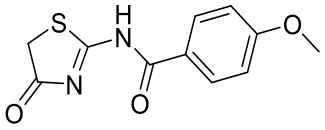

Following the general procedure G, the product was obtained as a yellow solid after filtration and washing using 1 M HCl, water, ethanol, and diethyl ether (118.40 mg, 0.47 mmol, 64%). **^{1}H NMR** (700 MHz, DMSO-d_6) δ 12.41 (s, 1H), 8.17 – 8.02 (m, 2H), 7.13 – 6.99 (m, 2H), 3.95 (s, 2H), 3.85 (s, 3H). **^{13}C NMR** (176 MHz, DMSO-d_6) δ 176.38, 175.41, 174.71, 163.66, 131.93, 128.19, 114.37, 56.00.

3,4-Dimethoxy-N-(4-oxo-4,5-dihydrothiazol-2-yl)benzamide (**XXIV**):

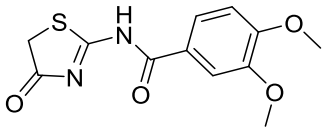

Following the general procedure G, the product was obtained as a yellow solid after filtration and washing using 1 M HCl, water, ethanol, and diethyl ether (66.20 mg, 0.24 mmol, 36%). **^{1}H NMR** (600 MHz, DMSO-d_6) δ 12.52 (s, 1H), 7.81 (dd, *J* = 8.4, 2.0 Hz, 1H), 7.65 (d, *J* = 2.0 Hz, 1H), 7.10 (d, *J* = 8.4 Hz, 1H), 3.94 (s, 2H), 3.85 (s, 3H), 3.83 (s, 3H).**^{13}C NMR** (151 MHz, DMSO-d_6) δ 167.57, 153.53, 148.89, 124.05, 123.64, 112.34, 112.13, 111.45, 56.20, 55.97.

4-Fluoro-N-(4-oxo-4,5-dihydrothiazol-2-yl)benzamide (**XXV**)

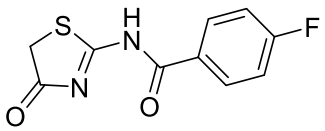

Following the general procedure G the product was obtained as a yellow solid after filtration and washing using 1 M HCl, water, ethanol, and diethyl ether (155.00 mg, 0.65 mmol, 99%). **^{1}H NMR** (600 MHz, DMSO-d_6) δ 12.58 (s, 1H), 8.29 – 8.12 (m, 2H), 7.37 (t, *J* = 8.9 Hz, 2H), 3.98 (s, 2H). **^{13}C NMR** (151 MHz, DMSO-d_6) δ 166.83, 166.34, 164.67, 133.31 (d, *J* = 9.8 Hz), 132.55 (d, *J* = 9.4 Hz), 116.87 (d, *J* = 22.3 Hz), 116.14 (d, *J* = 21.9 Hz), 35.49 – 34.78 (m).

1-Methyl-5-nitroindoline-2,3-dione (**XXVI**)

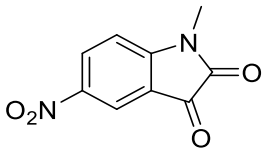

A mixture of 5-nitroindoline-2,3-dione (500.00 mg, 2.60 mmol, 1.00 equiv.) in DMF (10 mL) was cooled to 0 °C and NaH (60% dispersion in mineral oil, 122.00 mg, 3.04 mmol, 1.17 equiv.) was added and stirred for 5 minutes, followed by the dropwise addition of iodomethane (190.00 µL, 3.04 mmol, 1.17 equiv.). After two hours at rt, the reaction was poured onto NH_4Cl (aq., saturated) and extracted with EtOAc (3x). The combined organic layers were washed with brine and water and dried over $MgSO_4$. The solvents were removed under reduced pressure and purified by flash chromatography (DCM) to give 1-Methyl-5-nitroindoline-2,3-dione (484 mg, 2.35 mmol, 90%). **^{1}H NMR** (500 MHz, DMSO-*d*6) δ 8.55 (dd, *J* = 8.8, 2.4 Hz, 1H), 8.23 (d, *J* = 2.4 Hz, 1H), 7.36 (d, *J* = 8.8 Hz, 1H), 3.22 (s, 3H). **^{13}C NMR** (126 MHz, DMSO) δ 181.73, 159.37, 156.13, 143.41, 133.48, 119.43, 118.31, 111.41, 26.97.

5-Fluoro-1-methylindoline-2,3-dione (**XXVII**)

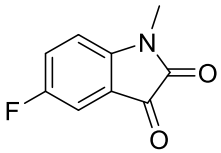

The synthesis was adapted from literature.[277] A mixture of 5-fluoroisatin (300.00 mg, 1.82 mmol, 1.00 eq) in DMF (10 mL) was cooled to 0 °C and NaH (60% dispersion in mineral oil, 85.00 mg, 2.13 mmol, 1.17 eq) was added and stirred for 5 minutes. Followed by the dropwise addition of iodomethane (132.00 µL, 2.13 mmol, 1.17 eq). After two hours at rt, the reaction was poured onto NH_4Cl (aq., saturated) and extracted with EtOAc (3x). The combined organic layers were washed with brine and water and dried over $MgSO_4$. The solvents were removed under reduced pressure and purified by flash chromatography (DCM) to give 5-fluoro-1-methylindoline-2,3-dione (322 mg, 1.82 mmol, 99%). **^{1}H NMR** (600 MHz, Chloroform-*d*) δ 7.37 – 7.29 (m, 2H), 6.89 – 6.83 (m, 1H), 3.26 (s, 3H).

6-Fluoro-1-methylindoline-2,3-dione (**XXVIII**)

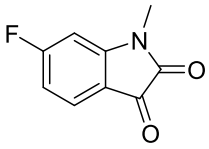

A mixture of 6-fluoroisatin (300.00 mg, 1.82 mmol, 1.00 eq) in DMF (10 mL) was cooled to 0 °C and NaH (60% dispersion in mineral oil, 85.00 mg, 2.13 mmol, 1.17 eq) was added and stirred for 5 minutes. Followed by the dropwise addition of iodomethane (132.00 µL, 2.13 mmol, 1.17 eq). After two hours at rt, the reaction was poured onto NH_4Cl (aq., saturated) and extracted with EtOAc (3x). The combined organic layers were washed with brine and water and dried over $MgSO_4$. The solvents were removed under reduced pressure and purified by flash chromatography (100% dichloromethane) to give 6-fluoro-1-methylindoline-2,3-dione (322 mg, 1.82 mmol, 99%). **^{1}H NMR** (700 MHz, Chloroform-*d*) δ 7.64 (dd, *J* = 8.3, 5.6 Hz, 1H), 6.79 (ddd, *J* = 9.1, 8.3, 2.2 Hz, 1H), 6.62 (dd, *J* = 8.6, 2.1 Hz, 1H), 3.25 (s, 3H).

N-(5-(5-Chloro-2-oxoindolin-3-ylidene)-4-oxo-4,5-dihydrothiazol-2-yl)-4-methoxybenzenesulfonamide (**105**)

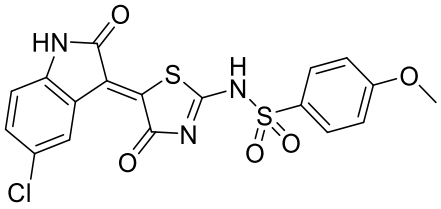

Following the general procedure H, the product was obtained as a red solid after filtration and washing using water, ethanol, and diethyl ether (193.90 mg, 0.43 mmol, 53%). **^{1}H NMR** (700 MHz, DMSO-d_6) δ 13.33 (s, 1H), 11.40 (s, 1H), 8.78 (d, *J* = 2.2 Hz, 1H), 7.91 – 7.79 (m, 2H), 7.44 (dd, *J* = 8.4, 2.2 Hz, 1H), 7.20 – 7.10 (m, 2H), 6.96 (d, *J* = 8.4 Hz, 1H), 3.85 (s, 3H).**^{13}C NMR** (176 MHz, DMSO-d_6) δ 168.72, 167.69, 167.69, 163.48, 143.16, 133.44, 132.46, 132.22, 129.32, 127.91, 126.64, 126.31, 121.71, 115.13, 112.39, 56.28. **HRMS**-ESI (*m/z*): calculated for $[M+H]^+$ $C_{18}H_{12}ClN_3O_5S_2$, 449.99797; found: 449.99816.

4-Methoxy-N-(5-(5-methyl-2-oxoindolin-3-ylidene)-4-oxo-4,5-dihydrothiazol-2-yl)benzenesulfonamide (**107**)

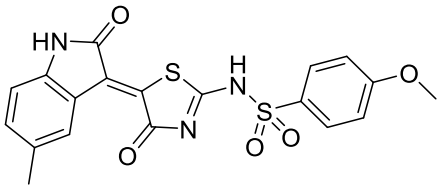

Following the general procedure H, the product was obtained as a red-brown solid after filtration and washing using water, ethanol, and diethyl ether (51.80 mg, 0.12 mmol, 71%). **^{1}H NMR** (600 MHz, DMSO-d_6) δ 13.20 (s, 1H), 11.15 (s, 1H), 8.59 (q, *J* = 0.9 Hz, 1H), 7.89 – 7.79 (m, 2H), 7.20 (ddd, *J* = 8.0, 1.8, 0.9 Hz, 1H), 7.18 – 7.13 (m, 2H), 6.83 (d, *J* = 8.0 Hz, 1H), 3.85 (s, 3H), 2.29 (s, 3H). **^{13}C NMR** (151 MHz, DMSO-d_6) δ 168.97, 168.11, 167.16, 163.41, 142.35, 133.75, 132.40, 131.25, 130.77, 129.26, 129.11, 128.29, 120.52, 115.09, 110.69, 56.27, 21.39. **HRMS**-ESI (*m/z*): calculated for $[M+H]^+$ $C_{19}H_{15}N_3O_5S_2$, 430.04531; found: 430.91353; 452.03459 $[M+Na]^+$.

N-(5-(5-Methoxy-2-oxoindolin-3-ylidene)-4-oxo-4,5-dihydrothiazol-2-yl)benzenesulfonamide (**108**)

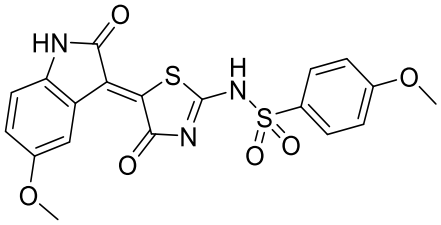

Following the general procedure H, the product was obtained as a red solid after filtration and washing using water, ethanol, and diethyl ether (35.10 mg, 0.08 mmol, 47%). **^{1}H NMR** (600 MHz, DMSO-d_6) δ 13.22 (s, 1H), 11.07 (s, 1H), 8.45 (d, *J* = 2.7 Hz, 1H), 7.87 – 7.81 (m, 2H), 7.18 – 7.14 (m, 2H), 7.00 (dd, *J* = 8.5, 2.7 Hz, 1H), 6.85 (d, *J* = 8.5 Hz, 1H), 3.85 (s, 3H), 3.75 (s, 3H). **^{13}C NMR** (151 MHz, DMSO-d_6) δ 168.91, 168.07, 167.32, 163.43, 155.05, 138.34, 132.36, 131.42, 129.27, 128.49, 121.06, 118.82, 115.10, 114.59, 111.32, 56.27, 55.96. **HRMS**-ESI (*m/z*): calculated for $[M+H]^+$ $C_{19}H_{15}N_3O_6S_2$, 446.04750; found: 446.04762.

4-Methoxy-N-(5-(5-nitro-2-oxoindolin-3-ylidene)-4-oxo-4,5-dihydrothiazol-2-yl)benzenesulfonamide (**109**)

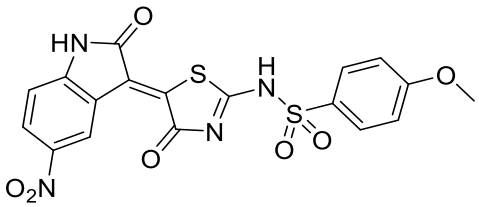

Following the general procedure H, the product was obtained as an orange solid after filtration and washing using water, ethanol, and diethyl ether (54.50 mg, 0.12 mmol, 71%). **^{1}H NMR** (600 MHz, DMSO-d_6) δ 13.38 (s, 1H), 11.94 (s, 1H), 9.65 (d, *J* = 2.5 Hz, 1H), 8.31 (dd, *J* = 8.7, 2.5 Hz, 1H), 7.88 – 7.82 (m, 2H), 7.19 – 7.15 (m, 2H), 7.13 (d, *J* = 8.7 Hz, 1H), 3.86 (s, 3H). **^{13}C NMR** (151 MHz, DMSO-d_6) δ 172.48, 169.34, 167.26, 163.53, 149.55, 142.69, 135.28, 132.10, 129.37, 128.79, 125.61, 123.83, 120.42, 115.15, 111.19, 56.29. **HRMS**-ESI (*m/z*): calculated for $[M+H]^+$ $C_{18}H_{12}N_4O_7S_2$, 461.02202; found: 461.02230.

4-Methoxy-N-(5-(1-methyl-5-nitro-2-oxoindolin-3-ylidene)-4-oxo-4,5-dihydrothiazol-2-yl)benzenesulfonamide (**110**)

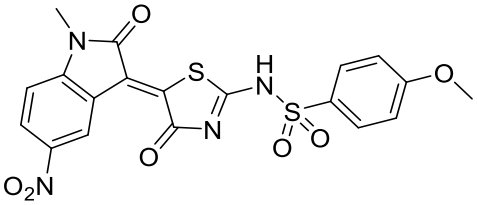

Following the general procedure H, the product was obtained as an orange-brown solid after filtration and washing using water, ethanol, and diethyl ether (52.90 mg, 0.11 mmol, 77%). **^{1}H NMR** (600 MHz, DMSO-d_6) δ 11.94 (s, 1H), 9.67 (dd, *J* = 10.7, 2.4 Hz, 1H), 8.40 (dd, *J* = 8.8, 2.4 Hz, 1H), 7.85 (dd, *J* = 8.8, 2.4 Hz, 2H), 7.37 (d, *J* = 8.8 Hz, 1H), 7.18 – 7.14 (m, 2H), 3.85 (s, 3H), 3.34 (s, 3H). **^{13}C NMR** (151 MHz, DMSO) δ 169.37, 167.96, 163.53, 150.15, 143.05, 132.11, 129.40, 129.37, 128.62, 123.83, 123.36, 119.74, 115.15, 111.20, 110.11, 56.30, 40.41, 40.27, 40.14, 40.00, 39.86, 39.72, 39.58, 27.40. **HRMS**-ESI (*m/z*): calculated for $[M+H]^+$ $C_{19}H_{13}N_4O_7S_2$, 475.03767; found: 475.03794.

4-Methoxy-N-(4-oxo-5-(2-oxoindolin-3-ylidene)-4,5-dihydrothiazol-2-yl)benzenesulfonamide (**111**)

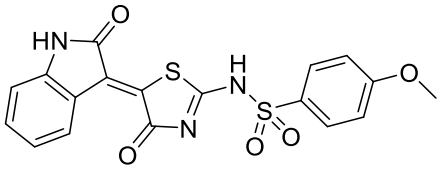

Following the general procedure H, the product was obtained as a red-brown solid after filtration and washing using water, ethanol, and diethyl ether (48.00 mg, 0.12 mmol, 68%). **^{1}H NMR** (600 MHz, DMSO-d_6) δ 13.21 (s, 1H), 11.27 (s, 1H), 8.79 – 8.74 (m, 1H), 7.87 – 7.82 (m, 2H), 7.40 (td, *J* = 7.7, 1.3 Hz, 1H), 7.18 – 7.14 (m, 2H), 7.07 (td, *J* = 7.7, 1.1 Hz, 1H), 6.95 (dt, *J* = 7.7, 0.9 Hz, 1H), 3.85 (s, 3H). **^{13}C NMR** (151 MHz, DMSO-d_6) δ 168.96, 168.06, 167.27, 163.42, 144.55, 133.31, 132.38, 131.21, 129.27, 128.73, 128.03, 122.57, 120.47, 115.10, 111.00, 56.27. **HRMS**-ESI (*m/z*): calculated for $[M+H]^+$ $C_{18}H_{13}N_3O_5S_2$, 416.03694; found: 416.03699.

4-Methoxy-N-(5-(1-methyl-2-oxoindolin-3-ylidene)-4-oxo-4,5-dihydrothiazol-2-yl)benzenesulfonamide (**112**)

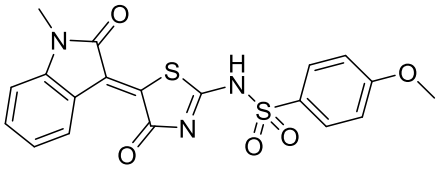

Following the general procedure H, the product was obtained as a red-brown solid after filtration and washing using water, ethanol, and diethyl ether (41.10 mg, 0.1 mmol, 59%). **^{1}H NMR** (600 MHz, DMSO-d_6) δ 13.25 (s, 1H), 8.77 (dd, *J* = 8.1, 1.2 Hz, 1H), 7.88 – 7.82 (m, 2H), 7.47 (td, *J* = 7.7, 1.2 Hz, 1H), 7.19 – 7.15 (m, 2H), 7.15 – 7.10 (m, 2H), 3.85 (s, 3H), 3.25 (s, 3H). **^{13}C NMR** (151 MHz, DMSO-d_6) δ 172.48, 167.83, 167.32, 163.45, 145.45, 133.18, 132.31, 131.86, 129.31, 128.40, 127.08, 123.10, 119.73, 115.11, 109.81, 56.28, 26.84. **HRMS**-ESI (*m/z*): calculated for $[M+H]^+$ $C_{19}H_{15}N_3O_5S_2$, 430.04531; found: 430.91367; 452.03465 $[M+Na]^+$.

N-(5-(5-Bromo-2-oxoindolin-3-ylidene)-4-oxo-4,5-dihydrothiazol-2-yl)-4-methoxybenzenesulfonamide (**113**)

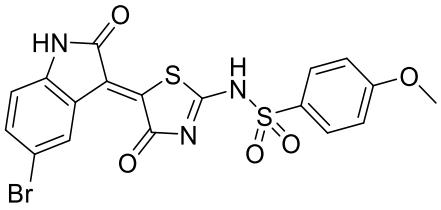

Following the general procedure H, the product was obtained as a red-brown solid after filtration and washing using water, ethanol, and diethyl ether (71.10 mg, 0.14 mmol, 85%). **^{1}H NMR** (600 MHz, DMSO-d_6) δ 13.30 (s, 1H), 11.40 (s, 1H), 8.92 (s, 1H), 7.84 (d, *J* = 8.5 Hz, 2H), 7.57 (d, *J* = 8.5 Hz, 1H), 7.16 (d, *J* = 8.5 Hz, 2H), 6.91 (d, *J* = 8.5 Hz, 1H), 3.85 (s, 3H).**^{13}C NMR** (151 MHz, DMSO-d_6) δ 168.61, 167.56, 167.41, 163.48, 143.51, 135.24, 133.45, 132.23, 130.70, 129.32, 126.50, 122.19, 115.13, 114.03, 112.87, 56.28. **HRMS**-ESI (*m/z*): calculated for $[M+H]^+$ $C_{18}H_{12}{}^{79}BrN_3O_5S_2$, 493.94018; found: 493.94571. Calculated for $[M+H]^+$ $C_{18}H_{12}{}^{81}BrN_3O_5S_2$, 495.94018; found: 495.94571.

N-(5-(5-Bromo-1-methyl-2-oxoindolin-3-ylidene)-4-oxo-4,5-dihydrothiazol-2-yl)-4-methoxybenzenesulfonamide (**114**)

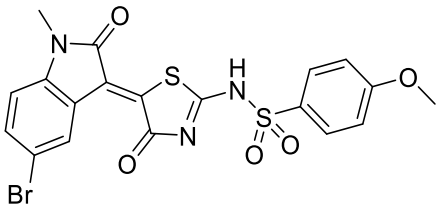

Following the general procedure H, the product was obtained as a red-brown solid after filtration and washing using water, ethanol, and diethyl ether (72.50 mg, 0.14 mmol, 82%). **^{1}H NMR** (600 MHz, DMSO-d_6) δ 13.36 (s, 1H), 8.92 (d, *J* = 2.1 Hz, 1H), 7.90 – 7.82 (m, 2H), 7.66 (dd, *J* = 8.4, 2.1 Hz, 1H), 7.19 – 7.15 (m, 2H), 7.11 (d, *J* = 8.4 Hz, 1H), 3.85 (s, 3H), 3.24 (s, 3H). **^{13}C NMR** (151 MHz, DMSO-d_6) δ 172.48, 167.46, 166.99, 163.50, 144.44, 135.06, 134.07, 132.17, 130.40, 129.36, 125.50, 121.37, 115.13, 114.69, 111.74, 56.29, 26.99. **HRMS**-ESI (*m/z*): calculated for $[M+H]^+$ $C_{19}H_{14}{}^{79}BrN_3O_5S_2$, 507.96310; found: 507.96353. Calculated for $[M+H]^+$ $C_{19}H_{14}{}^{81}BrN_3O_5S_2$, 509.96105; found: 509.96132.

4-Methoxy-N-(4-oxo-5-(2-oxo-1-phenylindolin-3-ylidene)-4,5-dihydrothiazol-2-yl)benzenesulfonamide (**115**)

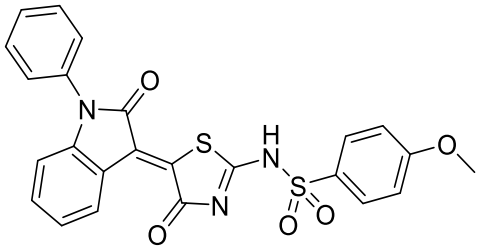

Following the general procedure H, the product was obtained as a red-brown solid after filtration and washing using water, ethanol, and diethyl ether (59.00 mg, 0.12 mmol, 71%). **^{1}H NMR** (600 MHz, DMSO-d_6) δ 13.32 (s, 1H), 8.91 (dd, *J* = 8.0, 1.2 Hz, 1H), 7.89 – 7.79 (m, 2H), 7.68 – 7.59 (m, 2H), 7.58 – 7.49 (m, 3H), 7.42 (td, *J* = 7.7, 1.3 Hz, 1H), 7.20 (td, *J* = 7.7, 1.2 Hz, 1H), 7.18 – 7.13 (m, 2H), 6.82 (dt, *J* = 7.9, 0.8 Hz, 1H), 3.85 (s, 3H). **^{13}C NMR** (151 MHz, DMSO-d_6) δ 172.48, 167.64, 167.24 – 167.09 (m), 166.98, 163.47, 145.20, 133.76, 133.18, 132.89 – 132.68 (m), 132.24, 130.25, 129.32, 129.15, 128.77, 127.36, 126.88, 123.69, 119.98, 115.12, 110.12, 56.28. **HRMS**-ESI (*m/z*): calculated for $[M+H]^+$ $C_{24}H_{17}N_3O_5S_2$, 492.026824; found: 492.06859.

N-(5-(7-Fluoro-2-oxoindolin-3-ylidene)-4-oxo-4,5-dihydrothiazol-2-yl)-4-methoxybenzenesulfonamide (**116**)

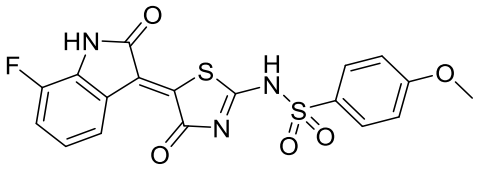

Following the general procedure H, the product was obtained as a red solid after filtration and washing using water, ethanol, and diethyl ether (46.30 mg, 0.11 mmol, 65%). **^{1}H NMR** (600 MHz, DMSO-d_6) δ 13.28 (s, 1H), 11.80 (s, 1H), 8.62 (dt, *J* = 7.9, 0.8 Hz, 1H), 7.87 – 7.82 (m, 2H), 7.37-7.33 (m, 1H), 7.19 – 7.14 (m, 2H), 7.09 (td, *J* = 8.2, 5.1 Hz, 1H), 3.85 (s, 3H). **^{13}C NMR** (151 MHz, DMSO-d_6) δ 168.81, 163.46, 147.86, 146.25, 132.28, 131.50 (d, *J* = 13.1 Hz), 129.31, 127.00, 124.68, 123.11 (dd, *J* = 7.5, 4.9 Hz), 119.69 (d, *J* = 16.7 Hz), 115.12, 56.28. **^{19}F NMR** (470 MHz, DMSO-d_6) δ -132.68 (dd, *J* = 10.0, 5.1 Hz). **HRMS**-ESI (*m/z*): calculated for $[M+H]^+$ $C_{18}H_{12}FN_3O_5S_2$, 434.02024; found: 434.02749; 456.00953 $[M+Na]^+$.

N-(5-(6-Fluoro-2-oxoindolin-3-ylidene)-4-oxo-4,5-dihydrothiazol-2-yl)-4-methoxybenzenesulfonamide (**117**)

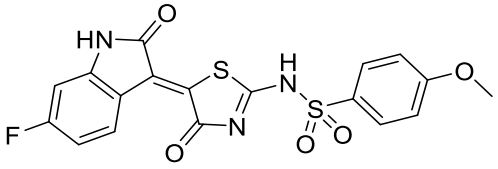

Following the general procedure H, the product was obtained as a red solid after filtration and washing using water, ethanol, and diethyl ether (61.20 mg, 0.14 mmol, 83%). **^{1}H NMR** (600 MHz, DMSO-d_6) δ 13.31 (s, 1H), 11.29 (s, 1H), 8.55 (dd, *J* = 10.1, 2.8 Hz, 1H), 7.87 – 7.82 (m, 2H), 7.27 (td, *J* = 8.8, 2.8 Hz, 1H), 7.19 – 7.14 (m, 2H), 6.94 (dd, *J* = 8.8, 4.6 Hz, 1H), 3.85 (s, 3H). **^{13}C NMR** (151 MHz, DMSO-d_6) δ 169.33, 167.92, 167.50 – 167.28 (m), 165.71, 164.05, 163.44, 146.69 (d, *J* = 12.6 Hz), 132.33, 130.98 (d, *J* = 10.1 Hz), 129.28, 126.87, 117.18, 115.11, 109.16 (d, *J* = 22.3 Hz), 99.09 (d, *J* = 27.4 Hz), 56.28. **^{19}F NMR** (565 MHz, DMSO-d_6) δ -104.23. **HRMS**-ESI (*m/z*): calculated for $[M+H]^+$ $C_{18}H_{12}FN_3O_5S_2$, 434.02752.; found: 434.02718.

N-(5-(5-Fluoro-2-oxoindolin-3-ylidene)-4-oxo-4,5-dihydrothiazol-2-yl)-4-methoxybenzenesulfonamide (**118**)

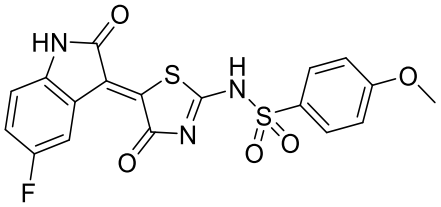

Following the general procedure H, the product was obtained as a red solid after filtration and washing using water, ethanol, and diethyl ether (38.60 mg, 0.09 mmol, 52%). **^{1}H NMR** (600 MHz, DMSO-d_6) δ 13.23 (s, 1H), 11.44 (s, 1H), 8.81 (dd, *J* = 8.9, 5.8 Hz, 1H), 7.86 – 7.82 (m, 2H), 7.18 – 7.14 (m, 2H), 6.90 (td, *J* = 9.1, 2.3 Hz, 1H), 6.77 (dd, *J* = 8.9, 2.3 Hz, 1H), 3.85 (s, 3H).**^{13}C NMR** (151 MHz, DMSO-d_6) δ 168.93, 167.76, 167.42, 163.48, 158.70, 157.14, 140.89, 132.24, 129.31, 127.30, 127.28, 121.10 (d, *J* = 10.3 Hz), 119.57 (d, *J* = 24.2 Hz), 115.31, 115.12, 111.77 (d, *J* = 8.2 Hz), 56.28, 40.53. **^{19}F NMR** (470 MHz, DMSO-d_6) δ -121.06 (td, *J* = 9.4, 4.4 Hz). **HRMS**-ESI (*m/z*): calculated for $[M+H]^+$ $C_{18}H_{12}FN_3O_5S_2$, 434.02752.; found: 434.02738.

N-(5-(7-Chloro-2-oxoindolin-3-ylidene)-4-oxo-4,5-dihydrothiazol-2-yl)-4-methoxybenzenesulfonamide (**119**)

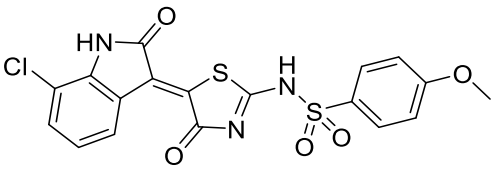

Following the general procedure H, the product was obtained as a red solid after filtration and washing using water, ethanol, and diethyl ether (64.80 mg, 0.14 mmol, 85%). **^{1}H NMR** (600 MHz, DMSO-d_6) δ 13.29 (s, 1H), 11.69 (s, 1H), 8.74 (d, *J* = 8.0 Hz, 1H), 7.88 – 7.82 (m, 2H), 7.48 (dt, *J* = 8.2, 1.2 Hz, 1H), 7.18 – 7.14 (m, 2H), 7.10 (td, *J* = 8.0, 1.0 Hz, 1H), 3.85 (s, 3H).**^{13}C NMR** (151 MHz, DMSO-d_6) δ 168.96, 167.63, 167.17, 163.47, 141.81, 133.47, 132.56, 132.26, 129.31, 127.12, 123.62, 122.18, 115.15, 115.12, 56.28. **HRMS**-ESI (*m/z*): calculated for $[M+H]^+$ $C_{18}H_{12}ClN_3O_5S_2$, 449.99069.; found: 449.99741.

N-(5-(6-Chloro-2-oxoindolin-3-ylidene)-4-oxo-4,5-dihydrothiazol-2-yl)-4-methoxybenzenesulfonamide (**120**)

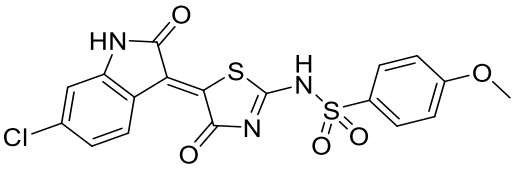

Following the general procedure H, the product was obtained as a red solid after filtration and washing using water, ethanol, and diethyl ether (61.70 mg, 0.14 mmol, 81%). **^{1}H NMR** (600 MHz, DMSO-d_6) δ 13.27 (s, 1H), 11.42 (s, 1H), 8.73 (d, *J* = 8.5 Hz, 1H), 7.88 – 7.77 (m, 2H), 7.18 – 7.14 (m, 2H), 7.13 (dd, *J* = 8.5, 2.0 Hz, 1H), 6.95 (d, *J* = 2.0 Hz, 1H), 3.85 (s, 3H).**^{13}C NMR** (151 MHz, DMSO-d_6) δ 168.98, 167.76, 167.28, 163.46, 145.74, 137.15, 132.28, 132.11, 129.93, 129.30, 126.68, 122.39, 119.35, 115.11, 110.96, 56.28. **HRMS**-ESI (*m/z*): calculated for $[M+H]^+$ $C_{18}H_{12}ClN_3O_5S_2$, 449.99069.; found: 449.99801.

N-(5-(5-Fluoro-1-methyl-2-oxoindolin-3-ylidene)-4-oxo-4,5-dihydrothiazol-2-yl)-4-methoxybenzenesulfonamide (**121**)

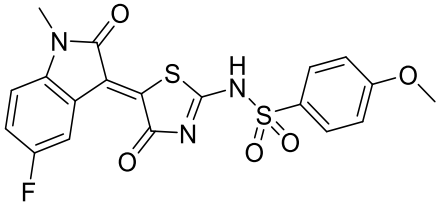

Following the general procedure H, the product was obtained as a red solid after filtration and washing using water, ethanol, and diethyl ether (61.10 mg, 0.14 mmol, 82%). **^{1}H NMR** (700 MHz, DMSO-d_6) δ 13.34 (s, 1H), 8.58 (dd, *J* = 10.0, 2.7 Hz, 1H), 7.91 – 7.79 (m, 2H), 7.36 (td, *J* = 8.8, 2.7 Hz, 1H), 7.18 – 7.12 (m, 3H), 3.85 (s, 3H), 3.25 (s, 3H). **^{13}C NMR** (176 MHz, DMSO-d_6) δ 167.22, 163.49, 159.04, 157.70, 141.84, 132.19, 129.34, 120.41 (d, *J* = 10.1 Hz), 119.23 (d, *J* = 24.6 Hz), 115.24, 115.13, 115.08, 110.70 (d, *J* = 8.1 Hz), 56.29, 27.02.**^{19}F NMR** (470 MHz, DMSO-d_6) δ -120.54 (td, *J* = 9.3, 4.3 Hz). **HRMS**-ESI (*m/z*): calculated for $[M+H]^+$ $C_{19}H_{14}FN_3O_5S_2$, 448.04317; found: 448.04331.

N-(5-(6-Fluoro-1-methyl-2-oxoindolin-3-ylidene)-4-oxo-4,5-dihydrothiazol-2-yl)-4-methoxybenzenesulfonamide (**122**)

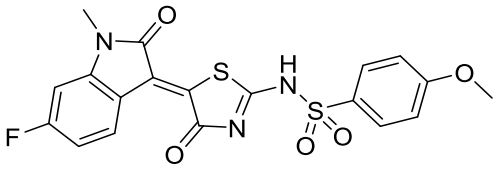

Following the general procedure H, the product was obtained as a red solid after filtration and washing using water, ethanol, and diethyl ether (50.00 mg, 0.11 mmol, 67%). **^{1}H NMR** (600 MHz, DMSO-d_6) δ 13.25 (s, 1H), 8.83 (dd, *J* = 8.7, 5.9 Hz, 1H), 7.88 – 7.80 (m, 2H), 7.20 – 7.11 (m, 3H), 6.96 (ddd, *J* = 9.5, 8.7, 2.5 Hz, 1H), 3.84 (s, 3H), 3.25 (s, 3H). **^{13}C NMR** (151 MHz, DMSO-d_6) δ 167.83, 165.96, 164.30, 163.45, 147.85 (d, *J* = 12.5 Hz), 132.29, 130.58 (d, *J* = 10.0 Hz), 129.30, 116.34, 115.11, 109.32 (d, *J* = 22.3 Hz), 98.67 (d, *J* = 28.3 Hz), 56.28, 27.15.**^{19}F NMR** (470 MHz, DMSO-d_6) δ -104.18, -106.76 (td, *J* = 9.8, 6.4 Hz). **HRMS**-ESI (*m/z*): calculated for $[M+H]^+$ $C_{19}H_{14}FN_3O_5S_2$, 448.04317; found: 448.04333.

N-(5-((1H-Indol-2-yl)methylene)-4-oxo-4,5-dihydrothiazol-2-yl)-4-methoxybenzenesulfonamide (**123**)

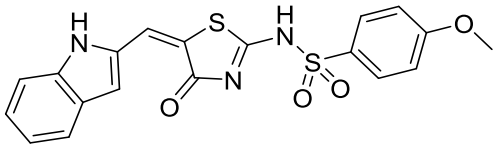

Following the general procedure H, the product was obtained as a yellow solid after filtration and washing using water and diethyl ether (22.70 mg, 0.06 mmol, 32%). **^{1}H NMR** (700 MHz, DMSO-d_6) δ 12.46 (s, 1H), 11.97 (s, 1H), 9.86 (s, 1H), 7.81 – 7.78 (m, 2H), 7.75 (dd, *J* = 8.2, 1.1 Hz, 1H), 7.46 (dq, *J* = 8.2, 1.0 Hz, 1H), 7.40 (dd, *J* = 2.2, 1.0 Hz, 1H), 7.34 (ddd, *J* = 8.2, 6.9, 1.1 Hz, 1H), 7.16 – 7.12 (m, 2H), 4.04 (s, 2H), 3.85 (s, 3H). **^{13}C NMR** (176 MHz, DMSO-d_6) δ 183.47, 174.21, 172.47, 163.24, 138.87, 136.81, 132.69, 129.16, 127.23, 126.82, 123.51, 120.95, 114.93, 114.62, 113.39, 56.22, 35.36. **HRMS**-ESI (*m/z*): calculated for $[M+H]^+$ $C_{19}H_{15}N_3O_4S_2$, 414.05767; found: 414.05767.

N-(5-(5-Chloro-2-oxoindolin-3-ylidene)-4-oxo-4,5-dihydrothiazol-2-yl)-4-methylbenzenesulfonamide (**124**)

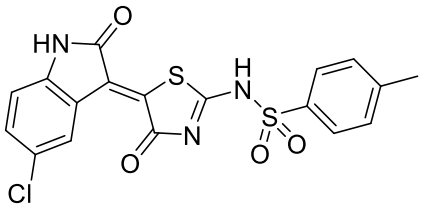

Following the general procedure H, the product was obtained as a red solid after filtration and washing using water, ethanol, and diethyl ether (172.0 mg, 0.4 mmol, 48%). **^{1}H NMR** (600 MHz, DMSO-d_6) δ 13.36 (s, 1H), 11.40 (s, 1H), 8.79 (d, *J* = 2.2 Hz, 1H), 7.88 – 7.72 (m, 2H), 7.50 – 7.39 (m, 3H), 6.96 (d, *J* = 8.4 Hz, 1H), 2.41 (s, 3H). **^{13}C NMR** (151 MHz, DMSO-d_6) δ 168.72, 168.31, 167.47, 144.50, 143.19, 137.81, 133.41, 132.50, 130.36, 127.92, 127.05, 126.70, 126.32, 121.70, 112.40, 21.54. **HRMS**-ESI (*m/z*): calculated for $[M+H]^+$ $C_{18}H_{12}ClN_3O_4S_2$, 434.00305; found: 434.00303.

N-(5-(5-Chloro-2-oxoindolin-3-ylidene)-4-oxo-4,5-dihydrothiazol-2-yl)benzenesulfonamide (**125**)

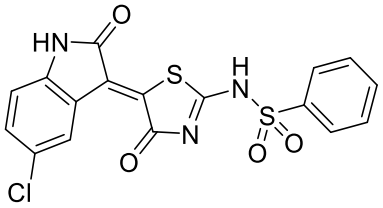

Following the general procedure H, the product was obtained as a red solid after filtration and washing using water, ethanol, and diethyl ether (166.5 mg, 0.3 mmol, 64%). **^{1}H NMR** (700 MHz, DMSO-d_6) δ 13.40 (s, 1H), 11.41 (s, 1H), 8.78 (d, *J* = 2.2 Hz, 1H), 8.00 – 7.86 (m, 2H), 7.77 – 7.70 (m, 1H), 7.69 – 7.63 (m, 2H), 7.44

(dd, *J* = 8.4, 2.2 Hz, 1H), 6.96 (d, *J* = 8.4 Hz, 1H). **^{13}C NMR** (176 MHz, DMSO-d_6) δ 168.74, 168.71, 167.49, 143.20, 140.65, 133.98, 133.39, 132.52, 129.97, 127.92, 126.98, 126.77, 126.33, 121.68, 112.41. **HRMS**-ESI (*m/z*): calculated for $[M+H]^+$ $C_{17}H_{10}ClN_3O_4S_2$, 419.98740; found: 419.98754.

N-(5-(5-Chloro-2-oxoindolin-3-ylidene)-4-oxo-4,5-dihydrothiazol-2-yl)-3,5-difluorobenzenesulfonamide (**126**)

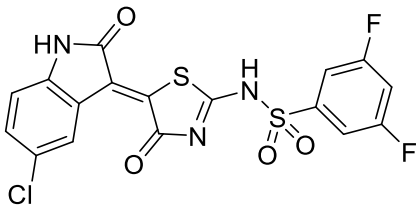

Following the general procedure H, the product was obtained as a red solid after filtration and washing using water, ethanol, and diethyl ether (60.40 mg, 0.13 mmol, 78%). **^{1}H NMR** (600 MHz, DMSO-d_6) δ 13.61 (s, 1H), 11.42 (s, 1H), 8.79 (d, *J* = 2.2 Hz, 1H), 7.71 (tt, *J* = 9.2, 2.4 Hz, 1H), 7.67 – 7.59 (m, 2H), 7.46 (dd, *J* = 8.4, 2.2 Hz, 1H), 6.97 (d, *J* = 8.4 Hz, 1H).**^{13}C NMR** (151 MHz, DMSO-d_6) δ 172.48, 170.96, 170.95, 168.70, 167.93, 167.92, 163.53 (d, *J* = 12.2 Hz), 161.86 (d, *J* = 12.2 Hz), 144.00 (t, *J* = 8.6 Hz), 143.27, 133.90 – 132.63 (m), 132.65, 127.90, 126.94, 126.38, 121.64, 112.47, 111.04 – 110.60 (m), 109.70 (t, *J* = 25.7 Hz), 40.52. **^{19}F NMR** (470 MHz, DMSO-d_6) δ -105.88 (t, *J* = 6.9 Hz). **HRMS**-ESI (*m/z*): calculated for $[M+H]^+$ $C_{17}H_8ClF_2N_3O_4S_2$, 455.96128; found: 455.96874.

N-(5-(5-Chloro-2-oxoindolin-3-ylidene)-4-oxo-4,5-dihydrothiazol-2-yl)-3-nitrobenzenesulfonamide (**127**)

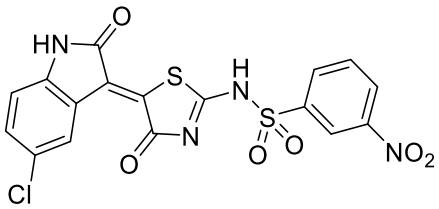

Following the general procedure H, the product was obtained as an orange solid after filtration and washing using water, ethanol, and diethyl ether (60.20 mg, 0.13 mmol, 76%). **^{1}H NMR** (600 MHz, DMSO-d_6) δ 12.69 (s, 1H), 11.42 (s, 1H), 8.80 (d, *J* = 2.2 Hz, 2H), 8.58 – 8.50 (m, 1H), 8.35 (d, *J* = 8.0 Hz, 1H), 7.96 (t, *J* = 8.0 Hz, 1H), 7.47 (dd, *J* = 8.4, 2.2 Hz, 1H), 6.98 (d, *J* = 8.4 Hz, 1H). **^{13}C NMR** (151 MHz, DMSO-d_6) δ 172.48, 171.02, 168.74, 168.29 148.36, 143.24, 142.34, 133.44, 133.02, 132.62, 132.10, 128.42, 127.90, 126.86, 126.36, 121.69, 112.47. **HRMS**-ESI (*m/z*): calculated for $[M+H]^+$ $C_{17}H_9ClN_4O_6S_2$, 464.96520; found: 464.94006.

4-(tert-Butyl)-N-(5-(5-chloro-2-oxoindolin-3-ylidene)-4-oxo-4,5-dihydrothiazol-2-yl)benzenesulfonamide (**128**)

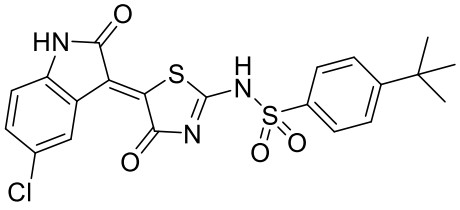

Following the general procedure H, the product was obtained as a red solid after filtration and washing using water, ethanol, and diethyl ether (60.00 mg, 0.13 mmol, 79%). **^{1}H NMR** (600 MHz, DMSO-d_6) δ 13.35 (s, 1H), 11.41 (s, 1H), 8.79 (d, *J* = 2.2 Hz, 1H), 7.88 – 7.80 (m, 2H), 7.70 – 7.65 (m, 2H), 7.45 (dd, *J* = 8.4, 2.2 Hz, 1H), 6.96 (d, *J* = 8.4 Hz, 1H), 1.31 (s, 9H). **^{13}C NMR** (151 MHz, DMSO-d_6) δ 168.72, 168.33, 167.48, 157.12, 143.19, 137.80, 133.43, 132.50, 127.92, 126.94, 126.82, 126.70,

126.32, 121.71, 112.41, 35.46, 31.21. **HRMS-**ESI (*m/z*): calculated for $[M+H]^+$ $C_{21}H_{18}ClN_3O_4S_2$, 476.05000; found: 476.05030.

2-Chloro-N-(5-(5-chloro-2-oxoindolin-3-ylidene)-4-oxo-4,5-dihydrothiazol-2-yl)-4-fluorobenzenesulfonamide (**129**)

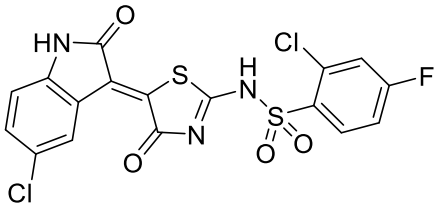

Following the general procedure H, the product was obtained as a red solid after filtration and washing using water, ethanol, and diethyl ether (61.50 mg, 0.13 mmol, 81%). **^{1}H NMR** (600 MHz, DMSO-d_6) δ 13.51 (s, 1H), 11.41 (s, 1H), 8.79 (d, *J* = 2.2 Hz, 1H), 8.20 (dd, *J* = 8.9, 5.9 Hz, 1H), 7.79 (dd, *J* = 8.6, 2.6 Hz, 1H), 7.51 (ddd, *J* = 8.9, 8.0, 2.6 Hz, 1H), 7.46 (dd, *J* = 8.4, 2.2 Hz, 1H), 6.97 (d, *J* = 8.4 Hz, 1H).**^{13}C NMR** (151 MHz, DMSO-d_6) δ 170.35, 168.71, 167.65, 165.62, 163.92, 143.28, 134.70 (d, *J* = 3.3 Hz), 133.97 (d, *J* = 11.6 Hz), 133.18, 133.18, 132.73, 132.66, 132.62, 127.94, 127.02, 126.35, 121.69, 120.06 (d, *J* = 26.2 Hz), 115.61 (d, *J* = 22.0 Hz), 112.45. **^{19}F NMR** (470 MHz, DMSO-d_6) δ -103.44. **HRMS-**ESI (*m/z*): calculated for $[M+H]^+$ $C_{17}H_8Cl_2FN_3O_4S_2$, 471.93901; found: 471.93950.

N-(5-(5-Chloro-2-oxoindolin-3-ylidene)-4-oxo-4,5-dihydrothiazol-2-yl)-4-cyclohexylbenzenesulfonamide (**130**)

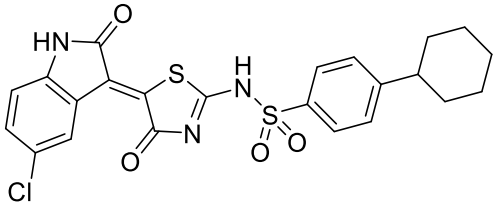

Following the general procedure H, the product was obtained as a red solid after filtration and washing using water, ethanol, and diethyl ether (60.10 mg, 0.12 mmol, 80%). **^{1}H NMR** (600 MHz, DMSO-d_6) δ 13.35 (s, 1H), 11.40 (s, 1H), 8.78 (d, *J* = 2.2 Hz, 1H), 7.82 (d, *J* = 8.4 Hz, 2H), 7.50 (d, *J* = 8.4 Hz, 2H), 7.44 (dd, *J* = 8.4, 2.2 Hz, 1H), 6.96 (d, *J* = 8.4 Hz, 1H), 2.62 (d, *J* = 29.3 Hz, 1H), 1.81-1.77 (m, 4H), 1.74 – 1.66 (m, 1H), 1.48 – 1.30 (m, 4H), 1.27-1.20 (m, 1H). **^{13}C NMR** (176 MHz, DMSO-d_6) δ 168.72, 168.23, 167.41, 154.00, 143.18, 138.09, 133.43, 132.49, 128.23, 127.91, 127.17, 126.69, 126.32, 121.70, 112.40, 44.14, 33.95, 26.59, 25.88. **HRMS-**ESI (*m/z*): calculated for $[M+H]^+$ $C_{23}H_{20}ClN_3O_4S_2$, 502.05838; found: 502.43341.

N-(5-(5-Chloro-2-oxoindolin-3-ylidene)-4-oxo-4,5-dihydrothiazol-2-yl)-[1,1'-biphenyl]-4-sulfonamide (**131**)

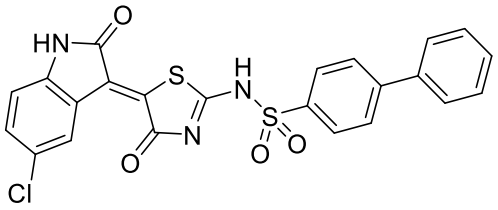

Following the general procedure H, the product was obtained as a red solid after filtration and washing using water, ethanol, and diethyl ether (61.10 mg, 0.12 mmol, 82%). **^{1}H NMR** (600 MHz, DMSO-d_6) δ 13.41 (s, 1H), 11.41 (s, 1H), 8.79 (d, *J* = 2.2 Hz, 1H), 8.02 – 7.96 (m, 2H), 7.96 – 7.92 (m, 2H), 7.77 – 7.72 (m, 2H), 7.52 (dd, *J* = 8.4, 7.0 Hz, 2H), 7.48 – 7.43 (m, 2H), 6.97 (d, *J* = 8.4 Hz, 1H). **^{13}C NMR** (151 MHz, DMSO-d_6) δ 168.73, 168.60, 167.51, 145.45, 143.21, 143.03,

139.34, 138.83, 133.36, 132.54, 129.65, 129.18, 128.15, 127.93, 127.70, 127.64, 126.78, 126.34, 121.70, 121.66, 112.43. **HRMS**-ESI (*m/z*): calculated for $[M+H]^+$ $C_{23}H_{14}ClN_3O_4S_2$, 496.01870; found: 496.01910.

4-(N-(5-(5-Chloro-2-oxoindolin-3-ylidene)-4-oxo-4,5-dihydrothiazol-2-yl)sulfamoyl)benzoic acid (**132**)

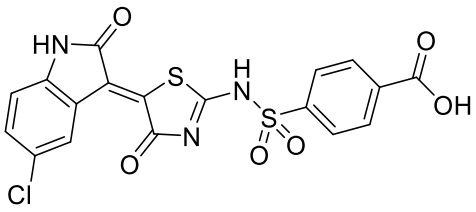

Following the general procedure H, the product was obtained as a red-brown solid after filtration and washing using water, ethanol, and diethyl ether (d.r. = 1:1) 47.0 mg, 0.1 mmol, 78%). **^{1}H NMR** (600 MHz, DMSO-d_6) δ 13.52 (s, 1H), 11.41 (s, 1H), 8.78 (d, *J* = 2.0 Hz, 1H), 8.35 (d, *J* = 2.0 Hz, 1H), 8.18 – 8.15 (m, 1H), 8.06 – 8.02 (m, 2H), 7.44 (dd, *J* = 4.4, 2.0 Hz, 1H), 6.96 (d, *J* = 8.4 Hz, 1H), 4.08 (s, 1H). **^{13}C NMR** (151 MHz, DMSO-d_6) δ 174.26, 168.70, 166.54, 144.75, 144.20, 143.31, 135.42, 132.63, 130.79, 127.92, 127.33, 126.88, 126.36, 121.66, 112.44, 35.66. **HRMS**-ESI (*m/z*): calculated for $[M+H]^+$ $C_{18}H_{10}ClN_3O_6S_2$, 463.97723; found: 463.97758.

5-Bromo-N-(5-(5-chloro-2-oxoindolin-3-ylidene)-4-oxo-4,5-dihydrothiazol-2-yl)-2-methoxybenzenesulfonamide (**133**)

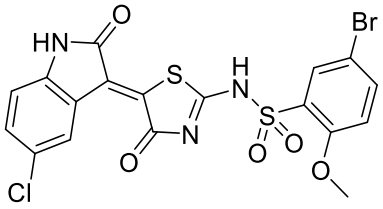

Following the general procedure H, the product was obtained as a red-brown solid after filtration and washing using water, ethanol, and diethyl ether (58.50 mg, 0.11 mmol, 79%). **^{1}H NMR** (600 MHz, DMSO-d_6) δ 13.42 (s, 1H), 11.40 (s, 1H), 8.82 (d, *J* = 2.2 Hz, 1H), 7.93 (d, *J* = 2.6 Hz, 1H), 7.88 (dd, *J* = 8.9, 2.6 Hz, 1H), 7.46 (dd, *J* = 8.4, 2.2 Hz, 1H), 7.26 (d, *J* = 8.9 Hz, 1H), 6.98 (d, *J* = 8.4 Hz, 1H), 3.85 (s, 3H). **^{13}C NMR** (151 MHz, DMSO-d_6) δ 169.88, 168.75, 167.48, 156.71, 143.23, 138.37, 133.47, 132.51, 130.92, 129.69, 127.92, 126.83, 126.30, 121.77, 116.33, 112.40, 111.62, 57.30. **HRMS**-ESI (*m/z*): calculated for $[M+H]^+$ $C_{18}H_{11}{}^{79}BrClN_3O_5S_2$, 527.90848; found: 527.90910. Calculated for $[M+H]^+$ $C_{18}H_{11}{}^{81}BrClN_3O_5S_2$, 529.90643; found: 529.90667.

N-(5-(5-Chloro-2-oxoindolin-3-ylidene)-4-oxo-4,5-dihydrothiazol-2-yl)methanesulfonamide (**134**)

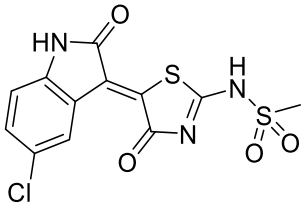

Following the general procedure H, the product was obtained as a brown solid after filtration and washing using water, ethanol, and diethyl ether (63.60 mg, 0.18 mmol, 74%). **^{1}H NMR** (700 MHz, DMSO-d_6) δ 13.35 (s, 1H), 11.38 (s, 1H), 8.80 (d, *J* = 2.3 Hz, 1H), 7.45 (dd, *J* = 8.3, 2.3 Hz, 1H), 6.96 (d, *J* = 8.3 Hz, 1H), 3.19 (s, 3H). **^{13}C NMR** (151 MHz, DMSO-d_6) δ 168.69, 167.55, 143.14, 133.52, 132.44, 127.90, 127.70, 126.51, 126.32, 121.69, 112.39, 42.12. **HRMS**-ESI (*m/z*): calculated for $[M+H]^+$ $C_{12}H_8ClN_3O_4S_2$, 357.97175; found: 357.97170.

N-(5-(5-Chloro-2-oxoindolin-3-ylidene)-4-oxo-4,5-dihydrothiazol-2-yl)-4-(trifluoromethyl)benzenesulfonamide (**135**)

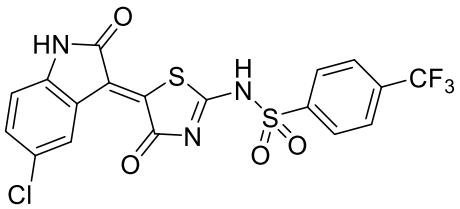

Following the general procedure H, the product was obtained as a red-brown solid after filtration and washing using water, ethanol, and diethyl ether (64.10 mg, 0.13 mmol, 85%). **^{1}H NMR** (700 MHz, DMSO-d_6) δ 13.51 (s, 1H), 11.42 (d, *J* = 5.1 Hz, 1H), 8.77 (d, *J* = 4.8 Hz, 1H), 8.13 (t, *J* = 6.4 Hz, 2H), 8.04 (dd, *J* = 8.4, 4.8 Hz, 2H), 7.45 (t, *J* = 7.1 Hz, 1H), 6.96 (dd, *J* = 8.4, 4.7 Hz, 1H). **^{13}C NMR** (176 MHz, DMSO-d_6) δ 170.32, 168.68, 167.69, 144.51, 143.26, 133.43 (q, *J* = 34.5, 33.6 Hz), 132.64, 128.05, 127.91, 127.20, 127.18, 126.96, 126.37, 124.63, 123.08, 121.63, 112.46, 55.79. **^{19}F NMR** (470 MHz, DMSO-d_6) δ -61.71. **HRMS**-ESI (*m/z*): calculated for $[M+H]^+$ $C_{18}H_9ClF_3N_3O_4S_2$, 487.97479; found: 487.97524.

N-(5-(5-Chloro-2-oxoindolin-3-ylidene)-4-oxo-4,5-dihydrothiazol-2-yl)naphthalene-2-sulfonamide (**136**)

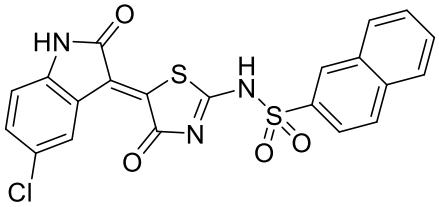

Following the general procedure H, the product was obtained as a red solid after filtration and washing using water, ethanol, and diethyl ether (65.60 mg, 0.14 mmol, 88%). **^{1}H NMR** (600 MHz, DMSO-d_6) δ 13.41 (s, 1H), 11.41 (s, 1H), 8.78 (d, *J* = 2.2 Hz, 1H), 8.62 (d, *J* = 1.9 Hz, 1H), 8.24 (dd, *J* = 8.4, 1.3 Hz, 1H), 8.18 (d, *J* = 8.7 Hz, 1H), 8.11 – 8.06 (m, 1H), 7.90 (dd, *J* = 8.7, 1.9 Hz, 1H), 7.74 (ddd, *J* = 8.2, 6.8, 1.3 Hz, 1H), 7.70 (ddd, *J* = 8.2, 6.8, 1.3 Hz, 1H), 7.44 (dd, *J* = 8.4, 2.2 Hz, 1H), 6.96 (d, *J* = 8.4 Hz, 1H). **^{13}C NMR** (151 MHz, DMSO-d_6) δ 168.77, 168.72, 167.51, 143.20, 137.66, 135.00, 133.39, 132.52, 132.13, 130.09, 129.94, 129.73, 128.37, 128.28, 127.97, 127.91, 126.77, 126.33, 122.54, 121.69, 112.41. **HRMS**-ESI (*m/z*): calculated for $[M+H]^+$ $C_{21}H_{12}ClN_3O_4S_2$, 470.00305; found: 470.00334.

N-(5-(5-Chloro-2-oxoindolin-3-ylidene)-4-oxo-4,5-dihydrothiazol-2-yl)-4-cyanobenzenesulfonamide (**137**)

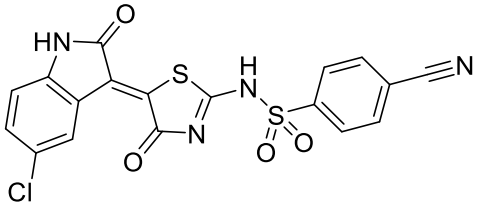

Following the general procedure H, the product was obtained as a bright red solid after filtration and washing using water, ethanol, and diethyl ether (49.10 mg, 0.11 mmol, 85%). **^{1}H NMR** (600 MHz, DMSO-d_6) δ 12.69 (s, 1H), 11.41 (s, 1H), 8.89 – 8.73 (m, 1H), 8.17 – 8.04 (m, 4H), 7.47 (dd, *J* = 8.4, 2.3 Hz, 1H), 6.98 (d, *J* = 8.4 Hz, 1H). **^{13}C NMR** (151 MHz, DMSO-d_6) δ 168.76, 144.82, 143.20, 134.08, 134.03, 132.55, 127.90, 127.76, 127.63, 126.73, 126.34, 121.72, 118.11, 116.10, 112.44, 21.53. **LC-MS** (*m/z*): calculated for $[M+H]^+$ $C_{18}H_9ClN_4O_4S_2$, 444.9; found: 444.8.

N-(5-(5-Chloro-2-oxoindolin-3-ylidene)-4-oxo-4,5-dihydrothiazol-2-yl)-4-fluorobenzenesulfonamide (**138**)

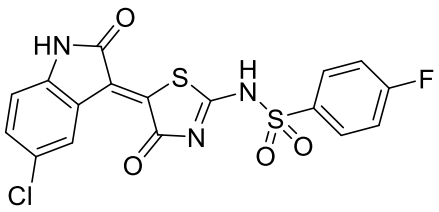

Following the general procedure H, the product was obtained as a red solid after filtration and washing using water, ethanol, and diethyl ether (63.9 mg, 0.15 mmol, 81%). **^{1}H NMR** (700 MHz, DMSO-d_6) δ 13.41 (s, 1H), 11.41 (s, 1H), 8.80 (s, 1H), 7.98 (d, *J* = 7.0 Hz, 2H), 7.66 – 7.27 (m, 3H), 6.98 (d, *J* = 8.3 Hz, 1H).**^{13}C NMR** (176 MHz, DMSO-d_6) δ 168.75, 165.85, 164.42, 143.18, 137.16, 132.52, 130.17 (d, *J* = 9.7 Hz), 127.91, 126.68, 126.32, 121.72, 117.15 (d, *J* = 22.5 Hz), 112.43, 55.84. **^{19}F NMR** (470 MHz, DMSO-d_6) δ -105.25. **HRMS**-ESI (*m/z*): calculated for $[M+H]^+$ $C_{17}H_9ClFN_3O_4S_2$, 437.97798; found: 437.19340.

N-(5-(5-Chloro-2-oxoindolin-3-ylidene)-4-oxo-4,5-dihydrothiazol-2-yl)-4-methylbenzamide (**139**)

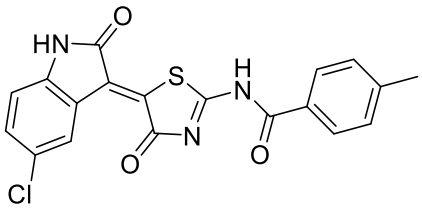

Following the general procedure H, the product was obtained as a red solid after filtration and washing using water, ethanol, and diethyl ether (94.7 mg, 0.24 mmol, 79%). **^{1}H NMR** (600 MHz, DMSO-d_6) δ 13.31 (s, 1H), 11.30 (s, 1H), 8.91 (s, 1H), 8.07 (d, *J* = 7.3 Hz, 2H), 7.44 (dd, *J* = 8.3, 2.2 Hz, 1H), 7.37 (d, *J* = 7.3 Hz, 2H), 6.95 (d, *J* = 8.3 Hz, 1H), 2.40 (s, 3H). **^{13}C NMR** (151 MHz, DMSO-d_6) δ 168.89, 144.62, 143.17, 142.02, 136.06, 132.40, 130.04, 129.81, 129.59, 129.02, 128.60, 127.94, 127.71, 126.21, 121.98, 112.22, 21.75. **HRMS**-ESI (*m/z*): calculated for $[M+H]^+$ $C_{19}H_{12}ClN_3O_3S$, 398.02879.; found: 397.05910.

N-(5-(5-Chloro-2-oxoindolin-3-ylidene)-4-oxo-4,5-dihydrothiazol-2-yl)-4-methoxybenzamide (**140**)

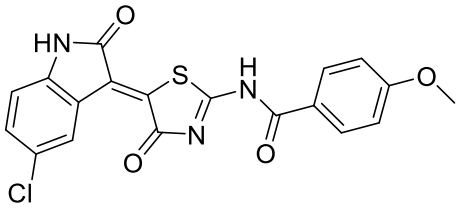

Following the general procedure H, the product was obtained as a red solid after filtration and washing using water, ethanol, and diethyl ether (69.7 mg, 0.17 mmol, 84%). **^{1}H NMR** (600 MHz, DMSO-d_6) δ 13.28 (s, 1H), 11.31 (s, 1H), 8.94 (s, 1H), 8.16 (d, *J* = 8.9 Hz, 2H), 7.46 (dd, *J* = 8.4, 2.3 Hz, 1H), 7.11 (d, *J* = 8.9 Hz, 2H), 6.97 (d, *J* = 8.4 Hz, 1H), 3.88 (s, 3H). **^{13}C NMR** (151 MHz, DMSO-d_6) δ 168.93, 168.76, 167.50, 164.10, 143.14, 143.08, 132.35, 132.26, 127.92, 127.58, 126.19, 126.05, 122.02, 114.58, 112.23, 111.88, 56.10. **HRMS**-ESI (*m/z*): calculated for $[M+H]^+$ $C_{19}H_{12}ClN_3O_4S$, 414.03098; found: 414.26945.

N-(5-(5-Chloro-2-oxoindolin-3-ylidene)-4-oxo-4,5-dihydrothiazol-2-yl)-3,4-dimethoxybenzamide (**141**)

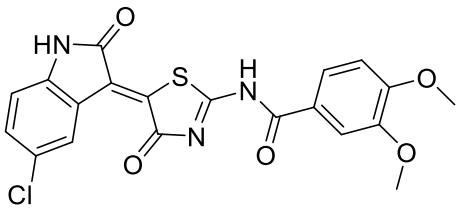

Following the general procedure H, the product was obtained as a red solid after filtration and washing using water, ethanol, and diethyl ether (55.4 mg, 0.12 mmol, 69%). **^{1}H NMR** (600 MHz, DMSO-d_6) δ 13.28 (s, 1H), 11.30 (s, 1H), 8.94 (s, 1H), 7.87 (dd, *J* = 8.4, 2.2 Hz, 1H), 7.71 (s, 1H), 7.46 (dd, *J* = 8.4, 2.2 Hz, 1H), 7.15 (d, *J* = 8.6 Hz, 1H), 6.97 (d, *J* = 8.4 Hz, 1H), 3.88 (s, 3H), 3.85 (s, 3H). **^{13}C NMR** (151 MHz, DMSO-d_6) δ 172.48, 168.94, 153.99, 148.99, 143.15, 132.92, 132.36, 130.12, 127.92, 126.20, 124.57, 123.68, 123.19, 122.03, 112.23, 111.89, 111.60, 56.28, 56.02. **LC-MS** (ESI) (*m/z*): calculated for $[M+H]^+$ $C_{20}H_{14}ClN_3O_5S$, 444.0; found: 444.8.

N-(5-(5-Chloro-2-oxoindolin-3-ylidene)-4-oxo-4,5-dihydrothiazol-2-yl)-4-fluorobenzamide (**142**)

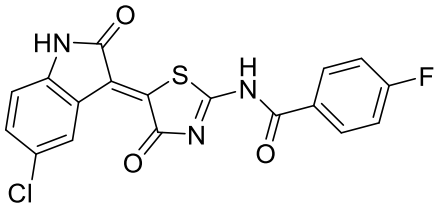

Following the general procedure H, the product was obtained as a red solid after filtration and washing using water, ethanol, and diethyl ether (63.9 mg, 0.16 mmol, 76%). **^{1}H NMR** (600 MHz, DMSO-d_6) δ 13.36 (s, 1H), 11.29 (s, 1H), 8.87 (d, *J* = 2.3 Hz, 1H), 8.21 (dd, *J* = 8.7, 5.7 Hz, 2H), 7.44 – 7.33 (m, 3H), 6.92 (d, *J* = 8.3 Hz, 1H). **^{13}C NMR** (151 MHz, DMSO-d_6) δ 168.82, 166.59, 164.92, 143.20, 143.02, 135.65, 132.86 (d, *J* = 9.7 Hz), 132.44, 131.46, 127.94, 127.60, 126.22, 121.90, 116.28 (d, *J* = 22.0 Hz), 112.19. **^{19}F NMR** (470 MHz, DMSO-d_6) δ -105.49. **LC-MS** (*m/z*): calculated for $[M+H]^+$ $C_{18}H_9ClFN_3O_3S$, 402.0; found: 401.6.

N-(5-(5-Chloro-2-oxoindolin-3-ylidene)-4-oxo-4,5-dihydrooxazol-2-yl)-4-methoxybenzenesulfonamide (**143**)

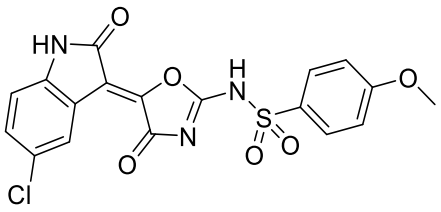

Following the general procedure H, the product was obtained as a beige solid after filtration and washing using water, ethanol, and diethyl ether (126.4 mg, 0.2 mmol, 100%). **^{1}H NMR** (600 MHz, DMSO-d_6) δ 12.63 (s, 1H), 10.74 (s, 1H), 7.86 (d, *J* = 8.4 Hz, 2H), 7.32 (dd, *J* = 8.3, 2.2 Hz, 1H), 7.13 (d, *J* = 8.4 Hz, 2H), 6.93 (s, 1H), 6.84 (d, *J* = 8.3 Hz, 1H), 3.85 (s, 3H). **^{13}C NMR** (151 MHz, DMSO-d_6) δ 174.18, 169.94, 162.99, 159.34, 141.81, 133.44, 130.93, 129.68, 128.39, 126.45, 125.23, 114.79, 112.22, 85.33, 75.57, 56.16. **HRMS**-ESI (*m/z*): calculated for $[M+H]^+$ $C_{19}H_{12}BrN_3O_6S_2$, 434.0; found: 434.0.

Benzoyl isothiocyanate (**144**)

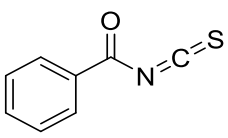

Benzoyl chloride (500.0 µL, 4.3 mmol, 1 equiv.) was added to a freshly prepared solution of NH_4SCN (327.9 mg, 4.3 mmol, 1 equiv.) in acetone (7 mL), and the mixture was stirred for 30 minutes at room temperature: The *in situ*-generated

benzoyl isothiocyanate was obtained after removing the solvent under reduced pressure. The product was used in the next step without further purification (703.3 mg, 4.3 mmol, 100%).

N-((4-Hydroxyphenyl)carbamothioyl)benzamide (**145**)

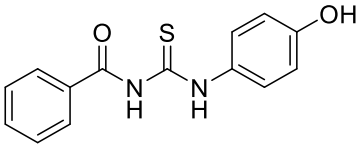

The benzoyl isothiocyanate (703.4 mg, 4.3 mmol, 1 equiv.) was resuspended in ethyl acetate (10 mL) and 4-aminophenol (470.3 mg, 4.3 mmol, 1 equiv.) was added. The mixture was stirred overnight and then poured into ice water with vigorous stirring. The resulting white solid was collected by vacuum filtration and dried to obtain the desired thiourea (688.76 mg, 4.09 mmol, 95%). Compound characterization correlates with previously reported characterization.[278]

1-(4-Hydroxyphenyl)thiourea (**146**)

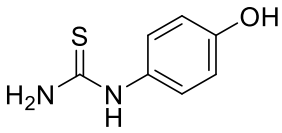

N-((4-hydroxyphenyl)carbamothioyl)benzamide (**145**) from the previous step was poured into a mixture of aqueous sodium hydroxide (4 M) and ethanol (1:1) and then heated to reflux for 1.5 h. The precipitating beige solid was collected *via* vacuum filtration and then washed with H_2O to yield the desired product (688.8 mg, 4.1 mmol, 95%). **^{1}H NMR** (600 MHz, DMSO-d_6) δ 12.95 (s, 1H), 9.36 (s, 1H), 7.96 (dd, *J* = 8.3, 1.4 Hz, 2H), 7.65 – 7.60 (m, 1H), 7.51 (t, *J* = 7.8 Hz, 2H), 6.77 – 6.69 (m, 1H). **^{13}C NMR** (151 MHz, DMSO-d_6) δ 167.78, 133.35, 131.21, 129.73, 129.04.

5-(5-Chloro-2-oxoindolin-3-ylidene)-2-((4-hydroxyphenyl)amino)thiazol-4(5H)-one (**147**)

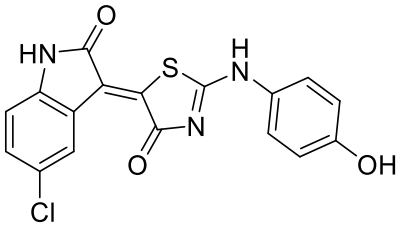

Following the general procedure I, the product was obtained as a red-brown solid after filtration and washing using water, ethanol, and diethyl ether (24.40 mg, 0.07 mmol, 20%). **^{1}H NMR** (700 MHz, DMSO-d_6) δ 11.60 (s, 1H), 11.23 (d, *J* = 7.6 Hz, 1H), 9.64 (s, 1H), 9.02 (d, *J* = 2.2 Hz, 1H), 7.71 – 7.53 (m, 2H), 7.39 (ddd, *J* = 12.0, 8.3, 2.2 Hz, 1H), 6.96 (d, *J* = 8.3 Hz, 1H), 6.87 – 6.81 (m, 2H). **^{13}C NMR** (176 MHz, DMSO-d_6) δ 180.72, 172.84, 169.22, 155.78, 142.07, 139.23, 131.15, 130.48, 127.54, 126.08, 124.08, 123.03, 122.26, 116.06, 111.95. **HRMS**-ESI (*m/z*): calculated for $[M+H]^+$ $C_{17}H_{10}ClN_3O_3S$, 372.02042; found: 372.02026.

2-((4-Hydroxyphenyl)amino)-5-(5-methyl-2-oxoindolin-3-ylidene)thiazol-4(5H)-one (**148**)

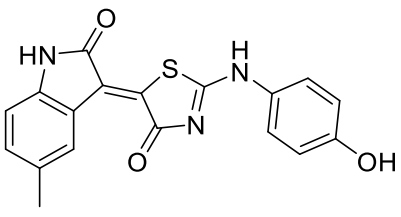

Following the general procedure I, the product was obtained as a red-brown solid after filtration and washing using water, ethanol, and diethyl ether (d.r. = 8:1) 34.8 mg, 0.1 mmol, 27%). **^{1}H NMR** (700 MHz, DMSO-d_6) δ 11.48 (s, 1H), 10.99 (d, *J* = 6.9 Hz, 1H), 9.61 (s, 1H), 8.85 – 8.72 (m, 1H), 7.66 – 7.56 (m, 1H), 7.18 – 6.98 (m, 2H), 6.87 – 6.81 (m, 3H), 2.32 (s, 3H). **^{13}C NMR** (176 MHz, DMSO-d_6) δ 180.72, 173.19, 169.50,

155.62, 141.18, 136.90, 132.33, 130.87, 129.79, 128.70, 125.55, 122.94, 121.06, 116.02, 110.27, 21.53. **HRMS**-ESI (*m/z*): calculated for $[M+H]^+$ $C_{17}H_{13}N_4O_5S$, 352.07504; found: 352.07473.

2-((4-Hydroxyphenyl)amino)-5-(5-methoxy-2-oxoindolin-3-ylidene)thiazol-4(5H)-one (**149**)

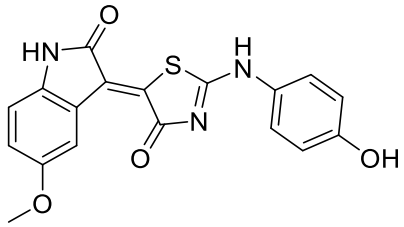

Following the general procedure I, the product was obtained as a brown solid after filtration and washing using water, ethanol, and diethyl ether (37.7 mg, 0.1 mmol, 28%). **^{1}H NMR** (700 MHz, DMSO-d_6) δ 11.51 (s, 1H), 10.90 (s, 1H), 9.61 (s, 1H), 8.70-8.62 (m, 1H), 7.66 – 7.56 (m, 1H), 7.03-6.94 (m, 2H), 6.82 (d, *J* = 6.3 Hz, 3H), 3.76 (s, 3H). **^{13}C NMR** (176 MHz, DMSO-d_6) δ 180.80, 173.14, 169.43, 155.65, 154.98, 137.19, 130.58, 129.82, 125.81, 122.95, 121.65, 117.29, 116.02, 114.45, 110.82, 55.94. **HRMS**-ESI (*m/z*): calculated for $[M+H]^+$ $C_{18}H_{13}N_3O_4S$, 368.06995; found: 368.06969.

2-((4-Hydroxyphenyl)amino)-5-(5-nitro-2-oxoindolin-3-ylidene)thiazol-4(5H)-one (**150**)

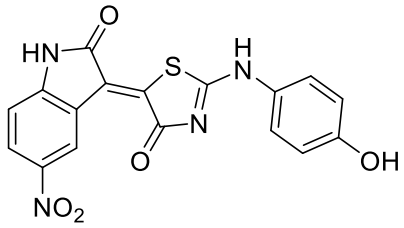

Following the general procedure I, the product was obtained as an orange solid after filtration and washing using water, ethanol, and diethyl ether (27.40 mg, 0.07 mmol, 19%). **^{1}H NMR** (700 MHz, DMSO-d_6) δ 11.75 (s, 1H), 11.66 (s, 1H), 9.85 (s, 1H), 9.66 (s, 1H), 8.29 – 8.15 (m, 1H), 7.61 (d, *J* = 8.6 Hz, 1H), 7.10 (s, 1H), 7.03 (s, 1H), 6.84 (d, *J* = 9.1 Hz, 2H). **^{13}C NMR** (176 MHz, DMSO-d_6) δ 180.56, 172.32, 169.81, 155.88, 148.56, 142.58, 140.95, 130.42, 127.61, 123.50, 123.05, 120.93, 116.43, 116.07, 110.70. **HRMS**-ESI (*m/z*): calculated for $[M+H]^+$ $C_{17}H_{10}N_4O_5S$, 383.04447; found: 383.04441.

5-(5-Bromo-2-oxoindolin-3-ylidene)-2-((4-hydroxyphenyl)amino)thiazol-4(5H)-one (**151**)

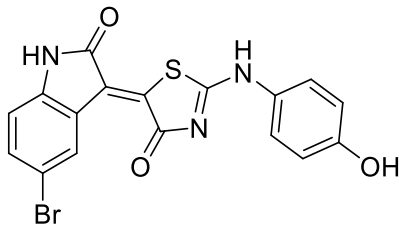

Following the general procedure I, the product was obtained as a red-brown solid after filtration and washing using water, ethanol, and diethyl ether (46.20 mg, 0.11 mmol, 30%). **^{1}H NMR** (700 MHz, DMSO-d_6) δ 11.60 (s, 1H), 11.25 (d, *J* = 7.9 Hz, 1H), 9.64 (s, 1H), 9.16 (d, *J* = 2.1 Hz, 1H), 7.63 – 7.60 (m, 1H), 7.52 (ddd, *J* = 10.9, 8.3, 2.1 Hz, 1H), 6.92 (d, *J* = 8.4 Hz, 1H), 6.88 (d, *J* = 8.3 Hz, 1H), 6.86 – 6.82 (m, 2H). **^{13}C NMR** (176 MHz, DMSO-d_6) δ 180.73, 172.82, 169.11, 155.79, 142.43, 139.24, 133.96, 130.31, 123.95, 123.03, 122.74, 116.41, 116.07, 113.87, 112.46. **LC-MS** (*m/z*): calculated for $[M+H]^+$ $C_{17}H_{10}BrN_3O_3S$, 416.0; found: 416.8.

5-(7-Fluoro-2-oxoindolin-3-ylidene)-2-((4-hydroxyphenyl)amino)thiazol-4(5H)-one (**152**)

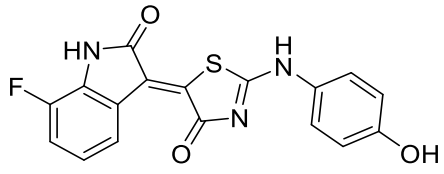

Following the general procedure I, the product was obtained as a red-brown solid after filtration and washing using water, ethanol, and diethyl ether (34.3 mg, 0.1 mmol, 26%). **^{1}H NMR** (600 MHz, DMSO-d_6) δ 11.62 (s, 1H), 11.57 (s, 1H), 9.63 (s,

1H), 8.83 (d, *J* = 7.9 Hz, 1H), 7.64 – 7.59 (m, 1H), 7.29 (dd, *J* = 10.2, 8.3 Hz, 1H), 7.10 (s, 2H), 6.87 – 6.80 (m, 2H). **^{13}C NMR** (151 MHz, DMSO-d_6) δ 180.51, 172.77, 169.31, 158.53, 155.74, 148.23 – 147.60 (m), 146.55 – 145.83 (m), 139.23, 130.51, 129.72, 124.42 (d, *J* = 3.8 Hz), 123.02, 122.72 (t, *J* = 5.7 Hz), 116.41, 116.05. **^{19}F NMR** (565 MHz, DMSO-d_6) δ -133.16 (dd, *J* = 10.3, 5.2 Hz), -133.21 (dd, *J* = 10.3, 5.2 Hz). **HRMS**-ESI (*m/z*): calculated for $[M+H]^+$ $C_{17}H_{10}FN_3O_3S$, 356.04997; found: 356.04981.

4-(N-(5-(5-Bromo-1-methyl-2-oxoindolin-3-ylidene)-4-oxo-4,5-dihydrothiazol-2-yl)sulfamoyl)benzoic acid (**154**)

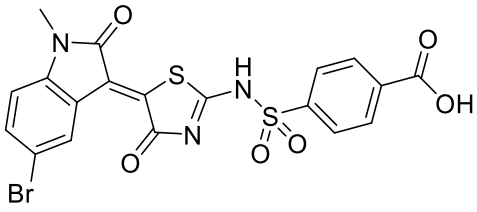

Following the general procedure H, the product was obtained as a diastereomeric mixture as a red-brown solid after filtration and washing using water, ethanol, and diethyl ether (74.90 mg, 0.14 mmol, 84%). **^{1}H NMR** (600 MHz, DMSO-d_6) δ 13.49 (s, 1H), 12.65 (s, 1H), 8.92 (d, *J* = 2.2 Hz, 1H), 8.21 – 8.14 (m, 2H), 8.05 – 8.02 (m, 2H), 7.66 (dd, *J* = 8.5, 2.2 Hz, 1H), 7.11 (d, *J* = 8.5 Hz, 1H), 3.24 (s, 3H). **^{13}C NMR** (151 MHz, DMSO-d_6) δ 174.26, 172.47, 166.99, 166.54, 144.51, 144.18, 135.43, 135.18, 130.79, 130.49, 130.41, 127.37, 125.71, 121.35, 114.73, 111.80, 27.01. **HRMS**-ESI (*m/z*): calculated for $[M+H]^+$ $C_{19}H_{12}{}^{79}BrN_3O_6S_2$, 521.94237; found: 521.94287. Calculated for $[M+H]^+$ $C_{19}H_{12}{}^{81}BrN_3O_6S_2$, 523.94079; found: 523.94079.

4-(N-(5-(1-Methyl-5-nitro-2-oxoindolin-3-ylidene)-4-oxo-4,5-dihydrothiazol-2-yl)sulfamoyl)benzoic acid (**155**)

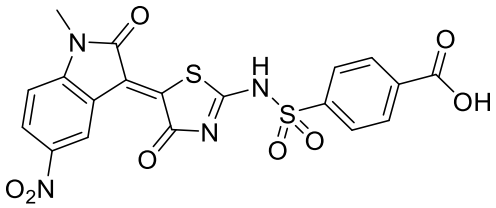

Following the general procedure H, the product was obtained as a diastereomeric mixture visible as an orange-brown solid after filtration and washing using water, ethanol, and diethyl ether (62.10 mg, 0.13 mmol, 75%). **^{1}H NMR** (700 MHz, DMSO-d_6) δ 13.54 (s, 1H), 9.66 (d, *J* = 2.4 Hz, 1H), 8.42 – 8.28 (m, 2H), 8.17 (d, *J* = 8.1 Hz, 2H), 8.04 (d, *J* = 8.1 Hz, 2H), 7.36 (d, *J* = 8.9 Hz, 1H), 3.33 (s, 3H). **^{13}C NMR** (176 MHz, DMSO-d_6) δ 172.48, 169.33, 168.54, 167.92, 166.54, 150.18, 144.09, 143.05, 142.71, 135.47, 130.79, 128.72, 127.40, 123.34, 119.67, 110.14, 27.41. **HRMS**-ESI (*m/z*): calculated for $[M+H]^+$ $C_{19}H_{12}BrN_3O_6S_2$, 489.00966; found: 488.32701.

4-(N-(5-(5-Bromo-2-oxoindolin-3-ylidene)-4-oxo-4,5-dihydrothiazol-2-yl)sulfamoyl)benzoic acid (**156**)

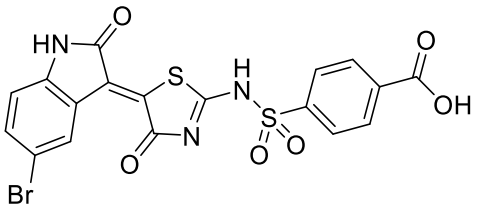

Following the general procedure H, the product was obtained as a red-brown solid after filtration and washing using water, ethanol, and diethyl ether (117.10 mg, 0.23 mmol, 69%). **^{1}H NMR** (600 MHz, DMSO-d_6) δ 13.51

(s, 1H), 11.41-11.33 (m, 1H), 9.01-8.91 (m, 1H), 8.39 – 8.31 (m, 1H), 8.21 – 8.13 (m, 1H), 8.08 – 7.99 (m, 2H), 7.57 (dd, *J* = 8.3, 2.1 Hz, 1H), 6.91 (dd, *J* = 8.3, 5.1 Hz, 1H), 4.07 (s, 1H). **^{13}C NMR** (151 MHz, DMSO-d_6) δ 173.88, 173.79, 168.25, 168.13, 166.07, 144.29, 143.75, 143.18, 143.10, 134.94, 130.30, 126.86, 121.90, 121.69, 113.58, 112.44, 39.94, 39.80, 39.66, 39.52, 39.38, 39.24, 39.10. **HRMS**-ESI (*m/z*): calculated for $[M+H]^+$ $C_{18}H_{10}{}^{79}BrN_3O_6S_2$, 507.91944; found: 507.94079. Calculated for $[M+H]^+$ $C_{18}H_{10}{}^{81}BrN_3O_6S_2$, 509.91739; found: 509.94287.

Methyl-4-(N-(5-(5-bromo-1-methyl-2-oxoindolin-3-ylidene)-4-oxo-4,5-dihydrothiazol-2-yl)sulfamoyl)benzoate (**159**)

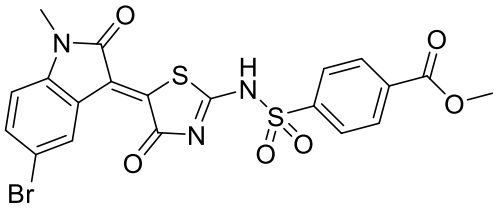

Following the general procedure H, the product was obtained as a red-brown solid after filtration and washing using water, ethanol, and diethyl ether (75.40 mg, 0.14 mmol, 88%). **^{1}H NMR** (500 MHz, DMSO-d_6) δ 13.54 (s, 1H), 8.94 (d, *J* = 2.7 Hz, 1H), 8.19 (d, *J* = 8.1 Hz, 2H), 8.06 (d, *J* = 8.1 Hz, 2H), 7.74 – 7.60 (m, 1H), 7.13 (d, *J* = 8.4 Hz, 1H), 3.90 (s, 3H), 3.25 (s, 3H). **^{13}C NMR** (126 MHz, DMSO-d_6) δ 171.94, 167.02, 165.53, 156.68, 144.54, 135.19, 134.79, 134.12, 133.84, 130.70, 130.41, 127.51, 125.72, 121.37, 114.72, 111.83, 53.19, 27.02. **HRMS**-ESI (*m/z*): calculated for $[M+H]^+$ $C_{20}H_{14}{}^{81}BrN_3O_6S_2$, 537.95074.; found: 537.95632; .559.94831.

3-(N-(5-(5-Bromo-1-methyl-2-oxoindolin-3-ylidene)-4-oxo-4,5-dihydrothiazol-2-yl)sulfamoyl)benzoic acid (**160**)

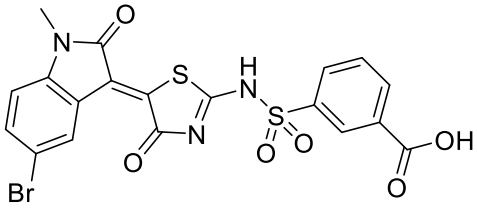

Following the general procedure H, the product was obtained as a red-brown solid after filtration and washing using water, ethanol, and diethyl ether ((d.r. = 3:1) 34.80 mg, 0.07 mmol, 74%). **^{1}H NMR** (700 MHz, DMSO-d_6) δ 13.57 (s, 1H), 9.44 (s, 1H), 9.19 (s, 1H), 8.95 (s, 1H), 8.39 (s, 1H), 8.24 (d, *J* = 7.8 Hz, 1H), 7.80 (t, *J* = 7.8 Hz, 1H), 7.68 (d, *J* = 8.5 Hz, 1H), 7.13 (d, *J* = 8.5 Hz, 1H), 3.25 (s, 3H). **^{13}C NMR** (176 MHz, DMSO-d_6) δ 180.45, 178.77, 167.64, 167.03, 144.51, 143.45, 141.73, 135.14, 134.35, 133.72, 130.73, 130.21, 127.47, 122.84, 121.38, 114.70, 111.80, 111.24, 27.02. **HRMS**-ESI (*m/z*): calculated for $[M+H]^+$ $C_{19}H_{12}{}^{79}BrN_3O_6S_2$, 521.94237; found: 521.94293. Calculated for $[M+H]^+$ $C_{19}H_{12}{}^{81}BrN_3O_6S_2$, 523.94032; found: 523.94073.

5.2.3 YTHDF2

5.2.3.1 SK-3-91-based molecules

2-(2-Azidoethoxy)ethan-1-ol (**199**)

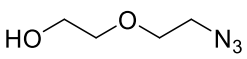

2-(2-Chloroethoxy)ethanol (1.0 mL, 9.5 mmol, 1.0 equiv.) was dissolved in distilled water (12 mL), and sodium azide (1.5 g, 23.7 mmol, 2.5 equiv.) was added thereto. The resulting mixture was stirred at 80°C for 16 h. The reaction mixture was cooled to

room temperature, poured into 5% NaOH (aq.) (20 mL), and stirred for approximately 10 min. The reaction mixture was extracted three times with diethyl ether, and the organic layer was dried over magnesium sulfate, filtered, and concentrated under reduced pressure to obtain the desired product (1.25 g, 9.5 mmol, 99%). **^{1}H NMR** (400 MHz, Chloroform-*d*) δ 3.77 – 3.74 (m, 2H), 3.70 (dd, *J* = 5.6, 4.5 Hz, 2H), 3.63 – 3.60 (m, 2H), 3.44 – 3.37 (m, 2H), 1.96 (s, 1H).

2-(2-Azidoethoxy)ethyl methanesulfonate (**200**)

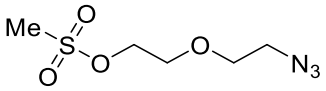

To a solution of intermediate **I** (1.3 g, 9.9 mmol, 1.0 equiv.) and Et_3N (2.75 mL, 19.80 mmol, 2.00 equiv.) in dry dichloromethane (10 ml) at 0°C, mesityl chloride (1.15 mL, 14.80 mmol, 1.50 equiv.) was added dropwise. Then, the reaction was stirred at room temperature for 6 h. After the desired reaction time the mixture was quenched with water and the aqueous phase was extracted with dichloromethane (3 x 25 ml). The organic layers were combined, washed with brine, and dried with anhydrous $MgSO_4$.After filtration, the solvent was removed under reduced pressure to afford the desired methanesulfonate as a colorless liquid (2.0 g, 9.8 mmol, 99%). **^{1}H NMR** (600 MHz, Chloroform-*d*) δ 4.42 – 4.35 (m, 2H), 3.81 – 3.68 (m, 4H), 3.67 – 3.37 (m, 2H), 3.07 (d, *J* = 8.3 Hz, 3H).

1-Azido-2-(2-bromoethoxy)ethane (**201**)

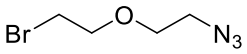

Intermediate **II** (2.0 g, 9.8 mmol, 1.0 equiv.) and LiBr (2.60 g, 29.45 mmol, 3.00 equiv.) were dissolved in acetone and refluxed for 16 h. After the desired reaction time, the solvent was evaporated, and the crude mixture was washed with water. The aqueous phase was extracted with dichloromethane (3 x 25 ml), and the resulting organic layers were combined, washed with brine, and dried using anhydrous $MgSO_4$. After filtration, the solvent was removed under reduced pressure to afford the desired linker (1.4 g, 7.1 mmol, 72%). **^{1}H NMR** (600 MHz, Chloroform-*d*) δ 3.87 – 3.75 (m, 3H), 3.72 – 3.62 (m, 2H), 3.48 (t, *J* = 6.2 Hz, 2H), 3.40 (t, *J* = 5.0 Hz, 1H).

2-(2,6-Dioxopiperidin-3-yl)-4-fluoroisoindoline-1,3-dione (**202**)

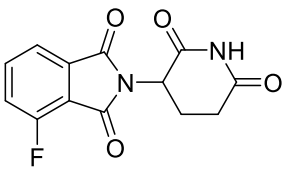

Sodium acetate (352.4 mg, 4.3 mmol, 2.0 equiv.) and 3-aminopiperidine-2,6-dione hydrochloride (353.50 mg, 2.15 mmol, 1.00 equiv.) were added to a solution of 3-fluorophthalic anhydride (356.8 mg, 2.1 mmol, 1.0 equiv.) in acetic acid (6 mL) and the mixture was stirred at 120°C for 4 h. After cooling to room temperature, the mixture was poured into ice water (20 mL) and stirred for additional 10 min. The resulting precipitate was filtered and washed with water, diethyl ether, and finally ethanol to afford the desired thalidomide **6** as a grey solid (451.00 mg, 1.63 mmol, 76%). **^{1}H NMR** (600 MHz, Chloroform-*d*) δ 8.08 (s, 1H), 7.78 (ddd, *J* = 8.2, 7.3, 4.3 Hz, 1H), 7.72 (d, *J* = 7.4 Hz, 1H), 7.43 (t, *J* = 8.5 Hz, 1H), 4.99 (dd, *J* = 12.6, 5.4 Hz, 1H), 2.96 – 2.89 (m, 1H), 2.89 – 2.71 (m, 2H), 2.16 (dtd, *J* = 12.4, 5.0, 2.3 Hz, 1H). **^{13}C NMR** (151 MHz, Chloroform-*d*) δ 170.80, 166.31 (d, *J* = 2.8 Hz), 164.13, 158.94, 157.17, 137.37 (d, *J* = 7.4 Hz), 134.01, 123.12 (d, *J* = 19.4 Hz), 120.28 (d, *J* = 3.7 Hz), 117.81

(d, *J* = 12.4 Hz), 49.67, 31.58, 22.71. **LC-MS** (**ESI**) (*m/z*) calculated for $C_{13}H_9FN_2O_4$ $[M+H]^+$ = 276.1; found: 276.2.

tert-Butyl (2-(2,6-dioxopiperidin-3-yl)-1,3-dioxoisoindolin-4-yl)glycinate (**203**)

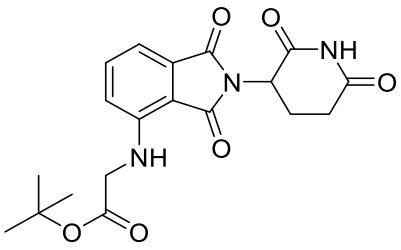

A solution of intermediate **III** (250.0 mg, 0.9 mmol, 1.0 equiv.) and *tert*-butyl 2-aminoacetate (148.4 µL, 1.1 mmol, 1.2 equiv.) in DMSO (3 mL) was added DIPEA (315.3 2 µL, 1.8 mmol, 2 equiv.). The reaction mixture was stirred overnight at 130°C and on completion, the solvent was removed in vacuo. The crude residue was purified by column chromatography (eluent system: 2% Methanol in dichloromethane) to afford the desired pomalidomide as a yellow solid (205.00 mg, 0.53 mmol, 59%). **^{1}H NMR** (600 MHz, Chloroform-*d*) δ 8.06 (s, 1H), 7.50 (ddd, *J* = 17.1, 8.4, 7.2 Hz, 1H), 7.15 (ddd, *J* = 7.3, 4.9, 0.6 Hz, 1H), 6.75 (ddd, *J* = 13.5, 8.5, 0.6 Hz, 1H), 4.93 (dd, *J* = 12.5, 5.4 Hz, 1H), 4.27 (s, 1H), 3.94 (s, 2H), 2.89 (dddd, *J* = 16.8, 4.1, 2.5, 1.2 Hz, 1H), 2.86 – 2.66 (m, 2H), 2.18 – 2.08 (m, 1H), 1.50 (s, 9H). **^{13}C NMR** (151 MHz, Chloroform-*d*) δ 171.15, 169.30, 168.70, 168.35, 167.72, 145.98, 136.36, 132.74, 116.87, 112.54, 111.26, 82.95, 49.14, 45.32, 39.54, 31.62, 28.26, 22.95. **LC-MS** (**ESI**) (*m/z*) calculated for $C_{19}H_{21}N_3O_6$ $[M+H]^+$ = 388.1; found: 388.1.

(2-(2,6-Dioxopiperidin-3-yl)-1,3-dioxoisoindolin-4-yl)glycine (**204**)

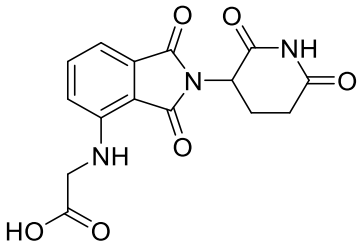

Intermediate **IV** (170.2 mg, 0.44 mmol) was dissolved in dichloromethane (3 mL) and TFA (1 mL) was added thereto. The mixture was stirred at room temperature for 2 h. After monitoring the full conversion of the reaction using LC-MS analysis, the solvent was removed in vacuo to give the desired product **204** (145.50 mg, 0.44 mmol, 99%), which was used in the next step without further purification. **LC-MS** (**ESI**) (m/z) calculated for $C_{15}H_{13}N_3O_6$ $[M+H]^+$ = 332.1; found: 332.1.

tert-Butyl 4-(4-((5-chloro-4-((2-(isopropylsulfonyl)phenyl)amino)pyrimidin-2-yl)amino)phenyl)piperazine-1-carboxylate (**205**)

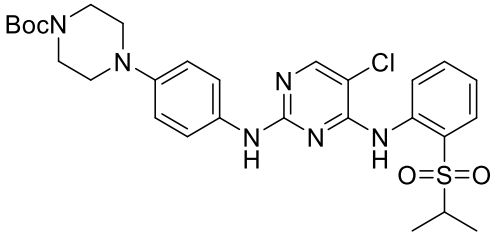

A solution of 2,5-dichloro-*N*-(2-(*iso*propylsulfonyl)phenyl)pyrimidin-4-amine (300.00 mg, 0.87 mmol, 1.00 equiv.), *tert*-butyl 4-(4-aminophenyl)piperazine-1-carboxylate (240.30 mg, 0.87 mmol, 1.00 equiv.) and *para*-toluenesulfonic acid monohydrate (164.80 mg, 0.87 mmol, 1 equiv.) in 1,4-dioxane (4 mL) was heated to 90°C for 16 h. After completion of the reaction (monitored by TLC) the reaction mixture was concentrated. The crude solid was purified by silica gel column chromatography by using 2% methanol in dichloromethane as eluents to get the title compound as a white solid (208.6 mg, 0.36 mmol, 41%). **^{1}H NMR** (500 MHz,

DMSO-d_6) δ 9.49 (s, 1H), 9.36 (s, 1H), 8.65 (s, 1H), 8.25 (s, 1H), 7.85 (dd, *J* = 8.0, 1.6 Hz, 1H), 7.76 (ddd, *J* = 8.7, 7.3, 1.7 Hz, 1H), 7.46 (d, *J* = 8.4 Hz, 2H), 7.42 – 7.35 (m, 1H), 6.93 – 6.84 (m, 2H), 3.47 (t, *J* = 6.3 Hz, 5H), 3.06 – 2.98 (m, 4H), 1.43 (s, 9H), 1.17 (d, *J* = 6.8 Hz, 6H). **^{13}C NMR** (126 MHz, DMSO-d_6) δ 158.33, 155.75, 155.21, 154.30, 146.94, 138.55, 135.43, 132.99, 131.40, 124.56, 123.97, 121.57, 116.95, 79.42, 55.32, 49.68, 28.54, 15.33. **LC-MS** (**ESI**) (*m/z*) calculated for $C_{28}H_{35}ClN_6O_4S$ $[M+H]^+$ = 587.2; found: 587.0.

5-Chloro-N-(2-(isopropylsulfonyl)phenyl)-N-(4-(piperazin-1-yl)phenyl)pyrimidine-2,4-diamine (**XLIV**)

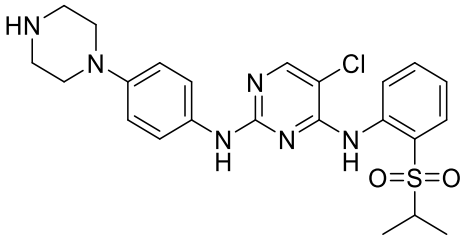

TFA was added (1 mL) to a solution of *tert*-butyl 4-(4-((5-chloro-4-((2-(*iso*propylsulfonyl)phenyl)amino)pyrimidin-2-yl)amino)phenyl)piperazine-1-carboxylate (208.60 mg, 0.36 mmol) in dichloromethane (3 mL), and the mixture was stirred at room temperature for 2 h. After completion of the reaction, the mixture was concentrated under reduced pressure. The TFA salt was used in the following step without further purification. **LC-MS** (**ESI**) (*m/z*) calculated for $C_{23}H_{27}ClN_6O_2S$ $[M+H]^+$ = 487.1; found: 487.2.

N-(4-(4-(2-(2-Azidoethoxy)ethyl)piperazin-1-yl)phenyl)-5-chloro-N-(2-(isopropylsulfonyl)phenyl)pyrimidine-2,4-diamine (**206**)

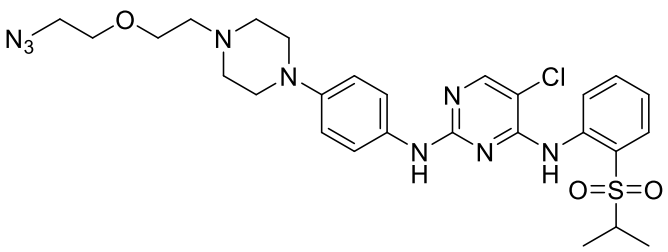

Intermediate **3** (152.40 mg, 0.28 mmol, 1.00 equiv.) was dissolved in acetonitrile (3 mL), to which was added intermediate **4** (65.60 mg, 0.34 mmol, 1.20 equiv.) and potassium carbonate (118.50 mg, 0.84 mmol, 3.00 equiv.). The resulting mixture was stirred at 80°C overnight, then cooled to room temperature and diluted with 5 mL of dichloromethane. The mixture was washed with water and the resulting biphasic solution was extracted using dichloromethane (3 x 15 mL). The organic layers were combined, dried with anhydrous $MgSO_4$, and filtered. The filtrate was then concentrated under reduced pressure and purified by column chromatography (methanol in dichloromethane (2%)) to yield **5** as a colorless oil (65.80 mg, 0.11 mmol, 39%). **^{1}H NMR** (700 MHz, Chloroform-*d*) δ 9.54 (s, 1H), 8.51 (dd, *J* = 8.4, 1.1 Hz, 1H), 8.04 (s, 1H), 7.82 (dd, *J* = 8.0, 1.6 Hz, 1H), 7.49 (ddd, *J* = 8.7, 7.2, 1.6 Hz, 1H), 7.37 – 7.30 (m, 2H), 7.16 (ddd, *J* = 8.2, 7.3, 1.1 Hz, 1H), 6.95 (d, *J* = 4.7 Hz, 1H), 6.84 – 6.81 (m, 2H), 5.23 (s, 2H), 3.77 (s, 2H), 3.63 – 3.59 (m, 2H), 3.37 – 3.31 (m, 3H), 3.31 – 3.19 (m, 4H), 3.16 (h, *J* = 6.8 Hz, 1H), 2.86 (d, *J* = 41.2 Hz, 4H), 1.24 (d, *J* = 6.9 Hz, 6H). **^{13}C NMR** (176 MHz, Chloroform-*d*) δ 158.09, 155.37, 155.23, 138.47, 134.49, 131.23, 124.38, 123.44, 123.09, 122.02, 117.23, 105.87, 69.99, 57.61, 55.62, 53.46, 53.44, 50.70, 48.98, 15.37. **LC-MS** (**ESI**) (*m/z*) calculated for $C_{27}H_{34}ClN_9O_3S$ $[M+H]^+$ = 600.2; found: 600.4.

N2-(4-(4-(2-(2-Aminoethoxy)ethyl)piperazin-1-yl)phenyl)-5-chloro-N4-(2-(isopropylsulfonyl)phenyl)pyrimidine-2,4-diamine (**214**)

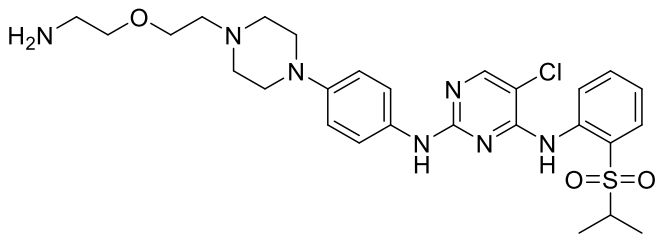

Intermediate **206** (65.80 mg, 0.11 mmol, 1.00 equiv.) was dissolved in THF (5 mL) and water (0.5 mL) under an argon atmosphere and triphenylphosphine (34.50 mg, 0.13 mmol, 1.20 equiv.) was added thereto. The reaction mixture was stirred overnight, then concentrated and dried under vacuum to give the desired intermediate as a yellow solid (62.30 mg, 0.11 mmol, 99%). The intermediate was used for the following step without further purification. **^{1}H NMR** (700 MHz, DMSO-d_6) δ 10.87 (s, 1H), 9.85 (s, 1H), 8.34 (d, *J* = 14.8 Hz, 4H), 7.89 (dd, *J* = 7.9, 1.5 Hz, 1H), 7.83 – 7.75 (m, 1H), 7.49 (t, *J* = 7.8 Hz, 1H), 7.38 (s, 2H), 6.94 (d, *J* = 8.4 Hz, 2H), 3.84 (t, *J* = 4.8 Hz, 2H), 3.72 – 3.69 (m, 4H), 3.57 (s, 2H), 3.50 (d, *J* = 4.8 Hz, 1H), 3.47 (q, *J* = 5.1 Hz, 2H), 3.40 (dt, *J* = 7.3, 3.8 Hz, 2H), 3.23 (q, *J* = 10.7 Hz, 2H), 3.01 (p, *J* = 5.2 Hz, 2H), 1.14 (d, *J* = 6.7 Hz, 6H). **^{13}C NMR** (176 MHz, DMSO-d_6) δ 167.43, 137.68, 135.47, 132.01, 131.53, 122.37, 116.86, 104.75, 72.63, 70.99, 66.88, 66.83, 63.92, 60.64, 55.31, 55.19, 51.25, 46.07, 44.10, 38.95, 15.29. **LC-MS** (**ESI**) (*m/z*) calculated for $C_{27}H_{36}ClN_7O_3S$ $[M+H]^+$ = 575.1; found: 575.2.

N-(2-(2-(4-(4-((5-Chloro-4-((2-(isopropylsulfonyl)phenyl)amino)pyrimidin-2-yl)amino)phenyl)piperazin-1-yl)ethoxy)ethyl)-2-((2-(2,6-dioxopiperidin-3-yl)-1,3-dioxoisoindolin-4-yl)amino)acetamide (**198**)

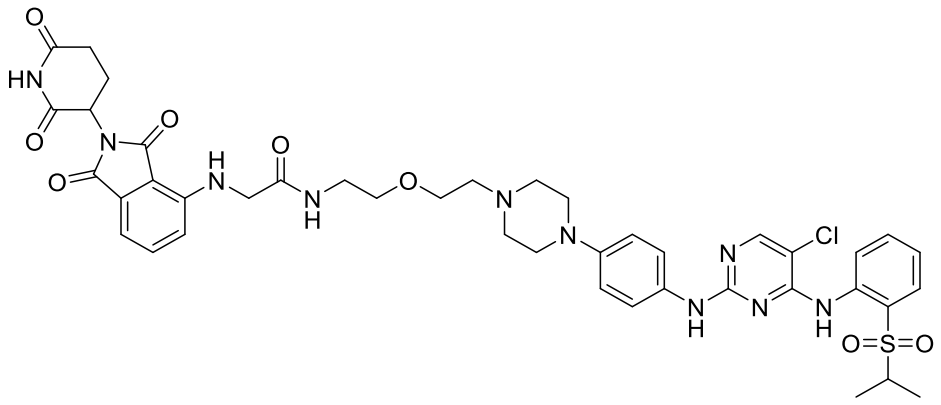

To the azide intermediate **206** (98.90 mg, 0.09 mmol, 1.00 equiv.) in anhydrous dichloromethane (3 mL) was added **204** (31.4 mg, 0.09 mmol, 1.1 equiv.) and (1-[bis(dimethylamino)methylene]-1*H*-1,2,3-triazolo[4,5-*b*]pyridinium 3-oxid hexafluorophosphate) (98.20 mg, 0.26 mmol, 3.00 equiv.) and DIPEA (45 µL, 0.26 mmol, 3.00 equiv.) and the reaction mixture was stirred for 2 h. Then, the mixture was concentrated in vacuo and the resulting residue was purified by reverse phase HPLC (gradient: 10-30% MeCN (+0.1%TFA) in water (+0.1% TFA)). Lyophilization afforded the desired degrader as a yellow solid (35.00 mg, 0.04 mmol, 46%). **^{1}H NMR** (600 MHz, DMSO-d_6) δ 11.11 (s, 1H), 9.68 (s, 1H), 9.53 (s, 1H), 9.42 (s, 1H), 8.64 (s, 1H), 8.26 (s, 1H), 8.25 (t, *J* = 5.7 Hz, 1H), 7.85 (dd, *J* = 8.0, 1.6

Hz, 1H), 7.78 – 7.70 (m, 1H), 7.59 (dd, *J* = 8.5, 7.1 Hz, 1H), 7.47 (d, *J* = 8.5 Hz, 2H), 7.40 – 7.35 (m, 1H), 7.08 (d, *J* = 7.1 Hz, 1H), 6.97 (t, *J* = 6.0 Hz, 1H), 6.93 – 6.89 (m, 2H), 6.87 (d, *J* = 8.5 Hz, 1H), 5.06 (dd, *J* = 12.8, 5.5 Hz, 1H), 3.98 (d, *J* = 3.7 Hz, 2H), 3.79 (t, *J* = 4.9 Hz, 2H), 3.71 (d, *J* = 12.9 Hz, 2H), 3.60 (d, *J* = 12.1 Hz, 2H), 3.53 (t, *J* = 5.7 Hz, 2H), 3.46 (p, *J* = 6.8 Hz, 1H), 3.41 – 3.33 (m, 4H), 3.22 (q, *J* = 10.8 Hz, 2H), 2.98 (t, *J* = 12.4 Hz, 2H), 2.88 (ddd, *J* = 17.0, 13.9, 5.5 Hz, 1H), 2.60 – 2.54 (m, 1H), 2.03 – 1.96 (m, 1H), 1.17 (d, *J* = 6.8 Hz, 6H). **^{13}C NMR** (151 MHz, DMSO-d_6) δ 173.26, 170.51, 169.28, 169.22, 167.74, 159.03, 158.79, 158.56, 158.33, 158.10, 155.35, 146.23, 145.43, 138.52, 136.73, 135.36, 133.46, 132.53, 131.43, 124.25, 124.03, 121.65, 119.31, 117.91, 116.85, 115.43, 113.49, 111.54, 110.36, 104.68, 69.56, 64.45, 55.44, 55.34, 51.82, 49.05, 46.60, 45.63, 38.67, 31.44, 22.61, 15.33. **HRMS**-ESI (*m/z*) calculated for $C_{42}H_{47}ClN_{10}O_8S$ $[M+H]^+$ = 887.2988; found, 887.3091. Calculated for $C_{42}H_{47}ClN_{10}O_8S$ $[M+2H]^{2+}$ = 444.1494; found, 444.1494.[263]

tert-Butyl (2-(4-(4-((5-chloro-4-((2-(isopropylsulfonyl)phenyl)amino)pyrimidin-2-yl)amino)phenyl)piperazin-1-yl)ethyl)carbamate (**208**)

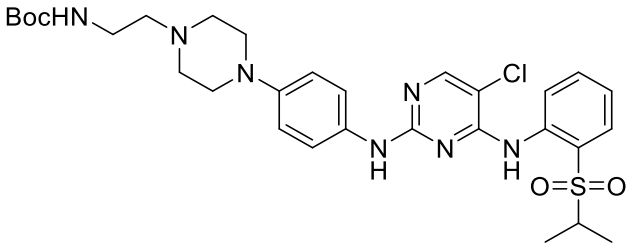

Intermediate **XLIV** (223.1 mg, 0.37 mmol, 1 equiv.) was dissolved in acetonitrile (5 mL), to which was added *tert*-butyl (2-bromoethyl)carbamate (99.80 mg, 0.45 mmol, 1.20 equiv.) and potassium carbonate (153.9 mg, 1.1 mmol, 3.0 equiv.). The resulting mixture was stirred at 80°C overnight, then cooled down to room temperature and diluted with 5 mL of dichloromethane. The mixture was washed with water and the resulting biphasic solution was extracted using dichloromethane (3 x 20 mL). The organic layers were combined, dried with anhydrous $MgSO_4$, and filtered. The filtrate was then concentrated under reduced pressure and purified by column chromatography (methanol in dichloromethane (2%)) to yield **208** as a colorless oil (111.10 mg, 0.18 mmol, 48%). **^{1}H NMR** (500 MHz, DMSO-d_6) δ 9.49 (s, 1H), 9.30 (s, 1H), 8.65 (s, 1H), 8.23 (s, 1H), 7.84 (dd, *J* = 8.0, 1.6 Hz, 1H), 7.77 – 7.70 (m, 1H), 7.42 (d, *J* = 8.4 Hz, 2H), 7.37 (td, *J* = 7.6, 1.2 Hz, 1H), 6.91 – 6.81 (m, 2H), 6.68 (t, *J* = 5.8 Hz, 1H), 3.48 – 3.41 (m, 1H), 3.08 (dt, *J* = 10.2, 5.6 Hz, 6H), 2.54 (d, *J* = 5.0 Hz, 4H), 2.38 (t, *J* = 6.8 Hz, 2H), 1.39 (s, 9H), 1.17 (d, *J* = 6.8 Hz, 6H). **^{13}C NMR** (126 MHz, DMSO-d_6) δ 158.42, 156.05, 155.75, 155.19, 147.18, 138.59, 135.38, 132.31, 131.38, 124.48, 124.09, 123.89, 121.78, 116.11, 104.41, 78.01, 64.60, 57.85, 55.36, 53.22, 49.36, 37.85, 28.74, 15.33. **LC-MS** (**ESI**) (*m/z*) calculated for $C_{30}H_{40}ClN_7O_4S$ $[M+H]^+$ = 630.2; found: 630.4.

N^2-(4-(4-(2-Aminoethyl)piperazin-1-yl)phenyl)-5-chloro-N^4-(2-(isopropylsulfonyl)phenyl)pyrimidine-2,4-diamine (**209**)

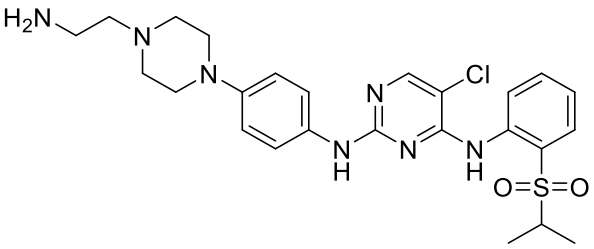

TFA was added (1 mL) to a solution of intermediate **208** (108.50 mg, 0.17 mmol) in dichloromethane (3 mL), and the mixture was stirred at room temperature for 2 h. After completion of the reaction, the mixture was concentrated under reduced pressure. The TFA salt was used in the following step without further purification. **LC-MS** (**ESI**) (*m/z*) calculated for $C_{25}H_{32}ClN_7O_2S$ $[M+H]^+$ = 530.2; found: 530.2.

4-((2-(4-(4-((5-Chloro-4-((2-(isopropylsulfonyl)phenyl)amino)pyrimidin-2-yl)amino)phenyl)piperazin-1-yl)-2-oxoethyl)amino)-2-(2,6-dioxopiperidin-3-yl)isoindoline-1,3-dione (**210**)

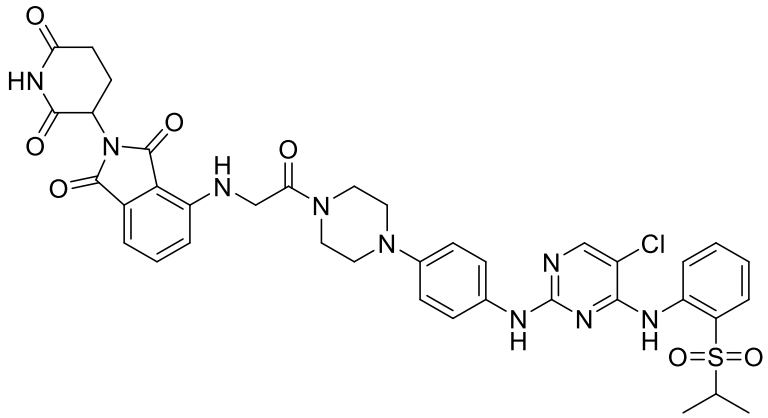

To a solution of intermediate **XLIV** (83.00 mg, 0.17 mmol, 1.00 equiv.) in DMSO (2 mL) was added 1-Hydroxy-7-azabenzotriazol (HOAt) (340.8 µL, 0.17 mmol, 1 equiv.), 1-Ethyl-3-(3-dimethylaminopropyl)carbodiimid hydrochloride (EDC·HCl) (32.70 mg, 0.17 mmol, 1.00 equiv.), 4-methylmorpholin (NMM) (93.70 µL, 0.85 mmol, 5.00 equiv.) and **204** (66.00 mg, 0.17 mmol, 1.00 equiv.) sequentially. The resulting solution was stirred at 25°C for 16 h before the reaction was poured into water (20 mL) and extracted with ethyl acetate (3 x 15 mL). The combined organic layers were washed with saturated brine (25 mL), dried over anhydrous $MgSO_4$, filtered, and evaporated under reduced pressure. The resulting residue was purified by silica gel column chromatography to yield the desired product as yellow solid (40.90 mg, 0.05 mmol, 30%). **^{1}H NMR** (600 MHz, DMSO-d_6) δ 11.11 (s, 1H), 9.50 (s, 1H), 9.36 (s, 1H), 8.66 (s, 1H), 8.25 (s, 1H), 7.85 (dd, *J* = 7.9, 1.6 Hz, 1H), 7.80 – 7.72 (m, 1H), 7.63 (dd, *J* = 8.5, 7.1 Hz, 1H), 7.47 (d, *J* = 8.5 Hz, 2H), 7.42 – 7.34 (m, 1H), 7.14 (d, *J* = 8.5 Hz, 1H), 7.12 – 7.05 (m, 2H), 6.99 – 6.89 (m, 2H), 5.08 (dd, *J* = 12.8, 5.5 Hz, 1H), 4.27 (d, *J* = 4.5 Hz, 2H), 3.68 (dt, *J* = 17.1, 5.2 Hz, 4H), 3.49 – 3.42 (m, 1H), 3.32 (s, 2H), 3.16 (t, *J* = 5.0 Hz, 2H), 3.10 (t, *J* = 5.3 Hz, 2H), 2.90 (ddd, *J* = 16.8, 13.7, 5.5 Hz, 1H), 2.10 – 2.00 (m, 1H), 1.17 (d, *J* = 6.7 Hz, 6H). **^{13}C NMR** (151 MHz, DMSO-d_6) δ 173.30, 170.56, 169.29, 168.69, 167.83, 166.90, 158.35, 155.74, 155.23, 146.78, 145.96, 138.57, 136.67, 135.40, 132.50, 131.40, 130.12, 123.97, 121.65, 118.75,

116.94, 116.86, 111.32, 110.04, 55.35, 49.82, 49.52, 49.06, 44.17, 41.96, 31.47, 22.62, 15.34. **HRMS**-ESI (*m/z*) calculated for $C_{38}H_{38}ClN_9O_7S$ $[M+H]^+$ = 800.2303; found: 800.2413.

N-(2-(4-(4-((5-Chloro-4-((2-(isopropylsulfonyl)phenyl)amino)pyrimidin-2-yl)amino)phenyl)piperazin-1-yl)ethyl)-2-((2-(2,6-dioxopiperidin-3-yl)-1,3-dioxoisoindolin-4-yl)amino)acetamide (**211**)

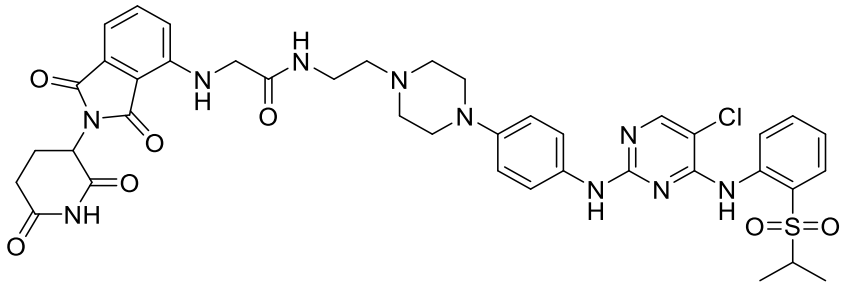

To the obtained TFA salt of **209** (135.30 mg, 0.21 mmol, 1.00 equiv.) in anhydrous dichloromethane (3 mL) was added **204** (76.50 mg, 0.23 mmol, 1.10 equiv.) and (1-[bis(dimethylamino)methylene]-1*H*-1,2,3-triazolo[4,5-*b*]pyridinium 3-oxid hexafluorophosphate) (HATU) (239.50 mg, 0.63 mmol, 3.00 equiv.) and DIPEA (108.90 µL, 0.63 mmol, 3.00 equiv.). and the reaction mixture was stirred for 3 h. Then, the mixture was concentrated in vacuo and the resulting residue was purified by reverse phase HPLC (gradient: 10-30% MeCN (+0.1%TFA) in water (+0.1% TFA)). Lyophilization afforded the desired product as a yellow solid (35.00 mg, 0.04 mmol, 37%). **^{1}H NMR** (600 MHz, DMSO-d_6) δ 11.04 (s, 1H), 9.66 (s, 1H), 9.44 (s, 1H), 9.34 (s, 1H), 8.57 (s, 1H), 8.36 (t, *J* = 5.9 Hz, 1H), 8.19 (s, 1H), 7.78 (dd, *J* = 8.0, 1.6 Hz, 1H), 7.72 – 7.65 (m, 1H), 7.55 (dd, *J* = 8.5, 7.1 Hz, 1H), 7.42 (d, *J* = 8.4 Hz, 2H), 7.30 (td, *J* = 7.6, 1.2 Hz, 1H), 7.04 (d, *J* = 7.1 Hz, 1H), 6.91 (t, *J* = 5.8 Hz, 1H), 6.89 – 6.83 (m, 3H), 5.01 (dd, *J* = 12.8, 5.4 Hz, 1H), 3.94 (d, *J* = 5.3 Hz, 2H), 3.67 (d, *J* = 13.0 Hz, 2H), 3.57 (d, *J* = 11.8 Hz, 2H), 3.49 – 3.43 (m, 2H), 3.38 (p, *J* = 6.8 Hz, 1H), 3.21 (t, *J* = 6.4 Hz, 2H), 3.14 (s, 2H), 2.92 – 2.78 (m, 3H), 1.96 (dtd, *J* = 13.1, 5.4, 2.3 Hz, 1H), 1.10 (d, *J* = 6.8 Hz, 6H). **^{13}C NMR** (151 MHz, DMSO-d_6) δ 173.29, 170.53, 170.05, 169.22, 167.76, 158.21, 155.58, 155.30, 146.27, 145.33, 138.55, 136.75, 135.37, 133.57, 132.55, 131.43, 123.99, 121.61, 118.01, 117.97, 116.90, 111.66, 110.48, 55.35, 55.03, 51.52, 49.06, 46.71, 45.81, 40.53, 34.11, 31.46, 22.64, 15.33. **LC-MS** (**ESI**): calculated for $C_{40}H_{43}ClN_{10}O_7S$ $[M+H]^+$ = 843.2; found: 843.0. **HRMS**-ESI (*m/z*) calculated for $C_{40}H_{43}ClN_{10}O_7S$ $[M+2H]^{2+}$ = 422.6363; found: 422.6444 $[M+2H]^{2+}$.

5-Chloro-N^4-(2-(isopropylsulfonyl)phenyl)-N^2-(4-(4-methylpiperazin-1-yl)phenyl)pyrimidine-2,4-diamine (**212**)

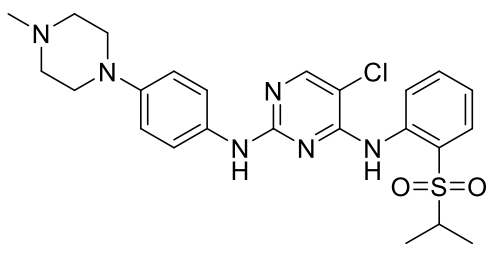

2,5-dichloro-*N*-(2-(*iso*propylsulfonyl)phenyl)pyrimidin-4-amine (50.00 mg, 0.14 mmol, 1.00 equiv.), 4-(4-methylpiperazin-1-yl)aniline (27.60 mg, 0.14 mmol, 1.00 equiv.) and *p*-toluenesulfonic acid monohydrate (27.50 mg, 0.14 mmol, 1.00 equiv.) were placed in a 25 mL

flask, and isopropanol was added (2 mL). The resulting suspension was heated to 85°C and stirred for 16 h until completion of the reaction monitored by TLC. Then, the mixture was cooled to room temperature, the solvent was removed under reduced pressure, and purification using silica gel column chromatography afforded the desired product as an off-white solid (44.10 mg, 0.09 mmol, 61%). **^{1}H NMR** (400 MHz, DMSO-d_6) δ 9.46 (s, 1H), 9.28 (s, 1H), 8.63 (s, 1H), 8.21 (s, 1H), 7.81 (dd, *J* = 7.9, 1.6 Hz, 1H), 7.71 (ddd, *J* = 8.7, 7.4, 1.7 Hz, 1H), 7.40 (d, *J* = 8.6 Hz, 2H), 7.35 (td, *J* = 7.6, 1.2 Hz, 1H), 6.87 – 6.81 (m, 2H), 3.43 (q, *J* = 6.8 Hz, 1H), 3.08 – 3.01 (m, 4H), 2.45 (t, *J* = 5.0 Hz, 4H), 2.21 (s, 3H), 1.15 (d, *J* = 6.8 Hz, 6H). **^{13}C NMR** (176 MHz, DMSO-d_6) δ 158.40, 155.74, 155.20, 146.93, 138.59, 135.39, 132.48, 131.39, 124.53, 124.12, 123.91, 121.70, 116.23, 104.43, 55.35, 54.91, 48.96, 45.85, 15.34. **LC-MS** (**ESI**) (*m/z*) calculated for $C_{24}H_{29}ClN_6O_2S$ $[M+H]^+$ = 501.2; found: 501.0.

5.2.3.2 Rationally designed fragments and small molecules

General Procedure L (*N*6-Alkylation)

To a solution of intermediate **215** or **217** (1.0 equiv.) in absolute ethanol (5 ml), methylamine (7% solution in THF, 1.1 equiv.) or cyclopropyl amine (1.1 equiv.) was added in the presence of triethylamine (1.1 equiv.). The reaction mixture was heated to 80°C and stirred for 3 h. Then, the reaction mixture was left to cool and concentrated under reduced pressure. The resulting crude residue was purified using silica gel column chromatography using the indicated eluent system.

6-Chloro-9-methyl-9H-purine (**215**)

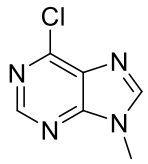

To a solution of 6-chloro-9*H*-purine (500.00 mg, 3.24 mmol, 1.00 equiv.) in anhydrous THF (8 mL), sodium hydride (60% dispersion in mineral oil, 194.10 mg, 4.85 mmol, 1.50 equiv.) was added portion wise at 0°C. After the suspension was stirred for 0.5 h in the ice bath, iodomethane (201.40 µL, 3.24 mmol, 1.00 equiv.) was added and the reaction mixture was stirred for another hour at room temperature. Subsequently, the mixture was diluted with ddH_2O and extracted with EtOAc (3 x 30 mL). The combined organic layer was dried with anhydrous $MgSO_4$ and the solvent was evaporated in vacuo. The crude solid was purified using silica gel column chromatography (elution system: Petroleum ether/ EtOAc (5:1)) to afford the desired product as a white solid (409.0 mg, 2.43 mmol, 75%). **^{1}H NMR** (400 MHz, DMSO-d_6): δ 3.72 (s, 3H), 8.72 (s, 1H), 9.15 (s, 1H).

6-Chloro-N^4-cyclopropylpyrimidine-4,5-diamine (**216**)

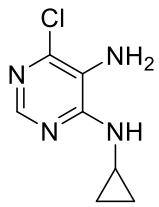

To a stirring solution of 4,6-dichloro-5-aminopyrimidine (250.00 mg, 1.52 mmol, 1.00 equiv.) in *iso*propanol (4 mL), was added cyclopropyl amine (105.60 µL, 1.52 mmol, 1.00 equiv.) and triethylamine (233.70 µL, 1.68 mmol, 1.10 equiv.) and the mixture was refluxed for 5 h. After the reaction was complete monitored by TLC (eluent system: Petroleum ether/ EtOAc (3:1), R_f = 0.4), the solvent was removed in vacuo and

the resulting crude was purified using silica gel column chromatography (eluent system: Petroleum ether/ EtOAc (4:1)) to give the desired substituted pyrimidine (205.5 mg, 1.1 mmol, 73%).

6-Chloro-9-cyclopropyl-9H-purine (**217**)

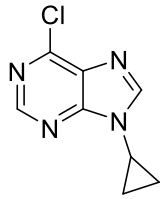

To a solution of intermediate **216** (186.5 mg, 1.0 mmol, 1.0 equiv.) in triethyl orthoformate (3.4 mL, 20.2 mmol, 20 equiv.) under an argon atmosphere was added concentrated HCl (12 M) and the mixture was stirred at room temperature for 5 h. After the reaction was complete (monitored by TLC and LC-MS) the solvent was removed under reduced pressure. The resulting crude mixture was purified using silica gel column chromatography (eluent system: Petroleum ether/ EtOAc = 3:1) to afford the desired chloropurine as a white solid (180.1 mg, 0.93 mmol, 92%). **^{1}H NMR** (400 MHz, Chloroform-*d*) δ 8.77 (s, 1H), 8.11 (s, 1H), 3.51 (d, *J* = 26.1 Hz, 1H), 1.25 (d, *J* = 36.9 Hz, 2H), 1.20 – 1.10 (m, 2H). **LC-MS** (**ESI**) (*m/z*): calculated for $C_8H_7ClN_4$ $[M+H]^+$ = 195.6; found: 195.1.

N,9-Dimethyl-9H-purin-6-amine (**218**)

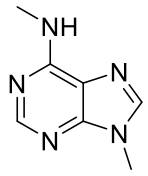

Following the general procedure L, the product was isolated as a white solid after purification using silica gel column chromatography (146.9 mg, 0.9 mmol, 61%) (eluent system: petroleum ether/ EtOAc (6:1)). **^{1}H NMR** (400 MHz, Chloroform-*d*) δ 8.42 (s, 1H), 7.70 (s, 1H), 5.90 (s, 1H), 3.81 (s, 3H), 3.21 (s, 3H).

N-Cyclopropyl-9-methyl-9H-purin-6-amine (**219**)

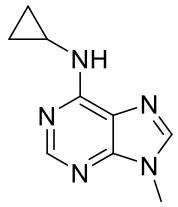

Following the general procedure L, the product was isolated as a white solid after purification using silica gel column chromatography (97.6 mg, 0.5 mmol, 90%) (eluent system: petroleum ether/ EtOAc (6:1)). **^{1}H NMR** (400 MHz, Chloroform-*d*) δ 8.48 (s, 1H), 7.71 (s, 1H), 5.96 (s, 1H), 3.81 (s, 3H), 3.12 – 2.94 (m, 1H), 0.92 (td, *J* = 7.0, 5.2 Hz, 2H), 0.65 (ddd, *J* = 7.0, 5.1, 3.8 Hz, 2H). **LC-MS** (**ESI**) (*m/z*): calculated for $C_9H_{11}N_5$ $[M+H]^+$ = 190.2; found: 190.2.

9-Cyclopropyl-N-methyl-9H-purin-6-amine (**220**)

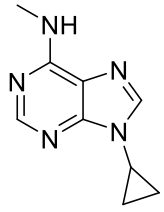

Following the general procedure L, the product was isolated as a white solid after purification using silica gel column chromatography (78.0 mg, 0.4 mmol, 98%) (eluent system: petroleum ether/ EtOAc (6:1)). **^{1}H NMR** (400 MHz, Chloroform-*d*) δ 8.44 (s, 1H), 7.72 (s, 1H), 5.83 (s, 1H), 3.42 (tt, *J* = 7.2, 3.8 Hz, 1H), 3.20 (d, *J* = 4.9 Hz, 3H), 1.25 – 1.13 (m, 2H), 1.13 – 1.05 (m, 2H). **LC-MS** (**ESI**) (*m/z*): calculated for $C_9H_{11}N_5$ $[M+H]^+$ = 190.2; found: 190.2.

N,9-Dicyclopropyl-9H-purin-6-amine (**221**)

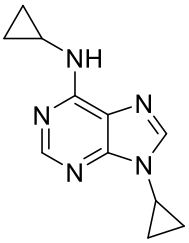

Following the general procedure L, the product was isolated as a white solid after purification using silica gel column chromatography (88.0 mg, 0.4 mmol, 99%) (eluent system: petroleum ether/ EtOAc (6:1)). **^{1}H NMR** (400 MHz, Chloroform-*d*) δ 8.52 (s, 1H), 7.75 (s, 1H), 5.98 (s, 1H), 3.43 (tt, *J* = 7.6, 3.9 Hz, 1H), 3.04 (s, 1H), 1.23 – 0.62 (m, 8H). **LC-MS** (**ESI**) (*m/z*): calculated for $C_{11}H_{13}N_5$ $[M+H]^+$ = 216.3; found: 216.4.

General Procedure M (Piperazine substitution)

Benzyl bromide (1 equiv.) was added to a stirred solution of *tert*-butyl piperazine-1-carboxylate (1 equiv.) and triethylamine (2 equiv.) in dichloromethane (4 ml). The solution was stirred at room temperature for 16 h and then concentrated in vacuo. The residue was purified by silica gel column chromatography using indicated eluent systems to give the desired piperazine.

tert-Butyl 4-(3-(methoxycarbonyl)benzyl)piperazine-1-carboxylate (**224**)

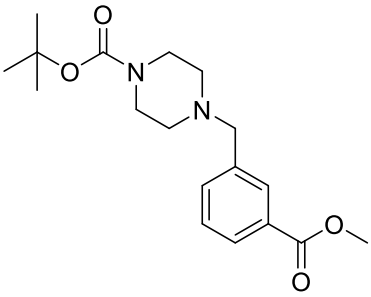

The intermediate **224** was synthesized according to the general procedure M. The product was obtained as a white solid (278.30 mg, 0.82 mmol, 62%) (eluent system: Petroleum ether/ EtOAc = 3:1)). **^{1}H NMR** (400 MHz, Chloroform-*d*) δ 8.00 (s, 3H), 7.45 (s, 1H), 3.92 (s, 5H), 3.52 (s, 4H), 2.50 (s, 4H), 1.44 (s, 9H). **LC-MS** (**ESI**) (*m/z*): calculated for $C_{18}H_{26}N_2O_4$ $[M+H]^+$ = 335.2; found: 335.2.

tert-Butyl 4-(4-(methoxycarbonyl)benzyl)piperazine-1-carboxylate (**225**)

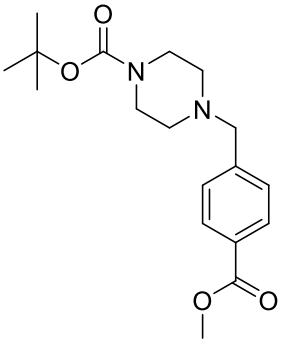

The intermediate **225** was synthesized according to the general procedure M. The product was obtained as a white solid (328.50 mg, 0.98 mmol, 75%) (eluent system: Petroleum ether/ EtOAc = 3:1)). **^{1}H NMR** (500 MHz, Chloroform-*d*) δ 7.97 (d, *J* = 8.3 Hz, 2H), 7.38 (d, *J* = 8.3 Hz, 2H), 3.89 (s, 3H), 3.40 (t, *J* = 5.1 Hz, 4H), 2.37 (t, *J* = 5.1 Hz, 4H), 1.43 (s, 9H). **^{13}C NMR** (126 MHz, Chloroform-*d*) δ 167.30, 155.10, 143.80, 129.90, 129.40, 129.20, 79.90, 62.90, 52.30, 28.70. **LC-MS** (**ESI**) (*m/z*): calculated for $C_{18}H_{26}N_2O_4$ $[M+H]^+$ = 335.2; found: 335.2.

tert-Butyl 4-(4-(methylsulfonyl)benzyl)piperazine-1-carboxylate (**226**)

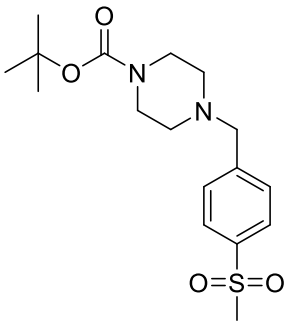

The intermediate **226** was synthesized according to the general procedure M. The product was obtained as a beige solid (285.50 mg, 0.81 mmol, 75%) (eluent system: Petroleum ether/ EtOAc = 4:1)). **^{1}H NMR** (500 MHz, Chloroform-*d*) δ 7.97 (d, *J* = 8.3 Hz, 2H), 7.38 (d, *J* = 8.3 Hz, 2H), , 3.39 (t, *J* = 5.1 Hz, 4H), 3.35 (s, 3H), 2.36 (t, *J* = 5.1 Hz, 4H), 1.43 (s, 9H). **LC-MS** (**ESI**) (*m/z*): calculated for $C_{17}H_{26}N_2O_4S$ $[M+H]^+$ = 355.2; found: 355.2.

tert-Butyl 4-(4-nitrobenzyl)piperazine-1-carboxylate (**227**)

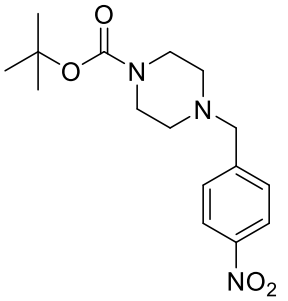

The intermediate **227** was synthesized according to the general procedure M. The product was obtained as a pale-yellow solid (714.1 mg, 2.2 mmol, 96%) (eluent system: Petroleum ether/ EtOAc = 5:1)). **^{1}H NMR** (700 MHz, Chloroform-*d*) δ 8.18 (s, 2H), 7.92 (d, *J* = 39.4 Hz, 1H), 7.66 – 7.30 (m, 1H), 4.43 – 3.83 (m, 2H), 3.70 – 3.33 (m, 4H), 3.22 – 1.93 (m, 4H), 1.39 (s, 9H). **^{13}C NMR** (176 MHz, Chloroform-*d*) δ 190.26, 154.34, 140.07, 140.06, 132.70, 130.50, 129.52, 124.83, 124.33, 124.05, 80.71, 60.40, 52.49, 43.48, 40.87, 28.32. **LC-MS** (**ESI**) (*m/z*): calculated for $C_{16}H_{23}N_3O_4$ $[M+H]^+$ = 322.2; found: 322.1.

Methyl 3-(piperazin-1-ylmethyl)benzoate (**228**)

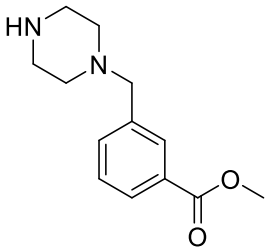

Trifluoroacetic acid (1 mL) was added to a solution of intermediate **224** (278.30 mg, 0.82 mmol) in dichloromethane (3 mL), and the mixture was stirred at room temperature for 2 h. After full consumption of the starting material (monitored by LC-MS) the solvent was removed under reduced pressure to give the intermediate as TFA salt (193.0 mg, 0.82 mmol, 99%). **LC-MS** (**ESI**) (*m/z*): calculated for $C_{13}H_{18}N_2O_2$ $[M+H]^+$ = 235.1; found: 235.1.

Methyl 4-(piperazin-1-ylmethyl)benzoate (**229**)

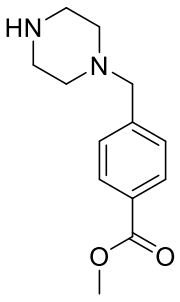

Trifluoroacetic acid (1 mL) was added to a solution of intermediate **225** (278.30 mg, 0.82 mmol) in dichloromethane (3 mL), and the mixture was stirred at room temperature for 2 h. After full consumption of the starting material (monitored by LC-MS) the solvent was removed under reduced pressure to give the intermediate as TFA salt (258.0 mg, 1.1 mmol, 99%). **LC-MS** (**ESI**) (*m/z*): calculated for $C_{13}H_{18}N_2O_2$ $[M+H]^+$ = 235.1; found: 235.1.

1-(4-(Methylsulfonyl)benzyl)piperazine (**230**)

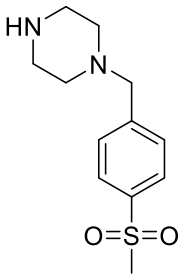

Trifluoroacetic acid (1 mL) was added to a solution of intermediate **226** (280.00 mg, 0.78 mmol) in dichloromethane (3 mL), and the mixture was stirred at room temperature for 2 h. After full consumption of the starting material (monitored by LC-MS) the solvent was removed under reduced pressure to give the intermediate as TFA salt (198.90 mg, 0.78 mmol, 99%). **LC-MS** (**ESI**) (*m/z*): calculated for $C_{12}H_{18}N_2O_2S$ $[M+H]^+$ = 255.1; found: 255.2.

1-(4-Nitrobenzyl)piperazine (**231**)

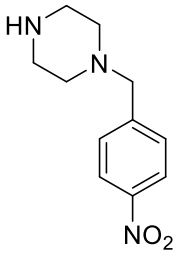

Trifluoroacetic acid (1 mL) was added to a solution of intermediate **227** (500.0 mg, 1.5 mmol) in dichloromethane (3 mL), and the mixture was stirred at room temperature for 2 h. After full consumption of the starting material (monitored by LC-MS) the solvent was removed under reduced pressure to give the intermediate as TFA salt (340.7 mg, 1.5 mmol, 99%). **LC-MS** (**ESI**) (*m/z*): calculated for $C_{12}H_{18}N_2O_2S$ $[M+H]^+$ = 222.1; found: 222.1.

Methyl 4-(6-chloro-9H-purin-9-yl)benzoate (**232**)

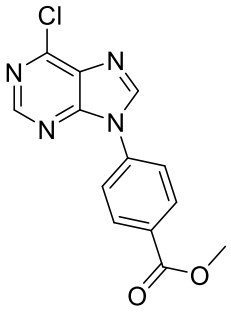

A mixture of 6-chloropurine (300.0 mg, 1.9 mmol, 1.0 equiv.), (4-(methoxycarbonyl)phenyl)boronic acid (698.6 mg, 3.9 mmol, 2.0 equiv.), anhydrous copper(II) acetate (352.6 mg, 1.9 mmol, 1 equiv.), triethylamine (541.1 µL, 3.9 mmol, 2 equiv.) in anhydrous DMF (5 mL) in the presence of 4 Å molecular sieves was stirred vigorously at room temperature overnight. After completion of the reaction, monitored by TLC and LC-MS, methanol was added, and the resulting mixture was filtered through a pad of celite. The filtrate was concentrated under reduced pressure and the crude material was purified by silica gel column chromatography (elution system: petroleum ether/ EtOAc = 5:1) to give the intermediate as an off-white solid (163.20 mg, 0.57 mmol, 29%). **^{1}H NMR** (700 MHz, Chloroform-*d*) δ 8.79 (s, 1H), 8.42 (s, 1H), 8.24 – 8.19 (m, 2H), 7.86 – 7.80 (m, 2H), 3.92 (s, 3H). **^{13}C NMR** (176 MHz, Chloroform-*d*) δ 164.77, 151.87, 151.05, 150.33, 142.45, 136.59, 131.36, 130.53, 129.37, 121.82, 51.55. **LC-MS** (**ESI**) (*m/z*): calculated for $C_{13}H_9ClN_4O_2$ $[M+H]^+$ = 289.0; found: 289.0.

Methyl 4-(6-(methylamino)-9H-purin-9-yl)benzoate (**233**)

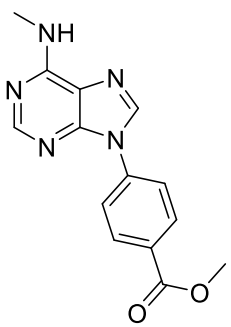

Following the general procedure L, the product was isolated as a white solid after purification using silica gel column chromatography (108.10 mg, 0.38 mmol, 58%) (eluent system: petroleum ether/ EtOAc (3:1)). **^{1}H NMR** (600 MHz, DMSO-d_6) δ 8.74 (s, 1H), 8.35 (s, 1H), 8.22 – 8.13 (m, 4H), 7.94 (s, 1H), 3.90 (s, 3H), 3.00 (s, 3H). **^{13}C NMR** (151 MHz, DMSO-d_6) δ 166.03, 155.73, 153.89, 148.60, 139.62, 139.55, 131.03, 128.41, 122.66, 120.48, 52.81, 27.51. **LC-MS** (**ESI**) (*m/z*): calculated for $C_{14}H_{13}N_5O_2$ $[M+H]^+$ = 284.1; found: 284.1.

4-(6-(Methylamino)-9H-purin-9-yl)benzoic acid (**234**)

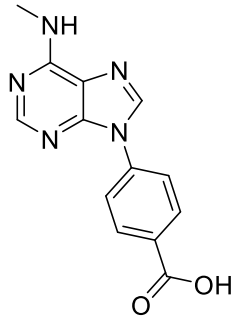

To a suspension of intermediate **233** (150.0 mg, 0.5 mmol, 1.0 equiv.) in THF (1.5 mL) was added water (1.5 mL) and sodium hydroxide (31.70 mg, 0.79 mmol, 1.50 equiv.). The mixture was stirred at room temperature for 3 h and then acidified using a 1 M aqueous HCl solution. The mixture was extracted with EtOAc (3 x 30 mL) and the organic layer was combined, washed with a saturated aqueous NaCl solution (20 mL), dried using anhydrous $MgSO_4$, and concentrated under reduced pressure to give the desired carboxylic acid **233** as a white solid (141.10 mg, 0.52 mmol, 99%). The intermediate was used in the following step without further purification. **^{1}H NMR** (700 MHz, DMSO-d_6) δ 13.21 (s, 1H), 8.81 (s, 1H), 8.42 (s, 1H), 8.18 – 8.13 (m, 2H), 8.10 (d, *J* = 8.2 Hz, 2H), 3.47 (s, 1H), 3.05 (s, 3H). **^{13}C NMR** (176 MHz, DMSO-d_6) δ 167.02, 153.80, 151.40, 148.05, 140.75, 138.74, 131.17, 130.17, 123.11, 120.35, 28.24. **LC-MS** (**ESI**) (*m/z*): calculated for $C_{13}H_{11}N_5O_2$ $[M+H]^+$ = 270.1; found: 270.1.

General Procedure N (Amide coupling–rationally designed compounds)

The deprotected piperazine (**228**-**231**) (1.0 equiv.) was added to a solution of carboxylic acid (**234**, **241** or **245**) (1.0 eq) and HATU (1.25 eq) in anhydrous DMF (5 mL) and triethylamine (3.5 equiv.). The reaction was stirred at room temperature for 16 h. After adding water and ethyl acetate to the mixture, the biphasic solution was transferred to a separation funnel and the aqueous layer was extracted using additional ethyl acetate (3 x 20 mL). The combined organic layer was washed with brine, dried over anhydrous $MgSO_4$, and the solvent was concentrated in vacuo. Purification of the resulting residue using silica gel column chromatography gave the desired compound.

Methyl 3-((4-(4-(6-(methylamino)-9H-purin-9-yl)benzoyl)piperazin-1-yl)methyl)benzoate (**235**)

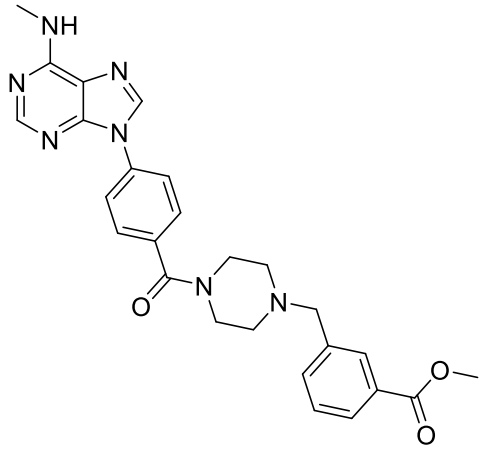

The intermediate **235** was synthesized according to the general procedure N. The product was obtained as a colorless oil (36.10 mg, 0.07 mmol, 20%) (eluent system: 3% MeOH in dichloromethane). **^{1}H NMR** (700 MHz, DMSO-d_6) δ 8.65 (s, 1H), 8.32 (s, 1H), 8.02 (d, *J* = 8.4 Hz, 2H), 7.93 (t, *J* = 1.8 Hz, 1H), 7.87 (dt, *J* = 7.8, 1.5 Hz, 1H), 7.63 – 7.55 (m, 4H), 7.50 (t, *J* = 7.7 Hz, 1H), 3.86 (s, 3H), 3.71 (d, *J* = 64.0 Hz, 2H), 3.60 (s, 3H), 3.05 – 2.95 (m, 4H), 2.44 (d, *J* = 40.7 Hz, 4H). **^{13}C NMR** (176 MHz, DMSO-d_6) δ 169.62, 168.59, 166.72, 153.75, 148.60, 139.68, 139.66, 139.17, 136.40, 135.11, 134.31, 130.14, 129.96, 129.23, 128.77, 128.43, 127.89, 123.00, 61.73, 52.62, 46.24, 27.51. **LC-MS** (**ESI**) (*m/z*): calculated for $C_{26}H_{27}N_7O_3$ $[M+H]^+$ = 486.5; found: 486.4.

Methyl 4-((4-(4-(6-(methylamino)-9H-purin-9-yl)benzoyl)piperazin-1-yl)methyl)benzoate (**236**)

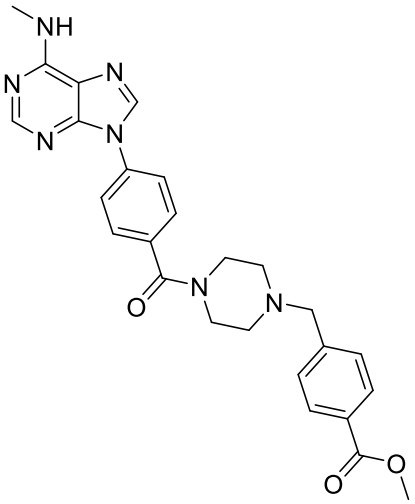

The intermediate **236** was synthesized according to the general procedure N. The product was obtained as a colorless oil (43.30 mg, 0.09 mmol, 24%) (eluent system: 3% MeOH in dichloromethane). **LC-MS** (**ESI**) (*m/z*): calculated for $C_{26}H_{27}N_7O_3$ $[M+H]^+$ = 486.5; found: 486.4.

(4-(6-(Methylamino)-9H-purin-9-yl)phenyl)(4-(4-(methylsulfonyl)benzyl)piperazin-1-yl)methanone (**237**)

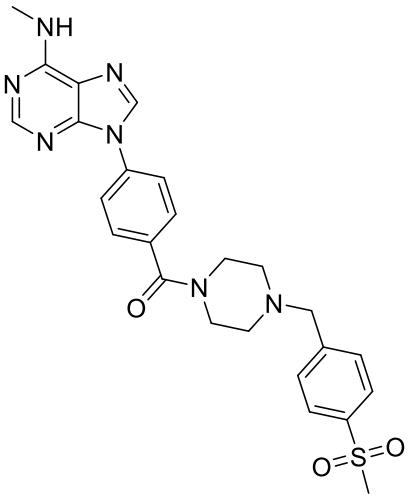

237 was synthesized according to the general procedure N. The product was obtained as a yellow oil (20.00 mg, 0.04 mmol, 26%) (eluent system: 1% MeOH in dichloromethane). **^{1}H NMR** (700 MHz, DMSO-d_6) δ 8.61 (s, 1H), 8.27 (s, 1H), 7.98 (dd, *J* = 15.1, 8.0 Hz, 4H), 7.70 (d, *J* = 7.9 Hz, 2H), 7.64 – 7.59 (m, 2H), 4.49 – 3.93 (m, 3H), 3.19 (s, 8H), 3.11 (d, *J* = 30.7 Hz, 3H), 2.93 (s, 3H). **^{13}C NMR** (176 MHz, DMSO-d_6) δ 166.74, 156.83, 156.64, 156.45, 156.26, 153.30, 151.23, 146.43, 140.05, 140.01, 137.79, 134.71, 131.94, 130.41, 127.01, 125.79, 121.02, 118.28, 115.77, 114.09, 49.35, 41.74, 25.57. **LC-MS** (**ESI**) (*m/z*): calculated for $C_{26}H_{27}N_7O_3$ $[M+H]^+$ = 506.6; found: 506.4.

(4-(6-(Methylamino)-9H-purin-9-yl)phenyl)(4-(4-nitrobenzyl)piperazin-1-yl)methanone (**238**)

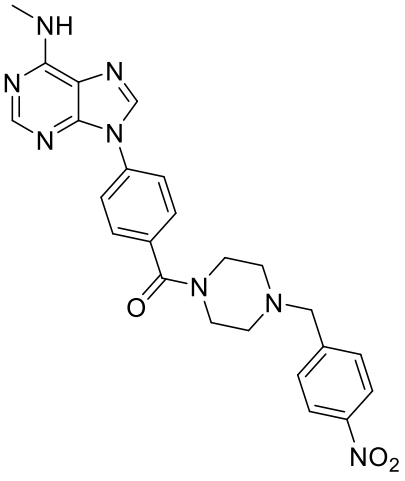

238 was synthesized according to the general procedure N. The product was obtained as a yellow oil (112.30 mg, 0.24 mmol, 64%) (eluent system: 1% MeOH in dichloromethane). **^{1}H NMR** (700 MHz, DMSO-d_6) δ 8.65 (d, *J* = 3.5 Hz, 1H), 8.32 (s, 1H), 8.24 – 8.18 (m, 1H), 8.10 – 7.95 (m, 3H), 7.89 (s, 1H), 7.65 – 7.60 (m, 1H), 7.60 – 7.51 (m, 2H), 5.76 (s, 1H), 3.68 (s, 2H), 3.45 (s, 2H), 3.25 (s, 2H), 3.02 – 2.96 (m, 3H), 1.19 – 1.12 (m, 4H). **^{13}C NMR** (176 MHz, DMSO-d_6) δ 169.63, 168.63, 153.74, 148.60, 147.13, 146.79, 139.68, 136.58, 135.98, 130.27, 128.77, 127.89,

123.89, 123.03, 61.24, 55.38, 46.25, 27.51, 14.56, 13.31. **LC-MS** (**ESI**) (*m/z*): calculated for $C_{24}H_{24}N_8O_3$ $[M+H]^+$ = 473.5; found: 473.4.

3-((4-(4-(6-(Methylamino)-9H-purin-9-yl)benzoyl)piperazin-1-yl)methyl)benzoic acid (**239**)

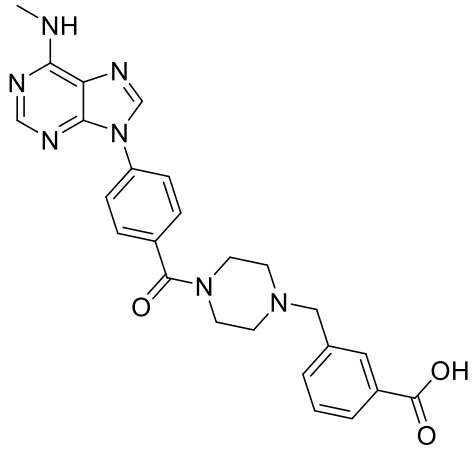

To a suspension of intermediate **235** (46.5 mg, 0.1 mmol, 1.0 equiv.) in THF (1 mL) was added water (1 mL) and sodium hydroxide (5.75 mg, 0.14 mmol, 1.5 equiv.). The mixture was stirred at room temperature for 3 h and then acidified using a 1 M aqueous HCl solution. The mixture was extracted with EtOAc (3 x 30 mL) and the organic layer was combined, washed with a saturated aqueous NaCl solution (20 mL), dried using anhydrous $MgSO_4$, and concentrated under reduced pressure. Purification of the crude product using silica gel column chromatography (eluent system: 5% MeOH in dichloromethane) afforded the desired compound as a beige solid (24.40 mg, 0.05 mmol, 54%). **^{1}H NMR** (500 MHz, DMSO-d_6) δ 12.95 (s, 1H), 8.66 (s, 1H), 8.32 (s, 1H), 8.02 (d, *J* = 8.4 Hz, 2H), 7.96 – 7.89 (m, 2H), 7.87 – 7.81 (m, 1H), 7.64 – 7.59 (m, 2H), 7.55 (d, *J* = 7.6 Hz, 1H), 7.45 (t, *J* = 7.6 Hz, 1H), 3.70 (d, *J* = 43.0 Hz, 2H), 3.59 (s, 2H), 3.52 – 3.46 (m, 1H), 3.10 – 2.88 (m, 4H), 2.49 – 2.30 (m, 4H). **^{13}C NMR** (126 MHz, DMSO-d_6) δ 168.59, 155.70, 153.75, 148.58, 139.68, 138.75, 136.39, 135.09, 133.61, 130.18, 128.92, 128.78, 128.55, 122.99, 120.33, 61.86, 45.73, 43.93, 27.52, 8.96. **LC-MS** (**ESI**) (*m/z*): calculated for $C_{25}H_{25}N_7O_3$ $[M+H]^+$ = 472.5; found: 472.4.

4-((4-(4-(6-(Methylamino)-9H-purin-9-yl)benzoyl)piperazin-1-yl)methyl)benzoic acid (**240**)

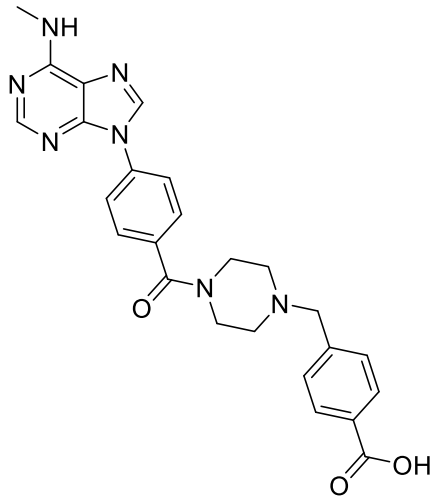

To a suspension of intermediate **236** (41.40 mg, 0.09 mmol, 1.0 equiv.) in THF (1 mL) was added water (1 mL) and sodium hydroxide (5.11 mg, 0.13 mmol, 1.5 equiv.). The mixture was stirred at room temperature for 3 h and then acidified using a 1 M aqueous HCl solution. The mixture was extracted with EtOAc (3 x 30 mL) and the organic layer was combined, washed with a saturated aqueous NaCl solution (20 mL), dried using anhydrous $MgSO_4$, and concentrated under reduced pressure. Purification of the crude product using silica gel column chromatography (eluent system: 5% MeOH in dichloromethane) afforded the desired compound as a beige solid (40.00 mg, 0.08 mmol, 99%). **^{1}H NMR** (500 MHz, DMSO-d_6) δ 12.99 (s, 1H), 8.66 (s, 1H), 8.32 (s, 1H), 8.02 (d, *J* = 8.2 Hz, 2H), 7.91 (dd, *J* = 10.9, 4.7 Hz, 3H), 7.65 – 7.57 (m, 2H), 7.44 (d, *J* = 8.0 Hz, 2H), 3.70 (d, *J* = 35.1 Hz, 2H), 3.59 (s, 2H), 3.17 (s, 1H), 3.06 – 2.90 (m, 3H), 2.49 – 2.25 (m, 4H), 1.26 – 1.18 (m, 1H). **^{13}C NMR** (126

MHz, DMSO-d_6) δ 168.60, 155.70, 153.75, 148.57, 143.37, 139.68, 136.40, 135.07, 129.77, 129.29, 128.78, 122.99, 120.32, 61.84, 53.24, 49.04, 47.67, 27.52. **LC-MS** (**ESI**) (*m/z*): calculated for $C_{25}H_{25}N_7O_3$ $[M+H]^+$ = 472.5; found: 472.4.

Methyl 4-(6-(cyclopropylamino)-9H-purin-9-yl)benzoate (**241**)

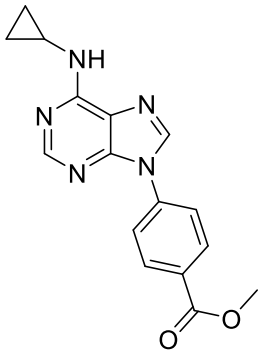

Following the general procedure L, the product was isolated as a white solid after purification using silica gel column chromatography (106.10 mg, 0.34 mmol, 99%) (eluent system: petroleum ether/ EtOAc (3:1)). **^{1}H NMR** (700 MHz, Chloroform-*d*) δ 8.84 (s, 1H), 8.46 (s, 1H), 8.14 – 8.06 (m, 2H), 8.02 – 7.94 (m, 2H), 2.91 (s, 1H), 1.21 – 1.13 (m, 1H), 0.85 (dt, *J* = 7.0, 3.4 Hz, 2H), 0.76 – 0.62 (m, 2H). 3.00 (s, 3H). **LC-MS** (**ESI**) (*m/z*): calculated for $C_{16}H_{15}N_5O_2$ $[M+H]^+$ = 310.1; found: 310.1.

4-(6-(Cyclopropylamino)-9H-purin-9-yl)benzoic acid (**242**)

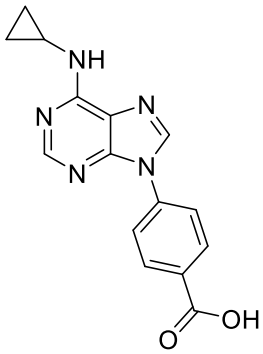

To a suspension of intermediate **241** (109.70 mg, 0.35 mmol, 1.0 equiv.) in THF (1.5 mL) was added water (1.5 mL) and sodium hydroxide (21.30 mg, 0.53 mmol, 1.5 equiv.). The mixture was stirred at room temperature for 3 h and then acidified using a 1 M aqueous HCl solution. The mixture was extracted with EtOAc (3 x 30 mL) and the organic layer was combined, washed with a saturated aqueous NaCl solution (20 mL), dried using anhydrous $MgSO_4$, and concentrated under reduced pressure to give the desired carboxylic acid **x** as a white solid (141.10 mg, 0.52 mmol, 99%). The intermediate was used in the following step without further purification. **^{1}H NMR** (700 MHz, DMSO-d_6) δ 9.69 (s, 1H), 8.84 (s, 1H), 8.46 (s, 1H), 8.14 – 8.06 (m, 2H), 8.02 – 7.94 (m, 2H), 2.91 (s, 1H), 1.21 – 1.13 (m, 1H), 0.85 (dt, *J* = 7.0, 3.4 Hz, 2H), 0.76 – 0.62 (m, 2H). **^{13}C NMR** (176 MHz, DMSO-d_6) δ 171.70, 157.22, 152.99, 146.87, 142.93, 135.95, 135.45, 128.43, 124.88, 85.77, 72.24, 55.78, 12.08. **LC-MS** (**ESI**) (*m/z*): calculated for $C_{15}H_{13}N_5O_2$ $[M+H]^+$ = 296.1; found: 296.1.

Methyl 4-((4-(4-(6-(cyclopropylamino)-9H-purin-9-yl)benzoyl)piperazin-1-yl)methyl)benzoate (**243**)

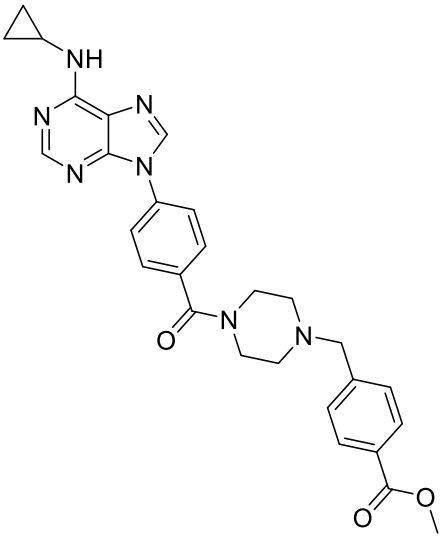

The intermediate **243** was synthesized according to the general procedure N. The product was obtained as a colorless oil (93.60 mg, 0.18 mmol, 45%) (eluent system: 2% MeOH in dichloromethane). **LC-MS** (**ESI**) (*m/z*): calculated for $C_{28}H_{29}N_7O_3$ $[M+H]^+$ = 512.6; found: 512.4.

4-((4-(4-(6-(Cyclopropylamino)-9H-purin-9-yl)benzoyl)piperazin-1-yl)methyl)benzoic acid (**244**)

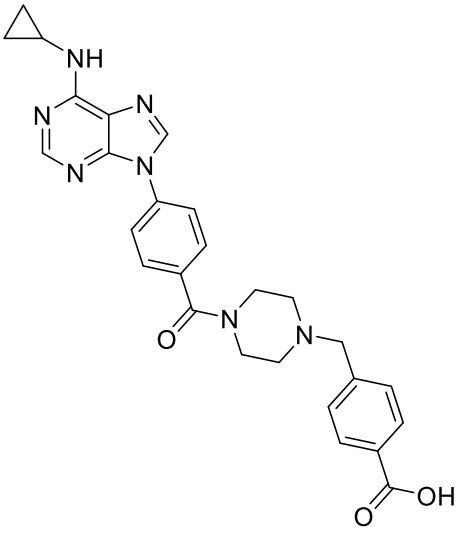

To a suspension of intermediate **243** (103.5 mg, 0.2 mmol, 1.0 equiv.) in THF (1.5 mL) was added water (1.5 mL) and sodium hydroxide (12.1 mg, 0.3 mmol, 1.5 equiv.). The mixture was stirred at room temperature for 3 h and then acidified using a 1 M aqueous HCl solution. Then, the solvent was removed under reduced pressure and the residue was re-dissolved in an ACN/ water mixture. Purification of the crude product using C18-reversed phase silica gel column chromatography (eluent system: 20% ACN in water (+0.1% TFA)) afforded the desired compound as a white solid (24.10 mg, 0.05 mmol, 24%). **^{1}H NMR** (700 MHz, DMSO-d_6) δ 12.66 (s, 1H), 8.58 (s, 1H), 8.26 (s, 1H), 8.00 (d, *J* = 22.8 Hz, 1H), 7.95 – 7.92 (m, 2H), 7.81 – 7.76 (m, 2H), 7.56 – 7.51 (m, 2H), 7.25 (d, *J* = 7.9 Hz, 2H), 3.48 (s, 2H), 3.33 (s, 4H), 2.97 (s, 1H), 2.41 – 2.23 (m, 4H), 0.68 (dt, *J* = 6.8, 3.3 Hz, 2H), 0.60 – 0.55 (m, 2H). **^{13}C NMR** (176 MHz, DMSO-d_6) δ 168.90, 168.60, 156.32, 153.61, 140.80, 139.94, 139.82, 136.35, 135.48, 135.16, 130.58, 129.57, 128.76, 128.70, 123.08, 122.12, 120.18, 62.07, 53.26, 52.70, 47.73, 42.12, 6.76. **LC-MS** (**ESI**) (*m/z*): calculated for $C_{25}H_{25}N_7O_3$ $[M+H]^+$ = 498.5; found: 498.4.

4-((6-Chloropyrimidin-4-yl)amino)benzoic acid (**245**)

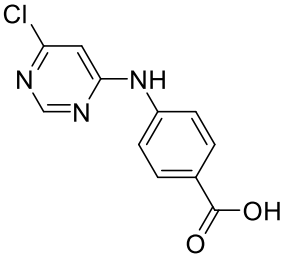

4,6-Dichloropyrimidine (923.50 mg, 6.20 mmol, 1.00 equiv.), 4-aminobenzoic acid (901.10 mg, 6.57 mmol, 1.10 equiv.) were heated at 90°C in a mixture of concentrated HCI (12 M, 0.1 mL), water (3.2 mL), and acetone (2.2 mL) for 4 h. Afterwards, the mixture was cooled to room temperature, filtered and washed using water, abs. EtOH and diethyl ether yielding the title compound as a white solid (1.4 g, 5.7 mmol, 92%). **^{1}H NMR** (700 MHz, DMSO-d_6) δ 12.70 (s, 1H), 10.19 (s, 1H), 8.57 (d, *J* = 0.9 Hz, 1H), 7.96 – 7.90 (m, 2H), 7.82 – 7.78 (m, 2H), 6.91 (d, *J* = 1.0 Hz, 1H). **^{13}C NMR** (176 MHz, DMSO-d_6) δ 167.39, 161.36, 158.92, 158.67, 143.74, 130.95, 125.10, 119.47, 106.63. **LC-MS** (**ESI**) (*m/z*): calculated for $C_{11}H_8ClN_3O_2$ $[M+H]^+$ = 250.6; found: 250.2.

Methyl 3-((4-(4-((6-chloropyrimidin-4-yl)amino)benzoyl)piperazin-1-yl)methyl)benzoate (**246**)

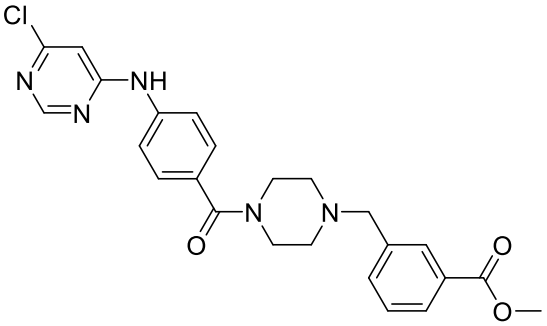

The intermediate **246** was synthesized according to the general procedure N. The product was obtained as a colorless oil (123.20 mg, 0.26 mmol, 44%) (eluent system: 2% MeOH in dichloromethane). **LC-MS** (**ESI**) (*m/z*): calculated for $C_{24}H_{24}ClN_5O_3$ $[M+H]^+$ = 466.9; found: 467.0.

3-((4-(4-((6-Chloropyrimidin-4-yl)amino)benzoyl)piperazin-1-yl)methyl)benzoic acid (**247**)

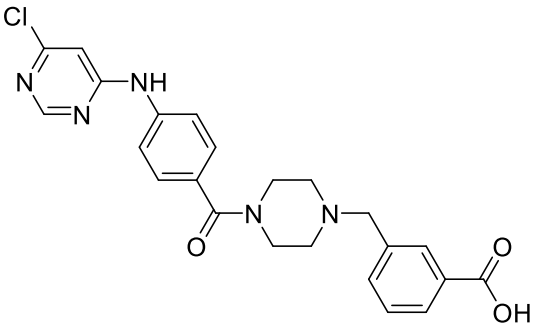

To a suspension of intermediate **246** (67.80 mg, 0.15 mmol, 1.0 equiv.) in THF (1.5 mL) was added water (1.5 mL) and sodium hydroxide (8.73 mg, 0.22 mmol, 1.5 equiv.). The mixture was stirred at room temperature for 3 h and then acidified using a 1 M aqueous HCl solution. Then, the solvent was removed under reduced pressure and the residue was re-dissolved in an ACN/ water mixture. Purification of the crude product using C18-reversed phase silica gel column chromatography (eluent system: 20% ACN in water (+0.1% TFA)) afforded the desired compound as a white solid (16.40 mg, 0.04 mmol, 25%). **^{1}H NMR** (700 MHz, DMSO-d_6) δ 10.25 (s, 1H), 8.44 (d, *J* = 0.9 Hz, 1H), 7.80 (t, *J* = 1.8 Hz, 1H), 7.74 (dt, *J* = 7.6, 1.5 Hz, 1H), 7.68 – 7.61 (m, 2H), 7.39 – 7.26 (m, 4H), 6.86 (d, *J* = 0.9 Hz, 1H), 3.47 (s, 2H), 3.37 – 3.29 (m, 4H), 2.38 – 2.24 (m, 4H). **^{13}C NMR** (176 MHz, DMSO-d_6) δ 169.19, 168.80, 161.54, 158.90, 158.47, 140.81, 138.03, 135.50, 132.04, 130.42, 130.24, 128.62, 128.44, 128.30, 119.94, 106.18, 62.23, 55.79, 53.02. **LC-MS** (**ESI**) (*m/z*): calculated for $C_{23}H_{22}ClN_5O_3$ $[M+H]^+$ = 452.9; found: 453.0.

5.2.3.3 Phenyl pyrazoles

General Procedure O (3-formylchromone synthesis):

A substituted 2-hydroxyacetophenone (1 equiv.) was dissolved in anhydrous dimethylformamide (3 mL). Phosphorus(V) oxychloride (2 equiv.) subsequently was added dropwise over 10 min and the reaction mixture was then stirred at ambient temperatures for 3 h. Afterward, ice-cold water (10 mL) was added, and the mixture was stirred for an additional 3 h. The resulting precipitate was filtered off, washed with ice-cold water, and allowed to dry. The residue was either used directly or purified using silica column chromatography to give the desired 3-formylchromone.[279]

General Procedure P (pyrazole synthesis):

A corresponding 3-formylchromone (1 equiv.) and substituted arylhydrazine (1 equiv.) were dissolved in ethanol (1.5 mL) and aqueous KOH (0.5 mL, 4 M, 4 equiv.) was added thereto. The reaction mixture was heated to 80°C and stirred for 16 h. After cooling to ambient temperatures, aqueous HCl (1 M) was added until pH < 1. The resulting precipitate was filtered off, washed with a small amount of water and ethanol, and allowed to dry. In case the purity of the compound was insufficient purification by silica gel column chromatography was conducted to give the desired pyrazole.

7-Fluoro-4-oxo-4H-chromene-3-carbaldehyde (**XLIV**)

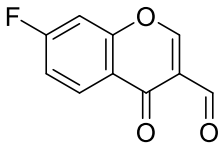

The intermediate was synthesized according to the general procedure O. The product was obtained as an orange solid and required no further purification (110.80 mg, yield 44%). **^{1}H NMR** (400 MHz, Chloroform-*d*) δ 10.31 (s, 1H), 8.45 (s, 1H), 8.29 – 8.23 (m, 1H), 7.19 – 7.14 (m, 2H); **LC-MS** (**ESI**) (*m/z*): calculated for $C_{10}H_5FO_3$ $[M+H]^+$ = 192.02; found: 193.00.

7-Chloro-4-oxo-4H-chromene-3-carbaldehyde (**XLV**)

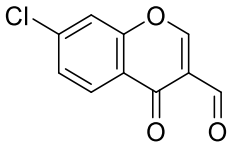

The intermediate was synthesized according to the general procedure O. The product was obtained as an orange solid and required no further purification (159.30 mg, yield 65%). **^{1}H NMR** (400 MHz, Chloroform-*d*) δ 10.30 (s, 1H), 8.44 (s, 1H), 8.17 (d, J = 8.5 Hz, 1H), 7.50 (d, J = 1.9 Hz, 1H), 7.41 (dd, J = 8.5, 1.9 Hz, 1H). **LC-MS** (**ESI**) (*m/z*): calculated for $C_{10}H_5ClO_3$ $[M+H]^+$ = 207.99; found: 208.80.

7-Methyl-4-oxo-4H-chromene-3-carbaldehyde (**XLVI**)

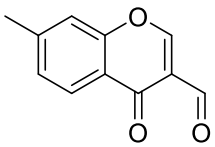

The intermediate was synthesized according to the general procedure O. The product was obtained as a red solid and required no further purification (94.30 mg, yield 70%). **^{1}H NMR** (400 MHz, DMSO-d_6) δ 10.10 (s, 1H), 8.86 (s, 1H), 8.01 (d, J = 8.1 Hz, 1H), 7.56 (s, 1H), 7.39 (dd, J = 8.2, 1.6 Hz, 1H), 2.47 (s, 3H). **LC-MS** (**ESI**) (*m/z*): calculated for $C_{11}H_8O_3$ $[M+H]^+$ = 188.05; found: 188.80.

8-Chloro-4-oxo-4H-chromene-3-carbaldehyde (**XLVI**)

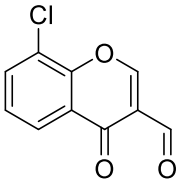

The intermediate was synthesized according to the general procedure O. The product was obtained as a pale yellow solid and required no further purification (25.70 mg, 21%). **^{1}H NMR** (700 MHz, Chloroform-*d*) δ 10.31 (s, 1H), 8.53 (s, 1H), 8.14 (dd, *J* = 8.0, 1.6 Hz, 1H), 7.75 (dd, *J* = 7.8, 1.6 Hz, 1H), 7.38 (t, *J* = 7.9 Hz, 1H). **LC-MS** (**ESI**) (*m/z*): calculated for $C_{10}H_5ClO_3$ $[M+H]^+$ = 209.0; found: 209.0.

5-Methoxy-4-oxo-4H-chromene-3-carbaldehyde (**XLVII**)

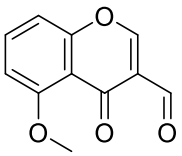

The intermediate was synthesized according to the general procedure O. The product was obtained as an orange solid and required no further purification (112.30 mg, yield 91%). **^{1}H NMR** (400 MHz, Chloroform-*d*) δ 10.28 (s, 1H), 8.32 (s, 1H), 7.55 (t, *J* = 8.4 Hz, 1H), 7.01 (dd, *J* = 8.4, 0.9 Hz, 1H), 6.83 (dd, *J* = 8.4, 0.9 Hz, 1H), 3.95 (s, 3H). **LC-MS** (**ESI**) (*m/z*): calculated for $C_{11}H_8O_4$ $[M+H]^+$ = 204.04; found: 205.00.

6,8-Difluoro-4-oxo-4H-chromene-3-carbaldehyde (**XLVIII**)

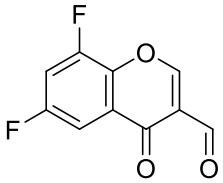

The intermediate was synthesized according to the general procedure O. The product was obtained as a beige solid and required no further purification (86.00 mg, yield 70%); no further purification; **^{1}H NMR** (400 MHz, Chloroform-*d*) δ 10.30 (s, 1H), 8.49 (s, 1H), 7.68 (ddd, *J* = 7.7, 3.0, 1.9 Hz, 1H), 7.26 (ddd, *J* = 9.8, 7.7, 3.0 Hz, 1H). **LC-MS** (**ESI**) (*m/z*): calculated for $C_{10}H_4F_2O_3$ $[M+H]^+$ = 210.01; found: 210.80.

1-Oxo-1H-benzo[f]chromene-2-carbaldehyde (**XLIX**)

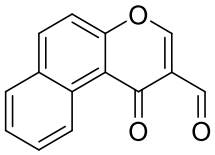

The intermediate was synthesized according to the general procedure O. The product was obtained as a pale yellow solid and required no further purification (104.20 mg, yield 87%). **^{1}H NMR** (400 MHz, Chloroform-*d*) δ 10.52 (s, 1H), 10.00 (ddq, *J* = 8.7, 1.3, 0.6 Hz, 1H), 8.56 (s, 1H), 8.17 (dd, *J* = 9.0, 0.6 Hz, 1H), 7.95 (ddd, *J* = 8.1, 1.4, 0.7 Hz, 1H), 7.82 (ddd, *J* = 8.6, 7.0, 1.5 Hz, 1H), 7.69 (dddd, *J* = 8.1, 6.9, 1.2, 0.5 Hz, 1H), 7.56 (d, *J* = 9.1 Hz, 1H). **LC-MS** (**ESI**) (*m/z*): calculated for $C_{14}H_8O_3$ $[M+H]^+$ = 224.05; found: 224.60.

3-(4-(2-Hydroxybenzoyl)-1H-pyrazol-1-yl)benzoic acid (**248**)

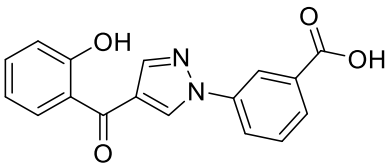

Compound **248** was synthesized using the general procedure P. The product was obtained as a yellow solid (29.50 mg, 0.10 mmol, 33%) without further purification. **^{1}H NMR** (500 MHz, DMSO-d_6) δ 13.32 (s, 1H), 11.07 (s, 1H), 9.21 (s, 1H), 8.49 (t, *J* = 2.0 Hz, 1H), 8.27 – 8.21 (m, 2H), 7.96 (dt, *J* = 7.7, 1.3 Hz, 1H), 7.78 (dd, *J* = 7.8, 1.7 Hz, 1H), 7.68 (t, *J* = 7.9 Hz, 1H), 7.52 (ddd, *J* = 8.7, 7.2, 1.7 Hz, 1H), 7.06 – 6.97 (m, 2H). **^{13}C NMR** (126 MHz, DMSO-d_6) δ 190.60, 167.00, 159.00, 143.20, 139.50, 134.80, 132.70, 132.50, 131.20, 130.50, 128.50, 124.50, 123.90, 123.80, 120.30, 119.70, 117.70; **LC-MS** (**ESI**) (*m/z*): calculated for $C_{17}H_{12}N_2O_4$ $[M+H]^+$ = 308.29; found: 304.20.

(2-Hydroxyphenyl)(1-phenyl-1H-pyrazol-4-yl)methanone (**249**)

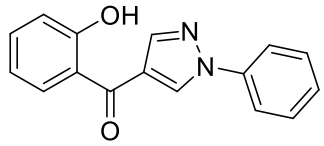

Compound **249** was synthesized using the general procedure P. The product was obtained as a yellow solid without further purification (66.30 mg, yield 58%). **^{1}H NMR** (600 MHz, DMSO-d_6) δ 11.09 (s, 1H), 9.10 (s, 1H), 8.21 (s, 1H), 7.98 (d, J = 8.0 Hz, 2H), 7.77 (dd, J = 7.8, 1.7 Hz, 1H), 7.58 – 7.50 (m, 3H), 7.41 (t, J = 7.4 Hz, 1H), 7.05 – 6.97 (m, 2H). **^{13}C NMR** (151 MHz, DMSO-d_6) δ 190.70, 159.00, 142.90, 139.30, 134.80, 132.10, 131.20, 130.00, 127.90, 124.30, 123.80, 119.80, 117.70. **HRMS**-ESI (*m/z*): calculated for $C_{16}H_{13}N_2O_2$ $[M+H]^+$ = 265.0972; found: 265.0966.

2-(4-(2-Hydroxybenzoyl)-1H-pyrazol-1-yl)benzoic acid (**250**)

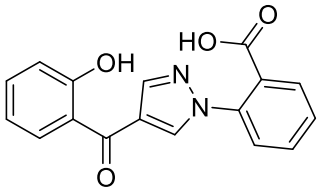

Compound **250** was synthesized using the general procedure P. The product was obtained as a yellow solid without further purification (26.50 mg, yield 60%). **^{1}H NMR** (700 MHz, DMSO-d_6) δ 13.11 (s, 1H), 11.21 (s, 1H), 8.78 (s, 1H), 8.16 (s, 1H), 7.85 (dd, J = 7.7, 1.3 Hz, 1H), 7.77 (dd, J = 7.8, 1.7 Hz, 1H), 7.74 – 7.69 (m, 2H), 7.61 (ddd, J = 7.6, 6.5, 2.1 Hz, 1H), 7.51 (ddd, J = 8.6, 7.2, 1.7 Hz, 1H), 7.02 (dd, J = 8.3, 1.1 Hz, 1H), 6.98 (td, J = 7.5, 1.1 Hz, 1H). **^{13}C NMR** (176 MHz, DMSO) δ 190.80, 167.60, 159.30, 142.40, 138.20, 135.60, 134.90, 132.50, 131.20, 131.10, 130.50, 129.30, 126.40, 123.50, 123.40, 119.70, 117.80. **HRMS**-ESI (*m/z*): calculated for $C_{17}H_{12}N_2O_4$ $[M+H]^+$ = 309.0870; found: 309.0866.

4-(4-(2-Hydroxybenzoyl)-1H-pyrazol-1-yl)benzoic acid (**251**)

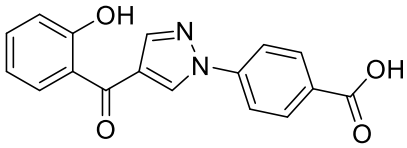

Compound **251** was synthesized using the general procedure P. The product was obtained as a yellow solid without further purification (29.60 mg, yield 33%). **^{1}H NMR** (600 MHz, DMSO-d_6) δ 13.11 (s, 1H), 11.02 (s, 1H), 9.21 (s, 1H), 8.26 (s, 1H), 8.15 – 8.06 (m, 4H), 7.75 (dd, J = 7.8, 1.8 Hz, 1H), 7.52 (ddd, J = 8.7, 7.3, 1.7 Hz, 1H), 7.05 – 6.97 (m, 2H). **^{13}C NMR** (151 MHz, DMSO) δ 190.50, 167.00, 158.90, 143.50, 142.30, 134.80, 132.60, 131.30, 131.10, 124.80, 124.00, 119.80, 119.40, 117.70. **HRMS**-ESI (*m/z*): calculated for $C_{17}H_{12}N_2O_4$ $[M+H]^+$ = 309.0870; found: 309.0866.

(1-(2-Fluorophenyl)-1H-pyrazol-4-yl)(2-hydroxyphenyl)methanone (**252**)

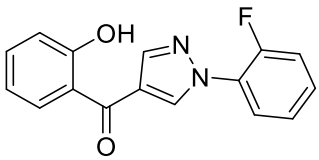

Compound **252** was synthesized using the general procedure P. The product was obtained as a yellow solid without further purification (13.20 mg, yield 33%). **^{1}H NMR** (500 MHz, DMSO-d_6) δ 10.99 (s, 1H), 8.76 (d, J = 2.1 Hz, 1H), 8.25 (s, 1H), 7.86 (td, J = 7.8, 7.4, 1.1 Hz, 1H), 7.71 (dd, J = 7.8, 1.7 Hz, 2H), 7.55 – 7.48 (m, 9H), 7.43 – 7.39 (m, 4H), 7.02 (dd, J = 8.2, 1.1 Hz, 3H), 7.01 – 6.95 (m, 4H). **^{13}C NMR** (126 MHz, DMSO) δ 158.70, 142.80, 134.70, 131.90, 130.90, 130.50,

130.40, 126.00, 125.80 (d), 124.10, 119.70, 119.60, 118.00, 117.70, 117.60, 117.40; **HRMS**-ESI (*m/z*): calculated for $C_{16}H_{11}FN_2O_2$ $[M+H]^+$ = 283.0805; found: 283.877.

(1-(4-Fluorophenyl)-1H-pyrazol-4-yl)(2-hydroxyphenyl)methanone (**253**)

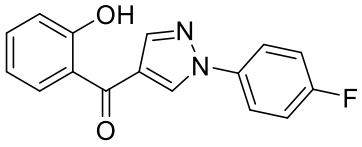

Compound **253** was synthesized using the general procedure P. The product was obtained as a yellow solid without further purification (51.90 mg, yield 64%). **^{1}H NMR** (400 MHz, Chloroform-*d*) δ 11.98 (s, 1H), 8.43 (d, *J* = 0.7 Hz, 1H), 8.17 (d, *J* = 0.7 Hz, 1H), 7.91 (dd, *J* = 8.0, 1.7 Hz, 1H), 7.77 – 7.69 (m, 2H), 7.53 (ddd, *J* = 8.7, 7.2, 1.7 Hz, 1H), 7.26 – 7.17 (m, 2H), 7.08 (dd, *J* = 8.4, 1.1 Hz, 1H), 6.98 (ddd, *J* = 8.2, 7.2, 1.2 Hz, 1H); **HRMS**-ESI (*m/z*): calculated for $C_{16}H_{12}N_2O_2$ $[M+H]^+$ = 283.0877; found: 283.0872.

(1-(2-Chlorophenyl)-1H-pyrazol-4-yl)(2-hydroxyphenyl)methanone (**254**)

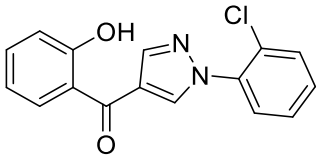

Compound **254** was synthesized using the general procedure P. The product was obtained as a beige solid without further purification (25.80 mg, yield 60%). **^{1}H NMR** (500 MHz, DMSO-d_6) δ 11.08 (s, 1H), 8.78 (s, 1H), 8.22 (s, 1H), 7.75 – 7.69 (m, 3H), 7.60 – 7.54 (m, 2H), 7.50 (ddd, *J* = 8.7, 7.3, 1.7 Hz, 1H), 7.02 (dd, *J* = 8.4, 1.1 Hz, 1H), 6.98 (td, *J* = 7.5, 1.2 Hz, 1H). **^{13}C NMR** (126 MHz, DMSO) δ 190.60, 159.00, 142.50, 137.40, 136.80, 134.80, 131.20, 131.00, 130.90, 128.80, 128.70, 123.80, 123.50, 119.70, 117.70. **HRMS**-ESI (*m/z*): calculated for $C_{16}H_{11}ClN_2O_2$ $[M+H]^+$ = 299.0582; found: 299.0577.

(1-(4-Chlorophenyl)-1H-pyrazol-4-yl)(2-hydroxyphenyl)methanone (**255**)

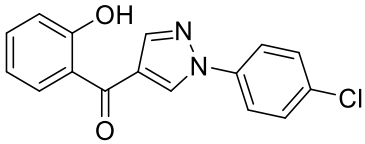

Compound **255** was synthesized using the general procedure P. The product was obtained as a yellow solid without further purification (16.40 mg, yield 19%). **^{1}H NMR** (400 MHz, Chloroform-*d*) δ 11.97 (s, 1H), 8.46 (s, 1H), 8.18 (s, 1H), 7.90 (dd, *J* = 8.0, 1.7 Hz, 1H), 7.74 – 7.68 (m, 2H), 7.53 (ddd, *J* = 8.7, 7.2, 1.7 Hz, 1H), 7.51 – 7.47 (m, 2H), 7.08 (dd, *J* = 8.4, 1.1 Hz, 1H), 6.98 (ddd, *J* = 8.3, 7.2, 1.2 Hz, 1H); **HRMS**-ESI (*m/z*): calculated for $C_{16}H_{12}ClN_2O_2$ $[M+H]^+$ = 299.0582; found: 299.0577.

(1-(4-Bromophenyl)-1H-pyrazol-4-yl)(2-hydroxyphenyl)methanone (**256**)

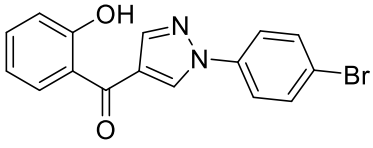

Compound **256** was synthesized using the general procedure P. The product was obtained as a brown solid without further purification (6.60 mg, yield 13%). **^{1}H NMR** (700 MHz, DMSO-d_6) δ 11.04 (s, 1H), 9.13 (s, 1H), 8.22 (s, 1H), 7.98 – 7.94 (m, 2H), 7.77 – 7.73 (m, 3H), 7.51 (ddd, *J* = 8.6, 7.2, 1.8 Hz, 1H), 7.02 (dd, *J* = 8.3, 1.1 Hz, 1H), 6.99 (td, *J* = 7.5, 1.1 Hz, 1H). **^{13}C NMR** (176 MHz, DMSO) δ 190.50, 158.90, 143.10, 138.60, 134.80, 132.90, 132.30, 131.10, 124.50, 123.90, 121.70, 120.40, 119.70, 117.70; **HRMS**-ESI (*m/z*): calculated for $C_{16}H_{12}BrN_2O_2$ $[M+H]^+$ = 343.0077; found: 343.0075.

(2-Hydroxyphenyl)(1-(o-tolyl)-1H-pyrazol-4-yl)methanone (**257**)

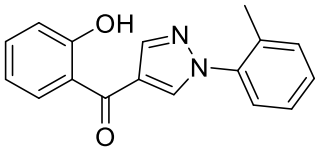

Compound **257** was synthesized using the general procedure P. The product was obtained as a brown solid without further purification (18.00 mg, yield 45%). **^{1}H NMR** (500 MHz, DMSO-d_6) δ 11.16 (s, 1H), 8.68 (d, J = 0.7 Hz, 1H), 8.19 (s, 1H), 7.78 (dd, J = 7.8, 1.7 Hz, 1H), 7.52 – 7.48 (m, 1H), 7.47 (dd, J = 7.9, 1.3 Hz, 1H), 7.46 – 7.43 (m, 2H), 7.38 (ddd, J = 7.7, 4.9, 3.6 Hz, 1H), 7.01 (dd, J = 8.3, 1.1 Hz, 1H), 6.98 (td, J = 7.5, 1.1 Hz, 1H), 2.24 (s, 3H). **^{13}C NMR** (126 MHz, DMSO) δ 190.80, 159.20, 142.20, 139.20, 136.00, 134.80, 133.60, 131.70, 131.20, 129.50, 127.20, 126.50, 123.70, 123.10, 119.70, 117.70, 18.20. **HRMS**-ESI (*m/z*): calculated for $C_{17}H_{15}N_2O_2$ $[M+H]^+$ = 279.1128; found: 279.1123.

(2-Hydroxyphenyl)(1-(p-tolyl)-1H-pyrazol-4-yl)methanone (**258**)

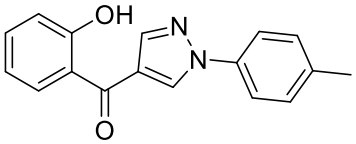

Compound **258** was synthesized using the general procedure P. The product was obtained as a brown solid without further purification (23.20 mg, yield 58%). **^{1}H NMR** (600 MHz, DMSO-d_6) δ 11.10 (s, 1H), 9.04 (s, 1H), 8.18 (s, 1H), 7.88 – 7.83 (m, 2H), 7.76 (dd, J = 7.8, 1.8 Hz, 1H), 7.51 (ddd, J = 8.7, 7.2, 1.7 Hz, 1H), 7.35 (d, J = 8.4 Hz, 2H), 7.02 (d, J = 8.4 Hz, 1H), 7.00 (t, J = 7.5 Hz, 1H), 2.37 (s, 3H); **^{13}C NMR** (151 MHz, DMSO) δ 190.60, 159.00, 142.70, 137.40, 137.10, 134.70, 131.90, 131.10, 130.40, 124.10, 123.80, 119.71, 119.70, 117.70, 20.90. **HRMS**-ESI (*m/z*): calculated for $C_{17}H_{15}N_2O_2$ $[M+H]^+$ = 279.1128; found: 279.1123.

(2-Hydroxyphenyl)(1-(2-methoxyphenyl)-1H-pyrazol-4-yl)methanone (**259**)

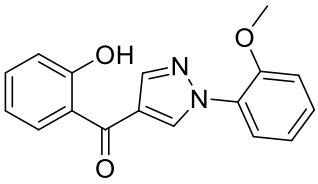

Compound **259** was synthesized using the general procedure P. The product was obtained as a brown solid without further purification (3.10 mg, yield 7%). **^{1}H NMR** (500 MHz, DMSO-d_6) δ 9.95 (s, 1H), 8.81 (d, J = 0.7 Hz, 1H), 8.26 (d, J = 0.9 Hz, 1H), 8.13 (dd, J = 8.0, 1.6 Hz, 1H), 7.84 (ddd, J = 8.7, 7.1, 1.7 Hz, 1H), 7.71 (dd, J = 8.6, 1.0 Hz, 1H), 7.53 (ddd, J = 8.1, 7.0, 1.1 Hz, 1H), 7.43 (dd, J = 7.9, 1.7 Hz, 1H), 6.94 (dd, J = 8.0, 1.3 Hz, 1H), 6.88 (td, J = 7.7, 1.3 Hz, 1H), 6.76 (td, J = 7.7, 1.7 Hz, 1H), 3.84 (s, 3H). **^{13}C NMR** (126 MHz, DMSO) δ 175.40, 156.20, 152.80, 145.60, 134.71, 134.70, 130.00, 126.10, 125.60, 123.70, 121.50, 120.30, 119.20, 119.10, 112.40, 111.30, 56.02. **HRMS**-ESI (*m/z*): calculated for $C_{17}H_{15}N_2O_3$ $[M+H]^+$ = 295.1004; found: 295.1077.

(2-Hydroxyphenyl)(1-(4-methoxyphenyl)-1H-pyrazol-4-yl)methanone (**260**)

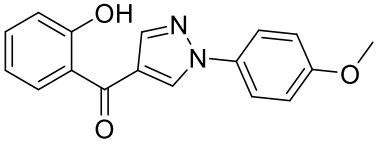

Compound **260** was synthesized using the general procedure P. The product was obtained as a grey solid without further purification (20.60 mg, yield 49%). **^{1}H NMR** (600 MHz, DMSO-d_6) δ 11.12 (s, 1H), 8.99 (s, 1H), 8.16 (s, 1H), 7.90 – 7.86 (m, 2H), 7.77 (dd, J = 7.8, 1.8 Hz, 1H), 7.51 (ddd, J = 8.7, 7.3, 1.7 Hz, 1H), 7.11 – 7.07 (m, 2H), 7.02 (dd, J = 8.3, 1.1 Hz, 1H), 6.99 (td, J = 7.5, 1.1 Hz, 1H), 3.82 (s, 3H). **^{13}C NMR** (151 MHz, DMSO) δ 190.70, 159.10, 158.90, 142.60, 134.70, 132.90, 131.80,

131.10, 123.90, 123.80, 121.40, 119.70, 117.70, 115.10, 55.90. **HRMS**-ESI (*m/z*): calculated for $C_{17}H_{15}N_2O_3$ $[M+H]^+$ = 295.1077; found: 295.1072.

(2-Hydroxyphenyl)(1-(6-methoxypyridin-3-yl)-1H-pyrazol-4-yl)methanone (**261**)

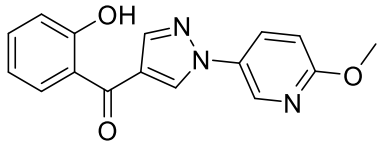

Compound **261** was synthesized using the general procedure P. The product was obtained as a brown solid without further purification (15.90 mg, yield 38%). **^{1}H NMR** (500 MHz, DMSO-d_6) δ 11.07 (s, 1H), 9.07 (d, *J* = 0.6 Hz, 1H), 8.75 (dd, *J* = 2.9, 0.6 Hz, 1H), 8.27 (dd, *J* = 8.9, 2.8 Hz, 1H), 8.21 (s, 1H), 7.76 (dt, *J* = 7.8, 2.1 Hz, 1H), 7.51 (ddd, *J* = 8.7, 7.3, 1.7 Hz, 1H), 7.03 (dd, *J* = 3.9, 0.9 Hz, 1H), 7.02 – 7.00 (m, 1H), 6.99 (dd, *J* = 7.6, 1.1 Hz, 1H), 3.92 (s, 3H). **^{13}C NMR** (126 MHz, DMSO) δ 190.50, 163.00, 159.00, 143.00, 138.60, 134.80, 132.50, 131.90, 131.10, 131.00, 124.20, 123.80, 119.70, 117.70, 111.50, 54.10. **HRMS**-ESI (*m/z*): calculated for $C_{16}H_{14}N_3O_3$ $[M+H]^+$ = 296.1030; found: 296.1024.

(2-Hydroxyphenyl)(1-(4-(trifluoromethoxy)phenyl)-1H-pyrazol-4-yl)methanone (**262**)

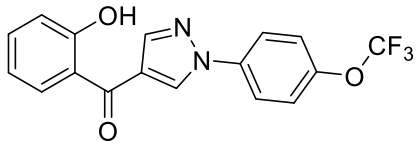

Compound **262** was synthesized using the general procedure P. The product was obtained as a pale orange solid without further purification (24.10 mg, yield 48%). **^{1}H NMR** (700 MHz, DMSO-d_6) δ 11.04 (s, 1H), 9.15 (s, 1H), 8.23 (s, 1H), 8.13 – 8.09 (m, 2H), 7.77 – 7.74 (m, 1H), 7.59 – 7.55 (m, 2H), 7.51 (ddt, *J* = 8.6, 7.3, 2.0 Hz, 1H), 7.04 – 7.01 (m, 1H), 7.01 – 6.98 (m, 1H). **^{13}C NMR** (176 MHz, DMSO) δ 190.60, 159.00, 147.40, 143.20, 138.20, 134.80, 132.60, 131.20, 125.20, 124.60, 123.90, 122.80, 121.60, 119.70, 117.70. **HRMS**-ESI (*m/z*): calculated for $C_{17}H_{12}F_3N_2O_3$ $[M+H]^+$ = 349.0795; found: 349.0792.

(2-Hydroxyphenyl)(1-(4-(trifluoromethyl)phenyl)-1H-pyrazol-4-yl)methanone (**263**)

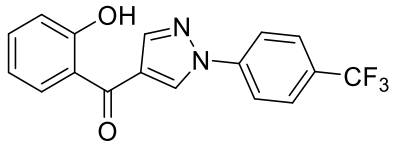

Compound **263** was synthesized using the general procedure P. The product was obtained as an orange solid without further purification (29.00 mg, yield 61%). **^{1}H NMR** (600 MHz, DMSO-d_6) δ 11.03 – 10.99 (m, 1H), 9.27 – 9.19 (m, 1H), 8.28 – 8.25 (m, 1H), 8.23 (d, *J* = 8.4 Hz, 1H), 8.17 – 8.07 (m, 2H), 7.93 (d, *J* = 8.6 Hz, 1H), 7.75 (dt, *J* = 7.8, 1.8 Hz, 1H), 7.54 – 7.49 (m, 1H), 7.05 – 7.02 (m, 1H), 7.00 (td, *J* = 7.5, 1.1 Hz, 1H). **^{13}C NMR** (151 MHz, DMSO) δ 190.50, 158.90, 143.60, 142.30, 134.80, 132.80, 131.30, 131.10, 127.30, 124.90, 124.00, 120.10, 119.80, 119.40, 117.70. **HRMS**-ESI (*m/z*): calculated for $C_{17}H_{12}F_3N_2O_2$ $[M+H]^+$ = 333.0845; found: 333.0843.

4-(4-(2-Hydroxybenzoyl)-1H-pyrazol-1-yl)benzonitrile (**264**)

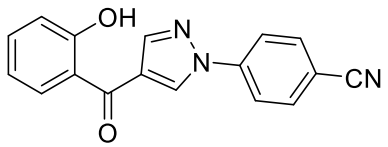

Compound **264** was synthesized using the general procedure P. The product was obtained as a pale-yellow solid without further purification (33.60 mg, yield 81%). **^{1}H NMR** (700 MHz, DMSO-d_6) δ 11.02 (s, 1H), 9.21 (s, 1H), 8.26 (s, 1H), 8.15 – 8.10 (m, 2H), 8.10 – 8.06 (m, 2H), 7.75 (dd, *J* =

7.7, 1.7 Hz, 1H), 7.51 (ddd, *J* = 8.6, 7.2, 1.7 Hz, 1H), 7.03 (dd, *J* = 8.3, 1.1 Hz, 1H), 7.00 (td, *J* = 7.5, 1.1 Hz, 1H). **^{13}C NMR** (176 MHz, DMSO) *δ* 190.50, 167.00, 158.90, 143.50, 142.30, 134.80, 132.60, 131.30, 131.10, 129.80, 124.80, 124.00, 119.80, 119.40, 117.70. **HRMS**-ESI (*m/z*): calculated for $C_{17}H_{11}N_3O_2Na$ $[M+Na]^+$ = 311.07, found: 309.00.

(2-Hydroxyphenyl)(1-(4-(methylsulfonyl)phenyl)-1H-pyrazol-4-yl)methanone (**265**)

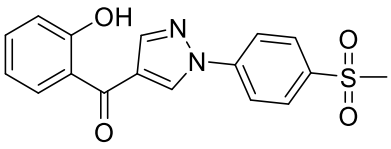

Compound **265** was synthesized using the general procedure P. The product was obtained as a beige solid without further purification (32.30 mg, yield 66%). **^{1}H NMR** (600 MHz, DMSO-d_6) *δ* 10.99 (s, 1H), 9.27 (s, 1H), 8.28 (d, *J* = 2.9 Hz, 2H), 8.27 (d, *J* = 2.0 Hz, 1H), 8.11 – 8.07 (m, 2H), 7.75 (dd, *J* = 7.8, 1.7 Hz, 1H), 7.52 (ddd, *J* = 8.3, 7.3, 1.7 Hz, 1H), 7.03 (dd, *J* = 8.3, 1.1 Hz, 1H), 7.01 (td, *J* = 7.5, 1.1 Hz, 1H), 3.29 (s, 3H).**^{13}C NMR** (151 MHz, DMSO) *δ* 190.40, 158.80, 143.70, 142.70, 139.50, 134.80, 132.90, 131.10, 129.20, 125.10, 124.00, 120.10, 119.80, 117.70, 43.90; **LC-MS** (**ESI**) (*m/z*) calculated for $C_{17}H_{14}N_2O_4S$ $[M+H]^+$ = 342.07; found: 342.80.

4-(4-(2-Hydroxybenzoyl)-1H-pyrazol-1-yl)benzenesulfonamide (**266**)

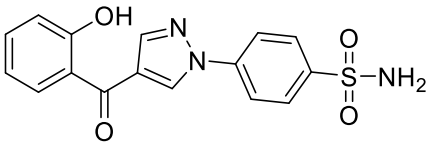

Compound **266** was synthesized using the general procedure P. The product was obtained as a beige solid without further purification (27.50 mg, yield 56%). **^{1}H NMR** (600 MHz, DMSO-d_6) *δ* 11.00 (s, 1H), 9.21 (s, 1H), 8.26 (s, 1H), 8.21 – 8.17 (m, 2H), 8.00 – 7.94 (m, 2H), 7.75 (dd, *J* = 7.8, 1.7 Hz, 1H), 7.54 – 7.49 (m, 1H), 7.48 (s, 2H), 7.03 (dd, *J* = 8.3, 1.1 Hz, 1H), 7.00 (td, *J* = 7.5, 1.1 Hz, 1H). **^{13}C NMR** (151 MHz, DMSO) *δ* 190.50, 158.80, 143.50, 143.00, 141.40, 134.80, 132.70, 131.10, 127.70, 124.90, 124.00, 119.81, 119.80, 117.70. **LC-MS** (**ESI**) (*m/z*) calculated for $C_{16}H_{13}N_3O_4S$ $[M+H]^+$ = 343.06; found: 344.00.

4-(4-(2-Hydroxy-4-methylbenzoyl)-1H-pyrazol-1-yl)benzoic acid (**267**)

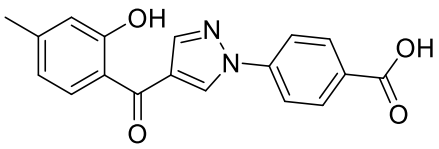

Compound **267** was synthesized using the general procedure P. The product was obtained as a brown solid without further purification (11.50 mg, yield 27%). **^{1}H NMR** (700 MHz, DMSO-d_6) *δ* 13.11 (s, 1H), 11.45 (s, 1H), 9.23 (s, 1H), 8.29 (s, 1H), 8.15 – 8.07 (m, 4H), 7.78 (d, *J* = 8.0 Hz, 1H), 6.86 (s, 1H), 6.84 (dd, *J* = 8.0, 1.6 Hz, 1H), 2.35 (s, 3H). **^{13}C NMR** (176 MHz, DMSO) *δ* 190.70, 167.00, 160.40, 146.50, 143.40, 142.30, 132.50, 131.70, 131.30, 129.80, 124.40, 120.90, 120.10, 119.40, 118.00, 21.80. **HRMS**-ESI (*m/z*): calculated for $C_{18}H_{15}N_2O_4$ $[M+H]^+$ = 323.1026; found: 323.1023.

4-(4-(2-Hydroxy-5-methylbenzoyl)-1H-pyrazol-1-yl)benzoic acid (**268**)

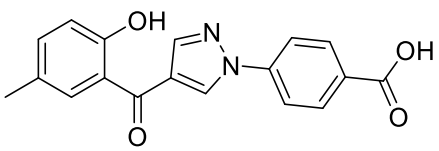

Compound **268** was synthesized using the general procedure P. The product was obtained as a yellow solid without further purification (32.00 mg, yield 60%). **^{1}H NMR** (500 MHz,

DMSO-d_6) δ 13.02 (s, 1H), 10.79 (s, 1H), 9.20 (s, 1H), 8.26 (s, 1H), 8.15 – 8.06 (m, 4H), 7.51 (d, J = 1.9 Hz, 1H), 7.32 (dd, J = 8.3, 2.2 Hz, 1H), 6.93 (d, J = 8.3 Hz, 1H), 2.30 (s, 3H). **^{13}C NMR** (126 MHz, DMSO) δ 190.60, 167.00, 156.70, 143.50, 142.40, 135.50, 132.60, 131.30, 130.90, 129.70, 128.50, 124.90, 123.70, 119.40, 117.60. **LC-MS** (**ESI**) (*m/z*) calculated for $C_{18}H_{14}N_2O_4$ $[M+H]^+$ = 322.10, found: 322.00.

4-(4-(5-Ethyl-2-hydroxybenzoyl)-1H-pyrazol-1-yl)benzoic acid (**269**)

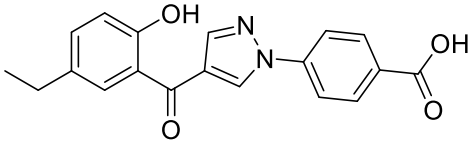

Compound **269** was synthesized using the general procedure P. The product was obtained as a yellow solid without further purification (33.50 mg, yield 61%). **^{1}H NMR** (600 MHz, DMSO-d_6) δ 13.04 (s, 1H), 10.76 (s, 1H), 9.19 (s, 1H), 8.25 (d, J = 0.5 Hz, 1H), 8.14 – 8.06 (m, 4H), 7.50 (d, J = 2.3 Hz, 1H), 7.36 (dd, J = 8.4, 2.3 Hz, 1H), 6.95 (d, J = 8.4 Hz, 1H), 2.62 (q, J = 7.6 Hz, 2H), 1.19 (t, J = 7.6 Hz, 3H). **^{13}C NMR** (151 MHz, DMSO) δ 190.60, 167.00, 156.80, 143.40, 142.40, 134.90, 134.30, 132.60, 131.30, 129.81, 129.80, 124.90, 123.80, 119.40, 117.70, 27.50, 16.20. **HRMS**-ESI (*m/z*): calculated for $C_{19}H_{17}N_2O_4$ $[M+H]^+$ = 337.1183, found: 337.1180.

4-(4-(2-Hydroxy-5-isopropylbenzoyl)-1H-pyrazol-1-yl)benzoic acid (**270**)

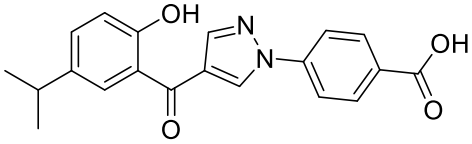

Compound **270** was synthesized using the general procedure P. The product was obtained as a yellow solid without further purification (31.00 mg, yield 54%). **^{1}H NMR** (500 MHz, DMSO-d_6) δ 13.09 (s, 1H), 10.71 (s, 1H), 9.18 (s, 1H), 8.23 (s, 1H), 8.15 – 8.06 (m, 4H), 7.49 (d, J = 2.3 Hz, 1H), 7.40 (dd, J = 8.5, 2.3 Hz, 1H), 6.96 (d, J = 8.5 Hz, 1H), 2.93 (hept, J = 6.9 Hz, 1H), 1.22 (s, 3H), 1.20 (s, 3H). **^{13}C NMR** (126 MHz, DMSO) δ 190.50, 167.00, 156.70, 143.40, 142.40, 139.50, 132.70, 132.60, 131.30, 129.70, 128.30, 125.10, 124.00, 119.40, 117.70, 32.80, 24.30. **HRMS**-ESI (*m/z*): calculated for $C_{20}H_{19}N_2O_4$ $[M+H]^+$ = 351.1339, found: 351.1338.

4-(4-(5-Fluoro-2-hydroxybenzoyl)-1H-pyrazol-1-yl)benzoic acid (**271**)

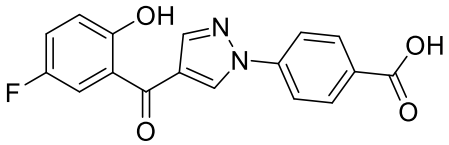

Compound **271** was synthesized using the general procedure P. The product was obtained as a yellow solid after purification using silica gel column chromatography (eluent system: 0-6% MeOH in dichloromethane) (19.00 mg, yield 35%). **^{1}H NMR** (700 MHz, DMSO-d_6) δ 13.13 (s, 1H), 10.49 (s, 1H), 9.19 (s, 1H), 8.24 (s, 1H), 8.13 – 8.07 (m, 4H), 7.40 (dd, J = 8.7, 3.2 Hz, 1H), 7.33 (td, J = 8.6, 3.2 Hz, 1H), 7.02 (dd, J = 9.0, 4.4 Hz, 1H). **^{13}C NMR** (176 MHz, DMSO) δ 188.60, 167.00, 156.00, 154.70, 153.70, 143.40, 142.30, 132.90, 131.30, 125.90 (d), 125.00, 120.60 (d), 119.40, 118.90 (d), 116.20 (d). **LC-MS** (**ESI**) (*m/z*) calculated for $C_{17}H_{11}FN_2O_4$ $[M+H]^+$ = 326.07; found: 327.00.

4-(4-(4-Fluoro-2-hydroxybenzoyl)-1H-pyrazol-1-yl)benzoic acid (**272**)

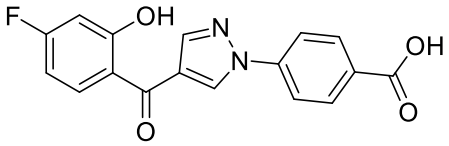

Compound **272** was synthesized using the general procedure P. The product was obtained as an orange solid without further purification (19.80 mg, yield 47%). **^{1}H NMR** (700 MHz, DMSO-d_6) δ 13.12 (s, 1H), 11.49 (s, 1H), 9.22 (s, 1H), 8.27 (s, 1H), 8.13 – 8.07 (m, 4H), 7.84 (dd, J = 8.7, 6.7 Hz, 1H), 6.87 – 6.81 (m, 2H). **^{13}C NMR** (176 MHz, DMSO) δ 189.30, 166.90, 165.10, 161.20 (d), 143.40, 142.30, 133.70 (d), 132.70, 131.30, 129.80, 124.70, 121.10, 119.40, 107.30 (d), 104.50 (d). **LC-MS** (**ESI**) (*m/z*) calculated for $C_{17}H_{11}FN_2O_4$ $[M+H]^+$ = 326.07; found: 326.80.

4-(4-(3,5-Difluoro-2-hydroxybenzoyl)-1H-pyrazol-1-yl)benzoic acid (**273**)

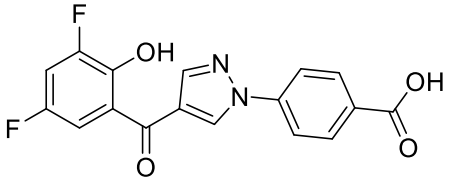

Compound **273** was synthesized using the general procedure P. The product was obtained as a brown solid without further purification (14.90 mg, yield 36%) **^{1}H NMR** (700 MHz, DMSO-d_6) δ 13.12 (s, 1H), 10.31 (s, 1H), 9.18 (s, 1H), 8.25 (s, 1H), 8.12 – 8.06 (m, 4H), 7.52 (ddd, J = 11.3, 8.6, 3.1 Hz, 1H), 7.22 (ddd, J = 8.4, 3.1, 1.6 Hz, 1H). **^{13}C NMR** (176 MHz, DMSO) δ 187.20, 166.90, 153.60, 152.50, 151.10, 143.20, 142.30, 133.30, 131.30, 129.80, 125.10, 119.40, 111.30 (d), 108.00 (t). **LC-MS** (**ESI**) (*m/z*) calculated for $C_{17}H_{10}F_2N_2O_4$ $[M+H]^+$ = 344.06; found: 344.80.

4-(4-(5-Chloro-2-hydroxybenzoyl)-1H-pyrazol-1-yl)benzoic acid (**274**)

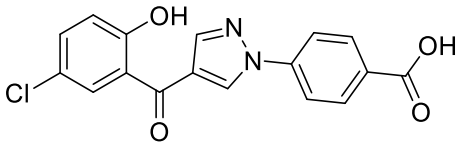

Compound **274** was synthesized using the general procedure P. The product was obtained as a yellow solid without further purification (26.70 mg, yield 47%). **^{1}H NMR** (500 MHz, DMSO-d_6) δ 12.97 (s, 1H), 10.60 (s, 1H), 9.17 (s, 1H), 8.21 (s, 1H), 8.13 – 8.06 (m, 4H), 7.51 – 7.46 (m, 2H), 7.03 (d, J = 8.6 Hz, 1H). **^{13}C NMR** (126 MHz, DMSO) δ 188.20, 167.00, 155.60, 143.30, 142.30, 132.90, 132.90, 131.30, 129.80, 129.30, 127.80, 125.30, 123.20, 119.40, 119.30; **LC-MS** (**ESI**) (*m/z*) calculated for $C_{17}H_{11}ClN_2O_4$ $[M+H]^+$ = 342.04; found: 342.80.

4-(4-(4-Chloro-2-hydroxybenzoyl)-1H-pyrazol-1-yl)benzoic acid (**275**)

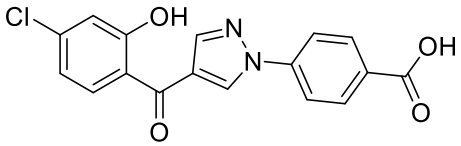

Compound **275** was synthesized using the general procedure P. The product was obtained as an orange solid without further purification (18.90 mg, yield 46%). **^{1}H NMR** (700 MHz, DMSO-d_6) δ 13.10 (s, 1H), 11.07 (s, 1H), 9.19 (s, 1H), 8.24 (s, 1H), 8.13 – 8.06 (m, 4H), 7.65 (d, J = 8.3 Hz, 1H), 7.08 (d, J = 2.0 Hz, 1H), 7.02 (dd, J = 8.3, 2.0 Hz, 1H). **^{13}C NMR** (176 MHz, DMSO) δ 188.90, 166.90, 158.70, 143.30, 142.30, 137.90, 132.80, 132.30, 131.30, 129.80, 125.10, 124.40, 119.80, 119.40, 117.20. **LC-MS** (**ESI**) (*m/z*) calculated for $C_{17}H_{11}ClN_2O_4$ $[M+H]^+$ = 342.04; found: 342.80.

4-(4-(3-Chloro-2-hydroxybenzoyl)-1H-pyrazol-1-yl)benzoic acid (**276**)

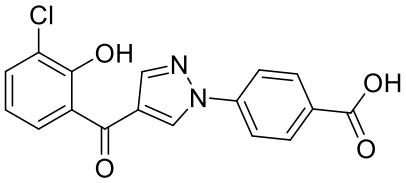

Compound **276** was synthesized using the general procedure P. The product was obtained as an orange solid without further purification (5.90 mg, yield 14%). **^{1}H NMR** (700 MHz, DMSO-d_6) δ 13.15 (s, 1H), 11.61 (s, 1H), 9.28 (s, 1H), 8.34 (s, 1H), 8.15 – 8.08 (m, 4H), 7.86 (dd, J = 7.8, 1.6 Hz, 1H), 7.74 (dd, J = 7.9, 1.5 Hz, 1H), 7.06 (td, J = 7.9, 5.0 Hz, 1H). **^{13}C NMR** (176 MHz, DMSO) δ 190.40, 155.10, 143.50, 142.57, 142.30, 135.10, 135.10, 133.10, 131.30, 130.30, 124.60, 124.00, 122.00, 120.70, 119.60. **LC-MS** (**ESI**) (*m/z*) calculated for $C_{17}H_{11}ClN_2O_4$ $[M+H]^+$ = 342.04; found: 343.00.

4-(4-(3,5-Dichloro-2-hydroxybenzoyl)-1H-pyrazol-1-yl)benzoic acid (**277**)

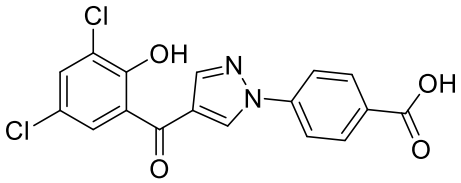

Compound **277** was synthesized using the general procedure P. The product was obtained as a yellow solid without further purification (38.50 mg, yield 62%). **^{1}H NMR** (600 MHz, DMSO-d_6) δ 13.11 (s, 1H), 10.88 (s, 1H), 9.24 (s, 1H), 8.29 (s, 1H), 8.13 – 8.07 (m, 4H), 7.82 (d, J = 2.6 Hz, 1H), 7.61 (d, J = 2.6 Hz, 1H). **^{13}C NMR** (151 MHz, DMSO) δ 187.90, 166.90, 152.00, 143.30, 142.20, 133.40, 132.80, 131.30, 129.90, 128.50, 128.50, 124.60, 123.80, 123.50, 119.50. **LC-MS** (**ESI**) (*m/z*) calculated for $C_{17}H_{10}Cl_2N_2O_4$ $[M+H]^+$ = 376.00; found: 376.80.

4-(4-(5-Bromo-2-hydroxybenzoyl)-1H-pyrazol-1-yl)benzoic acid (**278**)

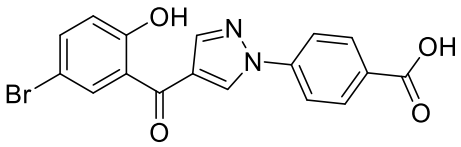

Compound **278** was synthesized using the general procedure P. The product was obtained as a yellow solid after purification using silica gel column chromatography (eluent system: 0-6% MeOH in dichloromethane + 0.1% AcOH) (7.10 mg, yield 11%). **^{1}H NMR** (600 MHz, DMSO-d_6) δ 13.07 (s, 1H), 10.60 (s, 1H), 9.17 (s, 1H), 8.20 (s, 1H), 8.09 (q, J = 8.6 Hz, 4H), 7.59 (dq, J = 5.5, 2.4 Hz, 2H), 6.98 (d, J = 9.5 Hz, 1H). **^{13}C NMR** (151 MHz, DMSO) δ 188.00, 167.00, 156.00, 143.30, 142.30, 135.70, 132.90, 132.00, 131.30, 129.80, 128.50, 125.60, 119.70, 119.40, 110.60. **LC-MS** (**ESI**) (*m/z*) calculated for $C_{17}H_{11}BrN_2O_4$ $[M+H]^+$ = 385.99, found: 384.80.

4-(4-(4-Bromo-2-hydroxybenzoyl)-1H-pyrazol-1-yl)benzoic acid (**279**)

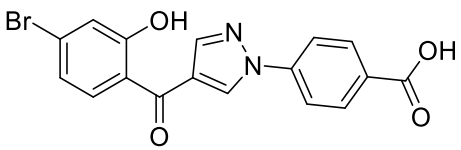

Compound **279** was synthesized using the general procedure P. The product was obtained as a yellow solid without further purification (24.10 mg, yield 63%). **^{1}H NMR** (600 MHz, DMSO-d_6) δ 13.09 (s, 1H), 11.00 (s, 1H), 9.18 (s, 1H), 8.24 (s, 1H), 8.14 – 8.07 (m, 4H), 7.55 (d, J = 8.3 Hz, 1H), 7.22 (d, J = 1.9 Hz, 1H), 7.16 (dd, J = 8.3, 1.9 Hz, 1H). **^{13}C NMR** (151 MHz, DMSO) δ 189.0, 166.9, 158.5, 143.3, 142.3, 132.9, 132.3, 131.3 (2C), 129.8, 126.6, 125.1, 124.8, 122.6, 120.1, 119.4 (2C). **LC-MS** (**ESI**) (*m/z*) calculated for $C_{17}H_{11}BrN_2O_4$ $[M+H]^+$ = 385.99, found: 386.60.

4-(4-(2-Hydroxy-5-methoxybenzoyl)-1H-pyrazol-1-yl)benzoic acid (**280**)

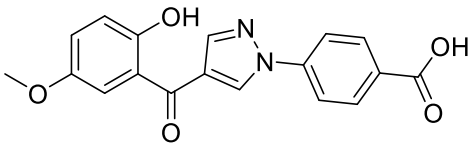

Compound **280** was synthesized using the general procedure P. The product was obtained as a yellow solid without further purification (18.50 mg, yield 33%). **^{1}H NMR** (700 MHz, DMSO-d_6) δ 13.16 (s, 1H), 10.33 (s, 1H), 9.20 (s, 1H), 8.25 (s, 1H), 8.13 – 8.05 (m, 4H), 7.15 – 7.08 (m, 2H), 6.96 (d, J = 8.8 Hz, 1H), 3.76 (s, 3H). **^{13}C NMR** (176 MHz, DMSO) δ 190.00, 167.00, 152.30, 152.20, 143.40, 142.20, 132.60, 132.60, 131.30, 125.00, 124.60, 121.40, 119.30, 118.70, 114.00, 56.00; **HRMS**-ESI (*m/z*): calculated for $C_{18}H_{15}N_2O_5$ $[M+H]^+$ = 339.0976; found: 339.0973.

4-(4-(2-Hydroxy-6-methoxybenzoyl)-1H-pyrazol-1-yl)benzoic acid (**281**)

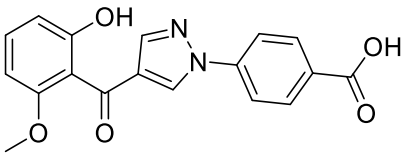

Compound **281** was synthesized using the general procedure P. The product was obtained as a red-brown solid without further purification (3.40 mg, yield 8%). **^{1}H NMR** (600 MHz, DMSO-d_6) δ 13.10 (s, 1H), 9.73 (s, 1H), 8.97 (d, J = 0.6 Hz, 1H), 8.10 – 8.03 (m, 4H), 7.99 (s, 1H), 7.26 – 7.21 (m, 1H), 6.61 – 6.55 (m, 2H), 3.68 (s, 3H); **^{13}C NMR** (151 MHz, DMSO) δ 206.90, 188.10, 166.90, 157.70, 155.50, 142.80, 142.40, 131.90, 131.30, 131.10, 127.40, 119.30, 117.60, 109.20, 102.80, 56.00; **LC-MS** (**ESI**) (*m/z*) calculated for $C_{18}H_{14}N_2O_5$ $[M+H]^+$ = 338.09; found: 339.0.

4-(4-(2-Hydroxy-5-nitrobenzoyl)-1H-pyrazol-1-yl)benzoic acid (**282**)

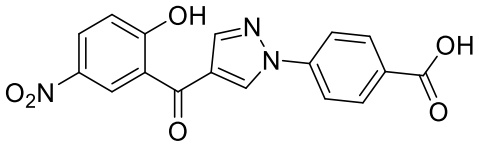

Compound **282** was synthesized using the general procedure P. The product was obtained as a yellow solid without further purification (36.30 mg, yield 63). **^{1}H NMR** (600 MHz, DMSO-d_6) δ 13.11 (s, 1H), 11.71 (s, 1H), 9.21 (s, 1H), 8.32 (dd, J = 9.1, 2.9 Hz, 1H), 8.28 (d, J = 2.9 Hz, 1H), 8.26 (s, 1H), 8.12 – 8.06 (m, 4H), 7.18 (d, J = 9.1 Hz, 1H). **^{13}C NMR** (151 MHz, DMSO) δ 186.90, 166.90, 162.00, 143.20, 142.20, 139.80, 133.20, 131.30, 129.80, 128.30, 127.40, 126.10, 125.40, 119.30, 117.90. **HRMS**-ESI (*m/z*): calculated for $C_{17}H_{12}N_3O_6$ $[M+H]^+$ = 354.0721; found: 354.0719.

4-(4-(5-Chloro-2-hydroxy-4-methylbenzoyl)-1H-pyrazol-1-yl)benzoic acid (**283**)

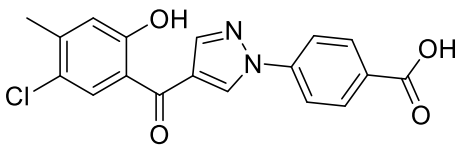

Compound **283** was synthesized using the general procedure P. The product was obtained as a yellow solid after purification using silica gel column chromatography (eluent system: 0-6% MeOH in dichloromethane + 0.1% AcOH) (19.00 mg, 47%). **^{1}H NMR** (600 MHz, DMSO-d_6) δ 13.05 (s, 1H), 10.80 (t, J = 90.5 Hz, 1H), 9.20 (s, 1H), 8.23 (s, 1H), 8.14 – 8.06 (m, 4H), 7.58 (s, 1H), 7.01 (s, 1H), 2.35 (s, 3H). **^{13}C NMR** (151 MHz, DMSO) δ 188.40, 167.00, 156.50, 143.30, 142.30, 141.80, 132.80, 131.30, 130.20, 129.90, 125.00, 124.50, 123.80, 120.00, 119.40, 20.40. **LC-MS** (**ESI**) (*m/z*) calculated for $C_{18}H_{13}ClN_2O_4$ $[M+H]^+$ = 356.06; found: 356.80.

4-(4-(2-Hydroxy-1-naphthoyl)-1H-pyrazol-1-yl)benzoic acid (**284**)

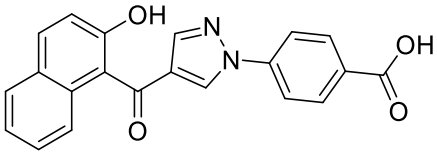

Compound **284** was synthesized using the general procedure P. The product was obtained as a beige solid without further purification (17.20 mg, yield 43%). **^{1}H NMR** (700 MHz, DMSO-d_6) δ 13.10 (s, 1H), 10.14 (s, 1H), 9.04 (s, 1H), 8.09 (s, 1H), 8.08 – 8.02 (m, 4H), 7.94 (d, *J* = 8.9 Hz, 1H), 7.89 (dd, *J* = 8.2, 1.4 Hz, 1H), 7.52 (dd, *J* = 8.5, 1.0 Hz, 1H), 7.41 (ddd, *J* = 8.4, 6.7, 1.4 Hz, 1H), 7.34 (ddd, *J* = 8.0, 6.7, 1.2 Hz, 1H), 7.28 (d, *J* = 8.9 Hz, 1H). **^{13}C NMR** (176 MHz, DMSO) δ 190.50, 166.90, 152.70, 143.00, 142.30, 132.50, 131.80, 131.50, 131.20, 129.70, 128.60, 128.10, 127.50, 123.50, 120.70, 119.30, 118.90; **HRMS**-ESI (*m/z*): calculated for $C_{21}H_{15}N_2O_4$ $[M+H]^+$ = 359.1038; found: 359.1024.

5.3 Biological evaluation

5.3.1 Methods for the identification and evaluation of LIN28 inhibitors

5.3.1.1 LIN28 expression and purification

Human LIN28A (residues 16-187) was expressed in *Escherichia coli BL21*(*DE3*). The culture was incubated at 37°C until absorbance reached 0.5–0.7 at 600 nm (OD600). Then, IPTG was added to a final concentration of 300 mM, and an induction was performed at 18°C overnight. Upon centrifugation, the bacterial pellet was resuspended in lysis buffer (pH = 7.5, 50 mM NaH_2PO_4, 300 mM NaCl, 0.1 mM PMSF) and lysed using a Microfluidizer. Afterward, a fresh portion of 0.1 mM PMSF and Triton X-100 (final concentration: 1%) were added. The lysate underwent clarification by ultracentrifugation at 23000 x g and 4°C for 1 h. Purification of the obtained protein occurred via immobilized nickel affinity chromatography (HisTrap, GE Healthcare) in a buffer containing 50 mM NaH_2PO_4 (pH = 8), 300 mM NaCl and 5% glycerol. For the gradient elution a maximum concentration of 0.5 M imidazole was used, the affinity tag was cleaved using His6-TEV-protease, and the protease and unspecific binders were separated by a second nickel affinity chromatography. LIN28A-containing fractions were concentrated and applied to a High Load Superdex 75 pg 16/ 600 column (GE Healthcare) with gel-filtration buffer (pH = 7.5, 30 mM NaH_2PO_4, 50 mM NaCl, 5% glycerol, 2 mM b-ME). The purified protein was concentrated and then stored at -80°C.

5.3.1.2 Fluorescence polarization assay

Fluorescence polarization assays were performed in black low-volume polystyrene 384 well plates (Cornig 4514). IC_{50} values were measured in technical triplicates. First, purified LIN28A (residues 16-187) was incubated for 30 min at a concentration of 200 nM with individual compounds in FP assay buffer (20 mM Tris, pH = 7, 100 mM NaCl, 5 mM $MgCl_2$, 2 mM glutathione (reduced), 0.1% NP-40). Afterward, FAM-labeled preE-*let-7f*-1 (mus musculus), synthesized by IDT, was added to a final concentration of 2 nM. Anisotropy was detected after incubation at room temperature using a TECAN Spark plate reader. Half maximal inhibitory concentrations (IC_{50}) were calculated using GraphPad Prism.

5.3.1.3 Compound screening

The Screening of compounds against LIN28 was performed by the Compound Management and Screening Center (COMAS) of the Max Planck Institute of Molecular Physiology. Compounds were used at 30 µM in FP assay buffer (20 mM Tris, pH 7, 100 mM NaCl, 5 mM MgCl2, 2 mM glutathione (reduced), 0.1% NP-40), and 40 µM LIN28A (residues: 16-187) and 2 nM FAM-labeled preE-*let-7f*-1 were used. The Pipetting of compounds occurred automatically with an ECHO 520 liquid handler, and subsequently, protein as well as RNA were dispensed using a multidrop dispenser with a 30-minute incubation time in between the individual additions. After 15 minutes, fluorescence polarization was measured on an EnVision plate reader, and total fluorescence was measured on a Paradigm plate reader.

Every plate contained a positive control consisting of a reaction without compound and a negative control consisting of a reaction without protein. Finally, data was analyzed using the software Quattro Workflow (Quattro Research GmbH).

5.3.1.4 Electrophoretic mobility shift assay (EMSA)

The electrophoretic mobility shift assay (EMSA) was used as a secondary assay to validate compounds identified as hit molecules in the FP assay. Therefore, purified LIN28A (residues: 16–187) was incubated with individual compounds and 5 U recombinant ribonuclease inhibitor (Takara Bio) in the EMSA reaction buffer (50 mM Tris, pH = 7.5, 100 mM NaCl, 10 mM β-mercaptoethanol, 50 µM $ZnCl_2$, 0.01% Tween 20, 12% glycerol and 2% DMSO) for 2 hours at room temperature. Then, preE-*let-7f-1*-Cy3 (*mus musculus*) (GGGGUAGUGAUUUUAC CCUGUUUAGGAGAU-Cy3, purchased from IDT) was added to a reaction volume of 50 µL and a final concentration of 5 nM. The final concentration of LIN28A was 10 nM and compound concentrations up to 75 µM were used. The reaction mixtures were incubated for an additional 15 minutes and 10 µL loading dye (40 % glycerol, 1.5x TAE) was added. 10 µL of each reaction was separated in an 8% polyacrylamide TAE gel at 4°C and 220 V for 1 hour using 0.25x TAE running buffer. Cy3 fluorescence was detected using a ChemiDoc MP (Bio-Rad) and 2 minutes of exposure time.

5.3.1.5 Nano differential scanning fluorimetry (nanoDSF)

Compounds at a final concentration of 75 µM were incubated with LIN28A protein (CSD residues: 16-126) for 45 minutes at room temperature in a buffer containing 30 mM NaH_2PO_4, 50 mM NaCl, and 1 mM $MgCl_2$ at pH = 8.0. Thermal protein stability was determined using a NanoTemper Prometheus NT.48 with a temperature rise from 20°C to 90°C increasing the temperature by 1°C per minute. Measurements were taken using standard capillaries. Intrinsic tryptophan fluorescence was recorded, and the ratio of fluorescence at 350 nm to that at 330 nm was determined. Calculations of the first derivative and the inflection point of the melting curve were performed using the software of the device.

5.3.1.6 Biolayer Interferometry (BLI)

Following the manufacturer's guidelines, recombinant LIN28A (CSD residues: 16-126) was biotinylated with EZ-Link Sulfo NHS-LC-LC-Biotin (Thermo Fisher Scientific) showing a labeling ratio of one biotin per protein. Excessive biotin reagent was removed using dialysis in a buffer containing 20 mM HEPES pH = 7.5, 150 mM NaCl, and 1 mM $MgCl_2$. After loading optimization, LIN28A was immobilized on SA biosensors (Sartorius). The dissociation and association of compounds were recorded in a buffer containing 20 mM HEPES pH 7.5, 150 mM NaCl, 1 mM $MgCl_2$, 0.05% Tween 20, 0.3 mg/mL BSA, and 1% DMSO. Data was measured and analyzed using the Octet Red384 instrument (Sartorius). Double referencing against samples without compound and sensors loaded with 10 µg/mL biocytin was performed instead of protein.

5.3.1.7 qPCR

JAR cells (obtained from DSMZ, German Collection of Microorganisms and Cell Cultures, Braunschweig, Germany, DSMZ no. ACC462) were plated in six-well plates and three independent replicates per individual compounds were treated at indicated concentrations (0.5% DMSO) for 24 h after which the total RNA was extracted using the RNeasy Mini Kit (Qiagen). Reverse transcription of 20 ng RNA was performed following the protocol of the TaqMan microRNA Reverse Transcription Kit (Applied Biosystems). Then, qPCR was done with TaqMan microRNA assays purchased from Applied Biosystems (Assay IDs: 001973, 002221, 002283) detecting for *let-7d* and *let-7i* using U6 snRNA as control. The assay was performed in two technical replicates from independent biological triplicates using TaqMan Universal Master Mix II, with UNG (Applied Biosystems) and a CFX Connect Real-Time PCR System S14 (BioRad). The obtained results were normalized to U6 snRNA expression and DMSO control using the $2^{-\Delta\Delta CT}$ method.

5.3.1.8 Docking analysis

Docking analysis of active compounds to the preE-*let-7* binding site of LIN28A (CSD residues: 16-187) (PDB code: 5UDZ) was performed with Schroedinger® Maestro 12.3. Three-dimensional structures of the compounds were prepared by calculating energy minimization with the MM2 function of PerkinElmer Chem3D® 20.1 and the chemical states were then generated using the ligand preparation module. For the preparation of the conformation of LIN28A, the protein preparation module was used to include hydrogen addition, water molecule removal, and energy minimization. For the reveal of crucial interactions of the RNA with LIN28A, to identify binding sites for small molecules, fragments of the miRNA were removed except for oligomers used as ligands. The potential binding site for docking was then generated by using the grid generation module. The grid was either generated using a preE-*let-7* fragment (A6-U8, U8eU11, or U13-A15) or crucial residues of LIN28A involved in binding to preE-*let-7*. Glide docking was subsequently performed by the glide dock module and evaluation occurred according to small molecule orientation, interactions between small molecules and LIN28A, docking score, and solvent exposure of small molecules. The interactions of compounds and LIN28A were visualized using PyMOL.

5.3.2 Methods for the identification and evaluation of METTL16 inhibitors

5.3.2.1 METTL16 expression and purification

A plasmid encoding the full-length human METTL16 sequence was gifted by Prof. Dr. Jessica A. Brown's lab. METTL16 (MTD: residues 1-291) was subcloned to a pOPIN plasmid containing N-terminal His tag, followed by an HRV 3C cleavage site. The plasmid was transformed into competent *Escherichia coli* Rosetta (DE3). Cells were cultured in fresh LB medium supplemented with 50 μg/mL kanamycin and 34 μg/mL chloramphenicol at 37°C in a 170-rpm shaker. After OD reached 0.8, the medium was chilled to 18°C, and IPTG was added to a final concentration of 0.5 mM to induce protein expression at 18°C for 16-20 h. Cells were harvested by 5000 x g, 18°C centrifugation for 15 min, then

the cell pellet was resuspended in lysis buffer containing 50 mM HEPES, pH = 7.5, 500 mM NaCl, 5% v/v glycerol, 0.5 mM TCEP, and 5 mM imidazole and supplemented with 1 mM PMSF. Then, cells were lysed by sonication on ice and the resulting lysate was centrifuged at 25000 x g at 4°C for 30 min and the supernatant was filtered and loaded to a nickel-affinity column (Ni Sepharose™ 6 Fast Flow, GE Healthcare). The column was equilibrated first using 50 mL lysis buffer, then 50 mL lysis buffer supplemented with 20 mM imidazole, then 30 mL lysis buffer supplemented with 30 mM imidazole, after which the protein finally was eluted using 15 mL lysis buffer supplemented with 300 mM imidazole. The eluate was treated with his-HRV-3C protease with the ratio of 1:30 w/w, and dialysis was performed in a buffer containing 50 mM HEPES, pH 7.5, 250 mM NaCl, 5% v/v glycerol and 0.5 mM TCEP overnight to lower the imidazole concentration to around 20 mM and to cleave the His tag. Subsequently, the protein was loaded onto another nickel affinity column to separate the cleaved His6-tag and his-HRV-3C protease. The METTL16-containing fractions were collected and concentrated using an Amicon ultra-centrifugal filter unit (Millipore). Finally, the protein was further purified by an SEC 75 column using SEC buffer (20 mM pH 7.5, 200 mM NaCl, 0.5 mM TCEP,2% v/v glycerol). The purity and size of METTL16 (MTD) were confirmed by SDS-PAGE and LC-MS and the purified protein was concentrated to 10 mg/mL, aliquoted, snap frozen using liquid nitrogen, and then stored at -80°C for the following experiments. His-tagged METTL16 (1-291) was purified following the same protocol, without protease cleavage and reverse nickel column chromatography.

5.3.2.2 Fluorescence polarization assay

The fluorescence polarization (FP) assay was performed using 384-well black plates (Corning #4514) in a total reaction volume of 20 μL, with the final concentration of METTL16 (MTD residues: 1-291) and FAM-MAT2A-hp1 RNA probe being 50 nM and 5 nM, respectively. Therefore, compounds were diluted in FP buffer and incubated with protein for 30 mins at room temperature, then the RNA probe was added and the fluorescence polarization was measured using a TECAN Spark plate reader, using an excitation wavelength of 485 nm and an emission wavelength of 535 nm with bandwidth of 20 nm. As a control 1% DMSO was used and the inhibition was calculated with the equation: inhibition=100%(Control-X)/(Control-Blank); Control: DMSO with protein and FAM-RNA; Blank: DMSO with FAM-RNA; X: compound with protein and FAM-RNA. The IC_{50} values were determined using GraphPad Prism. The FP assay using U6 snRNAΔ followed the same protocol as mentioned before, also using a final concentration of METTL16 MTD and U6 snRNA are 50 nM and 5 nM, respectively. The polarization was measured under an excitation wavelength of 630 nm and an emission wavelength of 680 nm with a bandwidth of 20 nm.

5.3.2.3 Compound screening

The screening was performed using a chemical library containing about 25,000 compounds provided by the COMAS of the Max Planck Institute of Molecular Physiology, using the aforementioned FP assay using 30 μM of compounds, 80 nM METTL16 (MTD residues: 1-291) and 2 nM FAM-MAT2A-

hp1 RNA (FAM-CUUGUUGGCGUAGGCUACAGAGAAGCCUU CAAG) in 384-well black plates (4514, Corning) with a final volume of 18 μL. Subsequently, 0.27 μL (2 mM compound stock solution) or 0.054 μL (10 mM compound stock solution) of compounds and the same volume of DMSO, functioning as control and blank group, were transferred to the plates using an ECHO machine. Then, 9 μL of the protein solution (or 9 uL buffer as Blank group) was dispensed to 160 nM protein solution using a Multidrop dispenser. After 30 min incubation at room temperature, 9 μL of 4 nM FAM-RNA solution was dispended to every well and the fluorescence polarization was measured by a TECAN Spark plate reader. The protein and FAM-RNA solutions were prepared using the FP buffer (20 mM HEPES, pH = 7.5, 50 mM NaCl, 0.05% v/v Tween 20, 0.05 mg/mL BGG). Primary screen hits were tested in serial dilutions to determine IC_{50} values and potential hit compounds were subsequently subjected to the orthogonal EMSA assay, to validate the activity against METTL16.

5.3.2.4 EMSA

For EMSA, METTL16 (MTD residues: 1-291) was incubated with indicated compounds or DMSO as a control in a buffer containing 20 mM HEPES, pH = 7.5, 50 mM NaCl, 0.05% v/v Tween 20, 0.05 mg/mL BGG at room temperature for 30 mins. Subsequently, a FAM-labelled MAT2A-hp1 RNA probe was added and incubated at room temperature for 10 min. Thereby, the final concentration of protein and RNA were 50 nM and 5 nM, respectively and 1% DMSO was used as control. After incubation with the RNA probe, the sample was loaded to a 6.6% native PAGE gel with 6x loading buffer (45 % H2O, 40 % glycerol, 15 % 10x TBE buffer, 0.1% bromphenol blue) and separated by electrophorese using a 0.5x TBE running buffer, at 120 V for 40 min at 4°C in the dark. The gel was then imaged by Chemi Doc MP (Bio-Rad). The EMSA using U6 snRNAΔ followed the same protocol, as the aforementioned with a final concentration of METTL16 (MTD residues: 1-291) and U6 snRNA at 50 nM and 5 nM, respectively. The EMSA using GGAUC-motif-containing RNA followed the same protocol, as the aforementioned with a final concentration of METTL16 (MTD residues: 1-291) and FAM-labeled-GGACU RNA at 600 nM and 5 nM, respectively. For EMSA showing RNA binding, indicated concentrations of fluorophore-labeled RNA were incubated with respective concentrations of METTL16 (MTD residues: 1-291) in EMSA buffer for 15 min at room temperature, then loaded to native PAGE gels and imaged with the method described above.

5.3.2.5 Differential scanning fluorimetry

The differential scanning fluorimetry (DSF) assay was performed in PBS buffer containing 2 mm DTT, in a total reaction volume of 20 μl with a final concentration of 1 μM METTL16 (MTD residues: 1-291) and 5×SYPRO Orange fluorescent dye (Sigma Aldrich S5692) and 0.35% DMSO (including DMSO from SYPRO Orange). The resulting melting curve was measured at a temperature gradient from 25°C to 95°C using increasements of 1°C each 30 seconds using a Bio-Rad CFX96 Real-Time PCR Detection System with the FRET scan mode. The midpoint of the transition (Tm) was obtained

by fitting the melting curve to Boltzmann sigmoidal in GraphPad Prism and the thermal shift (ΔTm) was calculated using the following equation ΔTm= Tm(compound)-Tm(DMSO).

5.3.2.6 SwitchSENSE biosensor assay

For the switchSENSE biosensor assay, a heliX instrument (Dynamic Biosensors) was used with a heliX adapter chip. The His-capture kit (HK-NTA-1) was used to functionalize and regenerate the chip. 100 nM, his-tagged METTL16 (MTD residues: 1-291) was captured to the surface and regenerated with imidazole solution (250 mM in 10 mM Tris, pH = 7.4, 140 mM NaCl, 0.05 % Tween20, 50 µM EDTA, 50 µM EGTA) after each measurement. PE140 buffer was used as running buffer (10 mM Na_2HPO_4/NaH_2PO_4, pH = 7.4, 140 mM NaCl, 0.05% Tween20, 50 µM EDTA) and 0.2% DMSO was used as blank. The association and dissociation flowrate were set at 200 µL/min, with an association time of 90 seconds and a dissociation time of 120 seconds. The resulting data was analyzed using heliOS with the "kinetics-mono & biphasic-free amplitudes fitting" mode.

5.3.2.7 Isothermal calorimetry assay

The isothermal calorimetry assay (ITC) was performed using the MicroCal PEAQ-ITC system (Malvern) at 25°C. METTL16 (MTD residues: 1-291) was directly used after purification. 700 µM protein in SEC buffer (20 mM pH = 7.5, 200 mM NaCl, 0.5 mM TCEP, 2% v/v glycerol) was supplemented with 0.5% DMSO and loaded into the syringe. Thereto, 50 µM compound in SEC buffer (final 0.5%DMSO) was loaded to the cell, and both samples were adjusted to 25°C and degassed before loading. The experiment was carried out using the reference power of 10, with 19 injections. Data were analyzed using MicroCal PEAQ-ITC Analysis Software.

5.3.2.8 *In vitro* methylation assay

Using the MTase Glo™ kit (Promega V7601), the methyltransferase activity of METTL16 (MTD residues: 1-291) was measured following the manufacturer's instructions. Therefore, the reaction was carried out in white 384-well plates (Corning #3824), with a total methyltransferase reaction volume of 8 µL, and final concentrations of METTL16, *MAT2A-hp1* and SAM being 1 µM, 1 µM, and 10 µM, respectively. 1% of DMSO was used as control and compounds were diluted in reaction buffer (20 mM Tris, pH 8.0, 50 mM NaCl, 1 mM EDTA, 3mM MgCl2, 0.1 mg/ml BSA, 1mM DTT) and preincubated with METTL16 for 30 min at room temperature. Double the amount of freshly prepared substrate solution was added to the reaction buffer containing *MAT2A-hp1* and SAM (supplemented in MTase Glo kit) and the mixture was allowed to stand for 1 h at room temperature. Then, 5x MTase-Glo Reagent was added and incubated for 30 min at room temperature, after which the MTase-Glo Detection Solution was added and incubated for another 30 min at room temperature. Luminescence was measured using a TECAN Spark plate reader. Varying the SAM concentrations, afforded the adjustment of the SAM concentration in 2x substrate solution. Finally, the inhibition was calculated using the

equation: inhibition = 100% (Control-X)/(Control-Blank), Control: DMSO with protein and RNA; Blank: DMSO with RNA; X: compound with protein and RNA.

5.3.2.9 Anti-proliferation assay

HAP1 and HCT116 cells were seeded in 96-well plates with 2000 cells/well and incubated overnight. Then, the compounds or DMSO (0.5%) as control were added. After 72 h of treatment, a CCK-8 solution (Vazyme, A311) was added to the wells and incubated at 37°C for 2 h. Afterward, the absorbance was measured at 450 nM using a TECAN Spark plate reader and finally, cell viability was calculated with the equation: Cell viability = 100% (X-Blank)/(Control-Blank); Control: the absorbance of DMSO treatment; Blank: the absorbance of only medium; X: the absorbance of compound treatment.

5.3.2.10 Colony formation assay

To visualize cellular effects upon compound treatment, MDA-MB-231 cells were collected and seeded with a density of 1000 cells per well into 24-well plates. After culturing the cells overnight, the medium was exchanged, and treated with indicated compounds or DMSO (0.5%) as control. The medium change and simultaneous compound treatment were performed every three days. After 7 days, the cell culture medium was discarded and cells were washed with PBS and fixed with 4% paraformaldehyde solution at room temperature for 15 min. After removal of the paraformaldehyde solution, the cells were washed with PBS again to remove excessive paraformaldehyde and then the cells were stained with 0.1% (w/v) crystal violet for 15 min. Finally, the cells were washed with H_2O to remove the remaining dye and then photographed.

5.3.2.11 RT-qPCR

The reverse transcription (RT) was conducted by using High-Capacity cDNA Reverse Transcription Kits (Thermo Fisher, 4368814) showing 500 ng of total RNA, and quantitative PCR (qPCR) was performed using PowerUp™ SYBR™ Green Master Mix (Thermo Fisher, A25742) with 10 μL volume. The cycling was performed using Bio-Rad CFX96 Real-Time PCR Detection System following the standard cycling mode (primer $T_m \geq 60°C$) of the manufacturer's protocol. The primers used are listed in Table S1. The P value was calculated using GraphPad Prism software's one-way ANOVA analysis.

Table 6: Sequence of used primers and oligonucleotides[a]

Primers/oligos	Sequence (5'-3')	Experiment	Source
288-METTL16_M1_Fwd	AAGTTCTGTTTCAGGGCCCGATGGCT CTGAGTAAATCAATGCATGCAAG	subclone	IDT
290-METTL16_D291_Rev	ATGGTCTAGAAAGCTTTAATCATAAA AACTCCAAGCTAAGGCCCATCTC	subclone	IDT
FAM-*MAT2A*-hp1	FAM-CUUGUUGGCGUAGGCUACAGAGA	FP, EMSA	IDT

MAT2A-hp1	AGCCUUCAAG CUUGUUGGCGUAGGCUACAGAGAAG CCUUCAAG	MTase Glo	IDT
Cy5-U6 snRNA Δ	Cy5-GGAUACAGAGAAGAUUAGCAUGGCC CCUGCGCAAGGAUGACACGCAAAUU CGU	FP, EMSA	IDT
FAM- GGACU-RNA	FAM-UUCUUCUGUGGACUGUG	FP, EMSA	IDT
GGACU-RNA	UUCUUCUGUGGACUGUG	MTase Glo	IDT
Pre-miR-17-hp	GUGCAGGUAGUGAUAUGUGCAUCU ACUGCAC	FP	IDT
Pre-miR-17-hp bp	GUGCAGGUAGAUGAUAUGUGCAUC UACCUGCAC	FP	IDT
Pre-miR-21-hp	GGGUUGACUGUUGAAUCUCAUGGCA ACCC	FP	IDT
*GAPDH*_Fwd	GAAGGTGAAGGTCGGAGTC	RT-qPCR	IDT
*GAPDH*_Rev	GAAGATGGTGATGGGATTTC	RT-qPCR	IDT
*MAT2A*_spliced_Fwd	GAATTTCGATCTCCGCCCTG	RT-qPCR	IDT
*MAT2A*_spliced_Rev	AGCCTACGCCAACAAGTCTG	RT-qPCR	IDT

[a]Note: RNAs were pre-folded by heating at 95 ˚C for 3 min and then slowly cooled to room temperature.

5.3.2.12 Dot blot assay

Concentrations of the total RNA were measured by using NanoDrop and calibrated by adding RNase-free water to each sample to the same concentration. The RNA samples were then heated at 95°C for 3 min and immediately cooled on ice to disrupt the formation of secondary structures. The total amount of RNA (1 μg) was dropped onto a positively charged nylon membrane (Invitrogen, AM10102). With the RNA side up, the membrane was then immediately transferred to the UVP Crosslinker (analytik jena) equipped with a 254 nM bulb and crosslinked under the UV light for 5 min twice. After this procedure, the membrane was washed in TBST (1x TBS with 0.1% Tween-20) for 10 min at room temperature and blocked with 5% skimmed milk in TBST for another hour at room temperature. The membrane was incubated with anti-m^{6}A antibody (Synaptic systems, 202003, 1 μg/mL) overnight at 4˚C and washed with TBST for 10 min three times. Then, the membrane was incubated with the secondary antibody HRP-conjugated Goat Anti-Rabbit (Proteintech, SA00001-2, 1: 3000) at 37°C, shaking for 1 h. The membrane was washed with TBST and detected with the Amersham ECL Prime Western Blotting Detection Reagent. After imaging, the membrane was washed once more with TBST

and finally stained with methylene blue (0.2% methylene blue in 0.2 M sodium acetate and 0.2 M acetic acid) as the loading control.

5.3.2.13 Docking analysis

To analyze a potential binding mode of aminothiazolones, computational analysis was conducted by docking the compounds to the RNA binding site of METTL16 (PDB code: 6B91)[179] For the analysis, Schrödinger® Maestro 12.3 was used. First, three-dimensional structures of compounds were prepared after calculating energy minimization by MM2 with PerkinElmer Chem3D® 22.2. Chemical states were generated with the ligand preparation module and METTL16 conformation with the protein preparation module. Protein preparation consisted of hydrogen addition, water molecule removal, and energy minimization. Crucial interactions of *MAT2A* 3'UTR with METTL16 were identified based on the resolved structure of the RNP complex and then used to identify potential binding sites for the aminothiazolones. The binding site for docking was generated by using the grid generation module at residues of METTL16 involved in the binding of *MAT2A* 3'UTR. Finally, the glide dock module was used and the results were evaluated according to interactions between small molecules and METTL16, small molecule orientations, docking scores, and solvent exposure patterns. The interactions of aminothiazolones and METTL16 were visualized using PyMOL.

5.3.2.14 Protein mass spectrometry

To investigate potential covalent interaction of the aminothiazolones and METTL16 (MTD residues: 1-291), the protein was first diluted to a final concentration of 30 µM in SEC buffer containing 20 mM pH = 7.5, 200 mM NaCl, 0.5 mM TCEP and 5% v/v glycerol, and incubated with DMSO or 100 µM compound (final 1% DMSO) at room temperature for either 30 min or 150 min. Then, the samples were analyzed on an Agilent 1260 II Infinity system equipped with an electrospray ion source in positive mode, run through a Desalting cartridge (AdvanceBio Desalting-RP, 2.1 mm, 12.5mm, Agilent) with a gradient of 5-80% acetonitrile (HPLC-grade) (+ 0.1% TFA) in double distilled water (+ 0.1% TFA) (flowrate: 0.4 mL/min, runtime: 6 min). The Spectra were deconvoluted using the ProMass software (Enovatia).

5.3.3 Methods for the identification and evaluation of YTHDF2 degrader and small-molecule inhibitors

5.3.3.1 Western blot

MCF7, MDA-MB-231, JAR, K562, MOLM13, A549, and Hela cell lines were seeded in 6-well plates with 1.0 × 106 cells/well and incubated overnight. Subsequently, the cells were detached with trypsin or collected directly and then washed with PBS (two times). To the cell lysis buffer (RIPA: 1 mM PMSF = 99: 1) (SERVA) was added and all samples were kept on ice for 30 min and then centrifuged at 4°C for 20 min at 12,000 rpm. The resulting supernatants were then collected and the protein concentration was determined by the BCA kit (SERVA). Afterward, the supernatants were transferred to clean tubes

with a 5× loading buffer and heated for 5 min at 95 °C. Primary antibody YTHDF2 (Proteintech, 24744-1-AP, 1: 15000) and secondary antibody Goat Anti-Rabbit IgG Antibody (H+L), HRP Conjugated (bs-0295G-HRP, 1:5000) were used. Chemiluminescent detection was performed using a ChemiDoc MP (Bio-Rad).

5.3.3.2 YTHDF2 expression and purification

A YTHDF2 (YTH-domain: residues 383-553) construct was subcloned to a pOPIN plasmid containing N-terminal His6 and GST tags. The plasmid was transformed to chemically competent *Escherichia coli BL21*(*DE3*). The culture was incubated in an LB medium at 37°C until absorbance reached 0.5–0.7 at 600 nm (OD600). Subsequently, expression of the fusion protein was induced by adding 300 µM IPTG at 18°C for 18 h. Then, the cells were collected and lysed via sonication in buffer (20 mM HEPES, pH = 7.4, 200 mM NaCl, 5% glycerol, 0.1 mM PMSF, 10 µg/mL DNase I, 10 µg/mL lysozyme, SIGMAFAST Protease inhibitor cocktail). The lysate underwent clarification by ultracentrifugation at 60000 x g and 4°C for 1 h and the resulting supernatant was purified by an immobilized nickel affinity chromatography using a 5 mL HisTrap column (Cytiva) which was equilibrated with a buffer containing 20 mM HEPES (pH = 7.4), 200 mM NaCl and 5% glycerol beforehand. For the gradient elution, a maximum concentration of 0.5 M imidazole was used, the affinity tag was cleaved using His6-HRV 3C protease, and the protease and unspecific binders were separated by a second nickel affinity chromatography (HisTrap column). YTHDF2-containing fractions were concentrated and further purified using a High Load Superdex 75 pg 16/600 column (Cytiva), which was equilibrated with a buffer containing 20 mM HEPES (pH = 7.4), 200 mM NaCl, and 5% glycerol. The purified protein was concentrated and then stored at -80°C.

5.3.3.3 Fluorescence polarization assay

The fluorescence polarization (FP) assays were performed in black low volume polystyrene 384 well plates (Cornig #4514) in a total reaction volume of 15 µL, with the final concentration of YTHDF2 (residues 383-553) and FAM-m^{6}A RNA probe being 20 nM and 5 nM respectively, in buffer containing 20 mM HEPES/KOH pH = 7.5, 50 mM NaCl, 0.005% Tween 20 and 1 mM GSH (DTT). After incubating the compounds with protein for 20 min, the RNA probe was added and incubated at 4˚C for an additional 30 min, and then the fluorescence polarization was measured using a TECAN Spark plate reader, using an excitation wavelength of 485 nm and an emission wavelength of 535 nm (bandwidth = 20 nm). Half maximal inhibitory concentrations (IC_{50}) were calculated using GraphPad Prism, calculated with the equation: inhibition rate=100% (Control-X)/(Control-Blank); Control: DMSO with protein and FAM-RNA; Blank: DMSO with FAM-RNA; X: compound with protein and FAM-RNA.

5.3.3.4 Compound screening

The screening of compounds against YTHDF2 was performed against a chemical library containing 15,000 compounds at the Compound Management and Screening Center (COMAS) of the Max Planck

Institute of Molecular Physiology. Therefore, 20 nM YTH-domain (residues: 383-553) and 5 nM FAM-17mer-m6A RNA (UUCUUCUGUGG(m^6)ACUGUG, purchased from IDT) were treated with compounds in FP assay buffer (20 mM HEPES/KOH pH = 7.5, 50 mM NaCl, 0.005% Tween 20 and 1 mM GSH (DTT)). The Pipetting of compounds occurred automatically with an ECHO 520 liquid handler, and subsequently, protein as well as RNA were dispensed using a multidrop dispenser with a 30-minute incubation time in between the individual additions. After 15 minutes, fluorescence polarization was measured on an EnVision plate reader, and total fluorescence was measured on a Paradigm plate reader. Every plate contained a positive control consisting of a reaction without compound and a negative control consisting of a reaction without protein. Finally, data was analyzed using the software Quattro Workflow (Quattro Research GmbH). Primary screen hits were tested in serial dilutions to determine the IC_{50} values.

5.3.3.5 EMSA

Compounds (varying concentrations from 3.1 µM to 100 µM) were incubated with 250 nM YTHDF2 (YTH-domain: residues: 383-553) and 20 nM FAM-17mer-RNA (UUCUUCUGUGG(m^6)ACUGUG) (purchased from IDT) in a buffer containing 20 mM HEPES, pH = 8.2, 50 mM NaCl, 0.05% Triton X-100, 5% v/v Glycerol for 20 min at 4°C. The samples were subjected to a 12% native polyacrylamide gel and run at 120 V for 90 min at 4°C using 0.5× TBE buffer. Afterward, the gels were imaged with a ChemiDoc MP (Bio-Rad), and Cy3/Alexa488 fluorescence was detected using a 1 min exposure time. Finally, band intensities were analyzed by ImageJ.

5.3.3.6 NanoDSF

Compounds at a final concentration of 50 µM were incubated with YTHDF2 protein (YTH-domain residues: 383-553) for 50 min at room temperature in a buffer containing 100mM KPi, pH 7.0, 250mM NaCl, 10% Glycerol. Thermal protein stability was determined using a NanoTemper Prometheus NT.48 with a temperature rise from 20°C to 90°C increasing the temperature by 1°C per minute. Measurements were taken using standard capillaries. Intrinsic tryptophan fluorescence was recorded, and the ratio of fluorescence at 350 nm to that at 330 nm was determined. Calculations of the first derivative and the inflection point of the melting curve were performed using the software of the device.

5.3.3.7 Cellular thermal stability assay (CETSA)

JAR cells were seeded on cell culture plates (100 mm) and incubated overnight. The cells were treated with 50 µM compound or 0.1% DMSO as a control, respectively, and incubated for 24 h. Afterwards, the cells were collected and washed in PBS and then lysed in a buffer containing RIPA: 1 mM to which PMSF = 99: 1 (SERVA) was added. The resulting lysates were then divided into 9 aliquots of 50 µL into 0.2 mL microcentrifuge tubes and incubated at a temperature gradient (40-64°C) on a PCR cycler for 3 min. After that, the lysates were frozen and thawed three times in dry ice and at room temperature for 3 min each. All tubes were then centrifuged at 4°C for 20 min at 12,000 rpm, supernatants were

collected and the protein concentration was determined by BCA kit (SERVA). The supernatants were transferred to clean tubes with a 5× loading buffer and heated for 5 min at 95 °C. Primary antibody YTHDF2 (Proteintech, 24744-1-AP, 1: 15000) and secondary antibody Goat Anti-Rabbit IgG Antibody (H+L), HRP Conjugated (bs-0295G-HRP, 1:5000) were used. Chemiluminescent detection was performed using a ChemiDoc MP (Bio-Rad).

5.3.3.8 Dot blot assay

K562 and JAR cell lines were seeded in 6-well plates with 1.0 × 106 cells/well and incubated overnight. The cells were detached directly and then washed with PBS. Total RNA was then extracted with the Aurum total RNA mini kit and the RNA concentration was determined by NANODROP 2000c (Thermo) and then heated for 5 min at 95°C. Primary antibody Rb pAb to *N*6-methyladenosine (m^6A) (abcam, ab286164, 1: 1000) and secondary antibody HRP-conjugated Affinipure Goat Anti-Rabbit IgG(H+L) (SA00001-2, 1:8000) were used. Chemiluminescent detection was performed using a ChemiDoc MP (Bio-Rad).

5.3.3.9 Cell cycle analysis

K562 cell line was seeded in 6-well plates with 1.0 × 106 cells/well and incubated overnight. Compounds were added in varying concentrations to the medium to the 6-well plates and the cells were then incubated for 24 h. Then, the cell cycle analysis kit (Sigma-Aldrich, MAK344) was used. The cells were detached with trypsin and washed with 2 mL ice-cold cell cycle assay buffer for each sample. After being centrifuged, the supernatant was removed, cells were fixed by adding 2 mL ice-cold 70% ethanol dropwise while vortexing to the cell pellet, and then placed on ice for 30 min. The cells were centrifuged at 400×g for 5 min, and the supernatant was removed. Cells were washed with 2 mL cell cycle assay buffer and then resuspended completely in 500 µL staining solution and protected from light exposure. After being incubated at room temperature for 30 min, each sample was analyzed by flow cytometry (Sony Biotechnology Cell Sorter SH800S) with proper machine settings and the data was analyzed by cell sorter software (Sony Biotechnology).

5.3.3.10 Apoptosis assay

For apoptosis assays, the K562 cell line was seeded in 6-well plates with 1.0 × 106 cells/well and incubated overnight. Compounds were added in varying concentrations to the medium to the 6-well plates and the cells were then incubated for 24 h. Afterward, the cells were detached with trypsin and washed twice with PBS and cold BioLegend's cell staining buffer. Then, 5 µL of FITC Annexin V and 10 µL of propidium iodide solution were added and the cells were gently vortexed and incubated for 15 min at room temperature (25°C) in the dark. After adding 400 µL of Annexin V binding buffer to each tube, the individual samples were analyzed by flow cytometry (Sony Biotechnology Cell Sorter SH800S) with proper machine settings and the data was analyzed by cell sorter software (Sony Biotechnology).

5.3.3.11 Anti-proliferation MTT assay

HCT116, K562, and JAR cells were seeded in 96-well plates with 3500 cells/well and were incubated for 8 h. The medium with different concentrations of compounds was added to the 96-well plates. Data was normalized to the medium (+0.1% DMSO). The cells were incubated for 72 h, and MTT solution (5 mg/mL, 20 µL) was added per well in the dark and incubated for an additional 4 h. The old medium was discarded and 150 µL DMSO was added per well. The absorbance of the well was measured by a TECAN plate reader at a wavelength of 492 nm.

5.3.3.12 Docking analysis

To analyze a potential binding mode of pyrazoles, computational analysis was conducted by docking the compounds to the RNA binding site of YTHDF2 (PDB code: 4RDN).[212] For the analysis, Schrödinger® Maestro 12.3 was used. First, three-dimensional structures of compounds were prepared after calculating energy minimization by MM2 with PerkinElmer Chem3D® 22.2. Chemical states were generated with the ligand preparation module and YTHDF2 conformation with the protein preparation module. Protein preparation included hydrogen addition, water molecule removal, and energy minimization. Crucial interactions of m^6A with YTHDF2 were identified based on the resolved structure of the protein-m^6A complex and then used to identify potential binding sites for the pyrazoles. The binding site for docking was generated using the grid generation module at residues of YTHDF2 crucial for binding m^6A. Finally, the glide dock module was used and the results were evaluated according to interactions between small molecules and YTHDF2, small molecule orientations, docking scores, and solvent exposure patterns. The interactions of pyrazoles and YTHDF2 were visualized using PyMOL.

6 References

1. Crick, F. Central Dogma of Molecular Biology. *Nature* **227**, 561–563 (1970).
2. Djebali, S. *et al.* Landscape of transcription in human cells. *Nature* **489**, 101–108 (2012).
3. The FANTOM Consortium and the RIKEN Genome Exploration Research Group Phase I & II Team*. Analysis of the mouse transcriptome based on functional annotation of 60,770 full-length cDNAs. *Nature* **420**, 563–573 (2002).
4. Quinn, E. M., Cormican, P., Kenny, E. M., Hill, M. & Anney, R. Development of Strategies for SNP Detection in RNA-Seq Data: Application to Lymphoblastoid Cell Lines and Evaluation Using 1000 Genomes Data. *PLoS One* **8**, 58815 (2013).
5. Cooper, T. A., Wan, L. & Dreyfuss, G. RNA and Disease. *Cell* **136**, 777–793 (2009).
6. Bartel, D. P. MicroRNAs: Genomics, Biogenesis, Mechanism, and Function. *Cell* **116**, 281–297 (2004).
7. Mattick, J. S. *et al.* Long non-coding RNAs: definitions, functions, challenges and recommendations. *Nat Rev Mol Cell Biol* **24**, 430–447 (2023).
8. Goodrich J. A. & Kugel J. F. Non-coding-RNA regulators of RNA polymerase II transcription. *Nat. Rev. Mol. Cell Biol.* **7**, 612–616 (2006).
9. Sanchez-Elsner, T., Gou, D., Kremmer, E. & Sauer, F. Noncoding RNAs of Trithorax Response Elements Recruit Drosophila Ash1 to Ultrabithorax. *Science (1979)* **311**, 1118–1123 (2006).
10. Donley, N., Smith, L. & Thayer, M. J. ASAR15, A cis-Acting Locus that Controls Chromosome-Wide Replication Timing and Stability of Human Chromosome 15. *PLoS Genet.* **11**, e1004923 (2015).
11. Sato, K., Akiyama, M. & Sakakibara, Y. RNA secondary structure prediction using deep learning with thermodynamic integration. *Nat. Commun.* **12**, 941 (2021).
12. Ding, Y. *et al.* In vivo genome-wide profiling of RNA secondary structure reveals novel regulatory features. *Nature* **505**, 696–700 (2014).
13. Maharana, S. *et al.* RNA buffers the phase separation behavior of prion-like RNA binding proteins. *Science (1979)* **360**, 918–921 (2018).
14. Cai, Z. *et al.* RIC-seq for global in situ profiling of RNA–RNA spatial interactions. *Nature* **582**, 432–437 (2020).
15. Delaunay, S., Helm, M. & Frye, M. RNA modifications in physiology and disease: towards clinical applications. *Nat. Rev. Gen.* **25**, 104–122 (2024).
16. Anderson, B. R. *et al.* Incorporation of pseudouridine into mRNA enhances translation by diminishing PKR activation. *Nucleic Acids Res.* **38**, 5884–5892 (2010).

17. Karikó, K. *et al.* Incorporation of pseudouridine into mRNA yields superior nonimmunogenic vector with increased translational capacity and biological stability. *Mol. Ther.* **16**, 1833–1840 (2008).
18. Karikó, K., Buckstein, M., Ni, H. & Weissman, D. Suppression of RNA recognition by Toll-like receptors: The impact of nucleoside modification and the evolutionary origin of RNA. *Immunity* **23**, 165–175 (2005).
19. Shatkin, A. J. Capping of Eucaryotic mRNAs. *Cell* **9**, 645–653 (1976).
20. Maquat, L. E., Tarn, W. Y. & Isken, O. The pioneer round of translation: Features and functions. *Cell* **142**, 368–374 (2010).
21. John D. Gross *et al.* Ribosome Loading onto the mRNA Cap Is Driven by Conformational Coupling between eIF4G and eIF4E. *Cell* **115**, 739–750 (2003).
22. Wells, S. E., Hillner, P. E., Vale, R. D. & Sachs, A. B. Circularization of mRNA by Eukaryotic Translation Initiation Factors. *Mol. Cell* **2**, 135–140 (1998).
23. Nichols, J. L. 'Cap' structures in maize poly(A)-containing RNA. *Biochim. Biophys. Acta* **563**, 490–495 (1979).
24. Desrosiers, R., Friderici, K. & Rottman, F. Identification of Methylated Nucleosides in Messenger RNA from Novikoff Hepatoma Cells (RNA methylation/RNA processing/methylnucleoside composition). *PNAS* **71**, 3971–3975 (1974).
25. Beemon, K. Localization of IV-Methyladenosine in the Rous Sarcoma Viru Genome. *J. Mol. Biol.* **113**, 165–179 (1977).
26. Dominissini, D. *et al.* Topology of the human and mouse m6A RNA methylomes revealed by m6A-seq. *Nature* **485**, 201–206 (2012).
27. Zaccara, S. & Jaffrey, S. R. A Unified Model for the Function of YTHDF Proteins in Regulating m6A-Modified mRNA. *Cell* **181**, 1582-1595.e18 (2020).
28. Xiao, W. *et al.* Nuclear m6A Reader YTHDC1 Regulates mRNA Splicing. *Mol. Cell* **61**, 507–519 (2016).
29. Roundtree, I. A. *et al.* YTHDC1 mediates nuclear export of N6-methyladenosine methylated mRNAs. *Elife* **6**, e31311 (2017).
30. Lee, M. H. & Schedl, T. *RNA-Binding Proteins. WormBook* (2006). doi:10.1895/wormbook.1.79.1.
31. Gerstberger, S., Hafner, M. & Tuschl, T. A census of human RNA-binding proteins. *Nat. Rev. Genet.* **15**, 829–845 (2014).
32. Wang, Z., Gerstein, M. & Snyder, M. RNA-seq: a revolutionary tool for transcriptomics. *Nat. Rev. Genet.* **10**, 57–63 (2009).
33. Mann, M. Functional and quantitative proteomics using SILAC. *Nat. Rev. Mol. Cell. Biol.* **7**, 952–958 (2006).

34. Corley, M., Burns, M. C. & Yeo, G. W. How RNA-Binding Proteins Interact with RNA: Molecules and Mechanisms. *Mol. Cell* **78**, 9–29 (2020).
35. Matera, A. G. & Wang, Z. A day in the life of the spliceosome. *Nat. Rev. Mol. Cell Biol.* **15**, 108–121 (2014).
36. Carlon, A. *et al.* Improved Accuracy from Joint X-ray and NMR Refinement of a Protein-RNA Complex Structure. *J. Am. Chem. Soc.* **138**, 1601–1610 (2016).
37. Wang, X. *et al.* Detecting protein and DNA/RNA structures in cryo-EM maps of intermediate resolution using deep learning. *Nat. Commun.* **12**, (2021).
38. Teplova, M. *et al.* Protein-RNA and protein-protein recognition by dual KH1/2 domains of the neuronal splicing factor Nova-1. *Structure* **19**, 930–944 (2011).
39. Lunde, B. M., Moore, C. & Varani, G. RNA-binding proteins: Modular design for efficient function. *Nat. Rev. Mol. Cell Biol.* **8**, 479–490 (2007).
40. Wu, P. Inhibition of RNA-binding proteins with small molecules. *Nat. Rev. Chem.* **4**, 441–458 (2020).
41. Gebauer, F., Schwarzl, T., Valcárcel, J. & Hentze, M. W. RNA-binding proteins in human genetic disease. *Nat. Rev. Genet.* **22**, 185–198 (2021).
42. Minuesa, G. *et al.* Small-molecule targeting of MUSASHI RNA-binding activity in acute myeloid leukemia. *Nat. Commun.* **10**, (2019).
43. Moerke, N. J. *et al.* Small-Molecule Inhibition of the Interaction between the Translation Initiation Factors eIF4E and eIF4G. *Cell* **128**, 257–267 (2007).
44. Bordeleau, M. E. *et al.* Functional characterization of IRESes by an inhibitor of the RNA helicase eIF4A. *Nat. Chem. Biol.* **2**, 213–220 (2006).
45. Fiorentino, F., Menna, M., Rotili, D., Valente, S. & Mai, A. METTL3 from Target Validation to the First Small-Molecule Inhibitors: A Medicinal Chemistry Journey. *J. Med. Chem.* **66**, 1654–1677 (2023).
46. Li, X., Xiong, X. & Yi, C. Epitranscriptome sequencing technologies: Decoding RNA modifications. *Nat. Methods.* **14**, 23–31 (2016).
47. Chen, K. *et al.* High-resolution N6-methyladenosine (m6A) map using photo-crosslinking-assisted m6A sequencing. *Angew. Chem., Int. Ed. Engl.* **54**, 1587–1590 (2015).
48. Linder, B. *et al.* Single-nucleotide-resolution mapping of m6A and m6Am throughout the transcriptome. *Nat. Methods.* **12**, 767–772 (2015).
49. Schwartz, S. *et al.* High-resolution mapping reveals a conserved, widespread, dynamic mRNA methylation program in yeast meiosis. *Cell* **155**, (2013).
50. Meyer, K. D. *et al.* Comprehensive analysis of mRNA methylation reveals enrichment in 3′ UTRs and near stop codons. *Cell* **149**, 1635–1646 (2012).
51. Dominissini, D. *et al.* Topology of the human and mouse m6A RNA methylomes revealed by m6A-seq. *Nature* **485**, 201–206 (2012).

52. Li, X. *et al.* Chemical pulldown reveals dynamic pseudouridylation of the mammalian transcriptome. *Nat. Chem. Biol.* **11**, 592–597 (2015).
53. Nishikura, K. A-to-I editing of coding and non-coding RNAs by ADARs. *Nat. Rev. Mol. Cell Biol.* **17**, 83–96 (2016).
54. Eisenberg, E. & Levanon, E. Y. A-to-I RNA editing - Immune protector and transcriptome diversifier. *Nat. Rev. Genet.* **19**, 473–490 (2018).
55. Agris, P. F. *et al.* Celebrating wobble decoding: Half a century and still much is new. *RNA Biol.* **15**, 537–553 (2018).
56. Kawahara, Y. *et al.* Frequency and fate of microRNA editing in human brain. *Nucleic Acids Res* **36**, 5270–5280 (2008).
57. Ambros, V. & Horvitz, H. R. Heterochronic Mutants of the Nematode Caenorhabditis elegans. *Science (1979)* **226**, 409–416 (1984).
58. Moss, E. G. & Lee, R. C. The Cold Shock Domain Protein LIN-28 Controls Developmental Timing in C. elegans and Is Regulated by the lin-4 RNA. *Cell* **88**, 637–646 (1997).
59. Moss, E. G. & Tang, L. Conservation of the heterochronic regulator Lin-28, its developmental expression and microRNA complementary sites. *Dev. Biol.* **258**, 432–442 (2003).
60. Yu, J. *et al.* Induced Pluripotent Stem Cell Lines Derived from Human Somatic Cells. *Science (1979)* **318**, 1917–1920 (2007).
61. Hanna, J. *et al.* Direct cell reprogramming is a stochastic process amenable to acceleration. *Nature* **462**, 595–601 (2009).
62. Hikasa, H., Sekido, Y. & Suzuki, A. Merlin/NF2-Lin28B-let-7 Is a Tumor-Suppressive Pathway that Is Cell-Density Dependent and Hippo Independent. *Cell Rep.* **14**, 2950–2961 (2016).
63. Nam, Y., Chen, C., Gregory, R. I., Chou, J. J. & Sliz, P. Molecular basis for interaction of let-7 MicroRNAs with Lin28. *Cell* **147**, 1080–1091 (2011).
64. Piskounova, E. *et al.* Lin28A and Lin28B inhibit let-7 MicroRNA biogenesis by distinct mechanisms. *Cell* **147**, 1066–1079 (2011).
65. Mayr, F., Schütz, A., Döge, N. & Heinemann, U. The Lin28 cold-shock domain remodels pre-let-7 microRNA. *Nucleic Acids Res.* **40**, 7492–7506 (2012).
66. Loughlin, F. E. *et al.* Structural basis of pre-let-7 miRNA recognition by the zinc knuckles of pluripotency factor Lin28. *Nat. Struct. Mol. Biol.* **19**, 84–91 (2012).
67. Darlix, J.-L., Lapadat-Tapolsky, M., de Rocquigny, H. & Roques, B. P. First Glimpses at Structure-function Relationships of the Nucleocapsid Protein of Retroviruses. *J. Mol. Biol.* **254**, 523–537 (1995).
68. Yamashita, S., Nagaike, T. & Tomita, K. Crystal structure of the Lin28-interacting module of human terminal uridylyltransferase that regulates let-7 expression. *Nat. Commun.* **10**, (2019).
69. Wilbert, M. L. *et al.* LIN28 binds messenger RNAs at GGAGA motifs and regulates splicing factor abundance. *Mol. Cell.* **48**, 195–206 (2012).

70. Bingsen, X. U., Zhang, K. & Huang, Y. Lin28 modulates cell growth and associates with a subset of cell cycle regulator mRNAs in mouse embryonic stem cells. *RNA* **15**, 357–361 (2009).
71. Parisi, S. *et al.* Identification of RNA-binding proteins that partner with Lin28a to regulate Dnmt3a expression. *Sci. Rep.* **11**, (2021).
72. Nam, Y., Chen, C., Gregory, R. I., Chou, J. J. & Sliz, P. Molecular basis for interaction of let-7 MicroRNAs with Lin28. *Cell* **147**, 1080–1091 (2011).
73. Kim, V. N., Han, J. & Siomi, M. C. Biogenesis of small RNAs in animals. *Nat. Rev. Mol. Cell Biol.* **10**, 126–139 (2009).
74. Krol, J., Loedige, I. & Filipowicz, W. The widespread regulation of microRNA biogenesis, function and decay. *Nat. Rev. Genet.* **11**, 597–610 (2010).
75. Victor Ambros. The functions of animal microRNAs. *Nature* **431**, 350–355 (2004).
76. Brenda J. Reinhart *et al.* The 21-nucleotide let-7 RNA regulates developmental timing in Caenorhabditis elegans. *Nature* **403**, 901–906 (2000).
77. Kumar, M. S., Lu, J., Mercer, K. L., Golub, T. R. & Jacks, T. Impaired microRNA processing enhances cellular transformation and tumorigenesis. *Nat. Genet.* **39**, 673–677 (2007).
78. Christine Mayr, Michael T. Hemann & David P. Bartel. Disrupting the Pairing Between let-7 and Hmga2 Enhances Oncogenic Transformation. *Science (1979)* **315**, 1574–1576 (2007).
79. Johnson, S. M. *et al.* RAS is regulated by the let-7 microRNA family. *Cell* **120**, 635–647 (2005).
80. Roush, S. & Slack, F. J. The let-7 family of microRNAs. *Trends Cell Biol.* **18**, 505–516 (2008).
81. Amy E. Pasquinelli *et al.* Conservation of the sequence and temporal expression of let-7 heterochronic regulatory RNA. *Nature* **408**, 86–89 (2000).
82. Lee, Y. *et al.* MicroRNA genes are transcribed by RNA polymerase II. *EMBO J.* **23**, 4051–4060 (2004).
83. Han, J. *et al.* Molecular Basis for the Recognition of Primary microRNAs by the Drosha-DGCR8 Complex. *Cell* **125**, 887–901 (2006).
84. Kim, V. N. MicroRNA precursors in motion: exportin-5 mediates their nuclear export. *Trends Cell Biol.* **14**, 156–159 (2004).
85. Liu, Z. *et al.* Cryo-EM Structure of Human Dicer and Its Complexes with a Pre-miRNA Substrate. *Cell* **173**, 1191-1203.e12 (2018).
86. Fareh, M. *et al.* TRBP ensures efficient Dicer processing of precursor microRNA in RNA-crowded environments. *Nat. Commun.* **7**, (2016).
87. Nguyen, T. D., Trinh, T. A., Bao, S. & Nguyen, T. A. Secondary structure RNA elements control the cleavage activity of DICER. *Nat. Commun.* **13**, (2022).
88. Gregory, R. I., Chendrimada, T. P., Cooch, N. & Shiekhattar, R. Human RISC couples microRNA biogenesis and posttranscriptional gene silencing. *Cell* **123**, 631–640 (2005).
89. Johnson, C. D. *et al.* The let-7 microRNA represses cell proliferation pathways in human cells. *Cancer Res.* **67**, 7713–7722 (2007).

90. Loughlin, F. E. *et al.* Structural basis of pre-let-7 miRNA recognition by the zinc knuckles of pluripotency factor Lin28. *Nat. Struct. Mol. Biol.* **19**, 84–91 (2012).
91. Mayr, F., Schütz, A., Döge, N. & Heinemann, U. The Lin28 cold-shock domain remodels pre-let-7 microRNA. *Nucleic Acids Res.* **40**, 7492–7506 (2012).
92. Ustianenko, D. *et al.* LIN28 Selectively Modulates a Subclass of Let-7 MicroRNAs. *Mol. Cell.* **71**, 271-283.e5 (2018).
93. Viswanathan, S. R., Daley, G. Q. & Gregory, R. I. Selective Blockade of MicroRNA Processing by Lin28. *Science (1979)* **320**, 97–100 (2008).
94. Wang, L. *et al.* LIN28 Zinc Knuckle Domain Is Required and Sufficient to Induce let-7 Oligouridylation. *Cell Rep.* **18**, 2664–2675 (2017).
95. Thornton, J. E., Chang, H. M., Piskounova, E. & Gregory, R. I. Lin28-mediated control of let-7 microRNA expression by alternative TUTases Zcchc11 (TUT4) and Zcchc6 (TUT7). *RNA* **18**, 1875–1885 (2012).
96. Heo, I. *et al.* TUT4 in Concert with Lin28 Suppresses MicroRNA Biogenesis through Pre-MicroRNA Uridylation. *Cell* **138**, 696–708 (2009).
97. Faehnle, C. R., Walleshauser, J. & Joshua-Tor, L. Mechanism of Dis3l2 substrate recognition in the Lin28-let-7 pathway. *Nature* **514**, 252–256 (2014).
98. Tan, F. E. *et al.* A Transcriptome-wide Translational Program Defined by LIN28B Expression Level. *Mol.Cell.* **73**, 304–313 (2019).
99. Yermalovich, A. V. *et al.* Lin28 and let-7 regulate the timing of cessation of murine nephrogenesis. *Nat. Commun.* **10**, (2019).
100. Robinton, D. A. *et al.* The Lin28/let-7 Pathway Regulates the Mammalian Caudal Body Axis Elongation Program. *Dev. Cell.* **48**, 396–405 (2019).
101. Chang, H. M., Triboulet, R., Thornton, J. E. & Gregory, R. I. A role for the Perlman syndrome exonuclease Dis3l2 in the Lin28-let-7 pathway. *Nature* **497**, 244–248 (2013).
102. Choi, S. A. *et al.* LIN28B is highly expressed in atypical teratoid/rhabdoid tumor (AT/RT) and suppressed through the restoration of SMARCB1. *Cancer Cell Int.* **16**, (2016).
103. Ma, X. *et al.* Lin28/let-7 axis regulates aerobic glycolysis and cancer progression via PDK1. *Nat. Commun.* **5**, (2014).
104. Viswanathan, S. R. & Daley, G. Q. Lin28: A MicroRNA Regulator with a Macro Role. *Cell* **140**, 445–449 (2010).
105. Hanahan, D. Hallmarks of Cancer: New Dimensions. *Cancer Discov.* **12**, 31–46 (2022).
106. Hanahan, D. & Weinberg, R. A. Hallmarks of cancer: The next generation. *Cell* **144**, 646–674 (2011).
107. Li, M., Chen, H. & Wu, T. LIN28: A cancer stem cell promoter for immunotherapy in head and neck squamous cell carcinoma. *Oral Oncol.* **98**, 92–95 (2019).

108. Walcher, L. *et al.* Cancer Stem Cells—Origins and Biomarkers: Perspectives for Targeted Personalized Therapies. *Front. Immunol.* **11**, (2020).
109. Yang, X. *et al.* Double-negative feedback loop between reprogramming factor LIN28 and microRNA let-7 regulates aldehyde dehydrogenase 1-positive cancer stem cells. *Cancer Res.* **70**, 9463–9472 (2010).
110. Chang, T.-C. *et al.* Lin-28B transactivation is necessary for Myc-mediated let-7 repression and proliferation. *PNAS* **106**, 3384–3389 (2009).
111. Dangi-Garimella, S. *et al.* Raf kinase inhibitory protein suppresses a metastasis signalling cascade involving LIN28 and let-7. *EMBO J.* **28**, 347–358 (2009).
112. Iliopoulos, D., Hirsch, H. A. & Struhl, K. An Epigenetic Switch Involving NF-κB, Lin28, Let-7 MicroRNA, and IL6 Links Inflammation to Cell Transformation. *Cell* **139**, 693–706 (2009).
113. Mani, S. A. *et al.* The Epithelial-Mesenchymal Transition Generates Cells with Properties of Stem Cells. *Cell* **133**, 704–715 (2008).
114. Valsesia-Wittmann, S. *et al.* Oncogenic cooperation between H-Twist and N-Myc overrides failsafe programs in cancer cells. *Cancer Cell* **6**, 625–630 (2004).
115. Trang, P. *et al.* Regression of murine lung tumors by the let-7 microRNA. *Oncogene* **29**, 1580–1587 (2010).
116. West, R. C. *et al.* HMGA2 is regulated by LIN28 and BRCA1 in human placental cells. *Biol. Reprod.* **100**, 227–238 (2019).
117. Segal, M. *et al.* Hydrophobically Modified let-7b miRNA Enhances Biodistribution to NSCLC and Downregulates HMGA2 In Vivo. *Mol. Ther. Nucleic Acids* **19**, 267–277 (2020).
118. Thakur, S., Sinhari, A., Jain, P. & Jadhav, H. R. A perspective on oligonucleotide therapy: Approaches to patient customization. *Front. pharmacol.* **13**, (2022).
119. Ghidini, A., Cléry, A., Halloy, F., Allain, F. H. T. & Hall, J. RNA-PROTACs: Degraders of RNA-Binding Proteins. *Angew. Chem. Int. Ed.* **60**, 3163–3169 (2021).
120. Békés, M., Langley, D. R. & Crews, C. M. PROTAC targeted protein degraders: the past is prologue. *Nat. Rev. Drug Discov.* **21**, 181–200 (2022).
121. Roos, M. *et al.* A Small-Molecule Inhibitor of Lin28. *ACS Chem. Biol.* **11**, 2773–2781 (2016).
122. Chen, Y. *et al.* LIN28/let-7/PD-L1 pathway as a target for cancer immunotherapy. *Cancer Immunol. Res.* **7**, 487–497 (2019).
123. Lekka, E. *et al.* Pharmacological inhibition of Lin28 promotes ketogenesis and restores lipid homeostasis in models of non-alcoholic fatty liver disease. *Nat. Commun.* **13**, (2022).
124. Xie, C. *et al.* Therapeutic potential of C1632 by inhibition of SARS-CoV-2 replication and viral-induced inflammation through upregulating let-7. *Signal Transduct. Target. Ther.* **6**, (2021).
125. Lim, D., Byun, W. G., Koo, J. Y., Park, H. & Park, S. B. Discovery of a Small-Molecule Inhibitor of Protein-MicroRNA Interaction Using Binding Assay with a Site-Specifically Labeled Lin28. *J. Am. Chem. Soc.* **138**, 13630–13638 (2016).

126. Lim, D., Byun, W. G. & Park, S. B. Restoring Let-7 microRNA Biogenesis Using a Small-Molecule Inhibitor of the Protein-RNA Interaction. *ACS Med. Chem. Lett.* **9**, 1181–1185 (2018).
127. Lightfoot, H. L., Miska, E. A. & Balasubramanian, S. Identification of small molecule inhibitors of the Lin28-mediated blockage of pre-let-7g processing. *Org. Biomol. Chem.* **14**, 10208–10216 (2016).
128. Wang, L. *et al.* Small-Molecule Inhibitors Disrupt let-7 Oligouridylation and Release the Selective Blockade of let-7 Processing by LIN28. *Cell Rep.* **23**, 3091–3101 (2018).
129. Lorenz, D. A. & Garner, A. L. A click chemistry-based microRNA maturation assay optimized for high-throughput screening. *Chem. Commun.* **52**, 8267–8270 (2016).
130. Lorenz, D. A. *et al.* Expansion of cat-ELCCA for the Discovery of Small Molecule Inhibitors of the Pre-let-7-Lin28 RNA-Protein Interaction. *ACS Med. Chem. Lett.* **9**, 517–521 (2018).
131. Garner, A. L. Cat-ELCCA: Catalyzing drug discovery through click chemistry. *Chem. Commun.* **54**, 6531–6539 (2018).
132. Rosenblum, S. L. *et al.* Live cell screening to identify RNA-binding small molecule inhibitors of the pre-let-7-Lin28 RNA-protein interaction. *RSC Med. Chem.* **15**, 1539–1546 (2024).
133. Boriack-Sjodin, P. A., Ribich, S. & Copeland, R. A. RNA-modifying proteins as anticancer drug targets. *Nat. Rev. Drug Discov.* **17**, 435–453 (2018).
134. Matsumura, Y., Wei, F. Y. & Sakai, J. Epitranscriptomics in metabolic disease. *Nat. Metab.* **5**, 370–384 (2023).
135. Deng, X. *et al.* RNA N6-methyladenosine modification in cancers: Current status and perspectives. *Cell Res.* **28**, 507–517 (2018).
136. Kan, R. L., Chen, J. & Sallam, T. Crosstalk between epitranscriptomic and epigenetic mechanisms in gene regulation. *Trends Genet.* **38**, 182–193 (2022).
137. Wang, X. *et al.* Structural basis of N6-adenosine methylation by the METTL3-METTL14 complex. *Nature* **534**, 575–578 (2016).
138. Wang, P., Doxtader, K. A. & Nam, Y. Structural Basis for Cooperative Function of Mettl3 and Mettl14 Methyltransferases. *Mol. Cell* **63**, 306–317 (2016).
139. Liu, J. *et al.* A METTL3-METTL14 complex mediates mammalian nuclear RNA N6-adenosine methylation. *Nat. Chem. Biol.* **10**, 93–95 (2014).
140. Garcias Morales, D. & Reyes, J. L. A birds'-eye view of the activity and specificity of the mRNA m6A methyltransferase complex. *Wiley Interdiscip. Rev. RNA* **12**, (2021).
141. Huang, W. *et al.* N6-methyladenosine methyltransferases: functions, regulation, and clinical potential. *J. Hematol. Oncol.* **14**, (2021).
142. Sepich-Poore, C. *et al.* The METTL5-TRMT112 N6-methyladenosine methyltransferase complex regulates mRNA translation via 18S rRNA methylation. *J. Biol. Chem.* **298**, (2022).
143. Ren, W. *et al.* Structure and regulation of ZCCHC4 in m6A-methylation of 28S rRNA. *Nat. Commun.* **10**, (2019).

144. Su, R. *et al.* METTL16 exerts an m6A-independent function to facilitate translation and tumorigenesis. *Nat. Cell Biol.* **24**, 205–216 (2022).
145. Pendleton, K. E. *et al.* The U6 snRNA m6A Methyltransferase METTL16 Regulates SAM Synthetase Intron Retention. *Cell* **169**, 824–835 (2017).
146. Aoyama, T., Yamashita, S. & Tomita, K. Mechanistic insights into m6A modification of U6 snRNA by human METTL16. *Nucleic Acids Res.* **48**, 5157–5168 (2020).
147. Mauer, J. *et al.* Reversible methylation of m6 Am in the 5′ cap controls mRNA stability. *Nature* **541**, 371–375 (2017).
148. Wei, J. *et al.* Differential m6A, m6Am, and m1A Demethylation Mediated by FTO in the Cell Nucleus and Cytoplasm. *Mol. Cell* **71**, 973-985.e5 (2018).
149. Fu, Y. *et al.* FTO-mediated formation of N6-hydroxymethyladenosine and N6-formyladenosine in mammalian RNA. *Nat. Commun.* **4**, (2013).
150. Jia, G. *et al.* N6-Methyladenosine in nuclear RNA is a major substrate of the obesity-associated FTO. *Nat. Chem. Biol.* **7**, 885–887 (2011).
151. Wei, J. *et al.* Differential m6A, m6Am, and m1A Demethylation Mediated by FTO in the Cell Nucleus and Cytoplasm. *Mol. Cell* **71**, 973-985.e5 (2018).
152. Kaur, S., Tam, N. Y., McDonough, M. A., Schofield, C. J. & Aik, W. S. Mechanisms of substrate recognition and N6-methyladenosine demethylation revealed by crystal structures of ALKBH5-RNA complexes. *Nucleic Acids Res.* **50**, 4148–4160 (2022).
153. Yue, B. *et al.* Essential role of ALKBH5-mediated RNA demethylation modification in bile acid-induced gastric intestinal metaplasia. *Mol. Ther. Nucleic Acids* **26**, 458–472 (2021).
154. Qu, J. *et al.* RNA demethylase ALKBH5 in cancer: from mechanisms to therapeutic potential. *J. Hem. Oncol.* **15**, (2022).
155. Lior Lasman *et al.* Context-dependent functional compensation between Ythdf m6A reader proteins. *Genes & Dev.* **34**, 1373–1391 (2020).
156. Shi, R. *et al.* Linking the YTH domain to cancer: the importance of YTH family proteins in epigenetics. *Cell Death Differ.* **12**, (2021).
157. Li, A. *et al.* Cytoplasmic m 6 A reader YTHDF3 promotes mRNA translation. *Cell Res.* **27**, 444–447 (2017).
158. Wang, X. *et al.* N6-methyladenosine modulates messenger RNA translation efficiency. *Cell* **161**, 1388–1399 (2015).
159. Ries, R. J. *et al.* m6A enhances the phase separation potential of mRNA. *Nature* **571**, 424–428 (2019).
160. Zaccara, S. & Jaffrey, S. R. A Unified Model for the Function of YTHDF Proteins in Regulating m6A-Modified mRNA. *Cell* **181**, 1582-1595.e18 (2020).
161. Liu, J. *et al.* N6-methyladenosine of chromosome-associated regulatory RNA regulates chromatin state and transcription. *Science* **367**, 580–586 (2020).

162. Widagdo, J., Anggono, V. & Wong, J. J. L. The multifaceted effects of YTHDC1-mediated nuclear m6A recognition. *Trends Genet.* **38**, 325–332 (2022).
163. Xiao, W. *et al.* Nuclear m6A Reader YTHDC1 Regulates mRNA Splicing. *Mol. Cell* **61**, 507–519 (2016).
164. Zhou, B. *et al.* N6-Methyladenosine Reader Protein YT521-B Homology Domain-Containing 2 Suppresses Liver Steatosis by Regulation of mRNA Stability of Lipogenic Genes. *Hepatol.* **73**, 91–103 (2021).
165. Mao, Y. *et al.* m6A in mRNA coding regions promotes translation via the RNA helicase-containing YTHDC2. *Nat. Commun.* **10**, (2019).
166. Huang, H. *et al.* Recognition of RNA N 6 -methyladenosine by IGF2BP proteins enhances mRNA stability and translation. *Nat. Cell Biol.* **20**, 285–295 (2018).
167. Meyer, K. D. *et al.* 5′ UTR m6A Promotes Cap-Independent Translation. *Cell* **163**, 999–1010 (2015).
168. Choe, J. *et al.* mRNA circularization by METTL3–eIF3h enhances translation and promotes oncogenesis. *Nature* **561**, 556–560 (2018).
169. Liu, N. *et al.* N6 -methyladenosine-dependent RNA structural switches regulate RNA-protein interactions. *Nature* **518**, 560–564 (2015).
170. Alarcón, C. R. *et al.* HNRNPA2B1 Is a Mediator of m6A-Dependent Nuclear RNA Processing Events. *Cell* **162**, 1299–1308 (2015).
171. Jiang, L. *et al.* Interaction of tau with HNRNPA2B1 and N6-methyladenosine RNA mediates the progression of tauopathy. *Mol. Cell* **81**, 4209-4227.e12 (2021).
172. He, P. C. & He, C. m6A RNA methylation: from mechanisms to therapeutic potential. *EMBO J.* **40**, (2021).
173. Wang, X. *et al.* Crosstalk between N6-methyladenosine modification and circular RNAs: current understanding and future directions. *Mol. Cancer* **20**, (2021).
174. Hong, J., Xu, K. & Lee, J. H. Biological roles of the RNA m6A modification and its implications in cancer. *Exp. Mol. Med.* **54**, 1822–1832 (2022).
175. Deng, X., Qing, Y., Horne, D., Huang, H. & Chen, J. The roles and implications of RNA m6A modification in cancer. *Nat. Rev. Clin. Oncol.* **20**, 507–526 (2023).
176. An, Y. & Duan, H. The role of m6A RNA methylation in cancer metabolism. *Mol. Cancer* **21**, (2022).
177. Pan, J., Huang, T., Deng, Z. & Zou, C. Roles and therapeutic implications of m6A modification in cancer immunotherapy. *Front. immunol.* **14**, (2023).
178. Doxtader, K. A. *et al.* Structural Basis for Regulation of METTL16, an S-Adenosylmethionine Homeostasis Factor. *Mol. Cell* **71**, 1001–1011 (2018).
179. Ruszkowska, A., Ruszkowski, M., Dauter, Z. & Brown, J. A. Structural insights into the RNA methyltransferase domain of METTL16. *Sci. Rep.* **8**, (2018).

180. Pendleton, K. E. *et al.* The U6 snRNA m6A Methyltransferase METTL16 Regulates SAM Synthetase Intron Retention. *Cell* **169**, 824–835 (2017).
181. Warda, A. S. *et al.* Human METTL16 is a N6 -methyladenosine (m6A) methyltransferase that targets pre-mRNAs and various non-coding RNAs. *EMBO Rep.* **18**, 2004–2014 (2017).
182. Li, C. *et al.* Overview of Methionine Adenosyltransferase 2A (MAT2A) as an Anticancer Target: Structure, Function, and Inhibitors. *J. Med. Chem.* **65**, 9531–9547 (2022).
183. Shima, H. *et al.* S-Adenosylmethionine Synthesis Is Regulated by Selective N6-Adenosine Methylation and mRNA Degradation Involving METTL16 and YTHDC1. *Cell Rep.* **21**, 3354–3363 (2017).
184. Bresson, S. M., Hunter, O. V., Hunter, A. C. & Conrad, N. K. Canonical Poly(A) Polymerase Activity Promotes the Decay of a Wide Variety of Mammalian Nuclear RNAs. *PLoS Genet.* **11**, (2015).
185. Pendleton, K. E., Park, S.-K., Hunter, O. V, Bresson, S. M. & Conrad, N. K. Balance between MAT2A intron detention and splicing is determined cotranscriptionally. *RNA* **24**, 778–786 (2018).
186. Su, R. *et al.* METTL16 exerts an m6A-independent function to facilitate translation and tumorigenesis. *Nat. Cell Biol.* **24**, 205–216 (2022).
187. Des Georges, A. *et al.* Structure of mammalian eIF3 in the context of the 43S preinitiation complex. *Nature* **525**, 491–495 (2015).
188. Sonenberg, N. & Hinnebusch, A. G. Regulation of Translation Initiation in Eukaryotes: Mechanisms and Biological Targets. *Cell* **136**, 731–745 (2009).
189. Barbieri, I. *et al.* Promoter-bound METTL3 maintains myeloid leukaemia by m6A-dependent translation control. *Nature* **552**, 126–131 (2017).
190. Gu, Y. *et al.* The evolving landscape of N6-methyladenosine modification in the tumor microenvironment. *Mol. Ther.* **29**, 1703–1715 (2021).
191. Chen, S. *et al.* N6-methyladenosine modification of HIV-1 RNA suppresses type-I interferon induction in differentiated monocytic cells and primary macrophages. *PLoS Pathog.* **17**, (2021).
192. Li, X., Ma, S., Deng, Y., Yi, P. & Yu, J. Targeting the RNA m6A modification for cancer immunotherapy. *Mol. Cancer* **21**, (2022).
193. Lu, T. X. *et al.* A New Model of Spontaneous Colitis in Mice Induced by Deletion of an RNA m6A Methyltransferase Component METTL14 in T Cells. *Cell Mol. Gastroenterol. Hepatol.* **10**, 747–761 (2020).
194. Dai, B. *et al.* Significance of RNA N6-Methyladenosine Regulators in the Diagnosis and Subtype Classification of Childhood Asthma Using the Gene Expression Omnibus Database. *Front. Genet.* **12**, (2021).
195. Vu, L. P. *et al.* The N6 -methyladenosine (m6A)-forming enzyme METTL3 controls myeloid differentiation of normal hematopoietic and leukemia cells. *Nat. Med.* **23**, 1369–1376 (2017).

196. Lin, S., Choe, J., Du, P., Triboulet, R. & Gregory, R. I. The m6A Methyltransferase METTL3 Promotes Translation in Human Cancer Cells. *Mol. Cell* **62**, 335–345 (2016).

197. Chen, M. *et al.* RNA N6-methyladenosine methyltransferase-like 3 promotes liver cancer progression through YTHDF2-dependent posttranscriptional silencing of SOCS2. *Hepatol.* **67**, 2254–2270 (2018).

198. Liu, J. *et al.* m6A mRNA methylation regulates AKT activity to promote the proliferation and tumorigenicity of endometrial cancer. *Nat. Cell Biol.* **20**, 1074–1083 (2018).

199. Dolbois, A. *et al.* 1,4,9-Triazaspiro[5.5]undecan-2-one Derivatives as Potent and Selective METTL3 Inhibitors. *J. Med. Chem.* **64**, 12738–12760 (2021).

200. Yankova, E. *et al.* Small-molecule inhibition of METTL3 as a strategy against myeloid leukaemia. *Nature* **593**, 597–601 (2021).

201. Ofir-Rosenfeld, Y. *et al.* STC-15, an oral small molecule inhibitor of the RNA methyltransferase METTL3, inhibits tumour growth through activation of anti-cancer immune responses associated with increased interferon signalling, and synergises with T cell checkpoint blockade. *Eur. J. Cancer* **174**, S123 (2022).

202. Brown, J. A., Kinzig, C. G., Degregorio, S. J. & Steitz, J. A. Methyltransferase-like protein 16 binds the 3'-terminal triple helix of MALAT1 long noncoding RNA. *PNAS* **113**, 14013–14018 (2016).

203. Li, L. *et al.* Role of human noncoding RNAs in the control of tumorigenesis. *PNAS* **106**, 12956–12961 (2009).

204. Carlile, G. W. *et al.* A novel triple combination of pharmacological chaperones improves F508del-CFTR correction. *Sci. Rep.* **8**, (2018).

205. Kantarjian, H. M. *et al.* Nilotinib (formerly AMN107), a highly selective BCR-ABL tyrosine kinase inhibitor, is effective in patients with Philadelphia chromosome–positive chronic myelogenous leukemia in chronic phase following imatinib resistance and intolerance. *Blood* **110**, 3540–3546 (2007).

206. Mitra, A., Manna, S., Kundu, R., Hazra, D. & Roychowdhury, A. Brute Force Virtual Drug Screening with Molecular Dynamics Simulation and MM/PBSA to Find Potent Inhibitors of METTL16. *IEEE/ACM Trans. Comput. Biol. Bioinform.* **20**, 2356–2361 (2022).

207. Selberg, S. *et al.* Novel RNA m6A methyltransferase METTL16 inhibitors. *bioRxiv* doi:10.1101/2023.03.27.534333.

208. Barbieri, I. & Kouzarides, T. Role of RNA modifications in cancer. *Nat. Rev. Cancer* **20**, 303–322 (2020).

209. Liao, S., Sun, H. & Xu, C. YTH Domain: A Family of N6-methyladenosine (m6A) Readers. *Genom. Proteom. Bionf.* **16**, 99–107 (2018).

210. Cui, L. *et al.* RNA modifications: importance in immune cell biology and related diseases. *Signal Transduct. Target. Ther.* **7**, (2022).

211. Du, H. *et al.* YTHDF2 destabilizes m6A-containing RNA through direct recruitment of the CCR4-NOT deadenylase complex. *Nat. Commun.* **7**, (2016).
212. Li, F., Zhao, D., Wu, J. & Shi, Y. Structure of the YTH domain of human YTHDF2 in complex with an m6A mononucleotide reveals an aromatic cage for m6A recognition. *Cell Res.* **24**, 1490–1492 (2014).
213. Zhu, T. *et al.* Crystal structure of the YTH domain of YTHDF2 reveals mechanism for recognition of N6-methyladenosine. *Cell Res.* **24**, 1493–1496 (2014).
214. Wang, X. *et al.* N6-methyladenosine-dependent regulation of messenger RNA stability. *Nature* **505**, 117–120 (2014).
215. Park, O. H. *et al.* Endoribonucleolytic Cleavage of m6A-Containing RNAs by RNase P/MRP Complex. *Mol. Cell* **74**, 494-507.e8 (2019).
216. Boo, S. H. *et al.* UPF1 promotes rapid degradation of m6A-containing RNAs. *Cell Rep.* **39**, (2022).
217. Chen, X., Zhou, X. & Wang, X. m6A binding protein YTHDF2 in cancer. *Exp. hematol. oncol.* **11**, (2022).
218. Wang, J. yan & Lu, A. qing. The biological function of m6A reader YTHDF2 and its role in human disease. *Cancer Cell Int.* **21**, (2021).
219. Paris, J. *et al.* Targeting the RNA m6A Reader YTHDF2 Selectively Compromises Cancer Stem Cells in Acute Myeloid Leukemia. *Cell Stem Cell* **25**, 137–148 (2019).
220. Yan, J. *et al.* LncRNA LINC00470 promotes the degradation of PTEN mRNA to facilitate malignant behavior in gastric cancer cells. *Biochem. Biophys. Res. Commun.* **521**, 887–893 (2020).
221. Tsuchiya, K. *et al.* YTHDF1 and YTHDF2 are associated with better patient survival and an inflamed tumor-immune microenvironment in non–small-cell lung cancer. *Oncoimmunology* **10**, (2021).
222. Li, Y. *et al.* RNA m6A reader YTHDF2 facilitates lung adenocarcinoma cell proliferation and metastasis by targeting the AXIN1/Wnt/β-catenin signaling. *Cell Death Dis.* **12**, (2021).
223. Zhao, C. *et al.* Loss of PDZK1 expression activates PI3K/AKT signaling via PTEN phosphorylation in gastric cancer. *Cancer Lett.* **453**, 107–121 (2019).
224. Chen, Z. *et al.* YTHDF2 is a potential target of AML1/ETO-HIF1α loop-mediated cell proliferation in t(8;21) AML. *Oncogene* **40**, 3786–3798 (2021).
225. Liu, R. *et al.* Tyrosine phosphorylation activates 6-phosphogluconate dehydrogenase and promotes tumor growth and radiation resistance. *Nat. Commun.* **10**, (2019).
226. Hou, J. *et al.* YTHDF2 reduction fuels inflammation and vascular abnormalization in hepatocellular carcinoma. *Mol. Cancer* **18**, (2019).
227. Li, W. *et al.* Hypoxia-induced vasculogenic mimicry formation in human colorectal cancer cells: Involvement of HIF-1a, Claudin-4, and E-cadherin and Vimentin. *Sci. Rep.* **6**, 37534 (2016).

228. Zhong, L. *et al.* YTHDF2 suppresses cell proliferation and growth via destabilizing the EGFR mRNA in hepatocellular carcinoma. *Cancer Lett.* **442**, 252–261 (2019).
229. Einstein, J. M. *et al.* Inhibition of YTHDF2 triggers proteotoxic cell death in MYC-driven breast cancer. *Mol. Cell* **81**, 3048–3064 (2021).
230. Nai, F. *et al.* Fragment Ligands of the m6A-RNA Reader YTHDF2. *ACS Med. Chem. Lett.* **13**, 1500–1509 (2022).
231. Wang, L. *et al.* YTHDF2 inhibition potentiates radiotherapy antitumor efficacy. *Cancer Cell* **41**, 1294–1308 (2023).
232. Micaelli, M. *et al.* Small-Molecule Ebselen Binds to YTHDF Proteins Interfering with the Recognition of N6-Methyladenosine-Modified RNAs. *ACS Pharmacol. Transl. Sci.* **5**, 872–891 (2022).
233. Jonathan Baell & Michael A. Walters. Chemical con artists foil drug discovery. *Nature* **513**, 481–483 (2014).
234. Goebel, G. Synthesis of Small-Molecule Modulators Targeting the Protein-RNA Interaction of Lin28 and Let-7. (2021).
235. Goebel, G. L. *et al.* Small molecules with tetrahydroquinoline-containing Povarov scaffolds as inhibitors disrupting the Protein–RNA interaction of LIN28–let-7. *Eur. J. Med. Chem.* **228**, (2022).
236. Hommen, P. *et al.* Chromenopyrazole−Peptide Conjugates as Small-Molecule Based Inhibitors Disrupting the Protein−RNA Interaction of LIN28-let-7. *ChemBioChem* **24**, (2023).
237. Borgelt, L. *et al.* Spirocyclic Chromenopyrazole Inhibitors Disrupting the Interaction between the RNA-Binding Protein LIN28 and Let-7. *ChemBioChem* **24**, (2023).
238. Borgelt, L. Discovery of Small-molecule Modulators of the RNA-binding Proteins LIN28 and RNase L. (2023).
239. Hommen, P. Design, synthesis, and evaluation of small molecules and associated bifunctional conjugates targeting the Protein–RNA interaction of LIN28 and let-7. (2022).
240. Povarov, L. S. Reactions of Acetals with Unsaturated Ethers. *Russ. Chem. Rev.* **34**, 639–656 (1965).
241. Galloway, W. R. J. D., Isidro-Llobet, A. & Spring, D. R. Diversity-oriented synthesis as a tool for the discovery of novel biologically active small molecules. *Nat. Commun.* **1**, (2010).
242. Lassalas, P. *et al.* Structure Property Relationships of Carboxylic Acid Isosteres. *J. Med. Chem.* **59**, 3183–3203 (2016).
243. Hohnen, L. Assay development and biological evaluation of small-molecule inhibitors targeting the protein-RNA interaction of LIN28 and let-7. (2021).
244. Johnson, B. M., Shu, Y. Z., Zhuo, X. & Meanwell, N. A. Metabolic and Pharmaceutical Aspects of Fluorinated Compounds. *J. Med. Chem.* **63**, 6315–6386 (2020).
245. Pan, Y. The dark side of fluorine. *ACS Med. Chem. Lett.* **10**, 1016–1019 (2019).

246. Zhang, X., Gong, Z., Li, J. & Lu, T. Intermolecular Sulfur···Oxygen Interactions: Theoretical and Statistical Investigations. *J. Chem. Inf. Model.* **55**, 2138–2153 (2015).

247. Nieuwland, C. & Fonseca Guerra, C. How the Chalcogen Atom Size Dictates the Hydrogen-Bond Donor Capability of Carboxamides, Thioamides, and Selenoamides. *Chem. Eur. J.* **28**, (2022).

248. Lea, W. A. & Simeonov, A. Fluorescence polarization assays in small molecule screening. *Expert. Opin. Drug Discov.* **6**, 17–32 (2011).

249. Hollingsworth, S. A. & Dror, R. O. Molecular Dynamics Simulation for All. *Neuron* **99**, 1129–1143 (2018).

250. Borgelt, L. *et al.* Trisubstituted Pyrrolinones as Small-Molecule Inhibitors Disrupting the Protein-RNA Interaction of LIN28 and Let-7. *ACS Med. Chem. Lett.* **12**, 893–898 (2021).

251. Borgelt, L. *et al.* N-Biphenyl Pyrrolinones and Dibenzofurans as RNA-Binding Protein LIN28 Inhibitors Disrupting the LIN28-Let-7 Interaction. *ACS Med. Chem. Lett.* **14**, 1707–1715 (2023).

252. Döbner, O. Ueber α-Alkylcinchoninsäuren und α-Alkylchinoline. *Justus Liebigs Ann. Chem.* **242**, 265–289 (1887).

253. Knoevenagel, E. Condensation von Malonsäure mit aromatischen Aldehyden durch Ammoniak und Amine. *Dtsch. Chem. Ges.* **31**, 2596–2619 (1898).

254. Wassermann, A. M., Camargo, L. M. & Auld, D. S. Composition and applications of focus libraries to phenotypic assays. *Frontiers Pharmacol.* **5**, (2014).

255. Ballatore, C., Huryn, D. M. & Smith, A. B. Carboxylic Acid (Bio)Isosteres in Drug Design. *ChemMedChem* **8**, 385–395 (2013).

256. Bashore, F. M. *et al.* Fused Tetrahydroquinolines Are Interfering with Your Assay. *J. Med. Chem.* **66**, 14434–14446 (2023).

257. Liu, Y. *et al.* Aminothiazolone Inhibitors Disrupt the Protein-RNA Interaction of METTL16 and Modulate the m6A RNA Modification. *JACS Au* **4**, 1436–1449 (2023).

258. Rautio, J., Meanwell, N. A., Di, L. & Hageman, M. J. The expanding role of prodrugs in contemporary drug design and development. *Nat. Rev. Drug Discov.* **17**, 559–587 (2018).

259. Wu, T. *et al.* Protocol for performing and optimizing differential scanning fluorimetry experiments. *STAR Protoc.* **4**, 102688 (2023).

260. Ballatore, C., Huryn, D. M. & Smith, A. B. Carboxylic Acid (Bio)Isosteres in Drug Design. *ChemMedChem* **8**, 385–395 (2013).

261. Strelow, J. M. A Perspective on the Kinetics of Covalent and Irreversible Inhibition. *SLAS Discov.* **22**, 3–20 (2017).

262. Goebel, G. L. *et al.* Profiling Cellular Morphological Changes Induced by Dual-targeting PROTACs of Aurora Kinase and RNA-binding Protein YTHDF2. *ChemBioChem* e202400183 (2024) doi:10.1002/cbic.202400183.

263. Donovan, K. A. *et al.* Mapping the Degradable Kinome Provides a Resource for Expedited Degrader Development. *Cell* **183**, 1714–1731 (2020).
264. Angers, S. *et al.* Molecular architecture and assembly of the DDB1–CUL4A ubiquitin ligase machinery. *Nature* **443**, 590–593 (2006).
265. Mullard, A. First targeted protein degrader hits the clinic. *Nat. Rev. Drug Discov.* **18**, 237–239 (2019).
266. Huang, H.-T. *et al.* A Chemoproteomic Approach to Query the Degradable Kinome Using a Multi-kinase Degrader. *Cell Chem. Biol.* **25**, 88–99 (2018).
267. Wurz, R. P. *et al.* Affinity and cooperativity modulate ternary complex formation to drive targeted protein degradation. *Nat. Commun.* **14**, (2023).
268. Toure, M. & Crews, C. M. Small-Molecule PROTACS: New Approaches to Protein Degradation. *Angew. Chem. Int. Ed.* **55**, 1966–1973 (2016).
269. Arkin, M. R. & Wells, J. A. Small-molecule inhibitors of protein–protein interactions: progressing towards the dream. *Nat. Rev. Drug Discov.* **3**, 301–317 (2004).
270. Hajduk, P. J. & Greer, J. A decade of fragment-based drug design: strategic advances and lessons learned. *Nat. Rev. Drug Discov.* **6**, 211–219 (2007).
271. Hughes, J., Rees, S., Kalindjian, S. & Philpott, K. Principles of early drug discovery. *Br. J. Pharmacol.* **162**, 1239–1249 (2011).
272. Li, J., Wu, L., Pei, M. & Zhang, Y. YTHDF2, a protein repressed by miR-145, regulates proliferation, apoptosis, and migration in ovarian cancer cells. *J. Ovarian Res.* **13**, 111 (2020).
273. Kobayashi, S. & Nagayama, S. A New Methodology for Combinatorial Synthesis. Preparation of Diverse Quinoline Derivatives Using a Novel Polymer-Supported Scandium Catalyst. *J. Am. Chem. Soc.* **118**, 8977–8978 (1996).
274. Zhang, J. *et al.* Potent Nonpeptide Endothelin Antagonists: Synthesis and Structure±Activity Relationships of Pyrazole-5-carboxylic Acids. *Bioorg. Med. Chem. Lett.* **10**, 2575–2578 (2000).
275. Alizadeh, N. *et al.* Evaluating the effects of disubstituted 3-hydroxy-1H-pyrrol-2(5H)-one analog as novel tyrosinase inhibitors. *Bioorg. Chem.* **126**, 105876 (2022).
276. Robertson, M. J. *et al.* 5-Aryl-2-(naphtha-1-yl)sulfonamido-thiazol-4(5: H)-ones as clathrin inhibitors. *Org. Biomol. Chem.* **14**, 11266–11278 (2016).
277. Liang, J. Y., Wang, H., Yang, Y. L., Shen, S. J. & Chen, J. X. Addition of carbamoylsilane to isatins: Highly efficient synthesis of 3-hydroxy-3-aminocarbonyl-2-oxindoles derivatives. *Tetrahedron Lett.* **58**, 2636–2639 (2017).
278. Mao, J. *et al.* Structure-Based Drug Design and Synthesis of Novel N-Aryl-2,4-bithiazole-2-amine CYP1B1-Selective Inhibitors in Overcoming Taxol Resistance in A549 Cells. *J. Med. Chem.* **65**, 16451–16480 (2022).
279. He, B., Phansavath, P. & Ratovelomanana-Vidal, V. Rh-Mediated Asymmetric-Transfer Hydrogenation of 3-Substituted Chromones: A Route to Enantioenriched cis-3-

(Hydroxymethyl)chroman-4-ol Derivatives through Dynamic Kinetic Resolution. *Org. Lett.* **21**, 3276–3280 (2019).

7 Abbreviations

A-to-I editing	Adenosine-to-inosine editing
Ac	Acetyl
Ac^4C	*N*4-acetylcytidine
ACN	Acetonitrile
ADAR	Adenosine deaminases acting on RNA
ADP	Adenosine diphosphate
AGO	Argonaut
ALKBH5	AlkB homolog 5
AlphaScreen	Amplified luminescent proximity homogenous assay screen
AML	Acute myelogenous leukemia
Boc	*tert*-butoxycarbonyl
b.p.	boiling point
BHQ	Black-hole-quencher
CAF	Chromatin assembly factor 1
carRNA	chromosome-associated regulatory RNAs
Cat-ELCCA	Catalytic enzyme-linked click chemistry assay
CCR4A	Carbon catabolite repressor protein 4A homolog
CBC	Cap-binding complex
CDK	Cyclin dependent kinase
CETSA	Cellular thermal shift assay
Clip-Seq	Crosslinking and immunoprecipitation-sequencing
CM	*C*-terminal catalytic module
c-Myc	Cellular Myelocytomatosis

CNOT1	CCR4-NOT transcription complex subunit 1
COSY	Correlated spectroscopy
CSC	Cancer stem cell
CSD	Cold shock domain
CRBN	Cereblon
CREB	cAMP-response element binding
Cryo-EM	Cryogenic electron microscopy
CuAAC	Copper(I)-catalyzed azide-alkyne cycloaddition
CUL4A	Cullin-4A
Cy3/5	Tetramethylindo(di)-carbocyanine 3/5
DCM	Dichloromethane
DDB1	Damaged DNA binding protein 1
DGCR8	DiGeorge syndrome critical region 8
DIPEA	*N*,*N*-Diisopropylethylamine
DNA	Deoxyribonucleic acid
DMAP	4-(dimethylamino)pyridine
DMF	Dimethylformamide
DMSO	Dimethyl sulfoxide
DOS	Diversity oriented synthesis
d.r.	diastereomeric ratio
Ds	Double-stranded
DSF	Differential scanning fluorimetry
EDC	1-ethyl-3-(3-dimethylaminopropyl)carbodiimid
eIF	Eukaryotic initiation factor

EDTA	Ethylenediaminetetraacetic acid
EGFP	Enhanced green fluorescent protein
EMSA	Electrophoretic mobility shift assay
EMT	Epithelial-to-mesenchymal transition
ELISA	Enzyme-linked immunosorbent assay
ESC	Embryonic stem cells
Et	Ethyl
EtOAc / EA	Ethyl acetate
EtOH	Ethanol
EXP5	Exportin 5
FAM	carboxyfluorescein
FI	Fluorescence intensity
FP	Fluorescence polarization
FRET	Fluorescence resonance energy transfer
FTO	Fat mass and obesity-associated protein
GTP	Guanosine triphosphate
h	hours
HAKAI	Cbl proto-oncogene-like 1
HATU	hexafluorophosphate azabenzotriazole tetramethyl uronium
HCC	Hepatocellular carcinoma
HRSP12	Heat-responsive protein 12
HIF-1α	Hypoxia-inducible factor 1α
HMBC	Heteronuclear multiple bond correlation
Hm^5C	5-Hydroxymethyl cytosine

HMGA-2	High mobility group A-2
HNRNP	Heterogeneous nuclear ribonucleoprotein
HOBt	1-hydroxybenzotriazole
HOMO	Highest occupied molecular orbital
Hp	Hairpin
HPLC/MS	High-performance liquid chromatography/mass spectrometry
HRMS	High-resolution mass spectroscopy
HRSP12	Heat-responsive protein 12
HSQC	Heteronuclear single-quantum coherence
HTRF	Homogeneous time-resolved fluorescence
HTS	High throughput screening
I	Inosine
IC_{50}	half inhibitory concentration
IGF2BP	insulin-like growth factor 2 mRNA-binding proteins
i-Pr	*iso*-propyl
iPSC	induced pluripotent stem cells
ITC	Isothermal calorimetry
LADME	Liberation, Absorption, Distribution, Metabolism and Excretion
LC-MS	Liquid chromatography-mass spectrometry
let-7	*lethal-7*
LIN28	human abnormal cell lineage protein 28
LIM	LIN28 interacting module
LUMO	Lowest unoccupied molecular orbital
lncRNA	long non-coding RNA

MALAT1	*Metastasis-associated lung adenocarcinoma transcript 1*
MAT2A	*methionine adenosyltransferase 2A*
m^1A	*N*1-methyladenosine
m^6A	*N*6-methyladenosine
m^3C	*N*3-methylcytidine
m^1G	*N*1-methylguanosine
Me	Methyl
MD	Molecular dynamics
MeCN	Acetonitrile
MeOH	Methanol
METTL3/5/14/16	Methyltransferase like3/5/14/16
m.p.	Melting point
miRNA	micro RNA
miR-98	micro RNA 98
mRNA	messenger RNA
MRP	Mitochondrial RNA processing
MTase	Methyltransferase
MTC	Methyltransferase complex
MTD	Methyltransferase domain
MTT	3-(4,5-dimethylthiazol-2-yl)-2,5-diphenyltetrazoliumbromide
ncRNA	non-coding RNA
NMR	Nuclear magnetic resonance
NMD	Nonsense-mediated mRNA decay
NLS	Nuclear localization signal

NoLS	Nucleolar localization signal
NSCLC	Non-small-cell lung cancer
o.n.	overnight
PAGE	Polyacrylamide gel electrophoresis
PAINS	Pan-assay interference compounds
PABPn1	poly(A)-binding protein 1
PAP	poly(A)-polymerase
PD-L1	Programmed cell death ligand 1
PE	Petroleum ether (b.p. = 40-60 °C)
PIC	Pre-initiation complex
psU (Ψ)	Pseudouridine
POI	Protein of interest
PPI	Protein–protein interaction
ppm	Parts per million
preE	pre-Element
pre-miRNA	Precursor miRNA
pri-miRNA	Primary miRNA
PRI	Protein–RNA interaction
PROTAC	Proteolysis targeting chimera
PTGR	Post-transcriptional gene regulation
p-TsOH	*para*-toluene sulfonic acid
PUS	Pseudouridine synthase
PyBOP	benzotriazol-1-yloxytripyrrolidinophosphonium hexafluorophosphate
Ran	Ras-related nuclear protein

Ras	Rat sarcoma
RBD	RNA binding domain
RBP	RNA–binding protein
R_f	Retardation factor
RIP-seq	RNA immunoprecipitation-sequencing
RISC	RNA-induced silencing complex
RMP	RNA–modifying protein
RNA	Ribonucleic acid
RNAi	RNA interference
RNA Pol II	RNA polymerase II
RNase	Ribonuclease
RNP	Ribonucleoprotein
rRNA	Ribosomal RNA
ROC1	Regulator of cullins 1
rt	Room temperature
RT-(q)PCR	Reverse transcription (quantitative) polymerase chain reaction
SAH	*S*-adenosylhomocysteine
SAM	*S*-adenosylmethionine
SAR	Structure-activity relationship
SARS-Cov2	Severe acute respiratory syndrome coronavirus 2
SH	Superfamily homology
siRNA	small interfering RNA
S_NAr	Nucleophilic aromatic substitution
snRNA	small nuclear RNA

snoRNA	small nucleolar RNA
SPR	Surface plasmon resonance
SRSF3	Splicing enhancer-binding SR protein 3
ss	Single-stranded
STD	Saturation transfer difference
TAE	Tris acetic acid EDTA containing buffer
t-Bu	*tert*-Butyl
TFA	Trifluoroacetic acid
THF	Tetrahydrofurane
THQ	Tetrahydroquinoline
TIC	Translation-initiation complex
TPD	Targeted protein degradation
TPEN	Tetrakis(2-pyridylmethyl)ethylenediamine
TRBP	Transactivation response element RBP
Tris	tris(hydroxymethyl)aminomethane
TRMT112	tRNA methyltransferase activator subunit 11-2
tRNA	transfer RNA
Ts	Toluenesulfonyl
TLC	Thin-layer chromatography
TUTase	Terminal uridylyltransferase
UHPLC	UltraHPLC
UPF1	Regulator of nonsense transcripts 1
UPS	Ubiquitin–proteasome system
UV	Ultraviolet

UTR	Untranslated region
VCR	Vertebrate conserved region
VHL	Von Hippel-Lindau
VIRMA	Vir-like m^6A methyltransferase-associated
WTAP	Wilms' tumor 1-associating protein
YTHDC1/2/3	YTH domain-containing protein 1/2/3
YTHDF1/2/3	YT521B homology domain family 1/2/3
ZC3H4/13	zinc finger CCCH-type containing 4/13
ZKD	Zinc Knuckle Domain

8 Appendix

Affidavit

Eidesstattliche Versicherung (Affidavit)

Name, Vorname
(Surname, first name)

Matrikel-Nr.
(Enrolment number)

Belehrung:

Wer vorsätzlich gegen eine die Täuschung über Prüfungsleistungen betreffende Regelung einer Hochschulprüfungsordnung verstößt, handelt ordnungswidrig. Die Ordnungswidrigkeit kann mit einer Geldbuße von bis zu 50.000,00 € geahndet werden. Zuständige Verwaltungsbehörde für die Verfolgung und Ahndung von Ordnungswidrigkeiten ist der Kanzler/die Kanzlerin der Technischen Universität Dortmund. Im Falle eines mehrfachen oder sonstigen schwerwiegenden Täuschungsversuches kann der Prüfling zudem exmatrikuliert werden, § 63 Abs. 5 Hochschulgesetz NRW.

Die Abgabe einer falschen Versicherung an Eides statt ist strafbar.

Wer vorsätzlich eine falsche Versicherung an Eides statt abgibt, kann mit einer Freiheitsstrafe bis zu drei Jahren oder mit Geldstrafe bestraft werden, § 156 StGB. Die fahrlässige Abgabe einer falschen Versicherung an Eides statt kann mit einer Freiheitsstrafe bis zu einem Jahr oder Geldstrafe bestraft werden, § 161 StGB.

Die oben stehende Belehrung habe ich zur Kenntnis genommen:

Official notification:

Any person who intentionally breaches any regulation of university examination regulations relating to deception in examination performance is acting improperly. This offence can be punished with a fine of up to EUR 50,000.00. The competent administrative authority for the pursuit and prosecution of offences of this type is the chancellor of the TU Dortmund University. In the case of multiple or other serious attempts at deception, the candidate can also be unenrolled, Section 63, paragraph 5 of the Universities Act of North Rhine-Westphalia.

The submission of a false affidavit is punishable.

Any person who intentionally submits a false affidavit can be punished with a prison sentence of up to three years or a fine, Section 156 of the Criminal Code. The negligent submission of a false affidavit can be punished with a prison sentence of up to one year or a fine, Section 161 of the Criminal Code.

I have taken note of the above official notification.

Ort, Datum
(Place, date)

Unterschrift
(Signature)

Titel der Dissertation:
(Title of the thesis):

Ich versichere hiermit an Eides statt, dass ich die vorliegende Dissertation mit dem Titel selbstständig und ohne unzulässige fremde Hilfe angefertigt habe. Ich habe keine anderen als die angegebenen Quellen und Hilfsmittel benutzt sowie wörtliche und sinngemäße Zitate kenntlich gemacht.
Die Arbeit hat in gegenwärtiger oder in einer anderen Fassung weder der TU Dortmund noch einer anderen Hochschule im Zusammenhang mit einer staatlichen oder akademischen Prüfung vorgelegen.

I hereby swear that I have completed the present dissertation independently and without inadmissible external support. I have not used any sources or tools other than those indicated and have identified literal and analogous quotations.

The thesis in its current version or another version has not been presented to the TU Dortmund University or another university in connection with a state or academic examination.*

*Please be aware that solely the German version of the affidavit ("Eidesstattliche Versicherung") for the PhD thesis is the official and legally binding version.

Ort, Datum
(Place, date)

Unterschrift
(Signature)